DOT/FAA/AR-xx/xx

Federal Aviation Administration
William J. Hughes Technical Center
Aviation Research Division
Atlantic City International Airport
New Jersey 08405

The FAA's Center of Excellence for UAS Research
ASSURE
Alliance for System Safety of UAS through Research Excellence

Annex A to Task A17: OSU Representative Fan Model and UAS Ingestion Studies

11/07/2022

Final Report

U.S. Department of Transportation
Federal Aviation Administration

NOTICE

THIRD PARTY RESEARCH. PENDING FAA REVIEW.

Technical Report Documentation Page

1. Report No.	2. Government Accession No.	3. Recipient's Catalog No.
FAA A11L.UAS.58		

4. Title and Subtitle	5. Report Date
Annex A to Task A17: OSU Representative Fan Model and UAS Ingestion Studies	(month and year printed)
	6. Performing Organization Code ASSURE: OSU
7. Author(s) Professor Kiran D'Souza, The Ohio State University (OSU) Dr. Dushyanth Sirivolu, OSU Mr. Mitchell Wong, OSU Dr. Eric Kurstak, OSU	8. Performing Organization Report No.
9. Performing Organization Name and Address The Ohio State University Aerospace Research Center 2300 West Case Road Columbus, OH 43235	10. Work Unit No. (TRAIS)
	11. Contract or Grant No.
12. Sponsoring Agency Name and Address U.S. Department of Transportation Federal Aviation Administration Office of Aviation Research Washington, DC 20591	13. Type of Report and Period Covered Final Report
	14. Sponsoring Agency Code 5401

15. Supplementary Notes
The Federal Aviation Administration Aviation William J. Hughes Technical Center Research Division COR was
16. Abstract

17. Key Words	18. Distribution Statement
Crashworthiness, Engine Ingestion, UAS, Ohio State University, OSU	This document is available to the U.S. public through the National Technical Information Service (NTIS), Springfield, Virginia 22161. This document is also available from the Federal Aviation Administration William J. Hughes Technical Center at actlibrary.tc.faa.gov.

19. Security Classif. (of this report)	20. Security Classif. (of this page)	21. No. of Pages	22. Price
Unclassified	Unclassified		

Form DOT F 1700.7 (8-72) Reproduction of completed page authorized

TABLE OF CONTENTS

LIST OF FIGURES

LIST OF TABLES

LIST OF ACRONYMS

AWG	Aerospace Working Group
CAD	Computer-Aided Design
CCW	Counter Clockwise
CFR	Code of Federal Regulations
COM	Center of Mass
EOS	Equation Of State
FAA	Federal Aviation Administration
FBO	Fan Blade Out
FE	Finite Element
LE	Leading Edge
GTL	Gas Turbine Laboratory
MFS	Mid-level Fan Speed
NIAR	National Institute for Aviation Research
OEM	Original Equipment Manufacturer
OSU	The Ohio State University
RPM	Revolutions Per Minute
SPH	Smoothed Particle Hydrodynamics
UAH	University of Alabama, Huntsville
UAS	Unmanned Aircraft System
UAV	Unmanned Aerial Vehicle

1. INTRODUCTION

The intent of this report is to describe a computational research program designed to create and simulate tests on a representative high bypass ratio fan. The newly designed fan includes key structural features found in modern high bypass ratio fans used for commercial transport. This report also intends to characterize the fan behavior when impacted with a common Unmanned Aerial Vehicle (UAV) at specific flight conditions, report on the computational results, and discuss future work. While a great deal is known about soft body impacts (usually birds) on propulsion systems, there is little literature on hard body impacts, such as UAVs. This work is a continuation of the first phase of Federal Aviation Administration (FAA) sponsored research on UAV engine ingestion work conducted at The Ohio State University (OSU)[1] Gas Turbine Laboratory (GTL). The first phase of research was limited in scope and modified an existing fan rig assembly model that was originally developed for fan blade-out simulations[2] of a generic mid-sized business class engine. The generic mid-sized business class model used in the first phase of research was not copied from any particular OEM engine design. The original model was modified to include a UAV model that was validated for conditions representative of a collision with the aircraft structure[3]. The current phase of research involves the development of a fan rig assembly model that is representative of a high bypass ratio fan (typically used in commercial transport) with regards to the structural and vibratory characteristics. This work also involves collaboration with the University of Alabama, Huntsville (UAH), which conducted high speed impact experiments with a UAV and its key hard components (motor, battery and camera) with a titanium test article. The titanium test article has similar features compared to the representative fan blade model for particular impact locations. These experiments were used by the National Institute for Aviation Research (NIAR) at Wichita State University to update and validate a quadcopter model at engine ingestion conditions. The validated quadcopter model and representative fan rig assembly model were then used by the OSU GTL to conduct a series of ingestion simulations to determine the most important parameters of the ingestion and how the UAV ingestion differentiates from a bird strike.

1.1 MOTIVATION

The use of Unmanned Aircraft Systems (UASs) has increased dramatically in recent years. As the number of UASs sold continues to increase, it is of the utmost importance that they are properly integrated into the airspace. The first priority in integrating UASs into the airspace is to keep them out of the space of manned aircraft to prevent collisions from occurring. The second priority in integrating UASs into the airspace is to create detect and avoid technologies to help prevent collisions when these aircraft do end up in the same airspace as manned aircraft. Finally, it is important to understand the effects of airborne collisions if they do occur, so that: the public can be educated of the hazards of these events; flight crews can be trained on what to expect during these scenarios; and critical design features of UASs can be better understood to influence future designs in this nascent industry to help mitigate potential damage. Preliminary computational work investigating UAV ingestions has shown that UASs can cause significantly more damage than birds[4]. This work seeks to provide additional studies of UAS ingestions with a fan model that has been specifically developed for this study and a UAS model validated for similar conditions to a UAS engine ingestion to provide a clearer understanding of the damage that occurs under a variety of conditions.

1.2 SCOPE OF WORK

The OSU GTL was responsible for coordinating the overall research program, supporting the planning and execution of experimental testing conducted at UAH, supporting the computational simulations and updating of the quadcopter models by NIAR[5], creating a fan rig model representative of structural and vibratory features with industrial partners, and carrying out the ingestion simulations with the fan and updated quadcopter model. The fan rig model does not contain most of the downstream components of the fan (i.e., compressor, combustor and turbine), and therefore any damage in these components is outside the scope of this research. The body of this report is focused on the primary tasks that OSU was responsible for: the creation of the fan rig model and the ingestion simulations. Key analysis and supporting tasks for the experiments at UAH and the work done by NIAR in updating the quadcopter model are included in the Appendices of this report. Appendix A discusses the development of the test matrix and some of the test conditions for the experiments. Appendix B discusses the development of the final test article used for the experiments.

The research was carried out in close collaboration with industrial engine manufacturers to create a Finite Element (FE) model of a representative high bypass ratio fan that allows capturing the critical features of a fan UAS impact. Wherever feasible, the FE models were developed with pre-existing material models to leverage previous work in the field. The UAV model used for the ingestions is a quadcopter model developed by NIAR[3] and updated in this research program to be validated for conditions similar to an engine ingestion as discussed in Annex B[5]. The ingestion simulations were carried out in LS-DYNA (a FE analysis software that specializes in highly nonlinear transient dynamic analysis) for a variety of impact scenarios. The specific scenarios were determined in consultation with industry partners and the FAA management team. The ingestion scenarios were simulated following the best practices set forth by the LS-DYNA Aerospace Working Group[6] (AWG).

2. REPRESENTATIVE FAN RIG MODEL

One of the key objectives of this research program was to create an open fan model that has representative structural and vibratory features of modern high-bypass ratio fans (typically used in commercial transport). This open fan model can then be used in this study to investigate UAV impacts with fans and could also be used in future computational investigations. The fan was not designed to match the aerodynamic features nor the aeroelastic response of modern engines. This task was carried out in close collaboration with engine Original Equipment Manufacturers (OEMs) to maximize its utility. Other key components of the fan-rig model were also created in close collaboration with industry and these include: the fan containment ring, nose cone, shaft, and blade retention systems. The purpose of the inclusion of these components was to provide reasonable boundary conditions for how the fan and UAV will interact during the collision. They provide additional insight into the expected forces and energies that are transmitted into these systems; however, trying to determine failure in components outside of the UAV and fan blade/disk was not a focus of this fan rig model.

2.1 JUSTIFICATION

There are a variety of fan designs that have been created for a number of engine architectures and each engine OEM tends to have their own preferences and designs. The type of fan chosen for this work consists of solid titanium blades, which all OEMs have familiarity with, and are appropriate for the 1.57 m (62 in) fan diameter. This fan diameter is close in size to several modern engines including: CFM56-7B – Boeing 737 (General Electric and Safran Aircraft Engines) 1.55 m (61 in) fan diameter; PW1700G – Embraer E-Jets (Pratt & Whitney) 1.425 m (56 in) fan diameter; PW1200G – Mitsubishi Reginal Jets (Pratt & Whitney) 1.425 m (56 in) fan diameter; PW6000 – Airbus A318 (Pratt & Whitney) 1.44 m (56.5 in) fan diameter; and BR715 – Boeing 717 (Rolls-Royce) 1.47 m (58 in) fan diameter. Currently, solid titanium fans in this size bracket are by far the most numerous products in service with a significant amount of flights. Therefore, probability would suggest that if an ingestion were to occur, it would most likely be on a single isle aircraft with engines that are similar to this representative model.

The fan geometry was created from scaling a smaller fan geometry up to the 1.57 m (62 in) fan diameter, and removing proprietary features that were related to the aerodynamics and not the structural properties of the fan. Since building a truly representative containment ring and nose cone was not feasible due to the myriad of existing architectures, these models were included only to provide appropriate boundary conditions for the ingestion. The containment ring and nose cone models were designed with input from engine OEMs to have reasonable geometries for this representative fan. The containment ring and nose cone parts were modeled with a linear elastic material with no failure to understand the expected loads they might encounter. The shaft was modeled as a rigid body.

The fan rotational speeds and aircraft speeds for this fan were identified for various phases of flight based on industrial guidance and a previously published FAA report[7], and are listed in Table 1.

Table 1. Engine rotational speeds for different phases of flight.

Phase of flight	Engine (RPM)	N1	Nominal flight speed
Take-off	5175	100%	67 m/s (130 kts)
Flight below 3,048 m (10,000 ft)	3623	70%	129 m/s (250 kts)
Cruise at 9,144 m (36,000 ft)	4657.5	90%	252 m/s (490 kts)
Approach	1138.5	22%	67 m/s (130 kts)

2.2 COMPUTER-AIDED DESIGN (CAD) MODELS

2.2.1 Representative Fan Geometry

The generic fan developed for this project is representative of the structural and vibratory properties of a modern high bypass ratio fan commonly used for commercial transport. The fan diameter is 1.57 m (62 in). The fan assembly includes an airfoil, dovetail, retainer, retention ring, disk and disk flange, which are all shown in Figure 1. In these types of fans, the airfoil and dovetail are a single unit, called a blade, that can be pulled out of their slot in the disk and replaced if damage or failure occurs (e.g., after a bird strike). A total of 24 blades were used in this representative fan model. Due to the nature of the disk flange, a two-blade model is needed to define a single cyclic sector model; therefore there are 12 cyclic sectors that are repeated to form the 24 blade model.

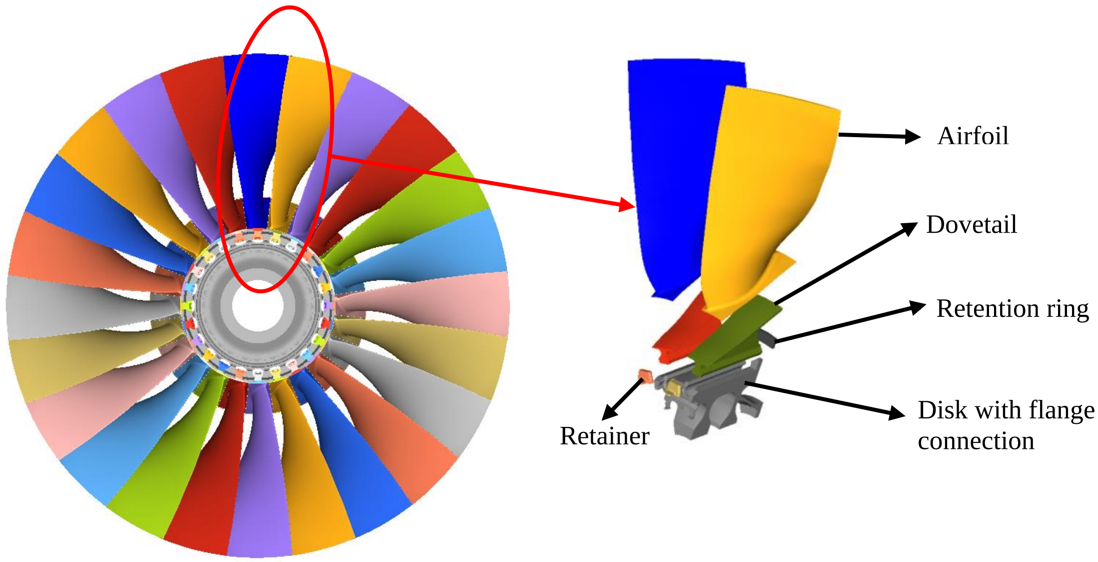

Figure 1. Components of the representative fan model.

The radial distance from the root of the disk to tip of the airfoil is 693 mm (27.3 in). The root of the airfoil is on an incline causing the radial span at the leading edge (549 mm) to be larger than the radial span at the trailing edge (442 mm) of the airfoil, as shown in Figure 2.

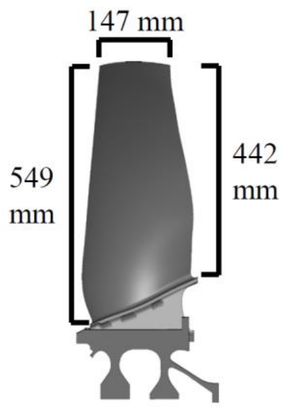

Figure 2. Side profile of blade with airfoil dimensions.

Additional information regarding the airfoil geometry is given in Figure 3, which shows some cross sections taken at different span locations. The cross sections of Figure 3 have span locations of 243.0, 276.1, 405.4, 534.1, 664.3, and 787.3 mm, if measured at the leading edge, and 338.8, 377.6, 417.5, 536.4, 668.1, and 787.1 mm, if measured at the trailing edge, for cross sections labeled A, B, C, D, E, and F, respectively. These span locations were measured radially from the centerline of the disk. The angle of twist in the airfoil is 63 degrees from the root to the tip.

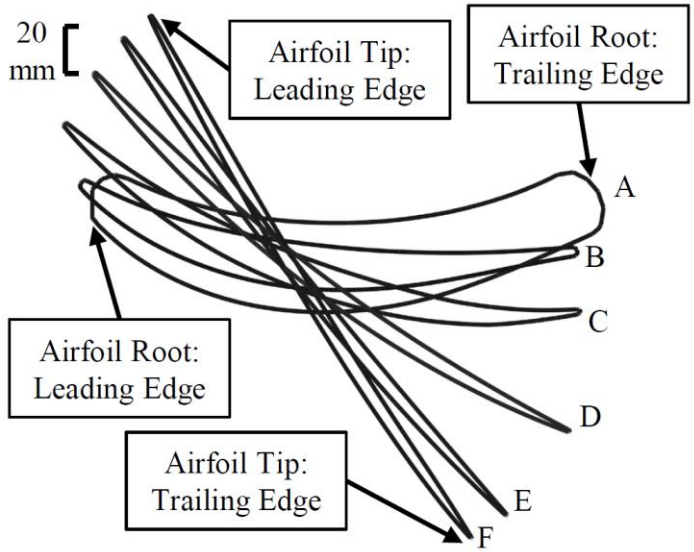

Figure 3. Chordwise profiles of the airfoils at different spanwise locations.

The dovetail used in this model has a flank length of 8.46 mm and a flank angle of 50 degrees. A layer of pad elements highlighted in red in Figure 4 were initially used in the contact region between the dovetail and disk. However, these elements were removed when conducting finite element simulations, and the contact in this region was defined using offset settings to provide a more stable and accurate result.

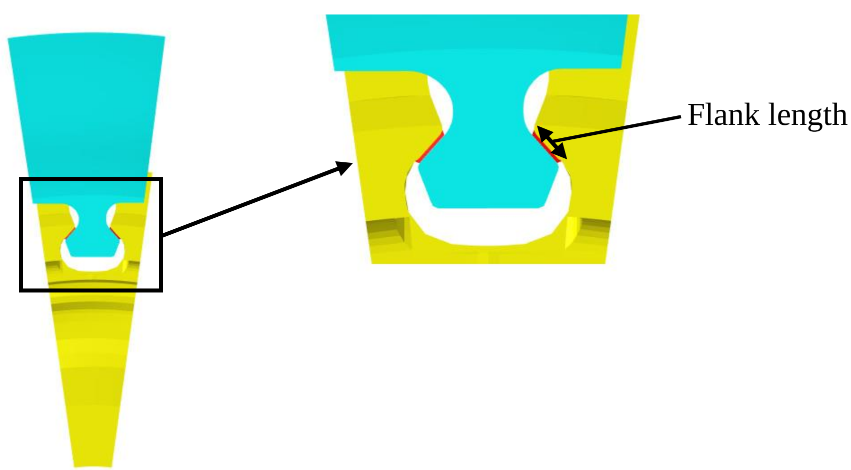

Figure 4. Contact region between the airfoil and disk parts.

The airfoil retainer is used to secure the dovetail into the disk after it is installed. This retainer prevents the blade from moving forward in the axial direction when the fan is generating thrust and placing axially loads on the disk and shaft. The retainer can be seen in Figure 5 and an example of its location in the full fan model can be seen in Figure 1.

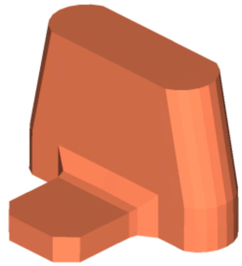

Figure 5. Retainer for blade root.

The retention ring, which is connected to the disk on the rear side of the fan, prevents the blades from sliding axially further than intended. The retention ring is a simple ring design and is shown in Figure 6.

Figure 6. Retention ring for backside of blade root.

The flange on the front of the disk provides a way to bolt the nose cone to the disk. The flange is shown in Figure 7 and is also indicated in Figure 1 as a part of the whole fan model. The diameter of the bolt holes on the disk flange are 6 mm and there are a total of 24 bolt holes for the full fan assembly. Due to the inclusion of the flange, a cyclic symmetric model of the fan requires two blades instead of one, which corresponds to including one full bolt hole and two half holes in the flange. This cyclic model is shown in Figure 1.

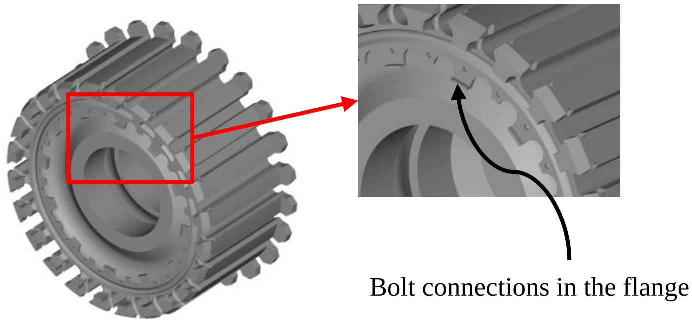

Figure 7. Flange on disk that connects to the nose cone.

2.2.2 Casing

Engine fans are contained within a casing to optimize airflow through the engine, protect the engine from foreign object debris, and contain fan blades during a blade-out event or other engine failure. The casing used for the fan assembly model created in this project is shown in Figure 8 and has a total length of 1.580 m (62.2 in) and an internal diameter of 1.586 m (62.44 in). A hot clearance (i.e., clearance when the fan is spinning at its nominal rotational speed) of 3.81 mm (0.15 in) is used between the airfoil and the internal diameter of the casing. The thickness of the casing at the inlet and outlet is 4.1 mm (0.16 in).

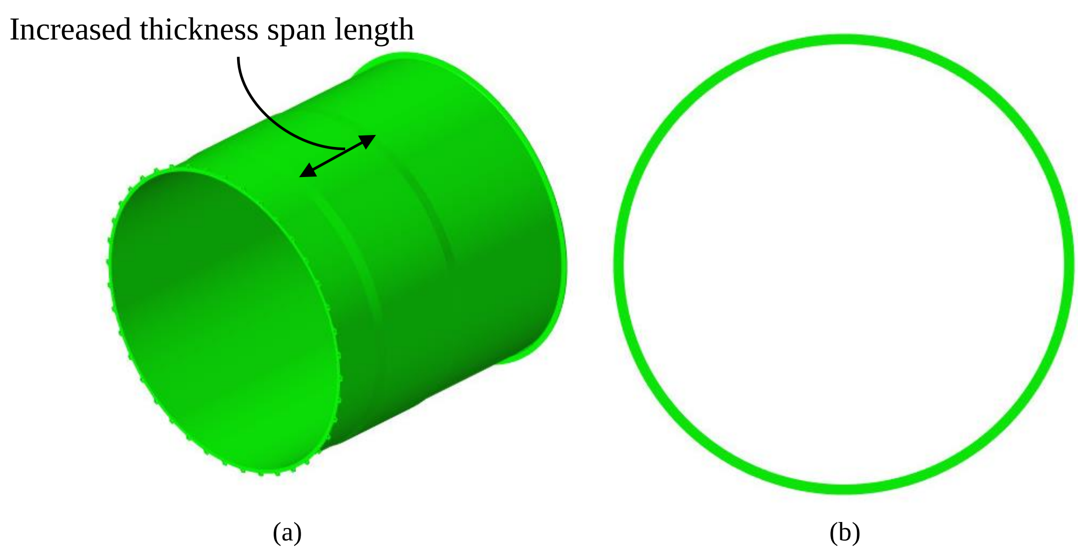

Figure 8. Fan casing (a) isometric view, and (b) front view.

The portion of the casing around the fan is designed to withstand a fan blade-out event to protect the aircraft in the event of a blade failure. The containment design often starts with an energy balance approach[6, 8, 9] to calculate the minimum thickness of the casing in the impact region. Engine manufacturers have a variety of containment architectures for different engine types and sizes with the intent of maximizing durability while minimizing weight. The engine manufacturers generally design the casing using their proprietary architectures and proprietary material models and run simulations in nonlinear transient dynamic simulation tools, like LS-DYNA, to build confidence in the design before bench tests and full certification tests are conducted on a prototype. In this model, the primary purpose of the casing is to provide an appropriate boundary condition for the fan to capture first order effects of the UAS ingestion, while also maximizing the parameter space for how the ingestions can occur (i.e., not having an inlet smaller than the fan diameter, which would restrict the UAV's entry into the engine). For this reason, the casing thickness around the fan was determined using the energy balance approach[6, 8, 9], which is outlined below.

To prevent failure of the engine casing, the kinetic energy of the blade during a blade-out event must be, at a minimum, matched by the strain energy of the plastically deformed region of the engine casing after being impacted. The kinetic energy of the blade is calculated based on its rotational motion just prior to the blade-out event:

$$KE = \frac{1}{2} I \omega^2, \tag{1}$$

where KE is the kinetic energy, I is the moment of inertia of the blade taken with respect to the rotational axis of the fan, and ω is the angular velocity of the fan blade.

The strain energy of the plastically deformed region of the engine casing is computed by multiplying the strain energy density of the material by its volume where the strain energy density is approximated as[8]

$$SE = \frac{1}{2}\left(\sigma_y + \sigma_{ult}\right)\varepsilon_f V, \tag{2}$$

where SE is the strain energy, σ_y is the yield strength, σ_{ult} is the ultimate strength, ε_f is the strain at fracture, and V is the volume of the plastically deformed material. The casing material chosen for this model is the titanium alloy Ti-6Al-4V and values of σ_y, σ_{ult}, and ε_f were obtained at strain rates of 1.0E-2 s^{-1}, 1.0 s^{-1}, and 1645 s^{-1} for this material from materials testing previously performed in the development of a material model for the titanium alloy in LS-DYNA[10]. The volume of the plastically deformed material is then the area of the initial impact, A_i, plus the enhanced area, A_e, shown in Figure 9, due to the propagation of the plastic wave for the duration required for the blade to pass through the thickness of the casing multiplied by the thickness of the casing, h:

$$V = (A_i + A_e)h. \tag{3}$$

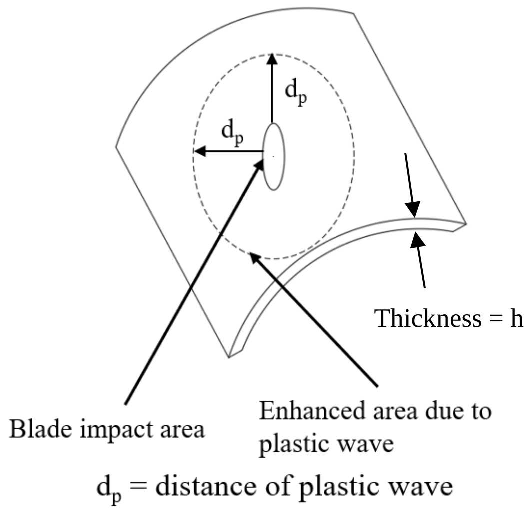

Figure 9. Plastically deformed region due to impact event.

The initial impact area is approximated as an ellipse with an area equivalent to the surface area of the blade tip. The plastic wave speed, v_p, which is required to determine the enhanced area is given by

$$v_p = \sqrt{\frac{K}{\rho}}, \tag{4}$$

where K is the bulk modulus of the titanium alloy and ρ is the density of the titanium alloy. The time required, t, for the blade to pass through the casing is approximated as

$$t = \frac{v_i}{h}, \tag{5}$$

where v_i is the impact velocity of the blade tip. The distance that the plastic wave travels, d_p, is then

$$d_p = v_p t, \tag{6}$$

and the enhanced area can then be computed.

The required casing thickness of the casing around the fan was computed to be 12 mm (0.47 in) over a span of 481.6 mm (18.96 in), with this section of the casing noted in Figure 8. Note that failure will be turned off for the material model of the casing and this computed casing thickness will provide an appropriate first order approximation of the casing response during an ingestion event.

2.2.3 Nose Cone

The type of nose cone selected for the representative fan assembly model is a bi-conic like design shown in Figure 10. The nose cone was modeled as aluminum, which is consistent with previous UAV engine ingestion work[1] and is a representative light weight material often used in aeronautical applications. The forward cone has a length L_1 = 211.4 mm (8.3 in) and a base radius R_1 = 182 mm (7.16 in), and is stacked on a frustum of a cone of length L_2 = 115.5 mm (4.47 in) and base radius of R_2 = 239.5 mm (9.42 in). The overall thickness of the nose cone is 2.5 mm (0.1 in), a clearance of 2.5 mm is maintained between the nose cone and the dovetail region, and a tip radius of 2.5 mm is used. The nose cone is rigidly connected to the fan assembly through 24 bolt connections at the disk flange located on the front of the fan.

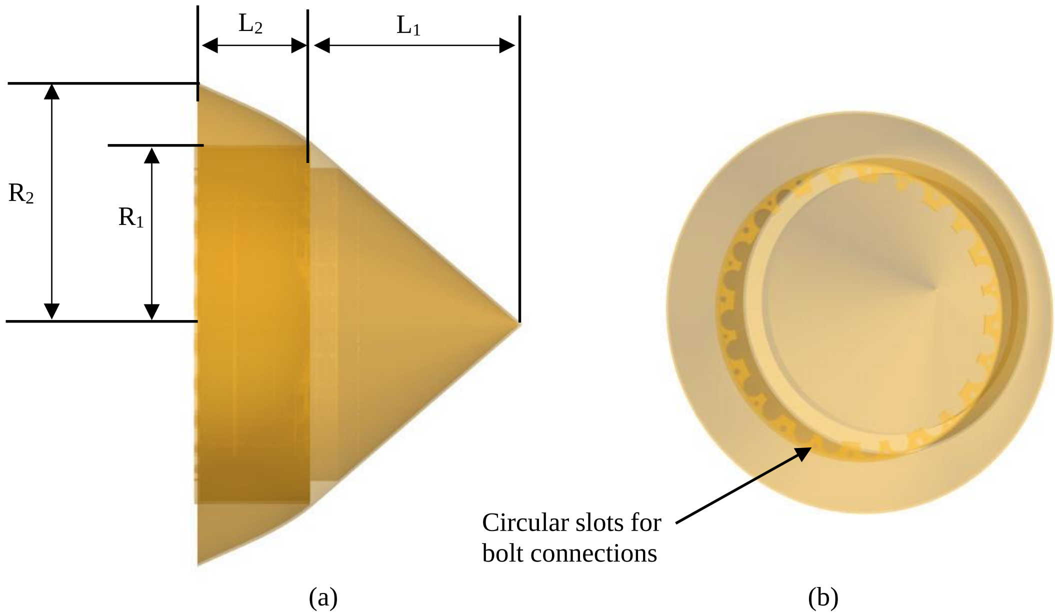

Figure 10. (a) Side view of the biconic nose cone (b) front oblique transparent view of biconic nose cone.

2.2.4 Shaft

The low pressure shaft connects the fan to the low pressure turbine to form the low pressure spool of the engine. The low pressure turbine extracts energy from the flow in order to drive the fan through the low pressure shaft. The CAD model for the shaft was based on drawings of the CFM56[11], a high bypass ratio turbofan. The shaft was modeled with a steel that is representative of the shaft material often used in a turbofan engines. The cylindrical shaft had a total length of 0.915 m (36 in) and is shown in Figure 11. The shaft has an internal diameter of 83.8 mm (3.3 in) and a thickness of 5 mm (0.2 in) along the majority of its length. There was a rapid expansion in diameter towards the forward face of the shaft where it meets the disk. The outer diameter of the front face of the shaft is 241.9 mm (9.5 in) and the holes on this face have a diameter of 18 mm (0.7 in).

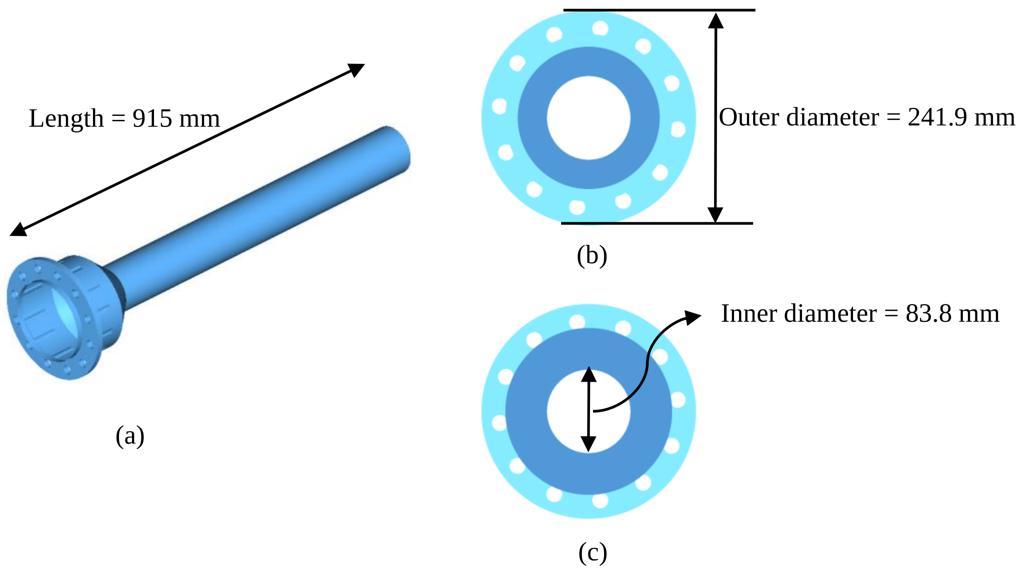

Figure 11. Shaft (a) isometric (b) front and (c) back views.

2.3 FINITE ELEMENT MODELS

2.3.1 Fan Assembly

The fan assembly is composed of the disk, disk flange, dovetail, airfoil, retainer, and retention ring. The disk, disk flange, and retention ring are treated as single contiguous parts while the dovetail, airfoil, and retainer are repeated parts for each of the 24 fan blades. How the FE model for each part was developed and integrated into the fan assembly is described below.

The disk, dovetail, airfoil, and retention ring are composed of a titanium alloy (Ti-6Al-4V) and were modelled using the *MAT_TABULATED_JOHNSON_COOK (*MAT_224) material model in LS-DYNA. The retainer is also composed of the same titanium alloy but was modelled as elastic using the *MAT_ELASTIC keyword. Material information for the Ti-6Al-4V alloy was obtained from a publicly available material model created in previous FAA projects[10, 12] and made available by the Aerospace Working Group[13, 14].

All components of the fan assembly were meshed using solid hexahedron elements and defined with a constant stress solid element (ELFORM=1) in their section cards. This under-integrated element formulation has the consequence of nonphysical, zero-energy modes of deformation called hourglass modes. To inhibit these hourglass modes there exist algorithms in LS-DYNA that can be invoked using the *HOURGLASS keyword. Each part with constant stress solid elements also had hourglass control defined with the type IHQ = 6 and the coefficient QM = 0.1.

The contact defined between the parts in the Fan assembly will be discussed in the context of each simulation. It should be recognized that in some simulations certain contact definitions were not included or additional contact definitions were applied depending on the dynamics involved in that specific simulation. The contact algorithms used in LS-DYNA make up a significant portion of the computational cost for a simulation, so contacts were only defined as needed.

A key consideration in constructing the mesh for the model is the level of refinement in the mesh. In particular, the level of refinement in the mesh airfoils where the UAV impacts is of utmost importance. A refinement study was conducted to determine the level of refinement in the airfoils to reach convergence from models of the angled titanium plates used for the validation of the UAS model. The results of this refinement study are included in Appendix B. Note that during the validation of the UAS model (detailed in Annex B[5]) with the experimental data (discussed in Annex C[15]) it was determined that three elements through the thickness of the airfoil was optimal for matching the mesh of the airfoil with the mesh of the UAV model (as discussed in the appendix to Annex B[5]). A mesh of the airfoil with part of the platform is shown in Figure 12.

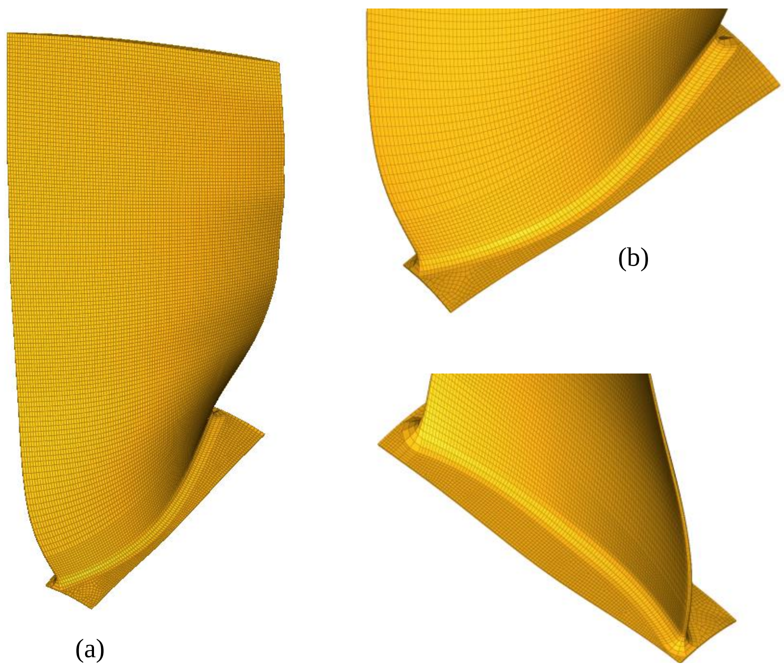

(a) (b) (c)

Figure 12. Airfoil mesh with three elements through the thickness (a) isometric view (b) suction side of the airfoil root and (c) pressure side of the airfoil root.

The mesh of the dovetail and blade platform is shown in

Figure 13. Note that, due to the complexity of the geometry of both the airfoil and the dovetail, these parts were split into two components and meshed separately to provide well behaved hexahedral meshes. Additionally, the airfoil shown in Figure 12 does include the top of the platform. The part was partitioned in this manner to move the contact region defined between the two parts below the higher stress region where the airfoil transitions into the platform. Erroneous element deletion did occur in preliminary analysis of the blade in the fillet region of the airfoil during impact simulations when the blade was partitioned where the airfoil meets the platform. The contact card defined between the airfoil and the platform is *CONTACT_TIED_SURFACE_TO_SURFACE. This contact formulation was the same across all simulations.

Figure 13. Mesh of dovetail and blade platform.

The disk was meshed to have a similar mesh density as the blade platform near the contact points and is shown in Figure 14.

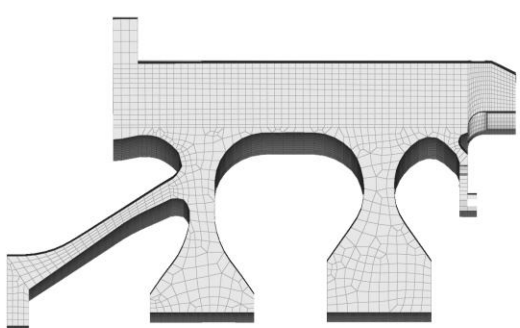

Figure 14. Side view of a sector of the fan disk mesh.

The disk flange was originally modeled as a separate part and its mesh is shown in Figure 15. The flange was then integrated with the disk part, and modeled as a single part in all the simulations.

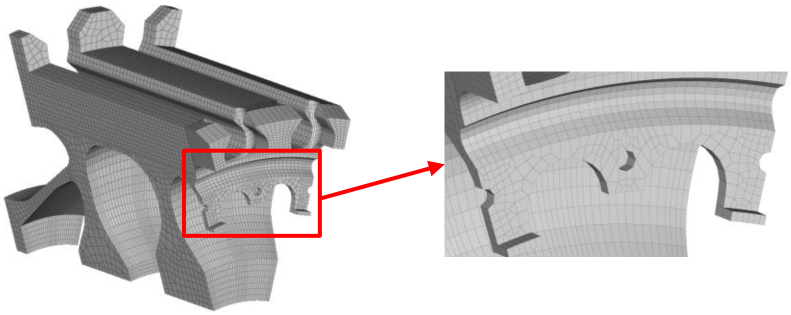

Figure 15. Disk flange mesh.

The retainer mesh is shown in

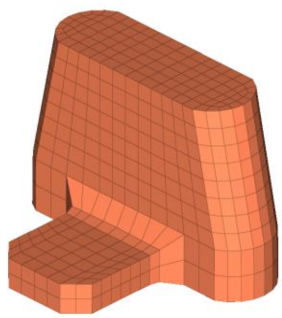

Figure 16 and a single sector of the retention ring mesh is shown in Figure 17. These parts had relatively simple geometries and the mesh density was selected to have a few elements through the thickness while maintaining good aspect ratios.

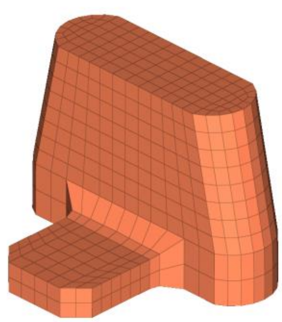

Figure 16. Single retainer mesh.

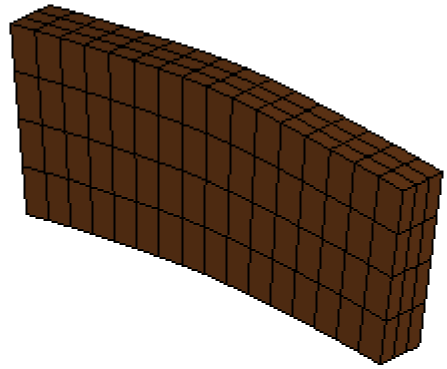

Figure 17. Mesh of a single sector of the retention ring.

Properties of the meshes of key components of the fan assembly are given in Table 2. A comparison is given with the AWG guidelines best practices[6]. Note that due to the complexity of the geometry and desire to have a fully hexahedral mesh not all of the AWG guidelines best practices could be met simultaneously.

Table 2. Properties of meshes of key components of the fan assembly.

AWG guidelines	Airfoil	Dovetail	Disk with flange	Retainer	Retention Ring
Elements through the thickness	3				
Total number of elements (per sector)	45,308	27,627	38,350	1,168	384
Warpage	1598 elements > 5 (Max. = 41.63)	3448 elements >5	1348 elements > 5 (Max. = 68.96)	Max. = 2.78	9 elements > 5 (Max. = 8.98)
Aspect ratio	1159 elements > 10 (Max. = 24.67) 2 elements greater than 23	Max. = 8.34	428 elements > 10 (Max. = 23.08)	Max. = 4.14	Max. = 2.76
Minimum length	0.192 mm	0.29 mm	0.25 mm	0.92 mm	2.42 mm
Maximum length	12.19 mm	7.57 mm	9.84 mm	4.33 mm	6.70 mm
Jacobian	148 elements < 0.5	565 elements	724 elements < 0.5	Min. = 0.5	Min. = 0.94

	(Min. 0.3)	< 0.5 (Min. 0.3)	(Min. 0.2)		
Minimum solid angle	10 elements < 20 deg (Min. = 11.81)	1 element < 20 deg (Min. = 19.71)	108 elements < 20 deg (Min. 9.88)	Min. = 29.98	Min. = 84.24
Maximum solid angle	729 elements > 135 (Max. Angle = 170.56)	3110 elements > 135 (Max. angle = 171.06)	4250 elements > 135 (Max. angle = 170.55)	10 elements > 135 (Max. angle = 154.33)	Max. = 95.90

2.3.2 Casing

The casing was modeled with the Ti-6Al-4V alloy elastic material model using the *MAT_ELASTIC keyword with the exact same properties as the retainer. The casing was meshed with quadrilateral shell elements. In the preliminary simulations, the default Belytschko-Tsay shell element formulation (ELFORM=2) was used but due to unstable energies in the casing due to the UAS impact, the element formulation was changed to a fully integrated shell element (ELFORM=16). The hourglass control type selected was IHQ=4 with coefficient QM=0.1 for the finalized UAS ingestion simulations. The casing model was not developed to evaluate containment during the ingestion. It was included to provide an appropriate boundary condition during the ingestion and to extract out energies imparted to the casing during the ingestion events. This simple geometry and material model can adequately address these needs at a low computational cost.

The casing did not undergo rotational motion like the other parts in the fan rig model, so a node set containing all of the nodes for the casing was created and these nodes were constrained to not translate in any direction. An oblique view of the casing is shown in Figure 18 with the constrained nodes indicated.

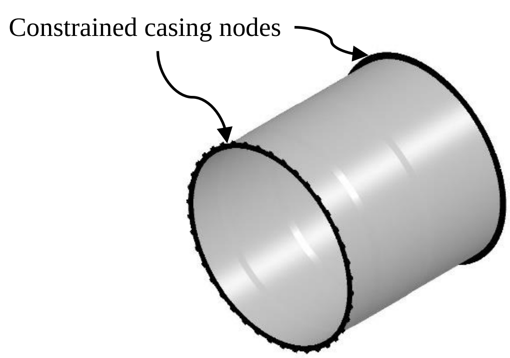

Figure 18. Oblique view of casing mesh with constrained nodes indicated.

2.3.3 Nose Cone

The bi-conic nose cone was composed of the aluminum 2024 alloy and was modelled as elastic using the *MAT_ELASTIC keyword. Material information for aluminum 2024 was obtained from prior FAA projects[16] with the material models being made available by the AWG[17]. The nose cone was meshed using solid hexahedron elements, and the element formulation used was the constant stress solid element (ELFORM=1). In the same manner as the fan assembly parts with the constant stress elements, the nose cone had hourglass control defined with the type IHQ = 6 and the coefficient QM = 0.1. An oblique view of the nose cone elements can be seen in Figure 19.

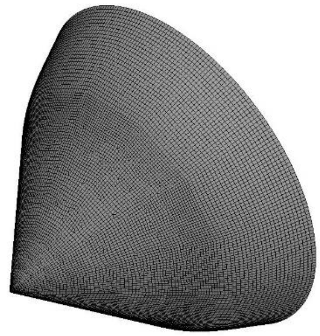

Figure 19. Oblique view of bi-conic nose cone mesh.

2.3.4 Shaft

The shaft was modeled as a rigid body using the *PART_INERTIA keyword with mass and inertia properties included. The shaft used the default Belytschko-Tsay shell element formulation (ELFORM=2), and hourglass controls IHQ=2 and QM=0.1. The keyword *MAT_RIGID was used to define the material for the shaft and the material properties were that of stainless steel[2]. The rotation of the shaft at various speeds for different cases in this report required the *BOUNDARY_PRESCRIBED_MOTION_RIGID keyword to be defined along with a vector in the direction of the rotational axis.

Due to the model being restricted to the fan assembly and no available information on the other downstream components that connect to the shaft (i.e., bearings, compressor stages and turbine stages), the shaft was modeled as a rigid body moving with the prescribed speed. Since the shaft is rigid, no contact was applied at the disk interface and instead the disk is simply driven with the same prescribed motion where it would interface with the shaft. Not including the shaft-disk contact simplifies the computational model without affecting the results. Note that the shaft is included only as a visual reference in the simulations. The shaft mesh is shown in Figure 20.

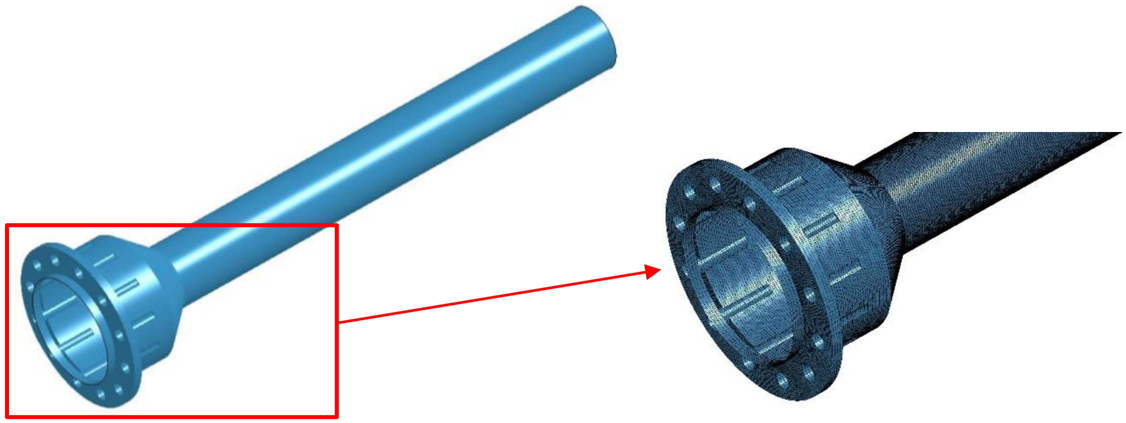

Figure 20. Shaft mesh.

2.4 DYNAMIC SIMULATIONS

Dynamic simulations were conducted on the fan model to ensure that it meets the key structural and vibratory requirements of a fan to meet certification requirements and provide reference information for further analysis.

2.4.1 Modal Analysis

A key structural requirement of the fan model was that the first bending mode of the fan does not experience a resonance condition under an engine order one excitation (EO1). A resonance condition would cause the fan blades to experience large vibrational amplitudes, leading to life cycle fatigue problems. Only the first bending mode was examined due to the higher likelihood of being excited by the incoming air. Similarly, only engine order one excitation was considered during the modal analysis post-processing. This analysis was done to ensure that the representative fan would be a viable fan design over its entire operational range at its size.

The modal analysis included only the blade and excluded any portion of the disk. The blade dovetail region was fully constrained, allowing only the airfoil to move. The fixed region is shown in Figure 21. Blade-alone modeling of the system and the accompanying constraints were chosen based on recommendations by participating engine manufacturers to better match their internal analysis best-practices. The rotational speed of the fan influences the final vibratory response of the system due to rotational speed effects such as stress-stiffening and spin-softening. For the purposes of running a pre-stressed modal analysis, the fan model was imported into ANSYS Mechanical APDL and a static structural analysis was run with a specified rotational speed. The rotational speed is modeled as radially outward forces with the magnitude dependent on the rotational speed. The static structural analysis considered large deflections, which achieves greater accuracy for static structural analyses by incrementally solving toward the final loading conditions and updating the system mass and stiffness matrices at each step. The calculated static stress field and the deformed airfoil shape from the static structural analysis were then used in the subsequent modal analysis to calculate the final natural frequencies.

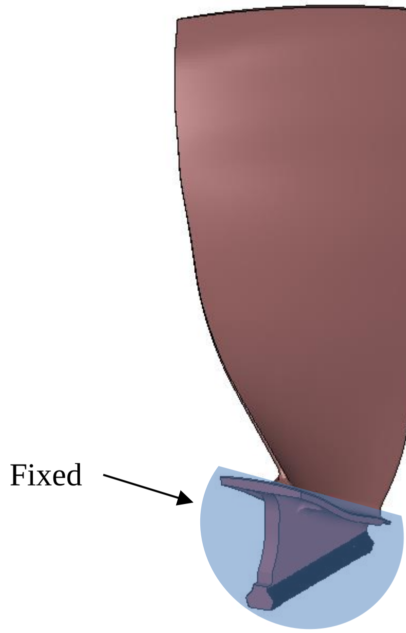

Figure 21. Blade-alone model showing portion of blade with fixed constraints.

The blade-alone, pre-stressed modal analyses were calculated at multiple rotational speeds between 0 and 6,000 Revolutions Per Minute (RPM) to capture the full non-linear effects. The resulting Campbell diagram is depicted in Figure 22, where the first bending mode natural frequency (black line), is shown to be increasing quadratically with rotational speed. Also depicted in Figure 22 are the first 10 engine order excitation lines, shown in blue. Three specific rotational speeds were of concern: 1) take off speed of 5175 RPM; 2) cruise speed of 4658 RPM; and 3) descent speed of 1139 RPM. There is no expected resonance of the blade at any of the three operating rotational speeds of the fan, or at any rotational speed within the operational speed range of the fan.

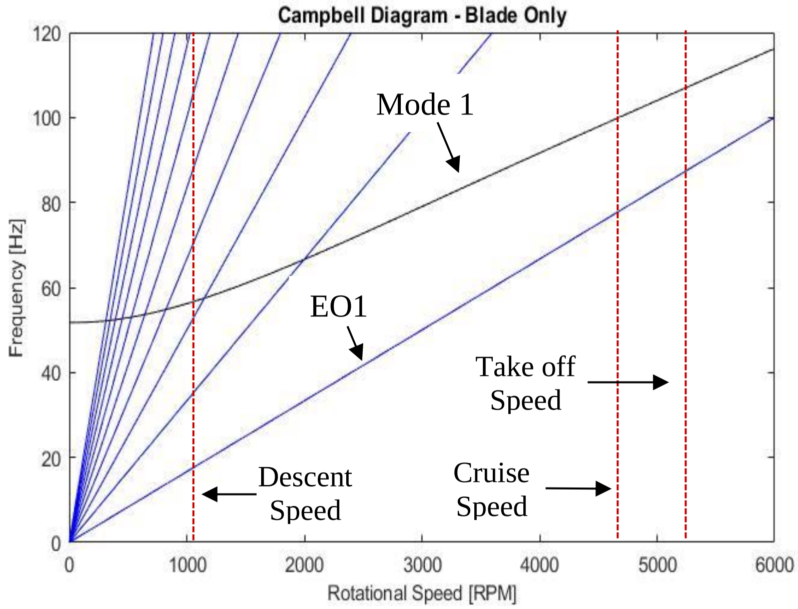

Figure 22. Blade-alone Campbell diagram.

The strain distribution on the pressure and suction side of the airfoil is also observed in Figure 23. The strain distribution shows more strain located near the airfoil root, with elevated values near the center region. Specific strain values are not reported because the deflection amount is unknown which would determine the final strain.

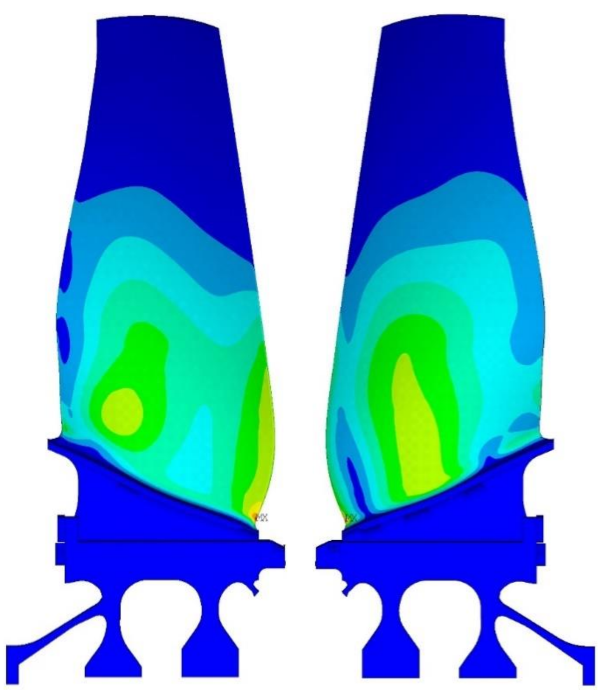

Figure 23. Pressure side (left) and suction side (right) strain distribution for the first mode.

2.4.2 Pre-stress Analysis

During operation of the engine, the fan can be rotating at a number of speeds. The higher the rotation speed, the larger the stresses in the blade and disk due to centrifugal loads. The fan design must be able to withstand these forces without any permanent plastic deformation. The stress in the fan and corresponding blade deflections can be computed using an explicit and/or implicit process. In this work, the implicit method used to conduct the pre-stress analysis will be discussed. This analysis will be used not only to compute the stresses in the blades to ensure the validity of the design, but also as a starting point for future dynamic simulations that will be discussed in this report (i.e., blade-out, bird ingestion, and UAS ingestion).

Consider a body of mass, m, rotating at constant angular velocity, ω, about an axis that is subject to a constant centrifugal load, F, given by

$$F = mr\omega^2, \tag{7}$$

where r is the distance from the axis of rotation to the center of gravity of the body. For a rotating fan blade, this force results in a constant stress in the blade called the pre-stress. The pre-stress must be incorporated into the fan model before further analysis such as a bird strike, blade out, or UAS impact can be performed. A two-step pre-stress analysis was performed in LS-DYNA by applying the centrifugal load using the implicit solver followed by the explicit solver to rotate the fan and verify the stability of the solution.

The high bypass-ratio fan model developed for this project has 24 blade sectors, but due to the geometry of the flange between the disk and nose cone, the fan model is symmetric for a 30° arc rather than a 15° arc. Taking advantage of the rotational symmetry in the fan, the implicit step of the pre-stress analysis was performed on a two-sector assembly shown in Figure 24 where the nodes shared by the disk and retention ring parts were merged. In this analysis, length was measured in millimeters, time in seconds, mass in metric tonnes, and force in newtons.

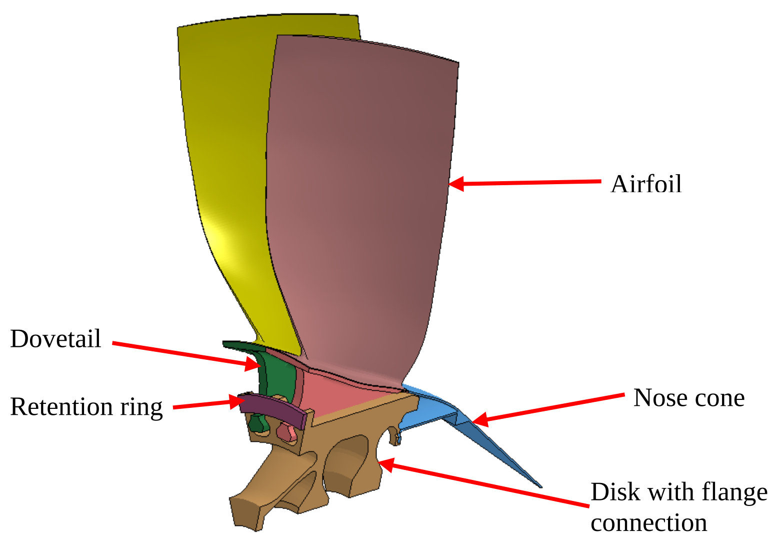

Figure 24. Two-sector assembly for implicit step of pre-stress analysis (retainer not visible).

For a rotating fan blade, there exists a pressure gradient between two sides of the blade with the higher pressure side called the pressure side and the lower pressure side called the suction side. Note that in this work, air pressure loads were neglected during these short duration dynamic simulations since the impact loads are greater by an order of magnitude. For the two fan sectors rotating in a counterclockwise direction, both sides are shown in Figure 25.

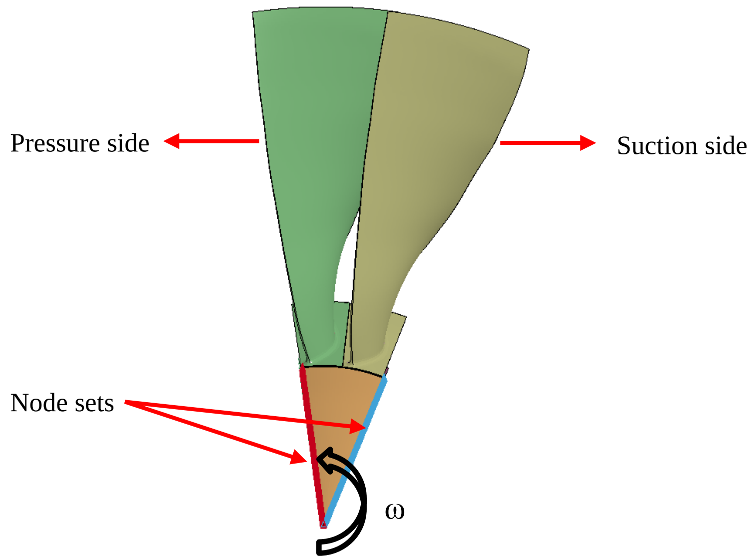

Figure 25. Pressure and suction side definitions used for defining node and segment sets.

The contact defined between the parts noted in Figure 24 for the pre-stress analysis are summarized in Table 3.

Table 3. Contact definitions used in pre-stress analysis.

Master Segment	**Slave Segment**	**Contact Type**
Dovetail Pressure Side	Disk Pressure Side	*AUTOMATIC_SURFACE_TO_SURFACE
Dovetail Suction Side	Disk Suction Side	*AUTOMATIC_SURFACE_TO_SURFACE
Disk	Retainer	*AUTOMATIC_SURFACE_TO_SURFACE
Dovetail	Retainer	*AUTOMATIC_SURFACE_TO_SURFACE
Retention Ring	Dovetail	*AUTOMATIC_SURFACE_TO_SURFACE
Dovetail	Airfoil	*TIED_SURFACE_TO_SURFACE
Retention Ring	Disk	*TIED_SURFACE_TO_SURFACE
Flange	Nose Cone	*TIED_SURFACE_TO_SURFACE

Each of the contacts in the table are for a single fan sector except for the contact between the flange and the nose cone, and the disk and the retention ring. The contacts were repeated for each sector (15° arc) while the flange and nose cone contact was repeated every two sectors (30° arc). The contacts were defined by first creating segmented node sets at the interface between parts, and these node sets were selected to be either the master segment or the slave segment set in accordance with Table 3. The *AUTOMATIC_SURFACE_TO_SURFACE keyword was used to define penalty-based contacts where the definition of the master and slave surfaces was arbitrary because the penetration check was performed twice. In addition to the default mandatory cards, card AB was used in the contact definition between the dovetail and disk on both the pressure and suction sides. In card A, SOFT=1 (soft constraint formulation), DEPTH=2 and BSORT=0 were used, and the rest were left as default values. In card B, SLDTHK value is set at 0.764 to represent the thickness of pad elements in the disk region. For the contact definition between the disk and retainer, the static and dynamic coefficients of friction were set to 0.5. The *CONTACT_TIED_SURFACE_TO_SURFACE keyword was used to define constraint-based contacts such that the segments in the contact are restricted to move together.

During the pre-stress analysis, it is important to maintain the same material, element formulation, and hourglass control definitions for each part during both the implicit and explicit steps. It is also necessary to maintain the same contact definitions between the various parts in both steps.

Boundary and loading conditions were applied in the implicit step to exploit the symmetry of the fan and to apply the proper loading to the fan. Node sets were defined on the pressure and suction sides of the disk, disk flange, retention ring, and nose cone as shown in Figure 25. Using these node sets, the requirement to only model two sectors for the implicit step was realized by defining the *BOUNDARY_CYCLIC keyword to exploit the rotational symmetry of the fan. The axial nodes at the rear of the disk were fixed, as shown in Figure 26, to prevent translational motion in the axial direction. The centrifugal force was applied as a body force load specified in terms of the rotational velocity of the fan (ω) using the *LOAD_BODY_RX keyword. The specified rotational velocity was gradually increased from zero to the desired RPM by defining a load curve in order to make the implicit solution more robust.

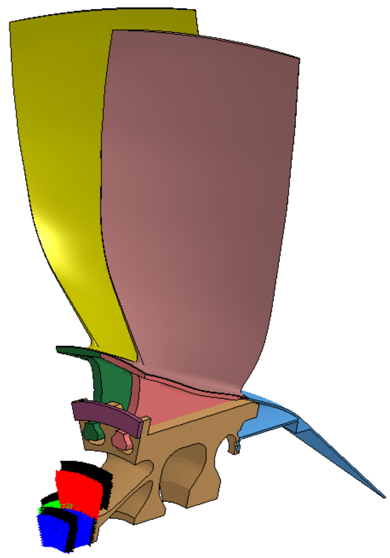

Figure 26. Nodes fixed in axial direction at the back of the disk.

The key information needed from the implicit step is the stress and strain information for each element due to the prescribed loads from the rotational motion of the fan. This information was obtained by defining the *INTERFACE_SPRINGBACK_LSDYNA keyword which output a file called “dynain” that contained the elements as well as their corresponding stresses and strains after the implicit solver was used. The information from the “dynain” file was then imported to perform the explicit step.

The objective of the explicit step was to verify that the pre-stress determined in the implicit step was correct. In the explicit step, the fan underwent two rotations and the stress at the blade root and middle of the blade were analyzed to verify that the fan did not have large fluctuations in stress as it was rotating at a given speed. The difference between the explicit and implicit step is not just in the solver used, but also involves changes to the boundary conditions and the addition of the engine casing and shaft to the model.

The *BOUNDARY_CYCLIC keyword used in the implicit step on the high and low boundaries of the disk, disk flange, retention ring, and nose cone was replaced with a constant rotation about the rotational axis of the fan by defining the *BOUNDARY_PRESCRIBED_MOTION_SET keyword for the same node sets with that had the cyclic boundary condition. The constant rotation was specified by defining a load curve for the desired RPM (Counter Clock Wise [CCW]) using *DEFINE_CURVE. To invoke the initial rotational velocity of the fan parts and nose cone, the *INITIAL_VELOCITY_ GENERATION keyword was defined at the desired RPM (CCW). The axial nodes at the rear of the disk were fixed in a similar manner as in the implicit step.

The casing and shaft were added in the explicit step for the cases when additional dynamic simulations needed to be simulated (i.e., blade-out, bird ingestion, UAV ingestion). These two parts did not interfere with the pre-stress analysis as there was no contact between these parts and the other parts in the model. Therefore, it was appropriate to not include them in the implicit step and include them only in the explicit step. The choice to model the shaft as a rigid body and not include contact between the shaft and the disk meant that it would not impact the pre-stress analysis.

The intended result of the pre-stress analysis was twofold: (1) to ensure the fan design can withstand the centrifugal loads; and (2) to have a rotating fan model where further dynamic simulations could be performed. Before using the results an explicit step, where the fan underwent two rotations was conducted in LS-DYNA. The purpose of these two rotations was to monitor the element stresses present at both the root of the fan blade and at the mid-span location. These stresses should be relatively constant with some computational noise expected. Figure 27 and Figure 28 show the stress as a function of time at the blade root and blade mid-span, respectively, for the two-sector model, for the highest rotation case where the fan is rotating at 5175 RPM (ω =541.9247 rad/s). Note that the implicit and explicit analysis was conducted for each rotational speed analyzed in this report and similar results were found for each case.

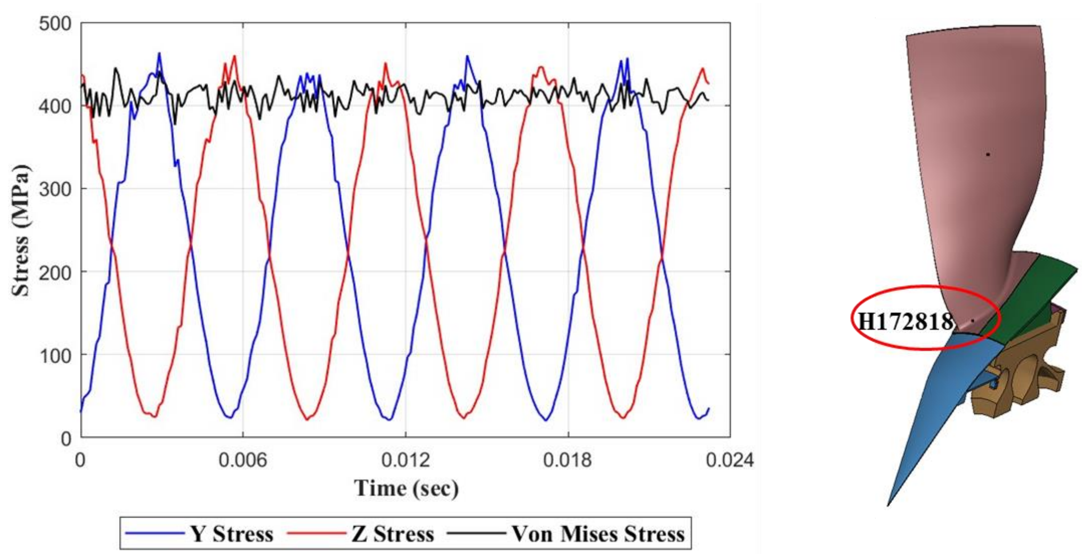

Figure 27. Element stress at blade root for two-sector model.

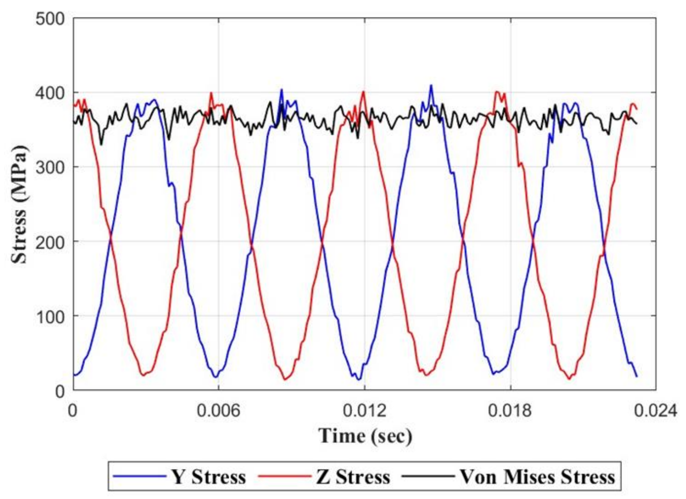

Figure 28. Element stress at blade mid-span for two-sector model.

The blade was rotating about the x-axis so there was a sinusoidal variation in the Y-Stress (σ_{yy}) and Z-Stress (σ_{zz}) measured using global coordinates. The von Mises stress did not vary due to rotation, as expected.

The corresponding von Mises stress contour of the whole fan sector is shown in Figure 29. The highest stress location in the blade is indicated with the value noted. This stress is well below the yield strength of the titanium alloy Ti-6Al-4V used for the fan, which is 1150 MPa[12].

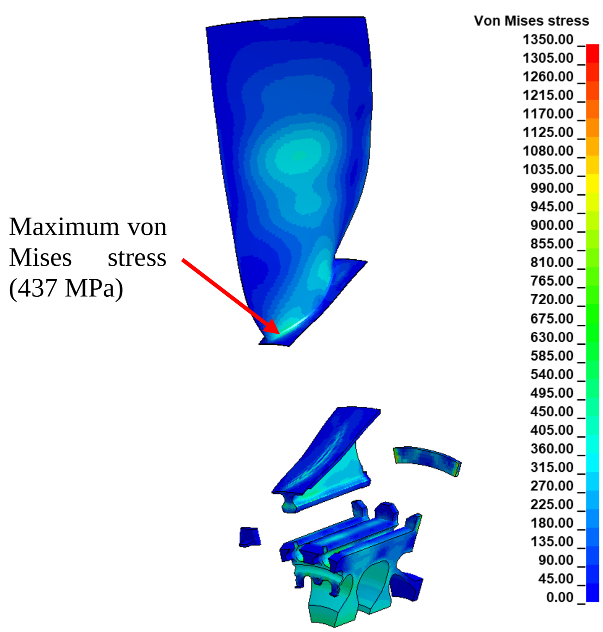

Figure 29. Stress in single sector after pre-stress analysis at highest rotational speed of 5175 rpm.

2.4.3 Bird Ingestion Simulations

From 1990-2019, 191,571 bird strike events involving civil aircraft were reported to the FAA with 11% of those instances involving striking of the aircraft engines[18]. Despite only 11% of those bird strikes involving the aircraft engines, 26% of the bird strikes involving damage to the aircraft component occurred when the engines were struck[18]. Bird ingestion events occur with enough regularity despite the FAA mitigation efforts that bird ingestion tests are required to be performed as part of the airworthiness certification process for aircraft engines. The details and requirements of these tests are found in Title 14 Code of Federal Regulations (CFR) 33.76[19]. In summary, there is a large bird ingestion test and medium flocking bird ingestion test with the weight and number of birds dependent on the inlet area of the engine. There are specified thrust profiles that the engine must follow for each test and hazardous engine effects that are not permitted.

These bird ingestion tests involve full engines and are very expensive for OEMs to complete; thus there is a strong motivation to be successful on the first attempt. Therefore, bird ingestion simulations are performed throughout the design phase to avoid failures during the certification tests. The fan blades are usually the most critical components, and their most critical location is targeted to be the impact area for the bird. The fan model developed for this research was designed to have structural characteristics comparable to high bypass ratio fans used commonly in commercial transport and would be expected to be able to pass these certification tests. To provide evidence of this, simulations of bird ingestion events were performed and analyzed to confirm the fan model would meet important test criteria and be in line with industrial experience. Certain requirements such as the exact thrust profiles and an uncontrolled fire were beyond the scope of this work, but the damage caused by the impact of the bird and resulting plastic deformation could be modeled. Extreme damage to the blades would suggest the possibility of uncontained high-energy debris and excessive plastic deformation could block the flow path, thus reducing the thrust below allowable levels. The bird ingestion simulations are supportive of the mechanical capability of the fan design. Without these simulations, it would not be possible to say if the UAS damage predicted would be reasonable.

The bird ingestion simulations performed were setup to model the large single bird ingestion test. Based on the inlet area of the fan rig model, the appropriate bird weight was 2.75 kg (6.05 lb.). The selection of an appropriate bird model is important for obtaining useful simulation results at a reasonable computational cost. The bird model selected for the bird ingestion simulations was taken and modified from the AWG website[20]. The model was validated by comparing LS-DYNA simulations to Hopkinson bar experimental results[21]. The bird was discretized using the Smoothed-Particle Hydrodynamics (SPH) method rather than the Lagrangian elements used for the fan rig model. An Equation Of State (EOS) was defined with the *EOS_LINEAR_POLYNOMIAL keyword with C1 set to 1846.63 MPa and C2 set to 12,014.25 MPa. The EOS was a piecewise polynomial that related the pressure to the density in the bird model and is defined below:

$$\begin{aligned} P(\mu) &= C_1\mu + C_2\mu^2 \quad && \mu \geq 0, \\ P(\mu) &= C_1\mu && \mu < 0, \\ \mu &= \rho/\rho_0 - 1, \end{aligned} \tag{8}$$

where P is the pressure, ρ is the current density, and ρ_0 was the initial density. Similarly, the first function was applied during a local compression and the second function was applied during a local expansion. The value of ρ_0 was assigned by using the *MAT_NULL keyword to be a value of 915.7 kg/m^3. In addition, a value of -6.8975 Pa was assigned to the pressure cutoff and a value of 1.379(10^{-3}) Pa-s was assigned to the dynamic viscosity under the *MAT_NULL keyword. The bird was composed of a total of 374,207 SPH particles arranged to have the geometry of a cylinder with hemispherical ends, as shown in Figure 30. The length of the cylinder, L, was 131.8 mm and the diameter, D, was 65.9 mm to give a ratio of length to diameter of two. The particles were discretized on a regular Cartesian grid to have 2 mm spacing between particles as this discretization gave similar results to a bird with 1 mm spacing at a reduced computational cost[21].

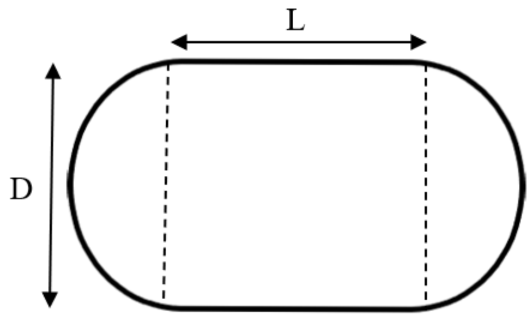

Figure 30. Geometry of bird model with aspect ratio of two.

For the bird ingestion simulations, six fan sectors and corresponding sections of the nose cone and shaft were used along with the casing and two dovetails, one at each end of the six fan sectors, to model the fan rig as shown in Figure 31. The decision to model the fan rig with multiple fan sectors for the bird ingestion simulations was based on best practices set forth by the AWG[6]. The two additional dovetails were included to give an appropriate boundary condition at the ends of the six fan sectors and prevent any nonphysical behavior in the simulations. These two dovetails are slightly different than the other dovetail parts because they follow the exact geometry of the dovetail rather than including some of the platform in the blade part. The additional dovetails were prescribed to rotate about the rotational axis of the fan at 5175 RPM (ω =541.9247 rad/s) and were constrained in the axial direction.

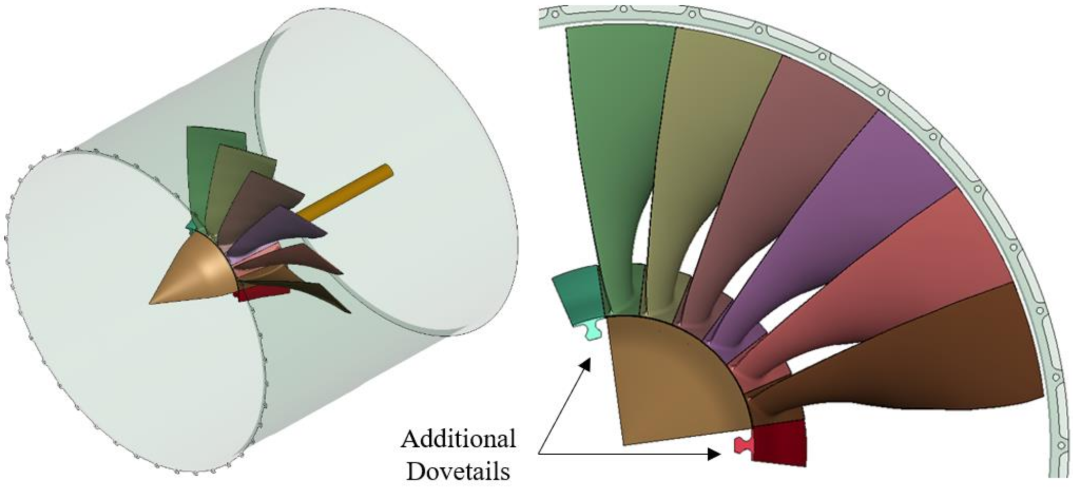

Figure 31. Six fan sector fan rig model, left is isometric view and right is front view.

Contact was defined between the bird and all of the blades and the casing through the use of the *CONTACT_AUTOMATIC_NODES_TO_SURFACE keyword where the slave nodes of the bird were checked for penetration of the master surfaces (blades and casing). In addition to the default mandatory cards, card A was used in the contact definition. In card A, SOFT=1 (soft constraint formulation), DEPTH=2 and BSORT=0 were used, and the rest were default values. While adjacent blades would never come into contact during normal operation, it is possible that during the bird ingestion that adjacent blades could come into contact due to large deformations. For that reason contact was defined between adjacent blades using the *CONTACT_AUTOMATIC_SURFACE_TO_SURFACE keyword where a two-way penetration check was performed in the implementation of the penalty based contact algorithm.

To establish the correct relative velocity for the bird impact, both the bird and the rotating parts of the six sector fan rig model needed to be given initial velocities. The initial velocity of the bird was set to 200 knots in the axial direction using the *INITIAL_VELOCITY_GENERATION keyword as this was the speed prescribed by CFR 33.76[19] for the large single bird ingestion. To invoke the initial rotational velocity of the fan parts and nose cone, the *INITIAL_VELOCITY_GENERATION keyword was defined with ω = -541.9247 rad/s (CCW). The shaft was prescribed to have the same rotational velocity using the *BOUNDARY_PRESCRIBED_MOTION_RIGID keyword since it is modeled as a rigid body. Note that the fan model is driven such that it does not slow down due to the ingestion similar to how a real engine would not immediately slow down due to a bird ingestion.

Three different bird ingestion cases were conducted at different radial locations along the blade (i.e., blade root, blade midspan, blade tip). The kinematics of the bird ingestion at the blade tip are shown in Figure 32 and the resulting plastic deformation in the fan is shown in Figure 33.

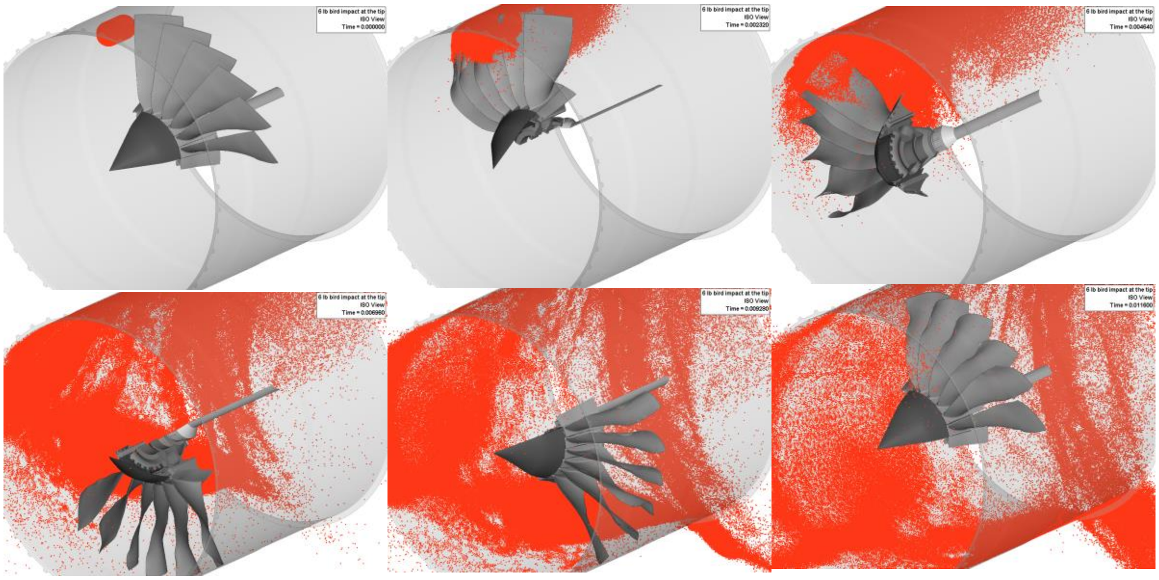

Figure 32. Kinematics of bird ingestion near blade tip.

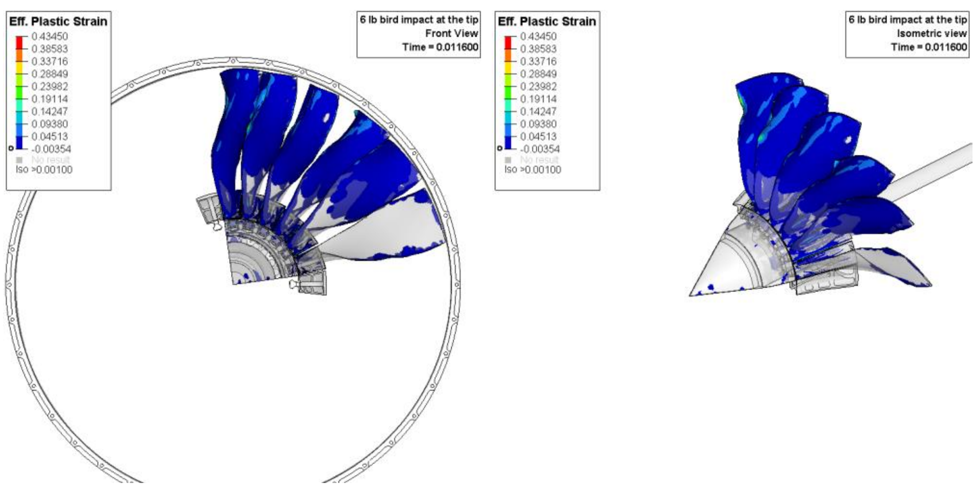

Figure 33. Resulting plastic deformation in fan from large bird ingestion near blade tip.

Similarly the kinematics of the bird ingestion at the blade midspan are shown in Figure 34 and the resulting plastic deformation in the fan is shown in Figure 35.

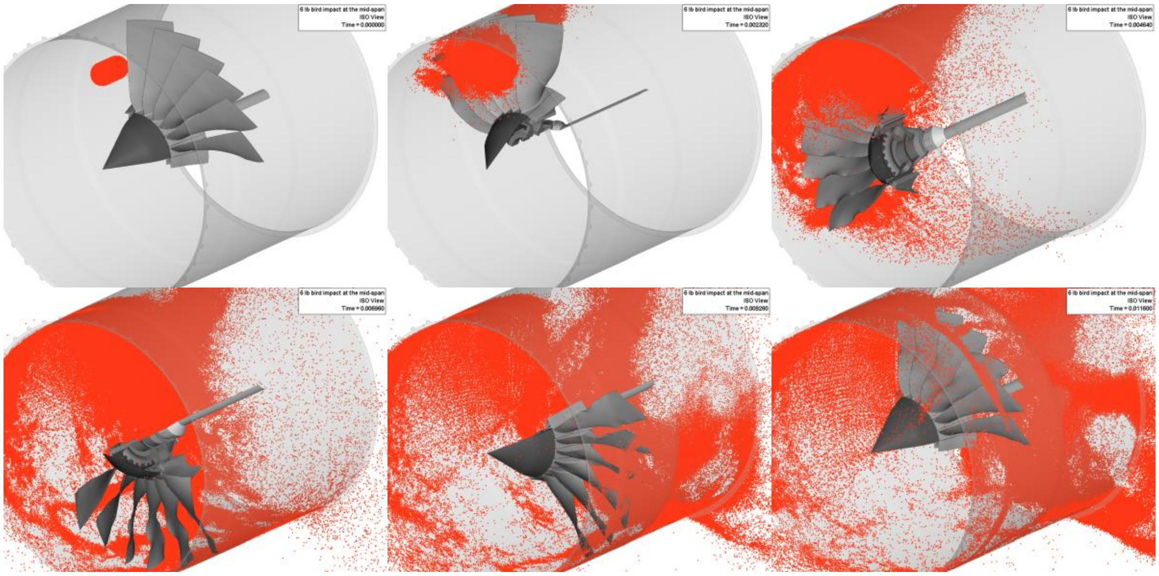

Figure 34. Kinematics of bird ingestion near blade midspan.

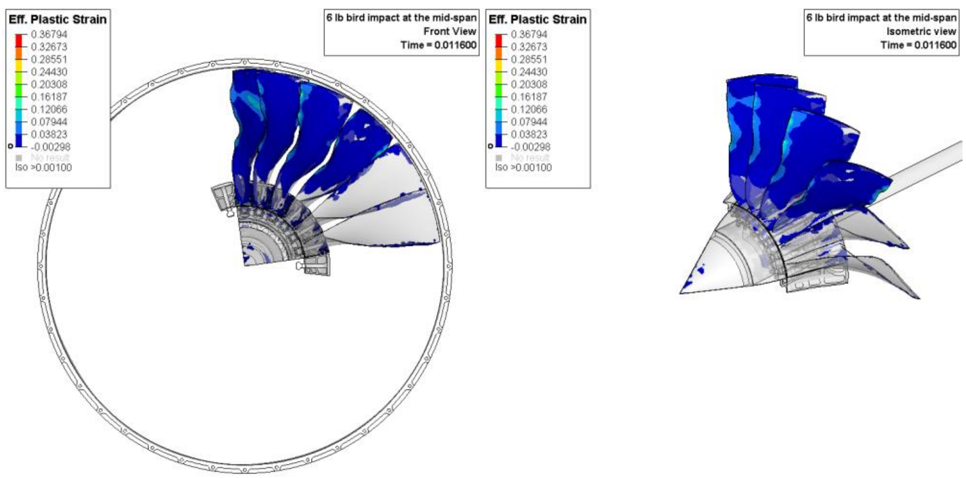

Figure 35. Resulting plastic deformation in fan from large bird ingestion near blade midspan.

Finally, the kinematics of the bird ingestion at the blade root are shown in Figure 36 and the resulting plastic deformation in the fan is shown in Figure 37.

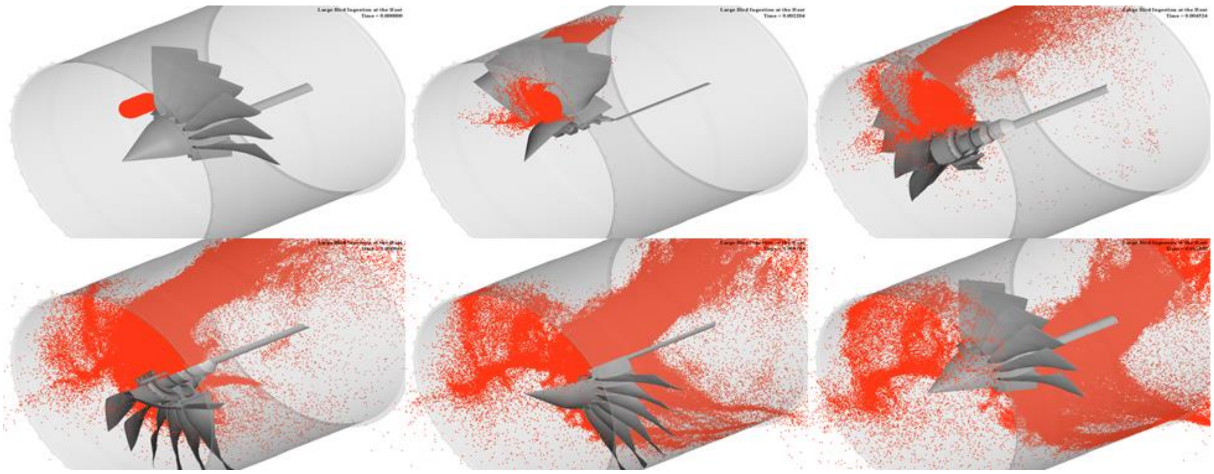

Figure 36. Kinematics of bird ingestion near blade root.

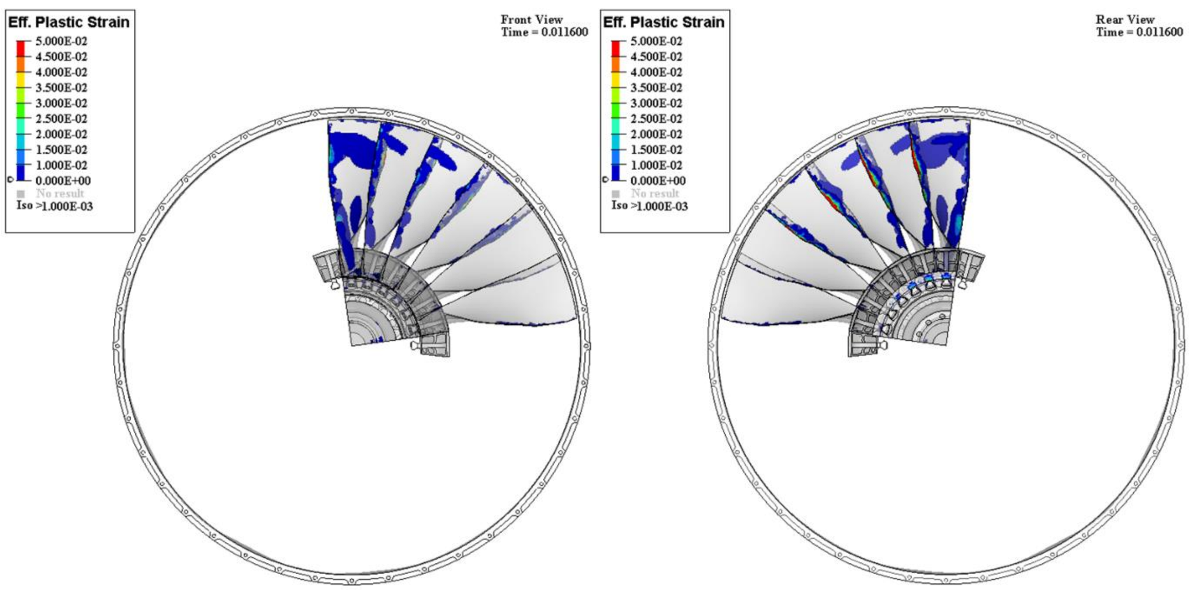

Figure 37. Resulting plastic deformation in fan from large bird ingestion near blade root.

The bird ingestion simulations show that there is some plastic deformation in the blades from the ingestion, with no signs of cracking or significant material loss in any of the cases. Also, there are no high root strains in the blades. This is consistent with industry experience with certified designs.

3. UAS MODEL

The quadcopter chosen for the engine ingestion is a model of the DJI Phantom 3 developed by NIAR[3]. The computational model was constructed from 3D scanning, static and dynamic testing of all critical components. The model was also validated with blunt force impacts against aluminum plates in the 100 – 250 knot speed range. This particular quadcopter model was chosen because of its ease of use and abundance. Note that the critical components in the quadcopter (motor, camera, and battery) are similar across a wide variety of models. In this research program, the quadcopter was updated and validated by NIAR[5] using experimental data conducted at UAH from impact testing of components and full UAVs with titanium plates[15]. A discussion of how the test article was selected is discussed in Appendix B and how the test matrix was created is discussed in Appendix A of this report. Images of the updated finite element model of the quadcopter used in this work are shown in Figure 38.

(a) Oblique view

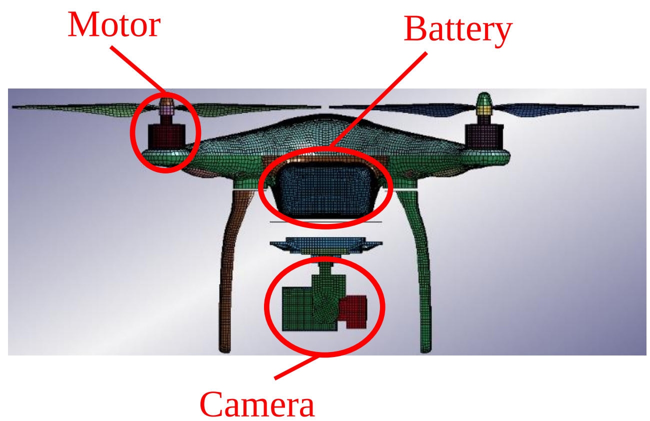

(b) Front view

Figure 38. Quadcopter Finite Element Method Model..

4. UAS-FAN COLLISION SIMULATIONS

This section will discuss the results of the experimentally validated UAS model described in Section 3 impacting the representative fan rig assembly model described in Section 2. First, the computational set-up of the ingestion simulations will be discussed in Section 4.1. Note that many of the settings and processes described in the bird ingestion simulation described in Section 2.4.3 were also used for the UAS ingestions in this Section. Next, the data processing and analyses for the different cases are presented in Section 4.2. Then, the damage severity evaluation matrix is given in Section 4.3. Afterwards, the test matrix for the sensitivity study and each of the cases is analyzed in Section 4.4. Section 4.5 then summarizes all of the sensitivity study results identifying critical factors in the ingestion. Finally, the critical factors from the sensitivity study are used to run a few phases of flight simulations with the expected worst-case conditions in Section 4.6.

4.1 SETTING UP THE INGESTION SIMULATIONS

Before running the ingestion simulations or the fan blade out case, a full fan model needed to be created. This fan model was developed from the ‘dynain’ output from the implicit pre-stress step at the desired rotational velocity of the fan. LS-DYNA was used to assemble all 12 cyclic sectors to create a full fan model with 24 blades. Initial stresses and strains from the pre-stressed one sector (two blade) model were copied and rotated to create 11 additional sectors. Node set, part sets, and contacts from the single sector model as defined in the implicit step were also copied to other sectors. In the final assembly, nodes on the co-planar symmetry edge in the disk, nose cone and retention ring were merged to remove duplicate nodes and create a singular disk, nose cone, and retention ring. A full fan model used in the LS-DYNA simulations includes one nose cone part, one disk part with flange attachment, one retention ring, 24 retainer parts, 24 blades, and 24 dovetail parts. A part set was defined using these 75 parts for various boundary conditions. In addition to these parts, a rigid shaft part and an elastic casing were included for boundary conditions and measuring containment energies.

For the simulations, default settings were used in the *CONTROL_TIMESTEP and *CONTROL_TERMINATION cards. Only the ENDENG value in the termination card was changed to 2.0. A change in total energy by 2% will cause the simulation to terminate due to this condition. This is done in accordance with the AWG modelling guideline document to stop the simulation due to stability issues associated with unphysical changes in the energy in the system.

A rotational boundary condition was defined using the *INITIAL_VELOCITY_GENERATION card on the fan model using a part set. The rotational velocity (ω) was set at 119.27 rad/s for low fan speed simulations. For the fan blade out condition, bird ingestion, and high fan speed simulations, the rotational velocity was set at 541.9 rad/s. A node set was defined in the disk at the interface of the disk and shaft to simulate a driven condition in the fan. In all the simulations, a rotational boundary condition is defined by *BOUNDARY_PRESCRIBED_MOTION_SET at this node set in the disk. The driven rotational velocity was defined to match the initial velocity conditions defined for the full fan model.

In the fan blade out and bird/UAS ingestion simulations, additional contacts were needed due to the interaction between various parts. These include self-contact in blades, contact between blades, nose cone and retainer, nose cone and disk lug area, blade and bird, blade and UAS, blades and casing, bird and casing, and UAS and casing. Contact definitions and associated master/slave surface definitions are described in Table 4.

Table 4. Contact settings for simulations.

Contact type	Master surface	Slave surface	Associated contact settings
*ERODING_SURFACE_TO_SURFACE	Fan model (defined as a part set)	UAS (defined as a part set)	fs = fd = 0.1, SFS = 0.5, SFM = 1, SOFT = 2, DEPTH = 25, BSORT = 5
*ERODING_SURFACE_TO_SURFACE	Casing (defined as a part)	UAS (defined as a part set)	fs = fd = 0.1, SFS = SFM = 1, SOFT = 2, DEPTH = 35, BSORT = 10
*AUTOMATIC_SURFACE_TO_SURFACE	Disk lug – suction side	Dovetail stack – suction side	fs = fd =0, SFS = SFM = 1, SOFT = 2, DEPTH = 35, BSORT = 10
*AUTOMATIC_SURFACE_TO_SURFACE	Disk lug – pressure side	Dovetail stack – pressure side	fs = fd =0, SFS = SFM = 1, SOFT = 2, DEPTH = 35, BSORT = 10
*AUTOMATIC_SURFACE_TO_SURFACE	Trailing blade platform – pressure side	Leading blade platform – suction side	fs = fd =0, SFS = SFM = 1, SOFT = 2, DEPTH = 35, BSORT = 10

*AUTOMATIC_NODES_TO_SURFACE	Casing	Quadcopter	fs = fd = 0, SOFT = 1, DEPTH = 25, BSORT = 5
*AUTOMATIC_SURFACE_TO_SURFACE	Nose cone	Disk	fs = fd = 0
*AUTOMATIC_SURFACE_TO_SURFACE	Nose cone	Retainer	fs = fd = 0

For the UAS ingestion simulations, the fan was prescribed with the desired rotational speed from Table 1 after a pre-stress analysis was conducted (as described in Section 2.4.2). The UAS was given an initial orientation and placed with its center of mass at the desired radial span location. These locations were chosen such that UAS could hit either towards the outer radius of the blade (without hitting the casing) or the inner radius of the blade (without hitting the nose cone) for each of the selected orientations. The nominal orientation of the UAS before it hits the fan is defined in Figure 39. Rotations of the UAS in roll, pitch, and yaw angles from the nominal orientation are also shown in Figure 39. Motors of the UAS are shown in different colors, and the same color representation is used to plot the velocities of the motors in each of the simulations in the following analysis.

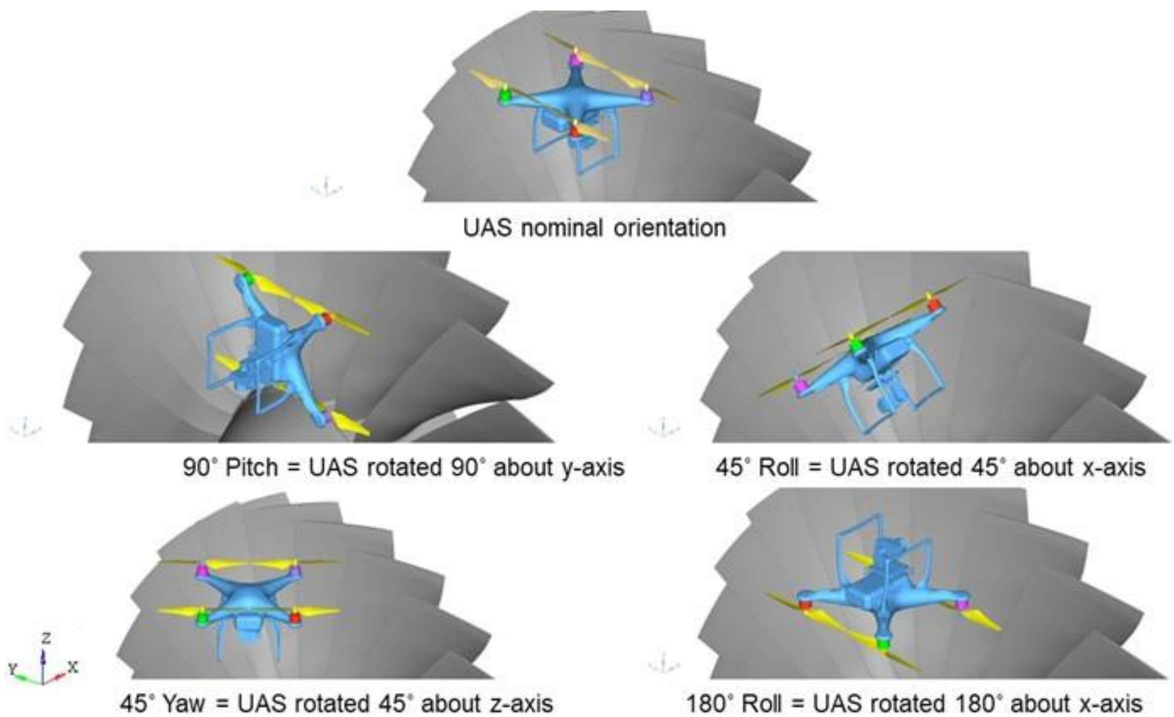

Figure 39. Orientation of UAS.

Note that the UAS shown in front of the fan in Figure 39 would be prescribed with the desired initial velocity normal to the face of the fan. Depending on the rotational speed of the fan and the translational speed of the UAS, the simulation times would vary. For the high speed fan rotations, one fan revolution was used. For the low speed fan rotations, a half a revolution was used. Also, due to the complexity of the computational models and the resulting computational cost of the simulations, there was a need to delete the UAS after it passes through the fan for the remainder of the simulation. These UAS parts were removed using a small restart option available in LS-DYNA. The UAS parts were deleted using the *DELETE_PART card. Binary dump files were created by LS-DYNA at frequencies defined in the initial program. These dump files in conjunction with the part deletion keyword file were used to restart the simulations. This approximation has little effect on the damage to the fan. Note that when the UAS parts are removed this can cause slight jump in the casing energy, and therefore casing energies are not reported after UAS deletion.

4.2 ANALYSIS OF INGESTION SIMULATIONS

After the completion of each ingestion simulation, several types of analyses were conducted. First, several steps were taken to ensure the stability and accuracy of the solution. Then, the simulation data was processed in a number of ways to provide useful metrics to understand and compare the different ingestion scenarios.

To ensure the stability and accuracy of the solution, a number of steps were taken for each simulation. First, the animations of the simulations were carefully inspected to ensure that all the contacts were behaving properly, and parts of the UAS and fan did not fictitiously pass through each other. Also, the total energy in the system as well as energy in individual components were analyzed to ensure reasonable transmission of energy between components, as well as the overall stability of the simulation.

To analyze and compare the results of the different ingestion simulations, a number of analyses were performed to assess the relative difference between cases in terms of (i) overall damage to the fan, (ii) imbalance in the rotor, (iii) loads on the retention systems, and (iv) containment.

(i) Two metrics were used to understand the overall damage to the system. Both metrics are important in understanding the ability of the fan to continue to provide thrust. The first metric is a plot of the effective plastic strain in the fan at the end of the simulation. This shows the distribution of the damage over the entire fan surface and can be used to understand the localized damage in each blade to understand how close it is to failure. The second metric is a quantitative measure of the overall damage in the fan using the damage indicator, D, that is defined on each element as

$$D = \int \frac{\dot{\epsilon}_p}{\epsilon_{pf}} dt, \tag{9}$$

where $\dot{\epsilon}_p$ is the plastic strain evolution and ϵ_{pf} is the plastic failure strain. Note that D varies from 0 (no damage) to 1 (element failure) and is a measure of the cumulative plastic strain in the element. In order to get a quantitative assessment of the whole fan a mass weighted average of D is used for all elements to get a composite D_{fan}

$$D_{fan} = \frac{\sum_i^N m_i D_i}{\sum_i^N m_i}, \tag{10}$$

where N is the number of elements in the fan, m_i is the mass of the i^{th} element and D_i is the cumulative plastic strain in the i^{th} element. The D_{fan} metric quantifies the damage in the fan as a whole structure.

(ii) To understand the imbalance in the rotor due to the ingestion, two analyses were carried out. Understanding the imbalance loads is important since it defines the structural and mount loads of the fan on the shaft. The first analysis is to identify the center of gravity of each of the blades. A comparison of the pre- and post-impact center of gravities shows where damage occurs in the fan and how it relates to imbalance in the rotor. The second analysis is to compute the forces in the disk that are acting on the rigid shaft. These forces give the overall imbalance load acting on the shaft.

(iii) To understand the loads on the retention systems, several loads in the fan rig assembly model were tracked. Understanding retention loads is important to prevent the possibility of multiple blade release. First, the resultant force acting on each retainer based on its contact with the nose cone, dovetail and disk is computed using the RCFORC command in LS-DYNA. Second, the resultant force on the retention ring from its contact with the disk and dovetail was also computed using the RCFORC command. Finally, resultant forces and moments from a sectional plane in the dovetail and airfoil of a damaged and undamaged blade are also computed, where Figure 40 indicates the airfoils and the plane where the forces and moments are computed.

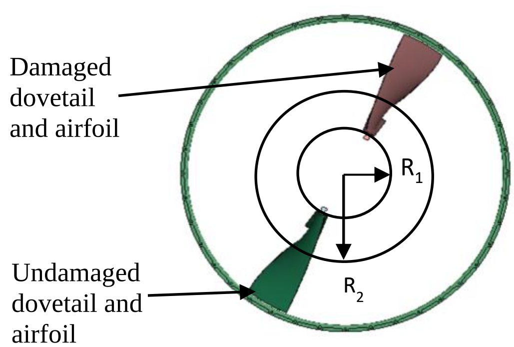

Radial distance of plane on dovetail (R_1) = 229 mm
Radial distance of plane on airfoil (R_2) = 369 mm

Figure 40. Damage and undamaged airfoil separated by 180 degrees and the sectional plane where the force and moments are computed.

(iv) To understand the relative difference between the UAS ingestions with relation to containment, the energy imparted to the casing was tracked using the MATSUM card in LS-DYNA. It is important to understand if the ingestion is likely to produce high energy debris beyond the capability of the containment system.

4.3 DAMAGE SEVERITY EVALUATION

The simulations conducted in this study are focused on understanding the effects of the UAS collision with an aircraft engine as it relates to damage in the fan, in particular. This fan damage has implications on rotor imbalance, blockage (which impacts thrust), containment, and retainment mechanisms. Note that the fan rig assembly model does not contain most of the downstream components of the fan (i.e., compressor, combustor and turbine), and therefore any damage in these components is out of the scope of this research.

The damage was separated into four severity levels based on discussion with the research team and the industrial partners, and are detailed in Table 5. Table 5 has four columns: (i) the damage severity level; (ii) the fan damage and its corresponding likely effect on the engine; (iii) the corresponding aircraft operational impact for that same level of engine damage; and (iv) the typical associated damage in the fan for the damage severity level. Note that severity levels 1-3 are within the engine certification envelope and correspond to damage that would be typically seen up to a single blade-out event, which engines must be certified to be able to contain and shut down safely. Severity level 4 is outside the certification envelope, which just means the engine is not certified for these damage levels, but makes no claims about the danger or safety at this level since it is unknown.

Table 5. Damage Severity Level Classification.

Severity	Fan (Engine) Damage	Aircraft Operational Impact	Typical Associated Damage
Level 1	Slight damage – Continued operation with negligible to small reduced thrust Within engine certification envelope	Minimal effect – Continued flight to destination. Inspection after landing.	• Small deformation of fan blades • No crack initiation (blade or disk)
Level 2	Moderate damage – More significant reduced thrust Within engine certification envelope	Moderate effect – Continued flight or rerouting as needed. Inspection after landing.	• Significant deformation of fan blades • Material loss of leading edges of blades • Visible cracking in **single** blade above mid-span • No disk crack initiation
Level 3	Significant damage – Potential engine shutdown Within engine certification envelope	Significant effect – Fewer options for rerouting. Emergency landing may be needed if damage occurs at critical flight phase. Inspection after landing.	• Significant material loss leading to an imbalance that is less than or equal to a single blade loss • Visible cracking in **single** blade below mid-span • Visible cracking in **multiple** blades above mid-span • No disk crack initiation

Level 4	Damage outside of design criteria and certification – Potential hazardous engine effect Beyond engine certification envelope	Significant effect – Ranging from need to reroute to emergency landing to catastrophic failure. Inspection after landing.	• Significant material loss in blades leading to an imbalance that is more than a single blade loss • High energy forward arc debris • Visible cracking of **multiple** blades below mid-span • Crack initiation in **disk**

It is important to note that Table 5 is only providing an initial assessment of the fan damage and is not classifying overall engine damage (since the model does not include most of the downstream components of the engine). The four classification levels are meant to span a large range of outcomes and not all of the levels will necessarily occur in the cases investigated with this one specific UAS (i.e., a smaller UAS could result in less damage and larger UAS could lead to greater damage). Table 5 provides a general damage severity classification for the fan rig assembly that can be used in future studies.

4.4 SENSITIVITY STUDY

A test matrix was defined to study how different parameters of the ingestion affect the fan damage. Lessons from previous research on UAS ingestions into a generic fan model[1] were used to inform the selection of the test matrix. Namely, the focus of the ingestions are at the high fan speed rotation at the outer radius with the highest relative translational velocity. It has been shown in the previous research that the greatest damage is expected to occur in these scenarios since it results in the highest relative velocity between the fan blades and the UAS. However, each of these parameters (i.e., fan rotational speed, relative translational velocity, and radial impact location) were also investigated in this project. Moreover, a number of different UAS impact orientations were also considered. The test matrix used for the sensitivity study is shown in Table 6.

Table 6. Test matrix for sensitivity study.

Simulation ID	Fan speed	Translational relative velocity	Impact location	Orientation of UAS
Fan Blade Out (FBO)	High	-	-	-
Bird (UAS mass)	High	High	High	-
LFS_LRV_LRS_90P	Low	Low	Low	90˚ pitch
LFS_LRV_HRS_Nom	Low	Low	High	0˚
LFS_HRV_LRS_90P	Low	High	Low	90˚ pitch
LFS_HRV_HRS_Nom	Low	High	High	0˚
HFS_LRV_LRS_90P	High	Low	Low	90˚ pitch
HFS_LRV_HRS_Nom	High	Low	High	0˚
HFS_HRV_LRS_90P	High	High	Low	90˚ pitch
HFS_HRV_HRS_Nom	High	High	High	0˚
HFS_HRV_HRS_45R	High	High	High	45˚ roll
HFS_HRV_HRS_90R	High	High	High	90˚ roll

HFS_HRV_HRS_45Y	High	High	High	45˚ yaw
HFS_HRV_HRS_90Y	High	High	High	90˚ yaw
HFS_HRV_HRS_180R	High	High	High	180˚ roll
HFS_HRV_LRS_Nom	High	High	Low	0˚

Note that for the fan speed, relative translational velocity, and impact locations there is a high and low value assigned. For the fan speed, the high value corresponds to 5175 RPM, which is the max speed at take-off for this engine. The low fan speed value corresponds to 1139 RPM, and is the rotational speed during approach for this engine. For the relative translational velocity, the high value corresponds to 250 kts (the maximum speed for an aircraft for flight below 10,000 ft.) and the low value corresponds to 130 kts (the minimum speed for take-off for this engine). The UAS was considered in the hover state with no translational velocity. For the radial impact location, the high and low correspond to the highest and lowest radial locations on the blade that can be impacted without directly hitting the nosecone or casing for the various orientations. Note that, for the direct orientation case, the low value corresponds to the center of mass of the UAS impacting about a 10% radial span, while the high value would impact about the 80% radial span. The different orientations correspond to rotations about the respective axis with respect to the direct orientation case, with those orientations defined in Figure 39.

In addition to the UAS ingestions, two reference cases were also added for comparison purposes. The first reference case is the blade-out simulation, since this serves as a useful reference point with regards to how much energy the containment system would need to be certified to contain and imbalance loads, etc. that the fan rig assembly model would need to handle to be certified for flight. The second reference case is the bird ingestion case where the bird model is similar to the one presented in Section 2.4.3 except that the weight has been scaled to match the UAS model weight of 1.22 kg (2.68 lbs). The bird ingestion is at the high fan speed, high translational relative velocity, and the center of mass impacts at about 80% radial span such that it is a good comparison point for many of the UAS impact cases.

It should be noted that there is a large difference in rotational speeds between the high and low fan speeds, which greatly affects the length of the computational simulation (a revolution for low fan speed is 52.68 ms, while it is 11.6 ms for high fan speed). Due to the computational costs and stability challenges with running the low fan speed simulations, it was decided to run the simulation for up to a half fan revolution instead of the full revolution. All high fan speed simulations were performed for one full fan rotation.

Due to the different orientations cases considered, the initial UAS Center Of Mass (COM) location changed between simulations. Table 7 shows the UAS COM position for each UAS ingestion. The origin is at the center of the disk 480.1 mm in the axial (positive x-direction) from the tip of the nose cone.

Table 7. Center of mass of UAS for ingestion simulations.

Simulation ID	x_{COM}(mm)	y_{COM} (mm)	z_{COM} (mm)
LFS_LRV_LRS_90P	-245.77	-1.302	395.32

LFS_LRV_HRS_Nom	-327	-1.302	681
LFS_HRV_LRS_90P	-245.77	-1.302	395.32
LFS_HRV_HRS_Nom	-327	-1.302	681
HFS_LRV_LRS_90P	-245.77	-1.302	395.32
HFS_LRV_HRS_Nom	-327	-1.302	681
HFS_HRV_LRS_90P	-245.77	-1.302	395.32
HFS_HRV_HRS_Nom	-327	-1.302	681
HFS_HRV_HRS_45R	-392.73	-41.75	642.94
HFS_HRV_HRS_90R	-425.34	-55.73	638.67
HFS_HRV_HRS_45Y	-415.47	-3.27	681.26
HFS_HRV_HRS_90Y	-395.34	3.32	671.26
HFS_HRV_HRS_180R	-327.36	1.302	622.73
HFS_HRV_LRS_Nom	-327.36	-1.302	391.26

4.4.1 Reference 1: Blade-Out Simulation

In addition to bird ingestion requirements, the FAA requires new engine designs to demonstrate that they can contain a fan blade-out event by undergoing blade-out testing before they are certified. Due to the variety of proprietary containment systems used by each of the engine manufacturers, developing a truly representative containment system for the fan rig assembly model was outside the scope of this work. Instead, as was previously discussed, a casing that provides appropriate boundary conditions that would not restrict the ingestion of the UAV was used. Moreover, a reasonable hot clearance was used between the rotating blades and the casing, and the thickness of the casing was chosen so that it would be reasonable value to withstand a high-speed blade impact for the selected titanium alloy.

The purpose of including this blade out simulation is to provide a reference for UAV simulations in terms of the amount of energy imparted to the casing as well as other loads acting on retention systems that occur during a blade-out event.

The fan blade out simulation was carried out with the pre-stressed model of the fan at the high fan speed of 5175 rpm (541.9 rad/s). For the fan blade out simulation, in accordance with industry standards, the first dovetail part is separated into two parts and the top platform section is rigidly tied with the airfoil root. The tied blade and dovetail section detach from the fan assembly at the start of the simulation (t = 0) and simulated for one full revolution. The section where the dovetail separates is indicated in Figure 41.

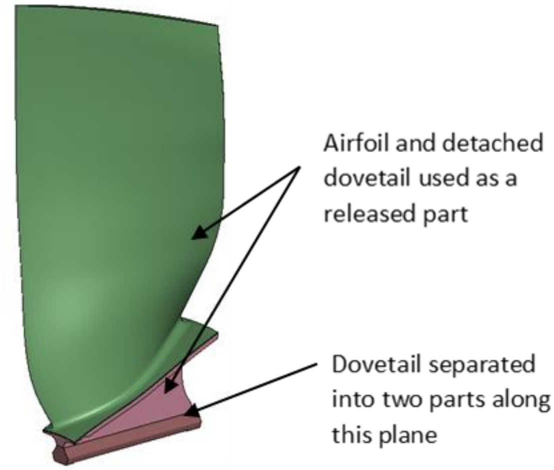

Figure 41. Released blade and portion of dovetail section in fan blade out simulation.

The kinematics of the blade-out simulation is shown in Figure 42. The ejected blade is red.

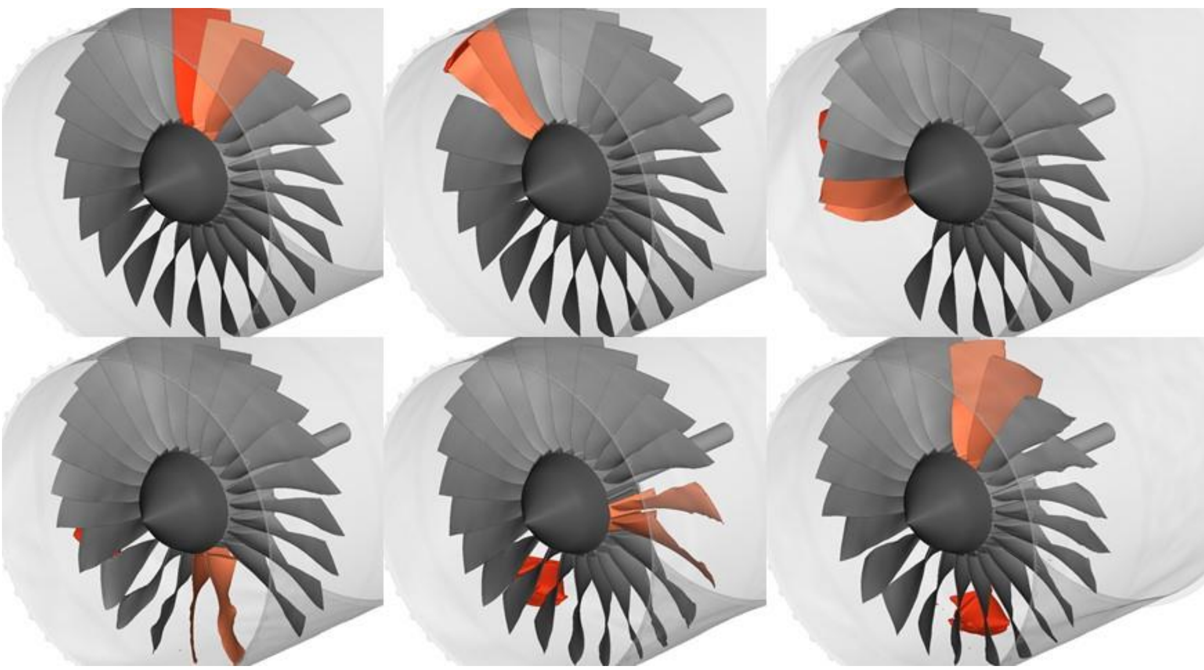

Figure 42. Kinematics of blade out event.

The effective plastic strain in the fan is shown in Figure 43.

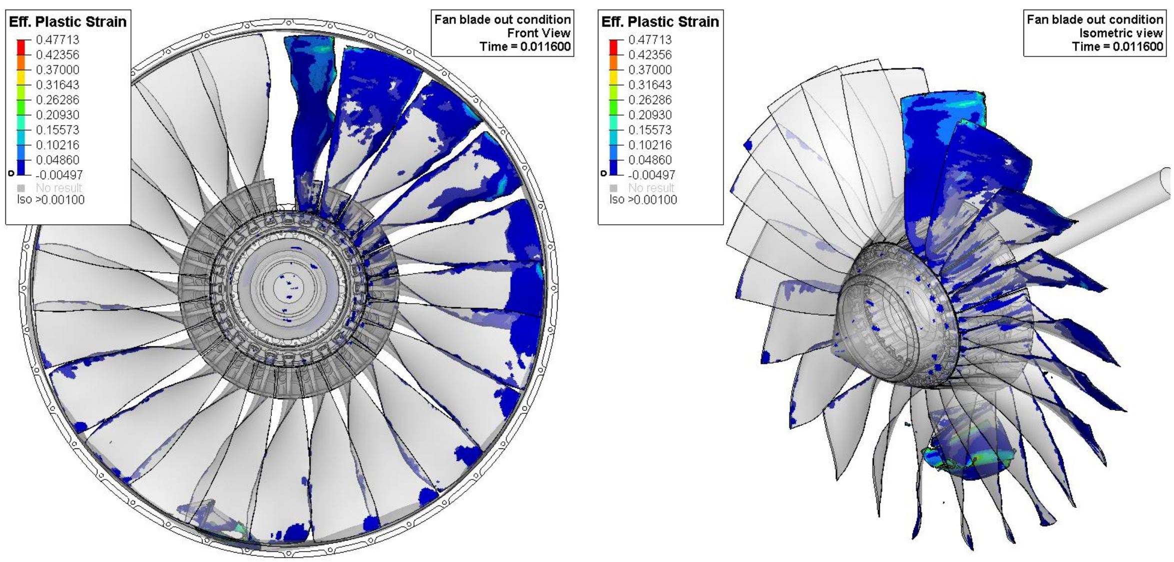

Figure 43. Effective plastic strain after a blade-out event.

Each blade's radial center of mass comparison pre- and post-blade-out are shown in Figure 44. The fan model post-blade-out is also shown for comparison. The damage level *D* (defined in Section 4.2) in the area of the fan with the most damage after the Fan Blade Out (FBO) event is also shown. The damage correlates well with the effective plastic strain. The loss of a blade and platform as well as the deformation in the other blades corresponds to damage severity level 3.

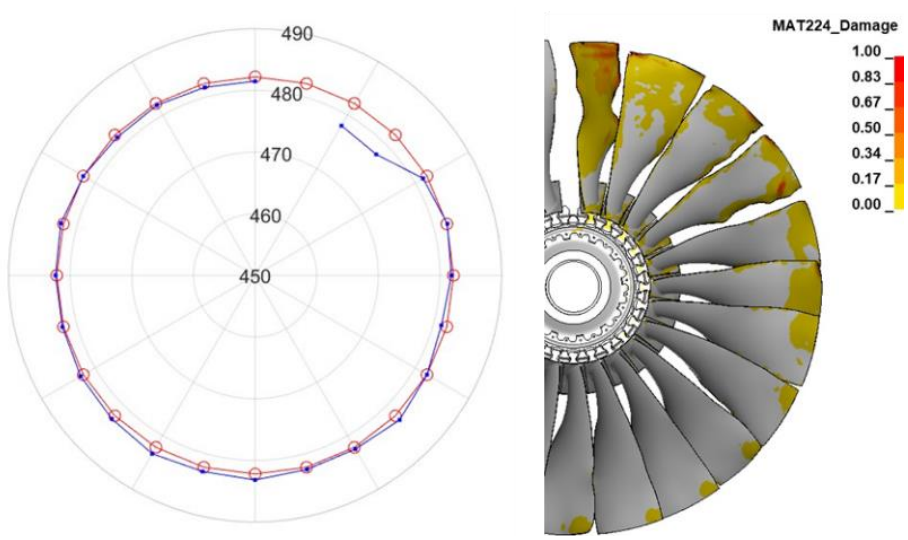

Figure 44. Center of mass of blades and fan model post blade-out.

The resultant moments and forces in a sectional plane (see Figure 40) are shown in Figure 45.

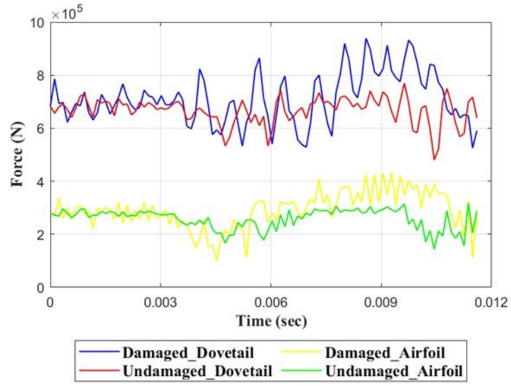

(a) forces

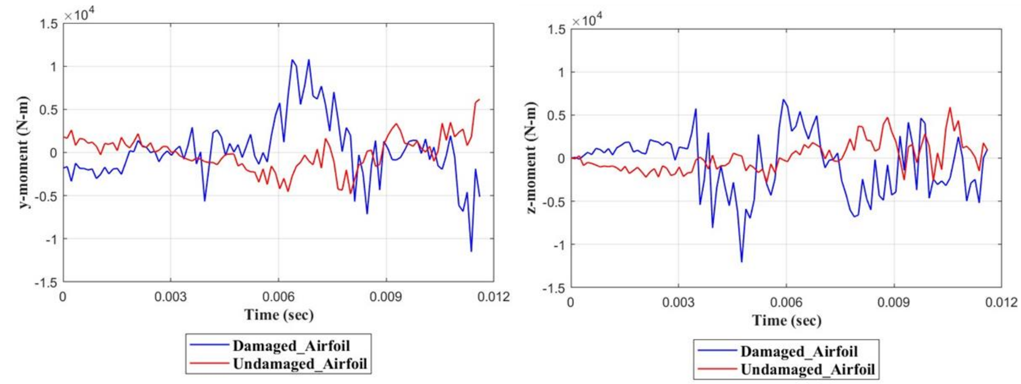

(b) moments about the y- and z-axes

Figure 45. Resultant (a) forces and (b) moments in a sectional plane of the airfoil and dovetail during the blade-out event.

For a global system in LS-DYNA, total energy reported in GLSTAT is the sum of internal energy, kinetic energy, sliding interface energy and hourglass energy. The energy ratio is defined as the ratio of total energy and the sum of initial total energy and external work.

$$Energy\ ratio = \frac{total\ energy}{(initial\ total\ energy + external\ work)}$$

Figure 46(a) shows the overall energy ratio in the system. Figure 46(b) shows the overall energy in the system. The bulk of the energy in the system is the kinetic energy in the fan. The reason why the total energy in the system increases slightly is because of the external work of the driven shaft. There is also significant internal energy in the system that will be shown more clearly in the breakout of the fan energies.

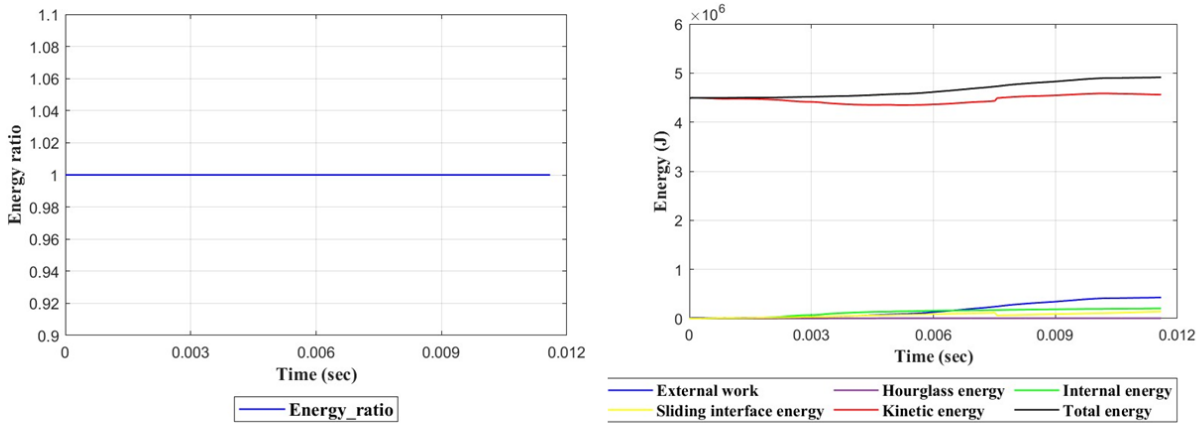

(a) energy ratio (b) energy in system

Figure 46. Overall energy in the system during the FBO case.

The kinetic and internal energy of the fan are shown in Figure 47. The majority of the energy of the fan is kinetic energy with balance being the internal energy that increases as the fan blade impacts other blades and the containment casing. Note that the internal energy is comprised of the elastic and plastic energy contained in the blades; therefore it has a general increasing trend as more plastic deformation or erosion of elements occurs, but it can also oscillate some as the elastic energy fluctuates.

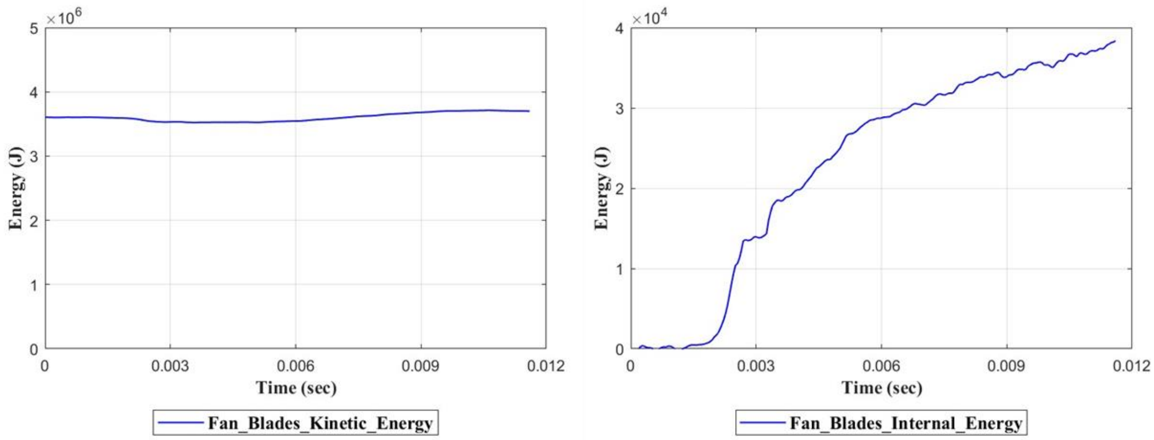

Figure 47. Energy in the fan blades during the FBO case.

The kinetic energy plot indicates the summation of kinetic energy in the fan blades without the released blade. As the simulation progresses, the released blade loses kinetic energy while impacting the casing and starts interacting with the trailing blades. The kinetic energy of the trailing blades is initially reduced as they impact the released blade. Internal energy also accumulates in these blades as they are plastically deformed during the impact. Due to the driven condition in the disk, the overall kinetic energy increases as external work is applied to overcome the losses due to the impact.

4.4.2 Reference 2: Bird Ingestion Simulation

The bird ingestion simulation was carried out with very similar conditions as many of the UAS ingestions with a high fan speed, high relative translational velocity and high radial span location with a 1.22kg (2.68 lb) bird. The bird has the same properties as the bird discussed in Section 2.4.3, but with a smaller mass equal to that of the UAS. The kinematics of the ingestion are shown in Figure 48.

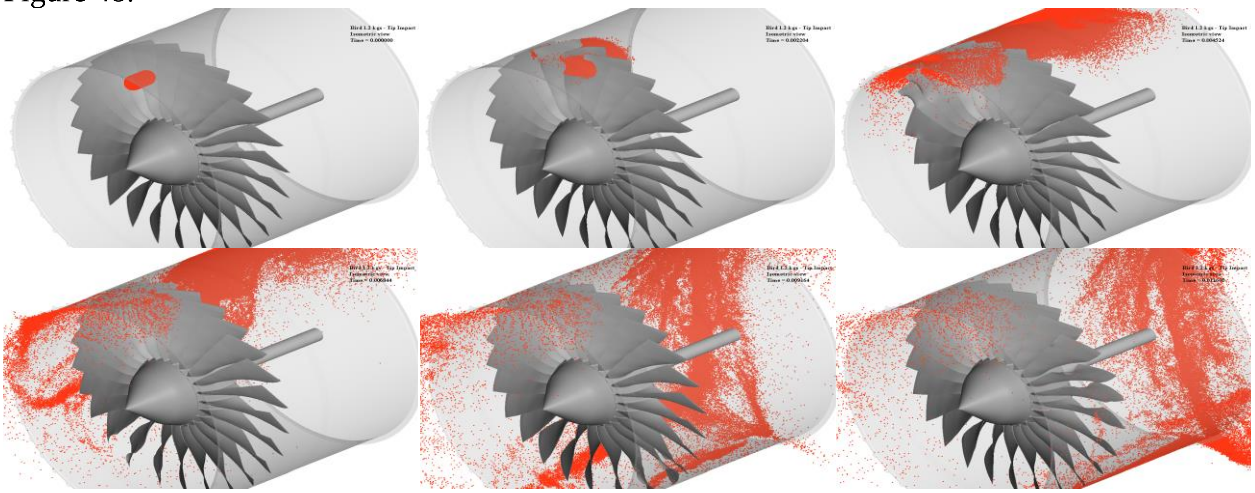

(a) isometric view

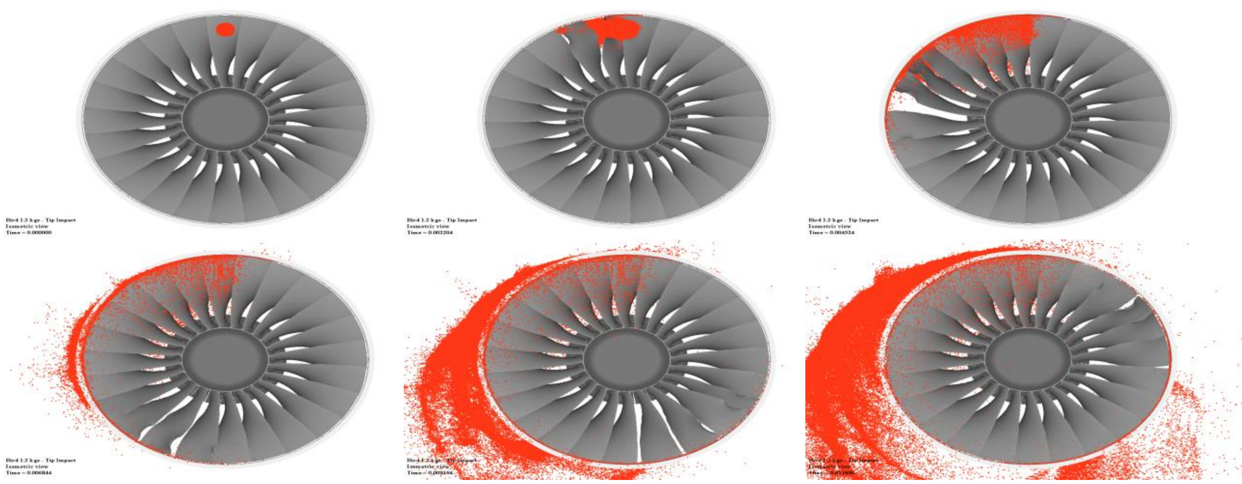

(b) front view

Figure 48. Kinematics of bird ingestion simulation.

The effective plastic strain in the fan is shown in Figure 49. There is significant deformation and cupping of the leading edges of multiple blades.

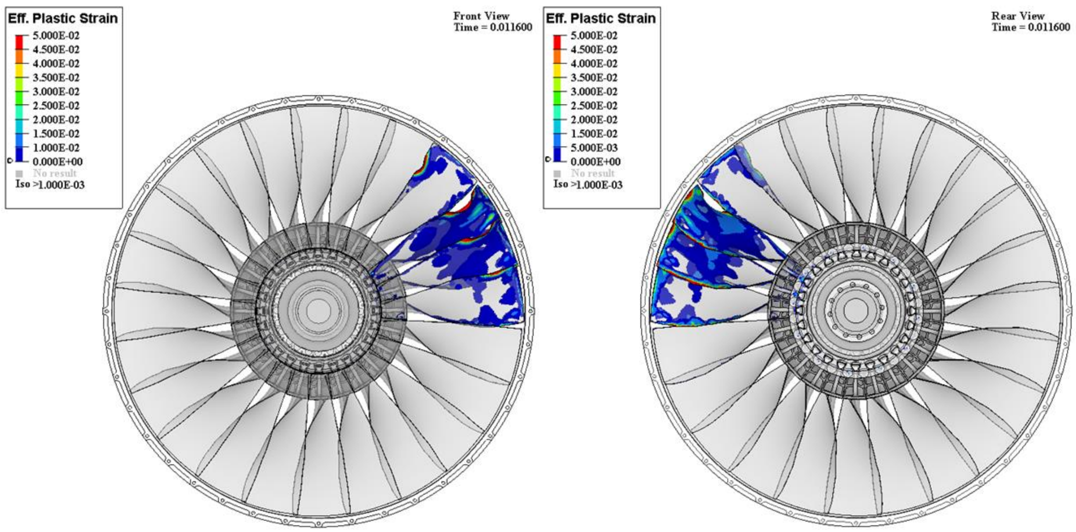

Figure 49. Effective plastic strain after a bird ingestion simulation.

Each blade's radial center of mass comparison pre- and post-blade-out are shown in Figure 50. The damage level *D* (defined in Section 4.2) in the area of the fan with the most damage after the bird ingestion is also shown. The damage correlates well with the effective plastic strain. The significant plastic deformation and cupping of the leading edge of multiple blades corresponds to damage severity level 2.

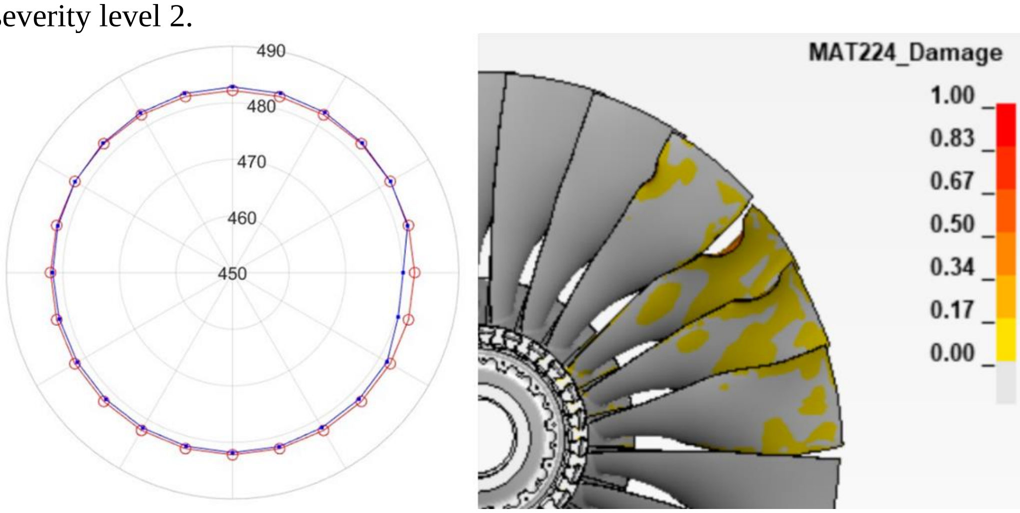

Figure 50. Center of mass of blades and fan model after bird ingestion.

The resultant moments and forces in a sectional plane (see Figure 40) are shown in Figure 51. Unlike the UAS ingestion and FBO cases, there is not a large variation in amplitude between the damaged and undamaged airfoils for this case.

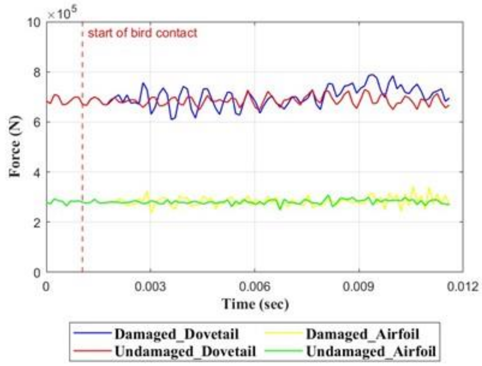

(a) forces

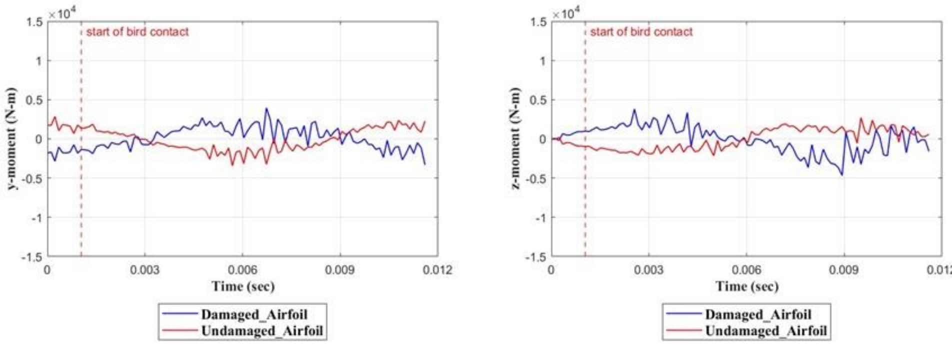

(b) moments about the y- and z-axes

Figure 51. Resultant (a) forces and (b) moments in a sectional plane of the airfoil and dovetail during the bird ingestion.

Figure 52(a) shows the overall energy ratio in the system. Figure 52(b) shows the overall energy in the system. The bulk of the energy in the system is the kinetic energy in the fan. The reason why the total energy in the system increases slightly is because of the external work of the driven shaft. There is also significant internal energy in the system that will be shown more clearly in the breakout of the fan energies.

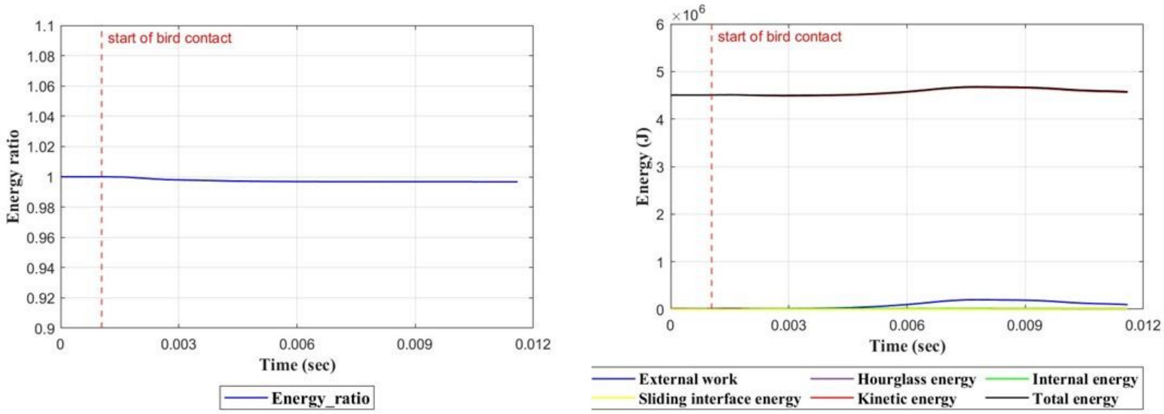

(a) energy ratio (b) energy in system

Figure 52. Overall energy in the system during the bird ingestion.

The kinetic and internal energy of the fan are shown in

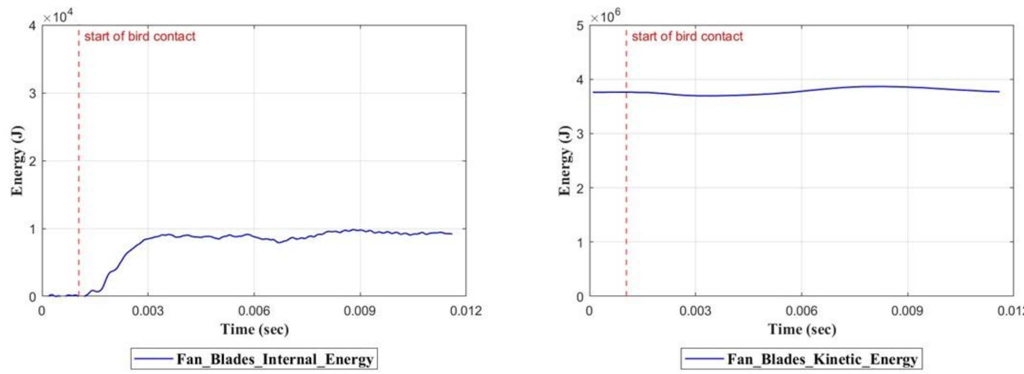

Figure 53. The majority of the energy of the fan is kinetic energy with the balance being the internal energy that increases as the fan impacts the bird and is plastically deformed.

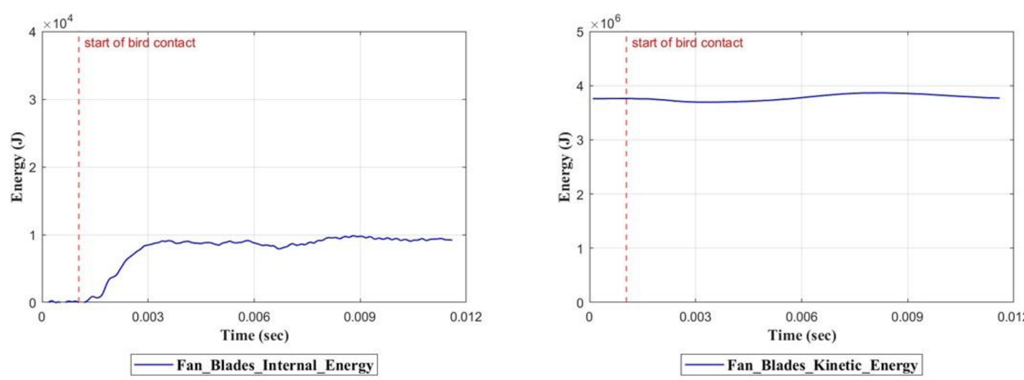

Figure 53. Energy in the fan blades during the bird ingestion.

4.4.3 Simulation LFS_LRV_LRS_90P

This case corresponded to a UAS ingestion with a low fan speed, low relative translational velocity, low radial span location, and 90 degree pitch orientation (see Figure 39). The kinematics of the ingestion are shown in Figure 54. In this case, due to the low translational relative velocity of the UAS and low rotational speed of the fan, only about 40% of a fan revolution was completed before termination of the simulation at approximately 20 ms.

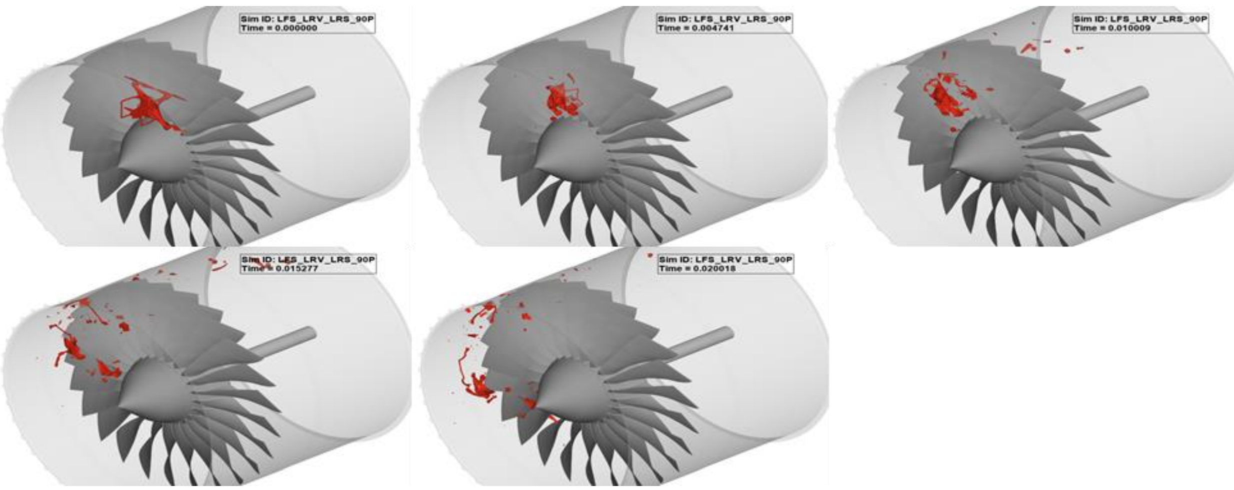

(a) isometric view

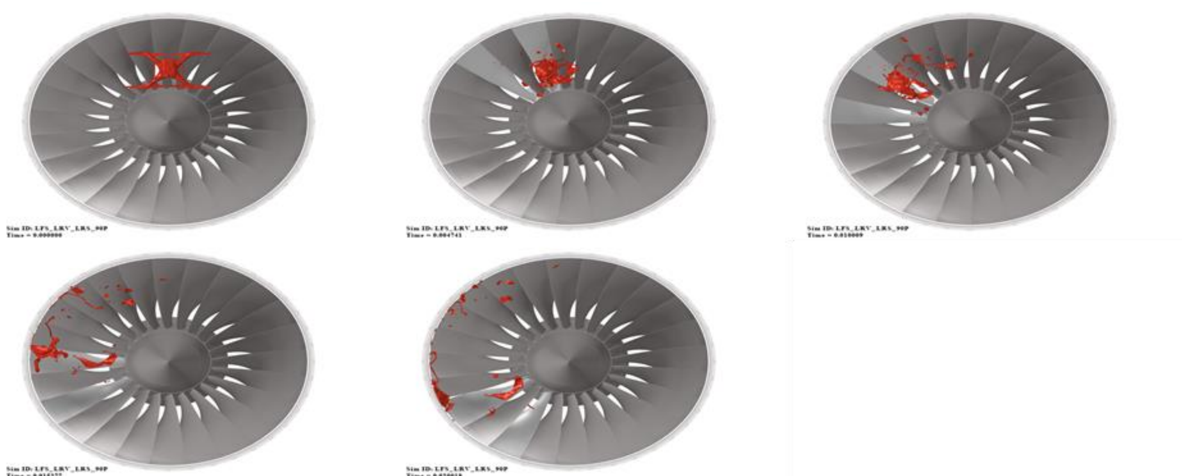

(b) front view

Figure 54. Kinematics of UAS ingestion simulation LFS_LRV_LRS_90P.

The effective plastic strain in the fan at the end of the simulation is shown in Figure 55 (front and rear views). For this case there is some minimal plastic strain in a few blades.

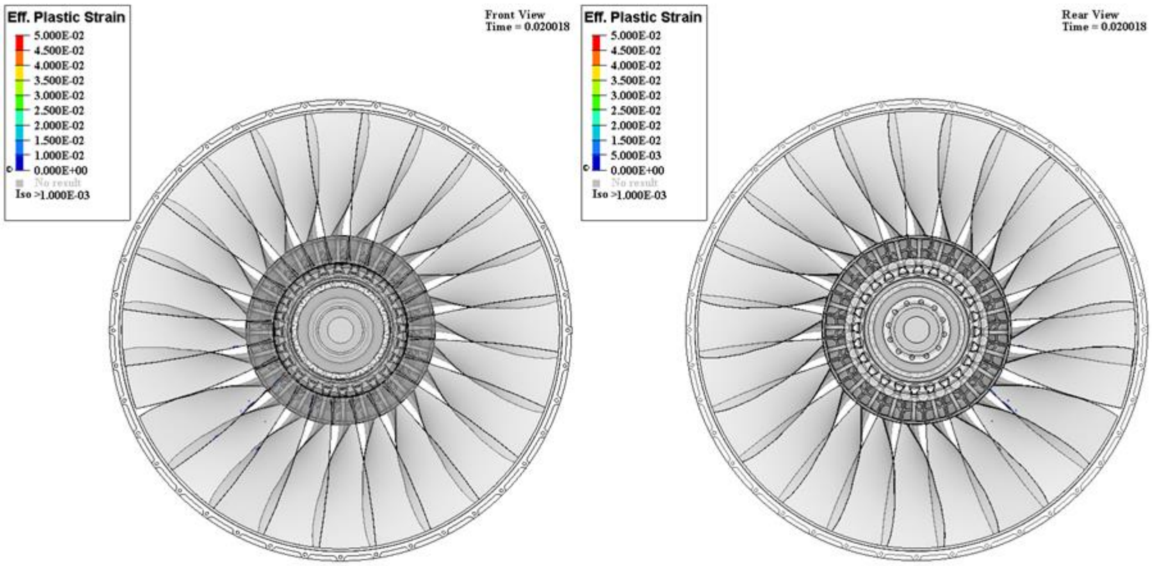

Figure 55. Effective plastic strain after UAS ingestion simulation LFS_LRV_LRS_90P.

Each blade's radial center of mass pre- and post-ingestion are shown in Figure 56. The damage level D (defined in Section 4.2) in the damaged area of the fan model after the UAS ingestion is also shown. The damage correlates well with the effective plastic strain, where there is minimal damage to the leading edge of a few blades. This corresponds to damage severity level 1.

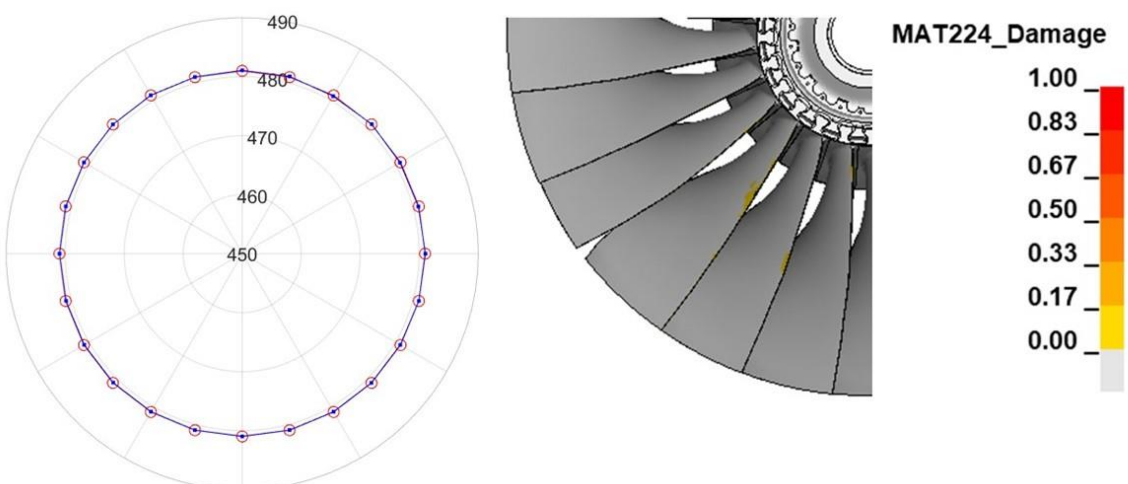

Figure 56. Center of mass of blades and fan model damage after UAS ingestion simulation LFS_LRV_LRS_90P.

The resultant moments and forces in a sectional plane (see Figure 40) during the ingestion are shown in Figure 57. Note that the damaged airfoil and dovetail has a significantly larger oscillation in the forcing and moment than the undamaged blade.

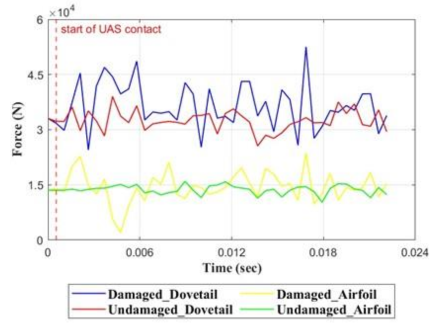

(a) forces

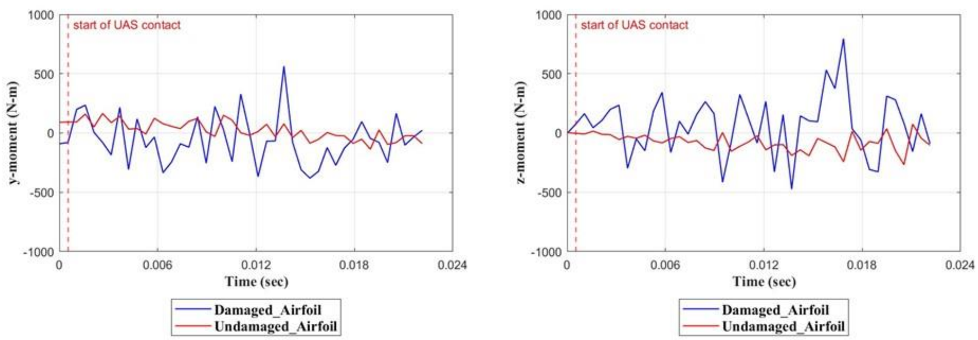

(b) moments about the y- and z-axes

Figure 57. Resultant (a) forces and (b) moments in a sectional plane of the airfoil and dovetail during UAS ingestion simulation LFS_LRV_LRS_90P.

Figure 58(a) shows the overall energy ratio in the system not including the eroded energy. Note that there is a slight drop in the energy ratio term because of the erosion of elements in the UAS during the ingestion. There is also slight increase around 15 ms that is common in these long duration simulations. Figure 58Figure 117(b) shows the overall energy in the system. The bulk of the energy in the system is the kinetic energy in the fan and the UAS. The reason why the total energy in the system increases slightly is because of the external work of the driven shaft. There is some internal energy in the system that will be shown more clearly in the breakout of the UAS and fan energies.

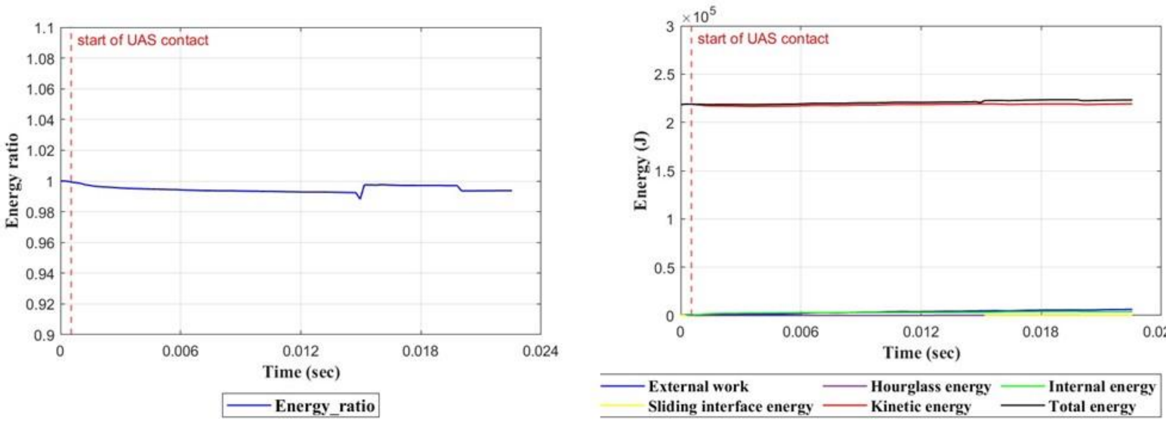

(a) energy ratio (b) energy in system

Figure 58. Overall energy in the system for LFS_LRV_LRS_90P.

Figure 59 shows the internal and kinetic energy in the UAS during the ingestion. Note that as contact is made, the internal energy increases while the kinetic energy decreases for the UAS. The increase in the internal energy is due to the plastic deformation and failure of UAS components. The decrease in the kinetic energy is due to the fact that during the impact many of the UAS parts are decelerated, however after this initial decrease some parts are accelerated by the fan as they are swept outwards radially causing an increase in kinetic energy. The velocities of the motors, camera and battery during the impact are all shown in

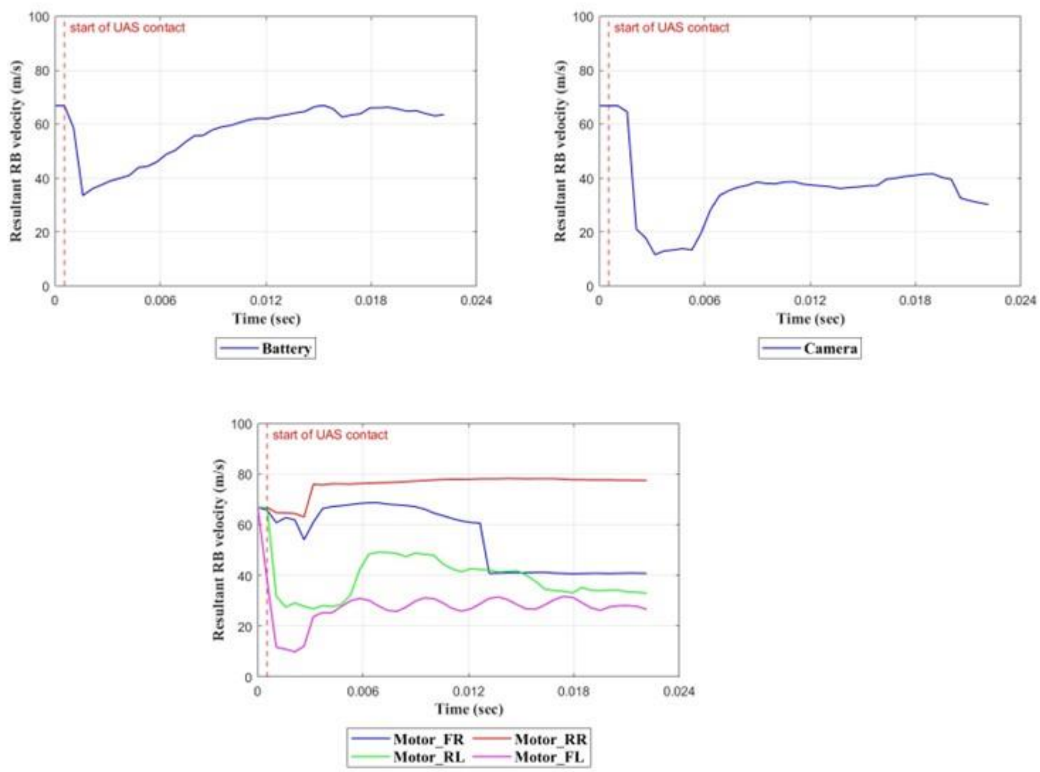

Figure 60 and agree with this assessment. The different color lines for the velocities of each motor correspond to the motor colors in Figure 39.

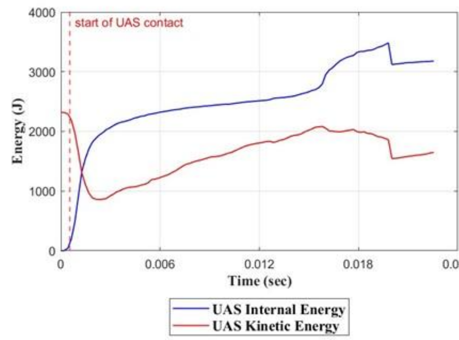

Figure 59. Internal and kinetic energies of the UAS for LFS_LRV_LRS_90P .

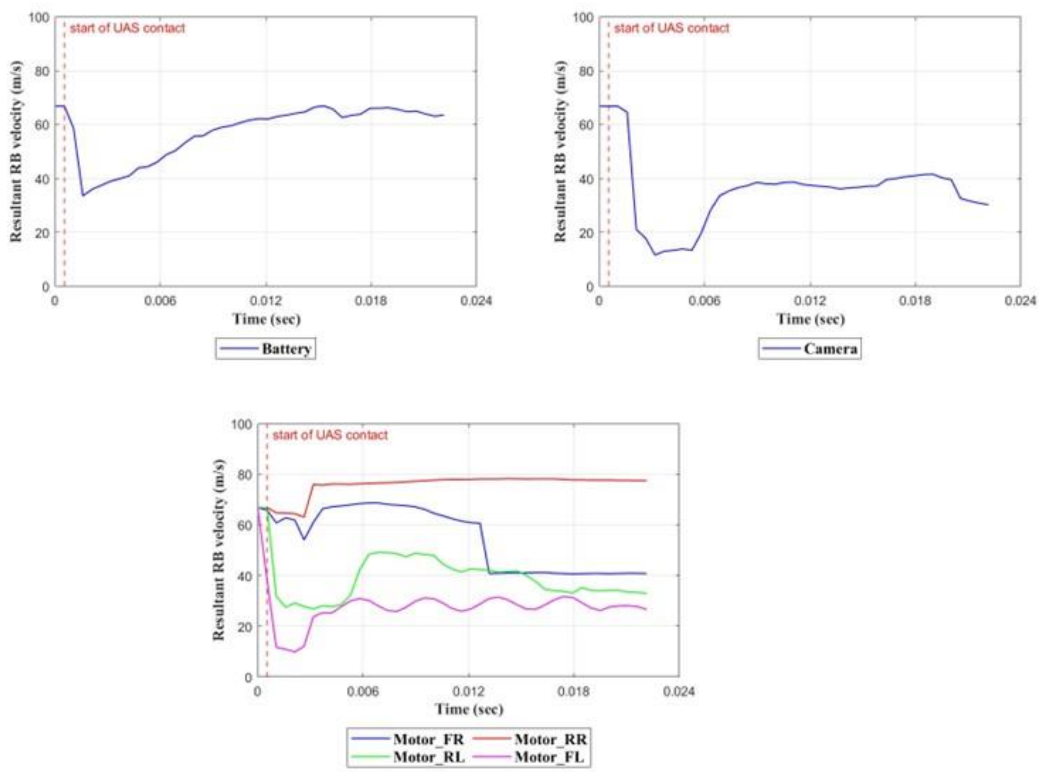

Figure 60. Resultant velocities of UAS components for LFS_LRV_LRS_90P.

The kinetic and internal energy of the fan are shown in

Figure 61. Note that the kinetic energy of the fan looks very similar to the overall energy in the system from Figure 58, since the bulk of the energy is in the fan. There is also some minor damage in the fan through the internal energy that increases while the fan is impacting the UAS.

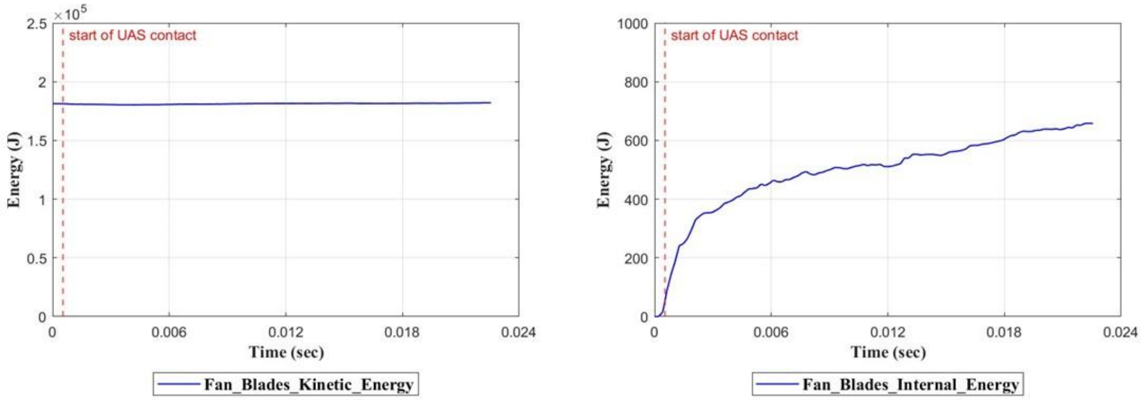

Figure 61. Energy in the fan blades during LFS_LRV_LRS_90P.

4.4.4 Simulation LFS_LRV_HRS_Nom

This case corresponded to a UAS ingestion with a low fan speed, low relative translational velocity, high radial span location, and nominal orientation (see Figure 39). The kinematics of the ingestion are shown in Figure 62. In this case, due to the low translational relative velocity of the UAS and low rotational speed of the fan about a half revolution of the fan was completed before termination of the simulation at approximately 26 ms. Also, the UAS was removed from the simulation at about 25 ms to speed up the computational time since it had cleared the fan stage.

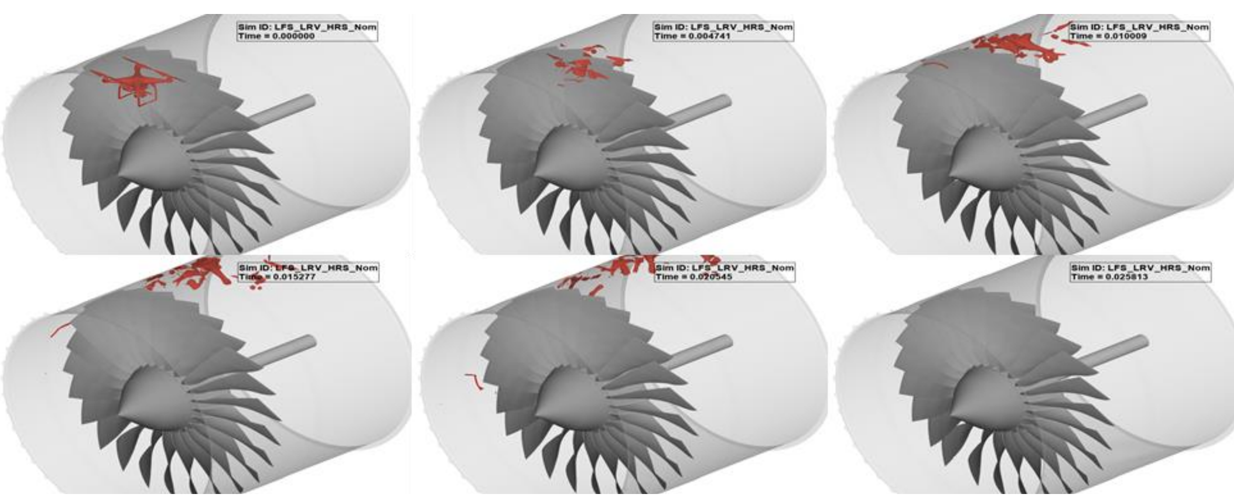

(a) isometric view

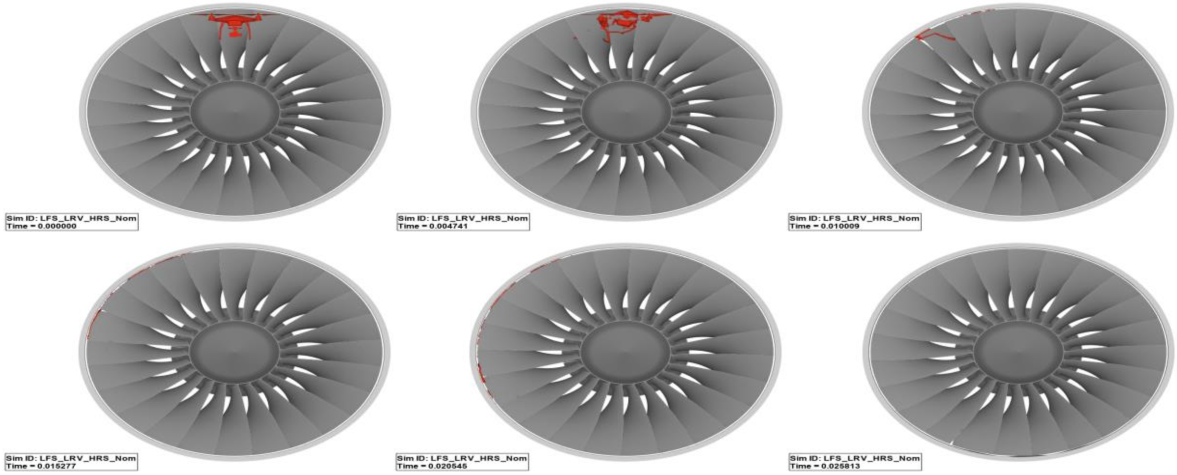

(b) front view

Figure 62. Kinematics of UAS ingestion simulation LFS_LRV_HRS_Nom.

The effective plastic strain in the fan at the end of the simulation is shown in Figure 63 (front and rear views). For this case there is some small plastic strain along the leading edge of a blade.

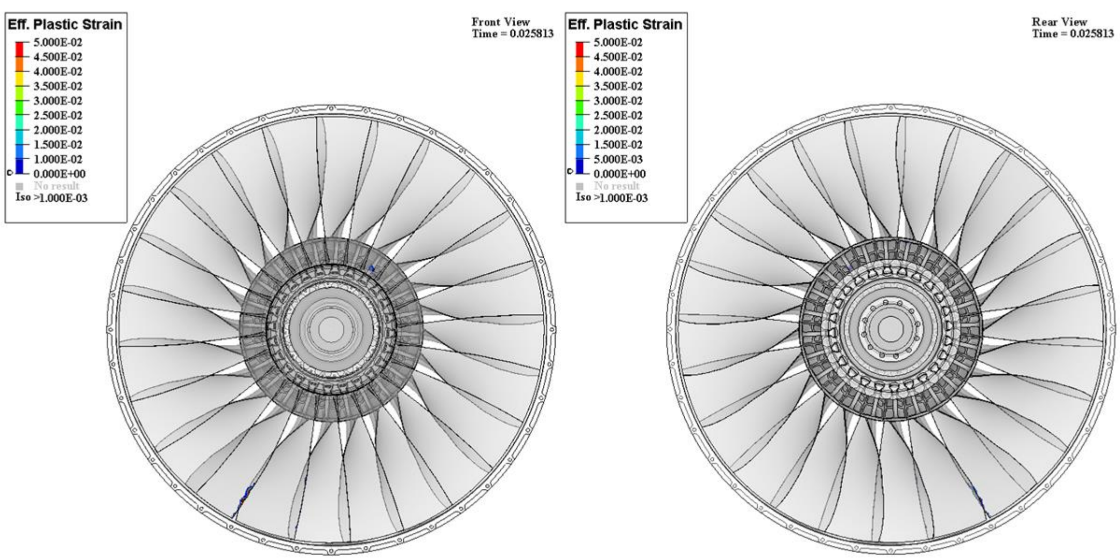

Figure 63. Effective plastic strain after UAS ingestion simulation LFS_LRV_HRS_Nom.

Each blade's radial center of mass pre- and post-ingestion are shown in Figure 64. The damage level *D* (defined in Section 4.2) in the damaged area of the fan model after the UAS ingestion is also shown. The damage correlates well with the effective plastic strain, where there is some damage to the leading edge of a blade. This corresponds to damage severity level 1.

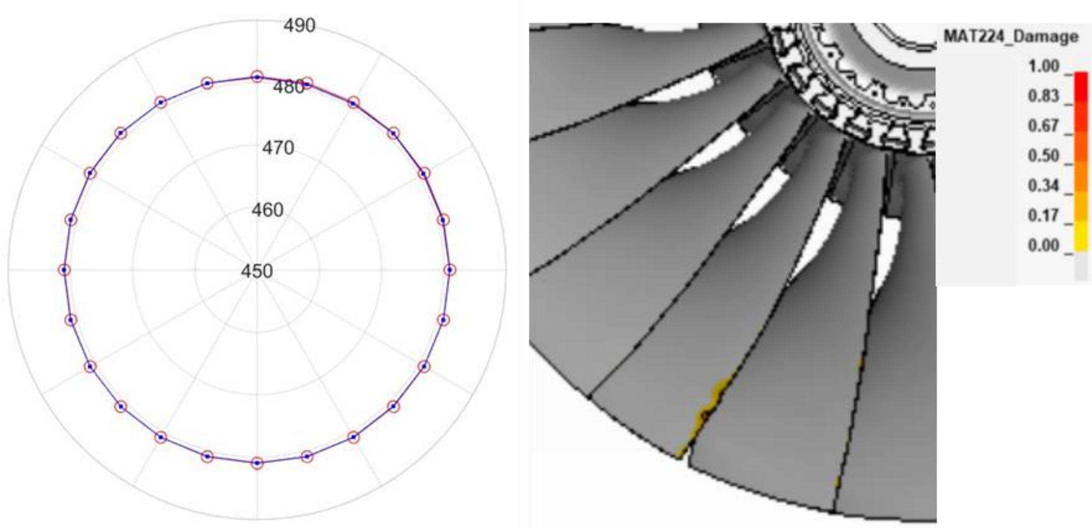

Figure 64. Center of mass of blades and fan model damage after UAS ingestion simulation LFS_LRV_HRS_Nom.

The resultant moments and forces in a sectional plane (see Figure 40) during the ingestion are shown in Figure 65. Note that the damaged airfoil has a significantly larger oscillation in the forcing and moment than the undamaged blade.

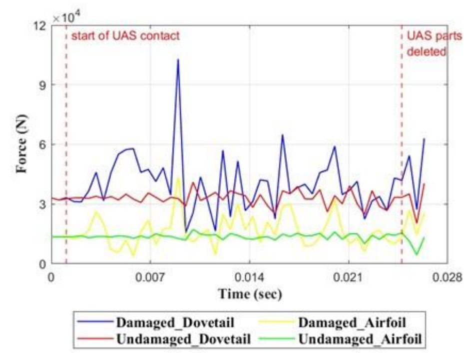

(a) forces

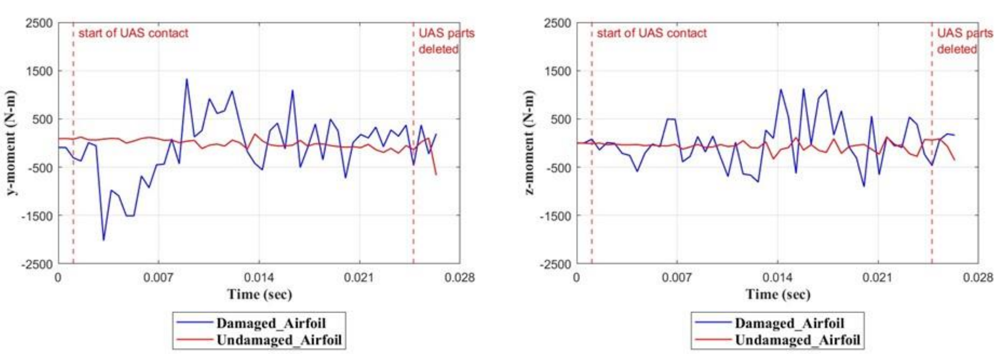

(b) moments about the y- and z-axes

Figure 65. Resultant (a) forces and (b) moments in a sectional plane of the airfoil and dovetail during UAS ingestion simulation LFS_LRV_HRS_Nom.

Figure 66(a) shows the overall energy ratio in the system not including the eroded energy. Note that there is a slight drop in the energy ratio term because of the erosion of elements in the UAS during the ingestion. There is also a slight increase around 15 ms that is common in these long duration simulations. Figure 66(b) shows the overall energy in the system. The bulk of the energy in the system is the kinetic energy in the fan and the UAS. The reason why the total energy in the system increases slightly is because of the external work of the driven shaft. There is some internal energy in the system that will be shown more clearly in the breakout of the UAS and fan energies.

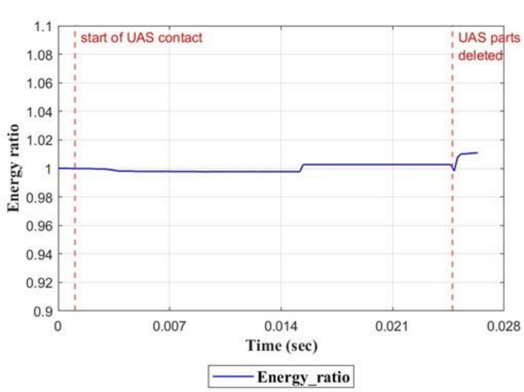

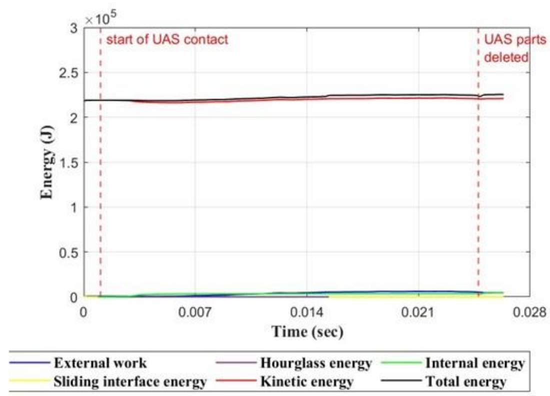

(a) energy ratio (b) energy in system

Figure 66. Overall energy in the system for LFS_LRV_HRS_Nom.

Figure 67 shows the internal and kinetic energy in the UAS during the ingestion. Note that as contact is made the internal energy increases while the kinetic energy decreases for the UAS. The increase in the internal energy is due to the plastic deformation and failure of UAS components. The decrease in the kinetic energy is due to the fact that during the impact many of the UAS parts are decelerated. The velocities of the motors, camera, and battery during the impact are all shown in Figure 68 and agree with this assessment. The different color lines for the velocities of each motor correspond to the motor colors in Figure 39.

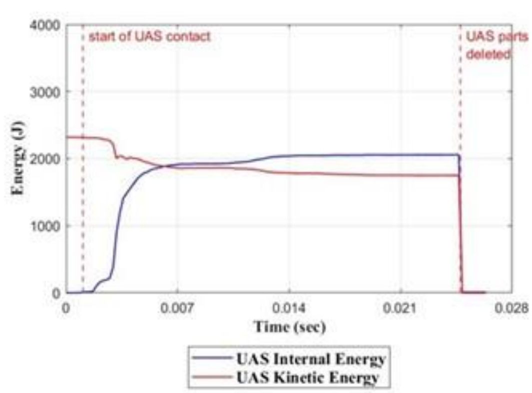

Figure 67. Internal and kinetic energies of the UAS for LFS_LRV_HRS_Nom.

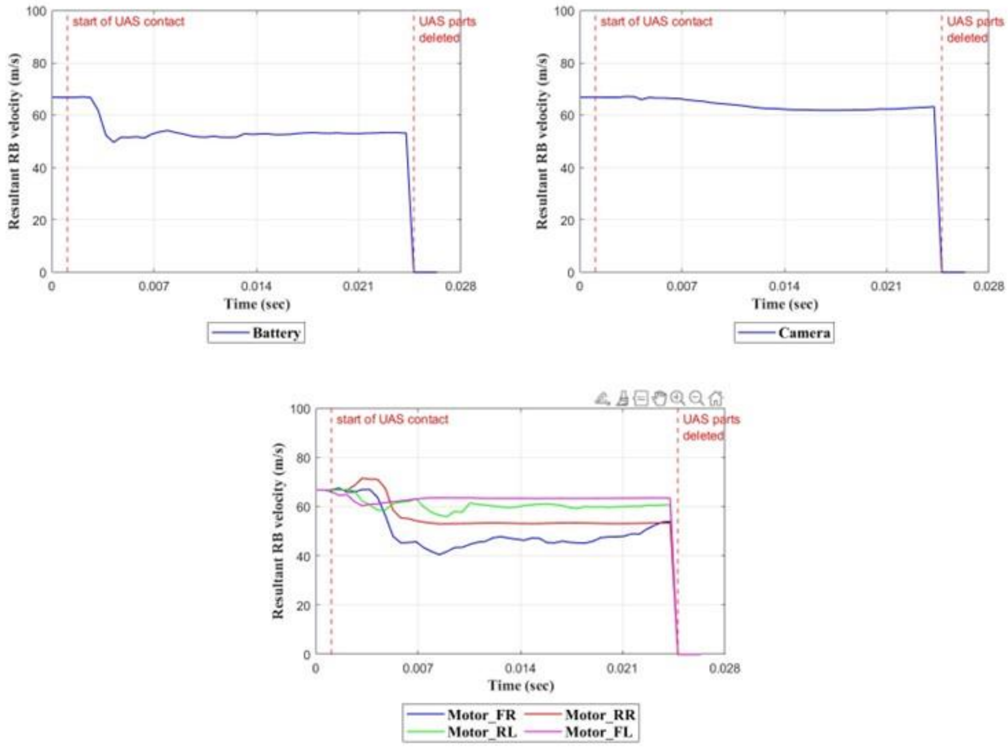

Figure 68. Resultant velocities of UAS components for LFS_LRV_HRS_Nom.

The kinetic and internal energy of the fan are shown in Figure 69. Note that the kinetic energy of the fan looks very similar to the overall energy in the system from Figure 66, since the bulk of the energy is in the fan. There is also some minor damage in the fan through the internal energy that increases while the fan is impacting the UAS.

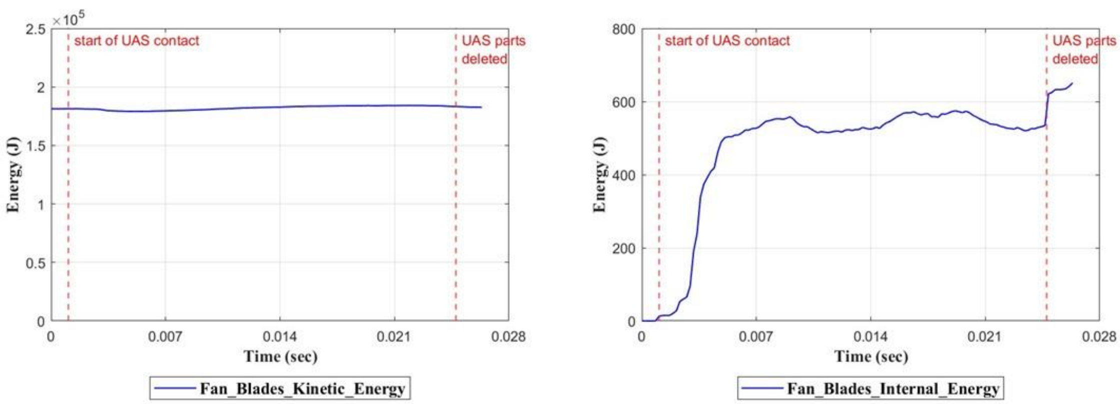

Figure 69. Energy in the fan blades during LFS_LRV_HRS_Nom.

4.4.5 Simulation LFS_HRV_LRS_90P

This case corresponded to a UAS ingestion with a low fan speed, high relative translational velocity, low radial span location, and 90 degree pitch orientation (see Figure 39). The kinematics of the ingestion are shown in Figure 70. In this case, due to the low rotational speed of the fan only a half revolution of the fan was completed before termination of the simulation at approximately 23 ms.

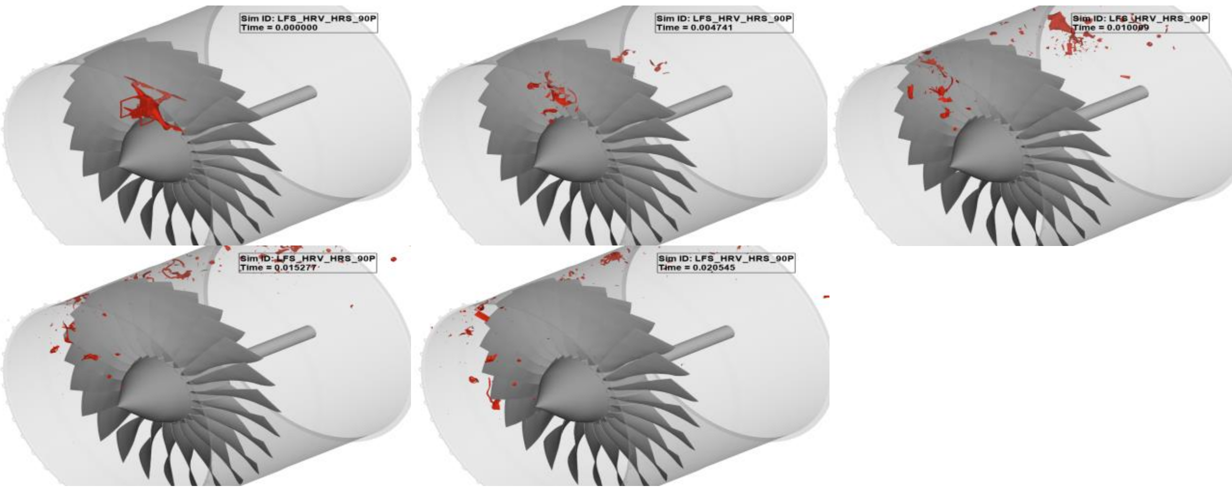

(a) isometric view

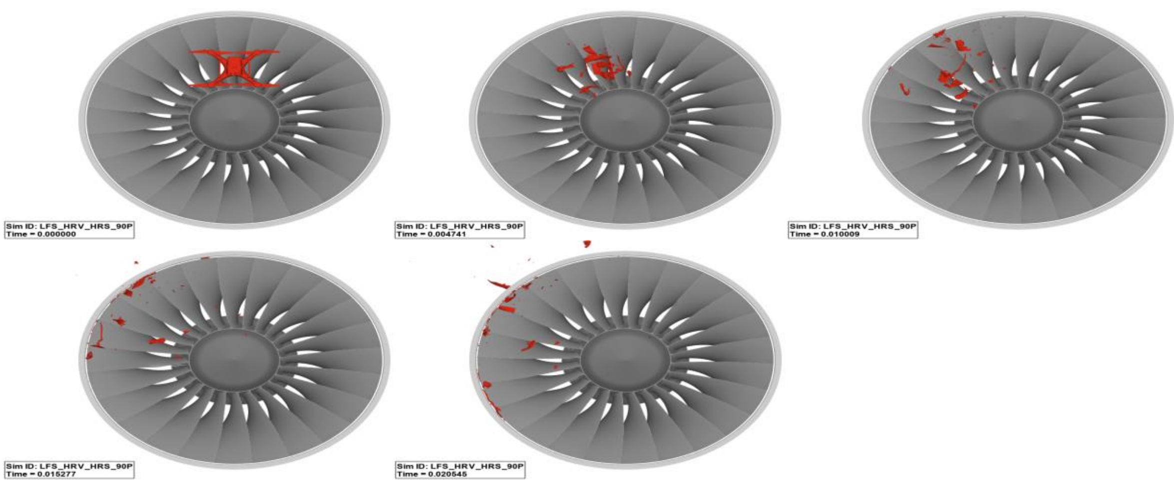

(b) front view

Figure 70. Kinematics of UAS ingestion simulation LFS_HRV_LRS_90P.

The effective plastic strain in the fan at the end of the simulation is shown in Figure 71 (front and rear views). For this case there is some plastic strain along the leading edge of a blade.

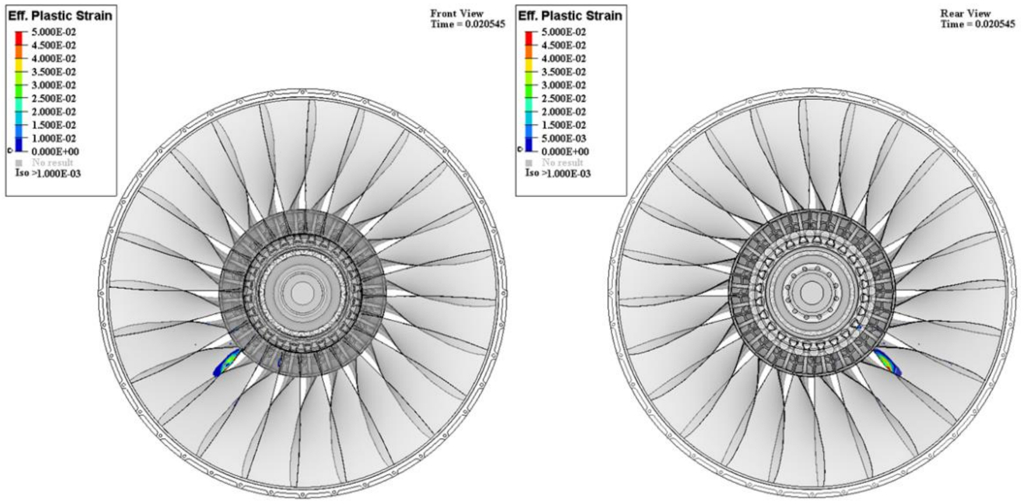

Figure 71. Effective plastic strain after UAS ingestion simulation LFS_HRV_LRS_90P.

Each blade's radial center of mass pre- and post-ingestion are shown in Figure 72. The damage level *D* (defined in Section 4.2) in the damaged area of the fan model after the UAS ingestion is also shown. The damage correlates well with the effective plastic strain, where there is some damage to the leading edge of a blade. This corresponds to damage severity level 1.

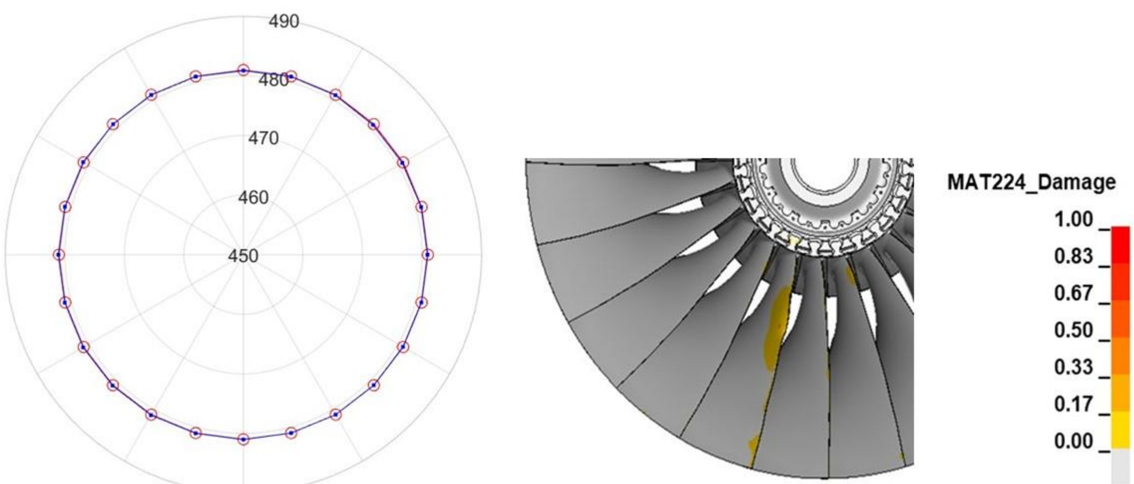

Figure 72. Center of mass of blades and fan model damage after UAS ingestion simulation LFS_HRV_LRS_90P.

The resultant moments and forces in a sectional plane (see Figure 40) during the ingestion are shown in Figure 73. Note that the damaged airfoil has a significantly larger oscillation in the forcing and moment than the undamaged blade.

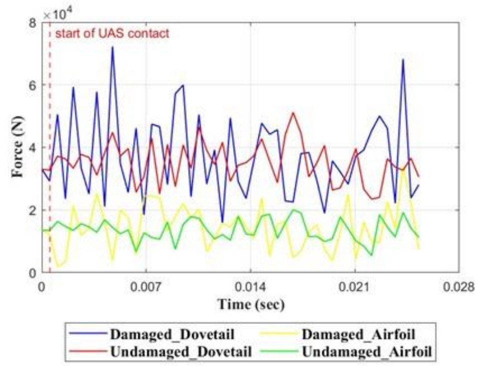

(a) forces

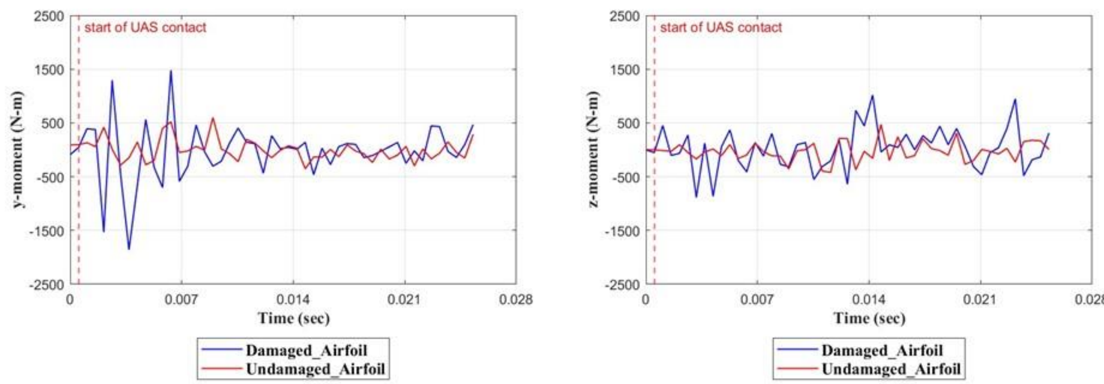

(b) moments about the y- and z-axes

Figure 73. Resultant (a) forces and (b) moments in a sectional plane of the airfoil and dovetail during UAS ingestion simulation LFS_HRV_LRS_90P.

Figure 74(a) shows the overall energy ratio in the system, not including the eroded energy. Note that there is a slight increase around 14 ms that is common in these long duration simulations. Figure 74(b) shows the overall energy in the system. The bulk of the energy in the system is the kinetic energy in the fan and the UAS. The reason why the total energy in the system increases slightly is because of the external work of the driven shaft. There is some internal energy in the system that will be shown more clearly in the breakout of the UAS and fan energies.

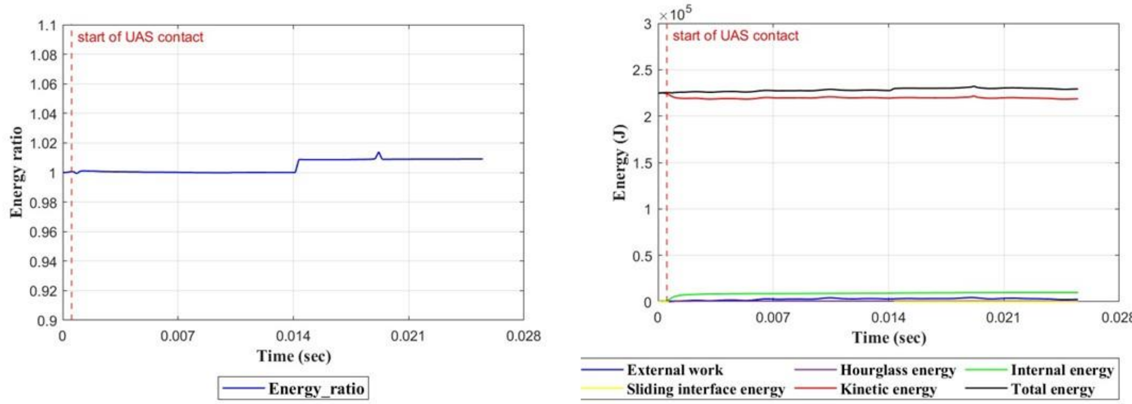

(a) energy ratio (b) energy in system

Figure 74. Overall energy in the system for LFS_HRV_LRS_90P.

Figure 75 shows the internal and kinetic energy in the UAS during the ingestion. Note that as contact is made the internal energy increases while the kinetic energy decreases for the UAS. The increase in the internal energy is due to the plastic deformation and failure of UAS components. The decrease in the kinetic energy is due to the fact that during the impact many of the UAS parts are decelerated. The velocities of the motors, camera, and battery during the impact are all shown in Figure 76 and agree with this assessment. The different color lines for the velocities of each motor correspond to the motor colors in Figure 39.

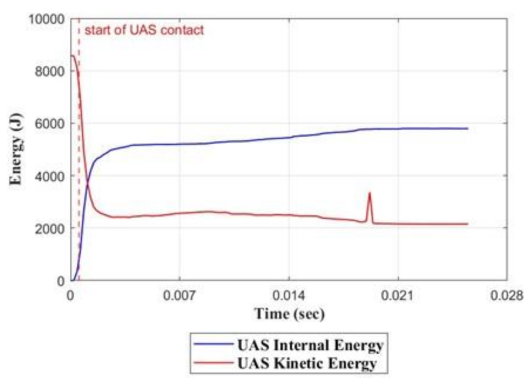

Figure 75. Internal and kinetic energies of the UAS for LFS_HRV_LRS_90P.

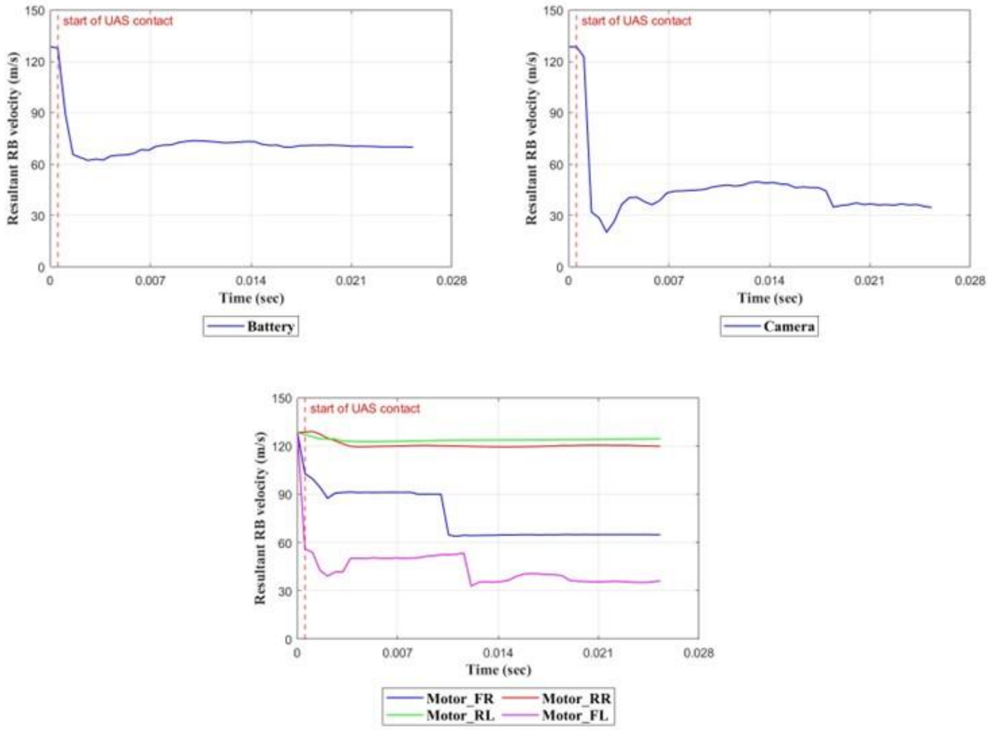

Figure 76. Resultant velocities of UAS components for LFS_HRV_LRS_90P.

The kinetic and internal energy of the fan are shown in Figure 77. Note that the kinetic energy of the fan looks very similar to the overall energy in the system from Figure 74, since the bulk of the energy is in the fan. There is also some damage in the fan through the internal energy that increases while the fan is impacting the UAS.

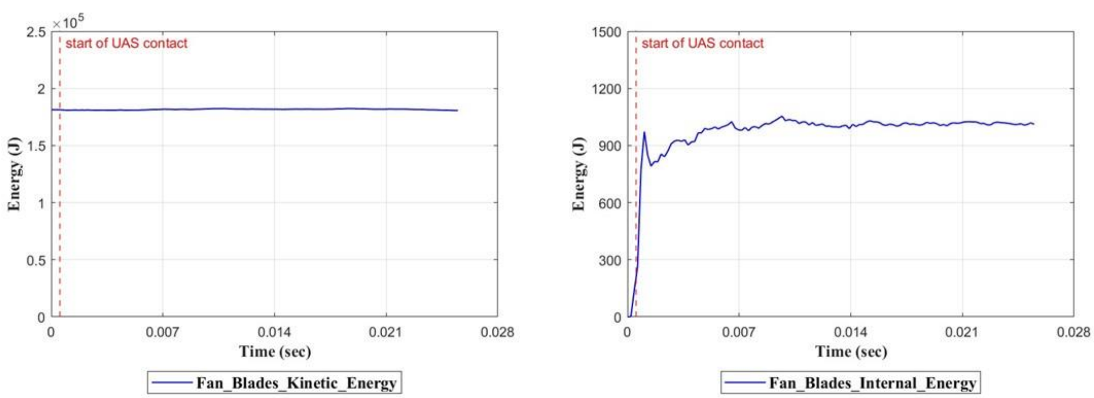

Figure 77. Energy in the fan blades during LFS_HRV_LRS_90P.

4.4.6 Simulation LFS_HRV_HRS_Nom

This case corresponded to a UAS ingestion with a low fan speed, high relative translational velocity, high radial span location, and nominal orientation (see Figure 39). The kinematics of the ingestion are shown in Figure 78. In this case, due to the low rotational speed of the fan only about a half revolution of the fan was completed before termination of the simulation at approximately 26 ms.

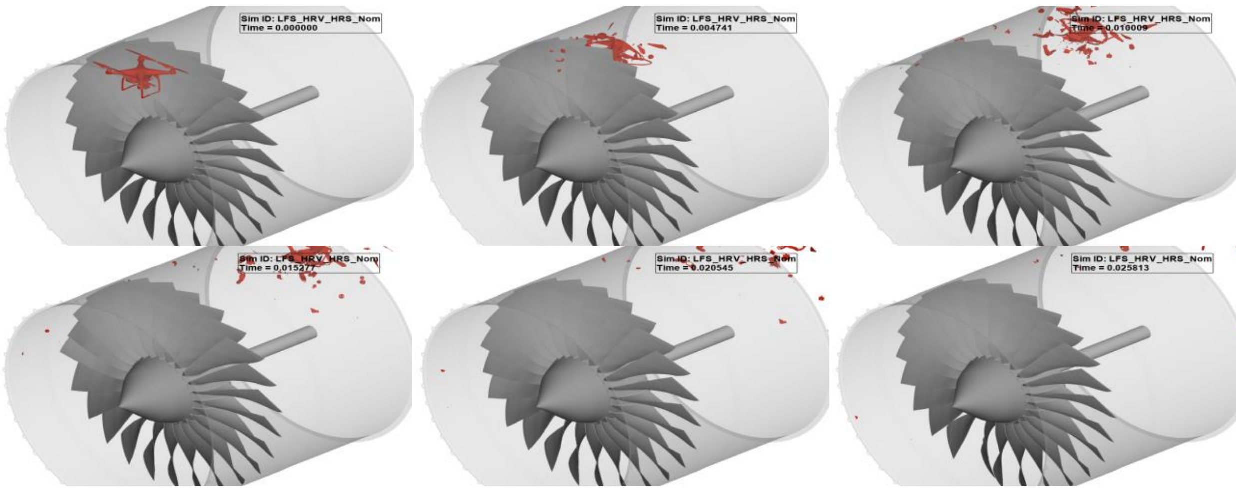

(a) isometric view

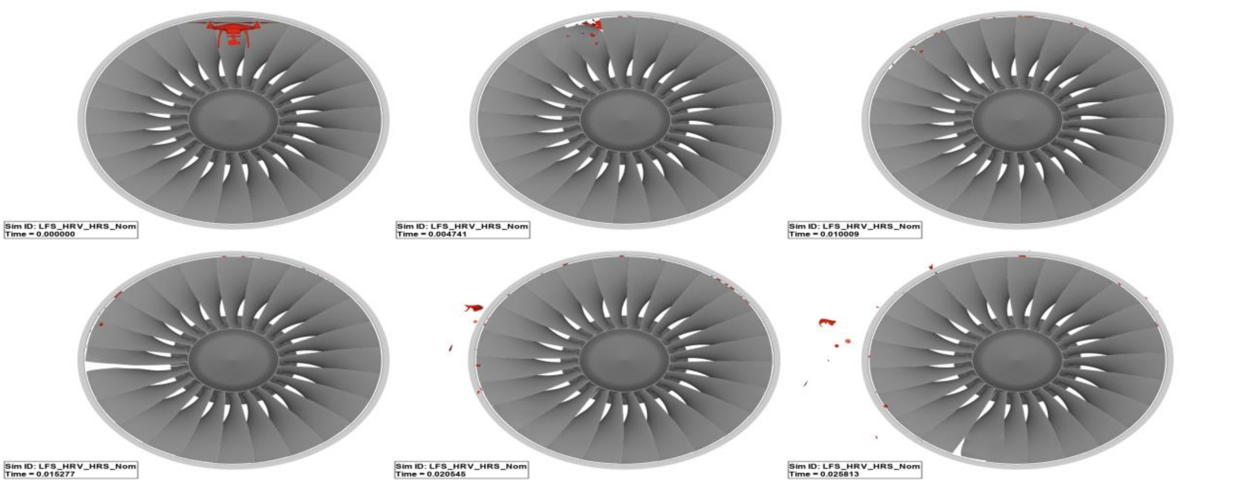

(b) front view

Figure 78. Kinematics of UAS ingestion simulation LFS_HRV_HRS_Nom.

The effective plastic strain in the fan at the end of the simulation is shown in Figure 79 (front and rear views). For this case there is some plastic strain in two blades.

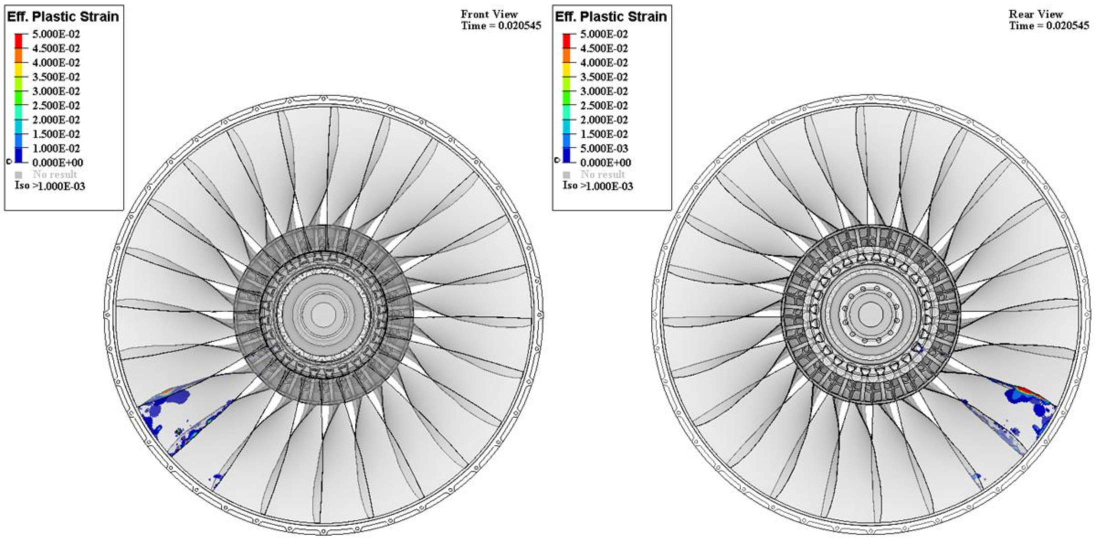

Figure 79. Effective plastic strain after UAS ingestion simulation LFS_HRV_HRS_Nom.

Each blade's radial center of mass pre- and post-ingestion are shown in Figure 80. The damage level *D* (defined in Section 4.2) in the damaged area of the fan model after the UAS ingestion is also shown. The damage correlates well with the effective plastic strain, where there is some damage concentrated in two blades. This corresponds to damage severity level 1.

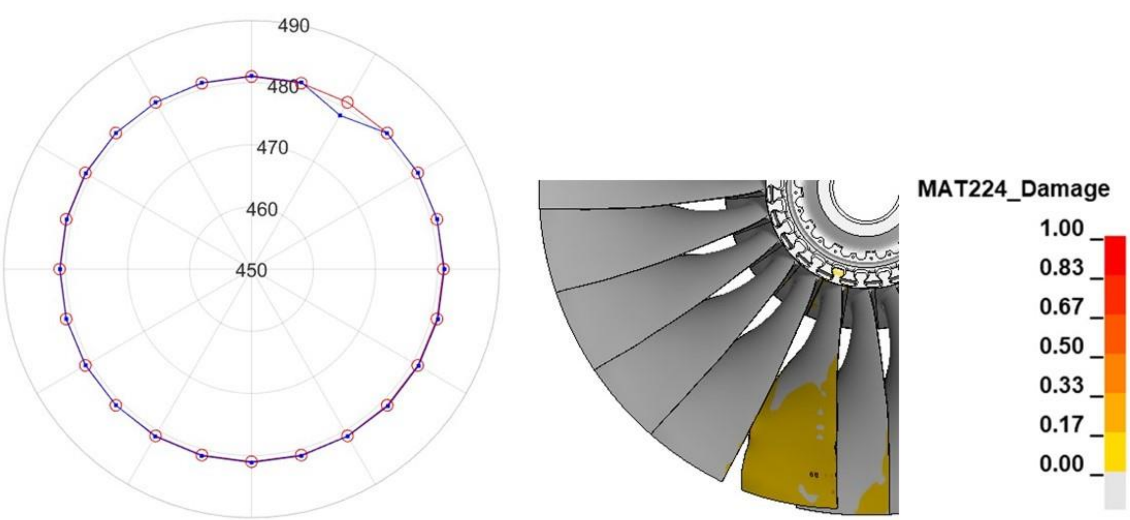

Figure 80. Center of mass of blades and fan model damage after UAS ingestion simulation LFS_HRV_HRS_Nom.

The resultant moments and forces in a sectional plane (see Figure 40) during the ingestion are shown in Figure 81. Note that the damaged airfoil has a significantly larger oscillation in the forcing and moment than the undamaged blade.

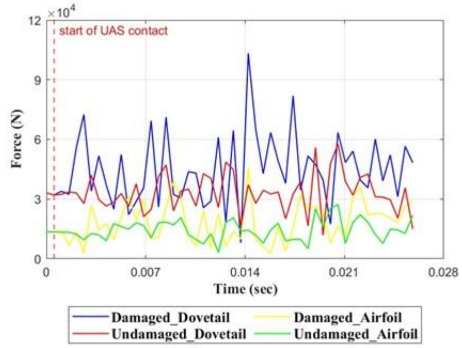

(a) forces

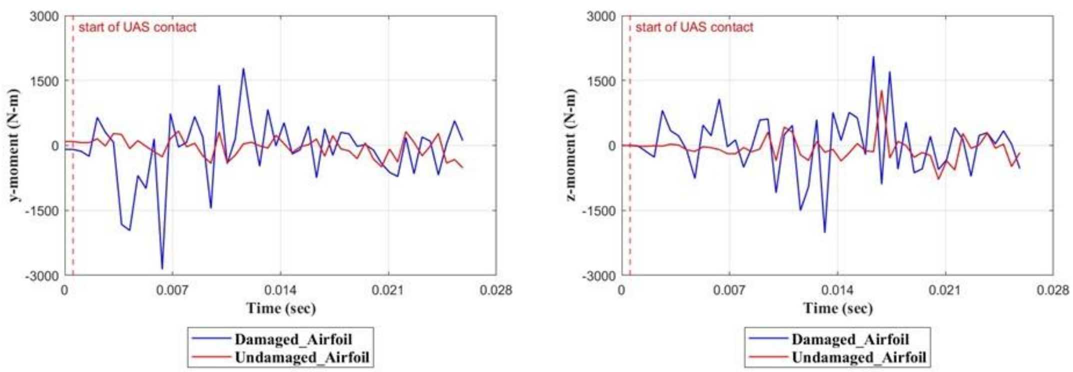

(b) moments about the y- and z-axes

Figure 81. Resultant (a) forces and (b) moments in a sectional plane of the airfoil and dovetail during UAS ingestion simulation LFS_HRV_HRS_Nom.

Figure 82(a) shows the overall energy ratio in the system, not including the eroded energy. Note that there is a slight increase around 14 ms that is common in these long duration simulations. Figure 82(b) shows the overall energy in the system. The bulk of the energy in the system is the kinetic energy in the fan and the UAS. The reason why the total energy in the system increases slightly is because of the external work of the driven shaft. There is some internal energy in the system that will be shown more clearly in the breakout of the UAS and fan energies.

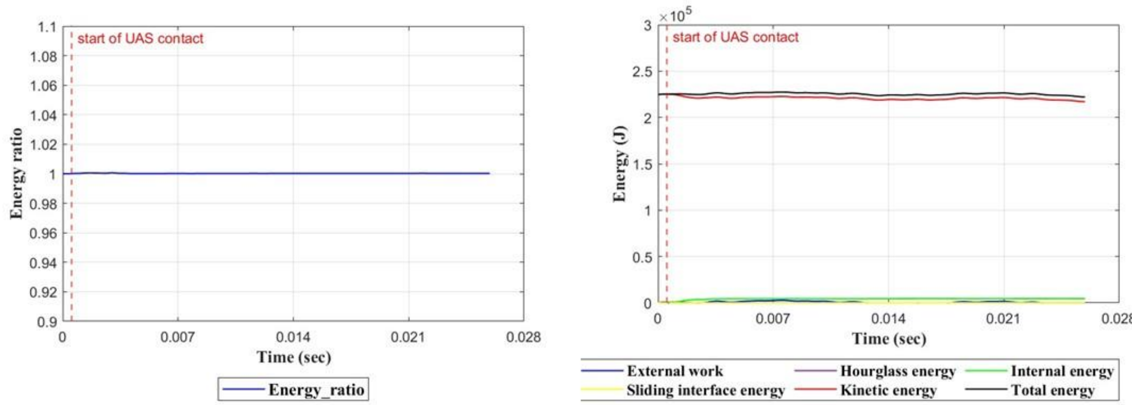

(a) energy ratio (b) energy in system

Figure 82. Overall energy in the system for LFS_HRV_HRS_Nom.

Figure 83 shows the internal and kinetic energy in the UAS during the ingestion. Note that as contact is made the internal energy increases while the kinetic energy decreases for the UAS. The increase in the internal energy is due to the plastic deformation and failure of UAS components. The decrease in the kinetic energy is due to the fact that during the impact many of the UAS parts are decelerated. The velocities of the motors, camera, and battery during the impact are all shown in Figure 84 and agree with this assessment. The different color lines for the velocities of each motor correspond to the motor colors in Figure 39.

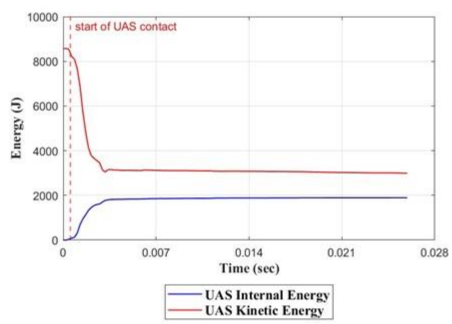

Figure 83. Internal and kinetic energies of the UAS for LFS_HRV_HRS_Nom.

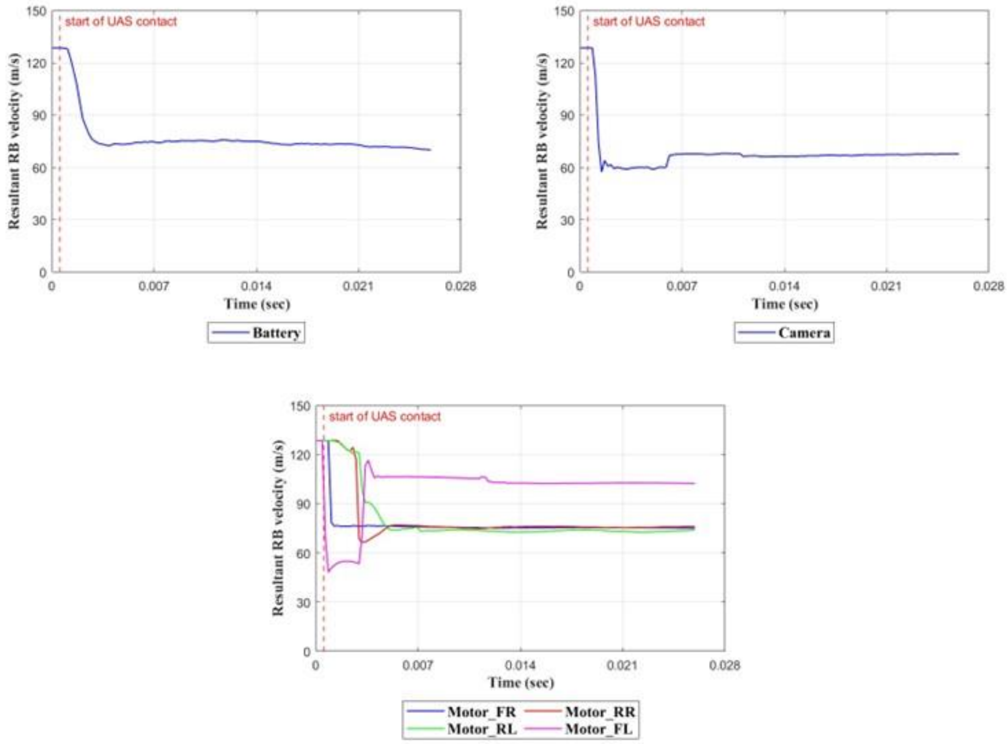

Figure 84. Resultant velocities of UAS components for LFS_HRV_HRS_Nom.

The kinetic and internal energy of the fan are shown in Figure 85. Note that the kinetic energy of the fan looks very similar to the overall energy in the system from Figure 82, since the bulk of the energy is in the fan. There is also some damage in the fan through the internal energy that increases while the fan is impacting the UAS.

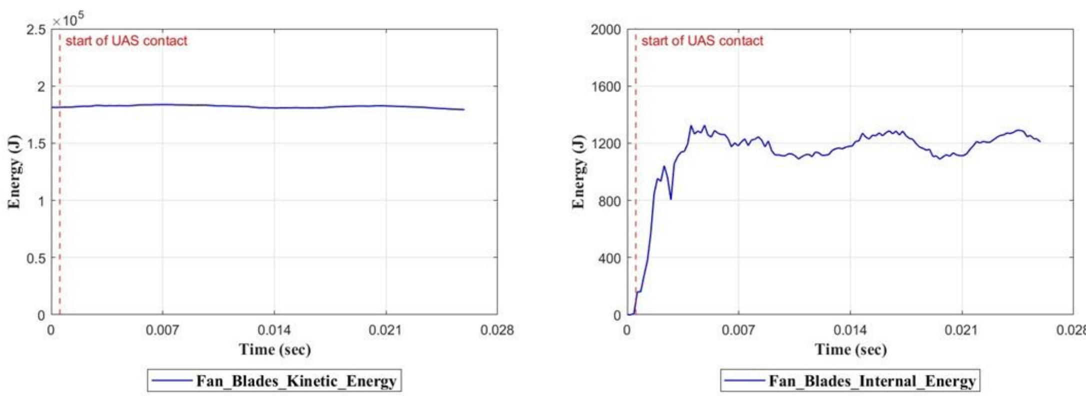

Figure 85. Energy in the fan blades during LFS_HRV_HRS_Nom.

4.4.7 Simulation HFS_LRV_LRS_90P

This case corresponded to a UAS ingestion with a high fan speed, high relative translational velocity, high radial span location, and the 90 degree pitch orientation (see Figure 39). The kinematics of the ingestion are shown in Figure 86. In all of the high fan speed simulations the fan was simulated for a full fan rotation, about 11.6 ms. The UAS parts were also deleted in these cases once they had cleared the fan region, in this case at approximately 8 ms, to improve the computational efficiency of the simulation.

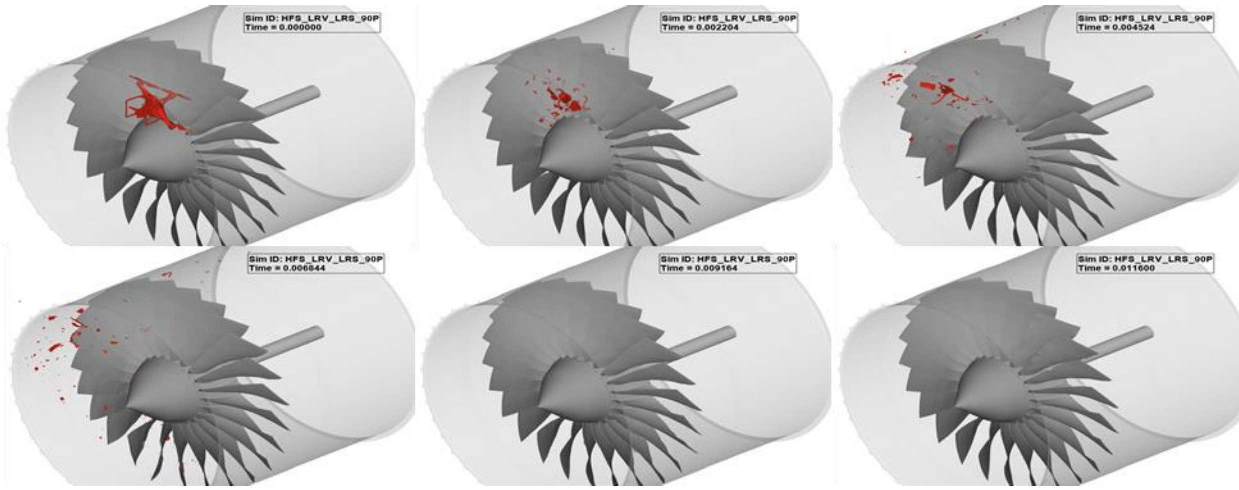

(a) isometric view

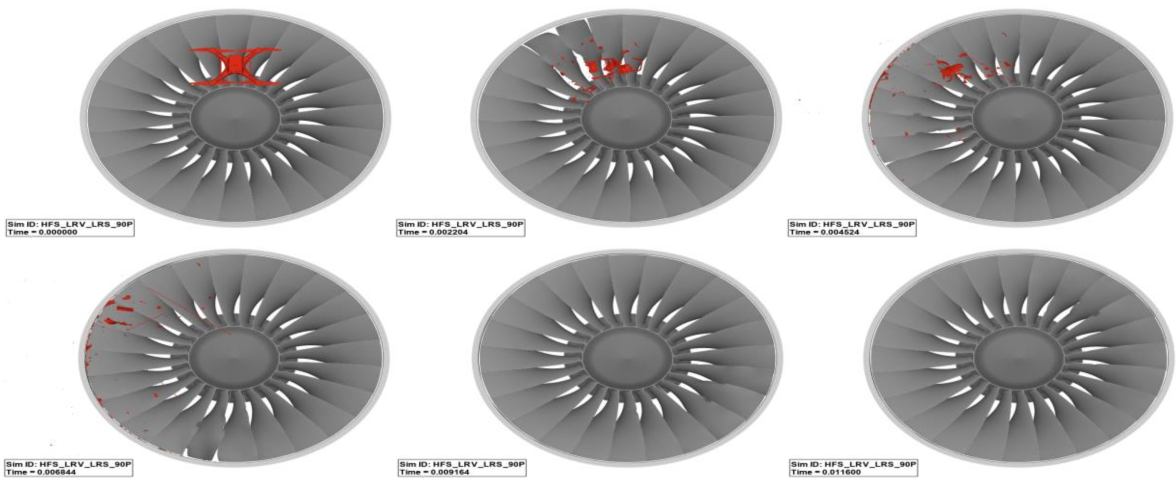

(b) front view

Figure 86. Kinematics of UAS ingestion simulation HFS_LRV_LRS_90P.

The effective plastic strain in the fan at the end of one fan rotation is shown in Figure 87 (front and rear views).

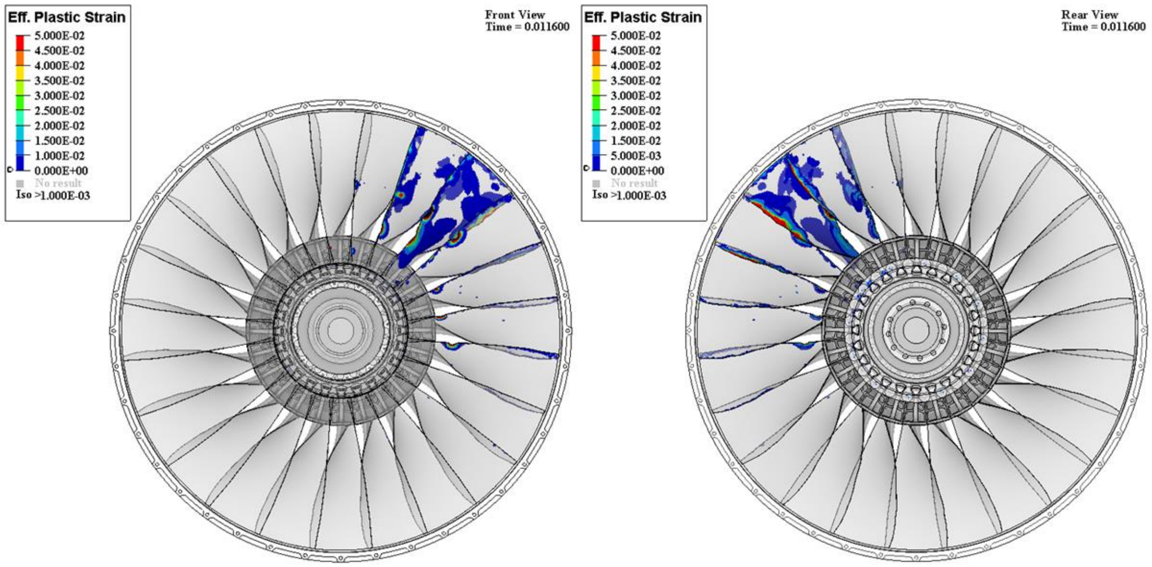

Figure 87. Effective plastic strain after UAS ingestion simulation HFS_LRV_LRS_90P.

Each blade's radial center of mass pre- and post-ingestion are shown in Figure 88. The damage level *D* (defined in Section 4.2) in the damaged area of the fan model after the UAS ingestion is also shown. The damage clearly shows plastic deformation and some material loss on the leading edge of multiple blades, this corresponds to damage severity level 2.

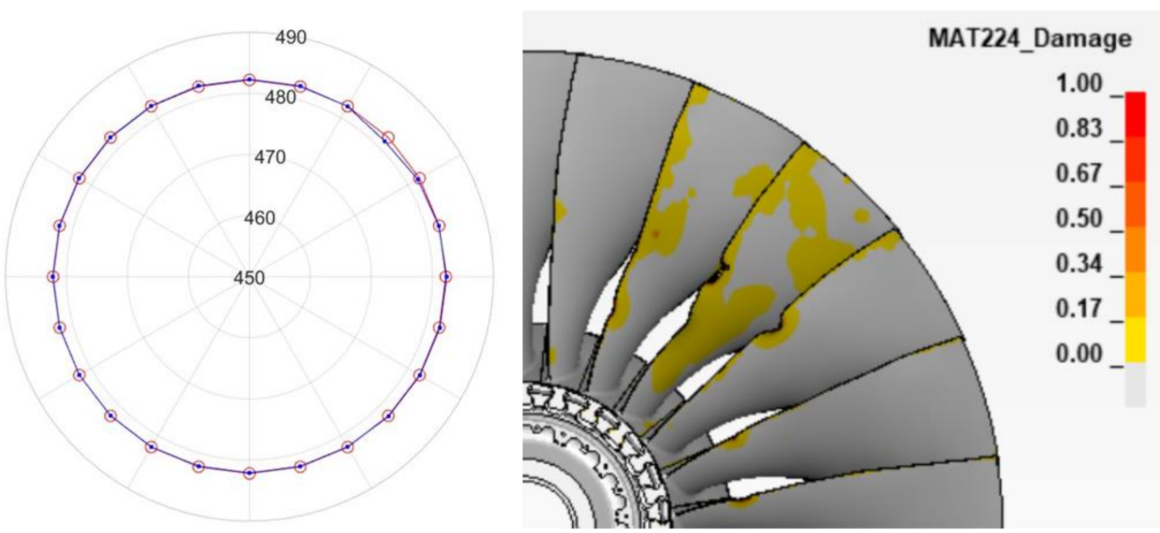

Figure 88. Center of mass of blades and fan model damage after UAS ingestion simulation HFS_LRV_LRS_90P.

The resultant moments and forces in a sectional plane (see Figure 40) during the ingestion are shown in Figure 89. Note that the damaged airfoil has a significantly larger oscillation in the forcing and moment than the undamaged blade.

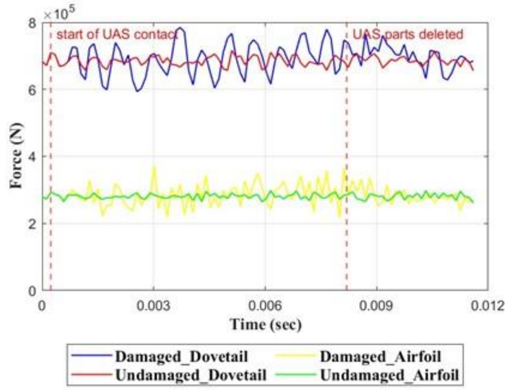

(a) forces

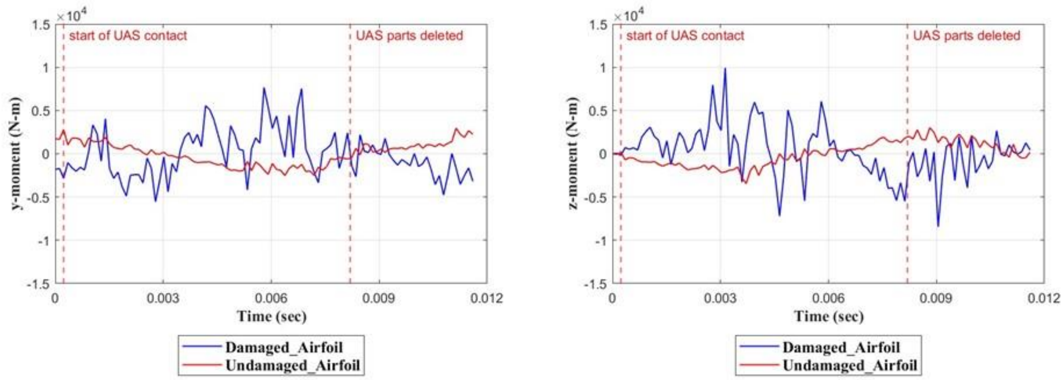

(b) moments about the y- and z-axes

Figure 89. Resultant (a) forces and (b) moments in a sectional plane of the airfoil and dovetail during UAS ingestion simulation HFS_LRV_LRS_90P.

Figure 90(a) shows the overall energy ratio in the system not including the eroded energy. Note that there is a slight drop in the energy ratio term because of the erosion of elements in the UAS and fan during the ingestion and then a sudden drop when the UAS is deleted after it clears the fan stage to speed up the calculation. Figure 90(b) shows the overall energy in the system. The bulk of the energy in the system is the kinetic energy in the fan and the UAS. The reason why the total energy in the system increases is because of the external work of the driven shaft. There is some internal energy in the system that will be shown in the breakout of the UAS and fan energies.

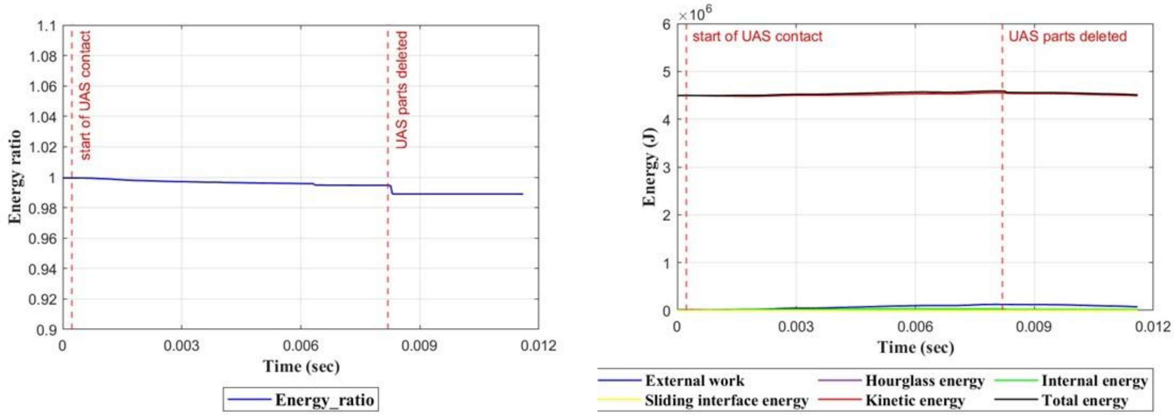

(a) energy ratio (b) energy in system

Figure 90. Overall energy in the system for HFS_LRV_LRS_90P.

Figure 91 shows the internal and kinetic energy in the UAS during the ingestion up until it is deleted from the simulation. Note that as contact is made both the internal and kinetic energy of the UAS increases. The increase in the internal energy is due to the plastic deformation and failure of UAS components. The initial increase in the kinetic energy is due to the fact that the fan is rotating at a high speed and accelerates many UAS parts as they are swept outward radially by the fan. The kinetic energy then starts to decrease as these components start impacting the stationary casing. The velocities of the motors, camera, and battery during the impact are all shown in Figure 92 and agree with this assessment. The different color lines for the velocities of each motor correspond to the motor colors in Figure 39.

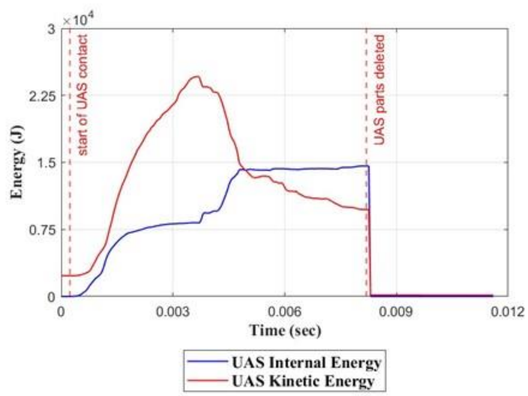

Figure 91. Internal and kinetic energies of the UAS for HFS_LRV_LRS_90P.

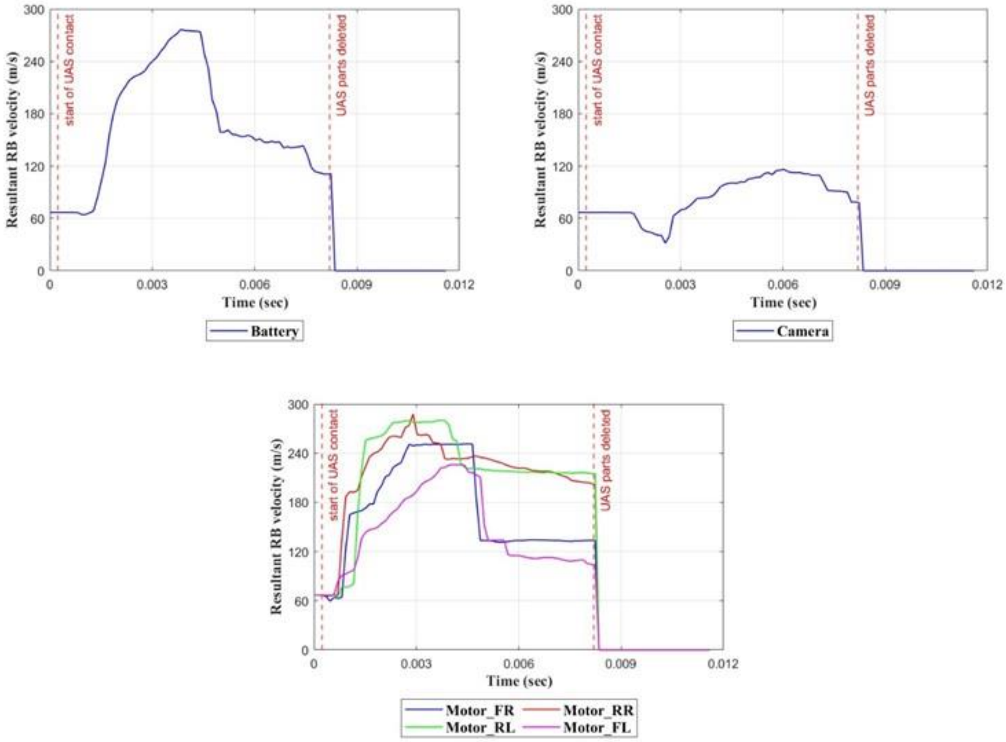

Figure 92. Resultant velocities of UAS components for HFS_LRV_LRS_90P.

The kinetic and internal energy of the fan are shown in Figure 93. Note that the kinetic energy of the fan looks very similar to the overall energy in the system from Figure 90, since the bulk of the energy is in the fan. There is also significant damage in the fan through the internal energy that increases while the fan is impacting the UAS.

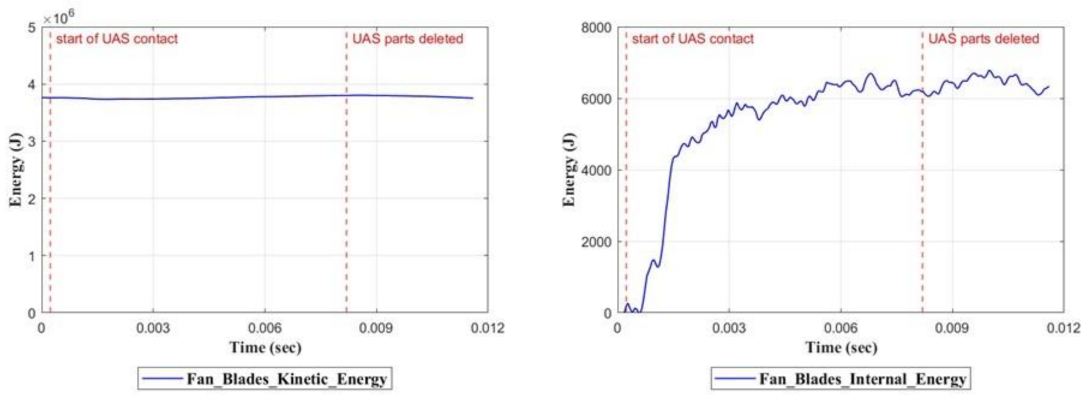

Figure 93. Energy in the fan blades during HFS_LRV_LRS_90P.

Finally, the breakdown of the energy in each blade starting with the top vertical blade as number 1 and counting upwards clockwise from there can be seen in Figure 94. Depending on the relative translational speed of the UAS and rotational speed of the fan one of the first few blades will be the first one to make contact with the UAS. In this case, mainly blades 2 through 8 made contact with the UAS during the ingestion. The blades with the largest variation in kinetic energy due to their deflection during impact tend to have the largest internal energy as well. In this case, blade 4 has the largest oscillation in kinetic energy and increase in internal energy, followed by blades 3 and 5, and then blades 2 and 6-8.

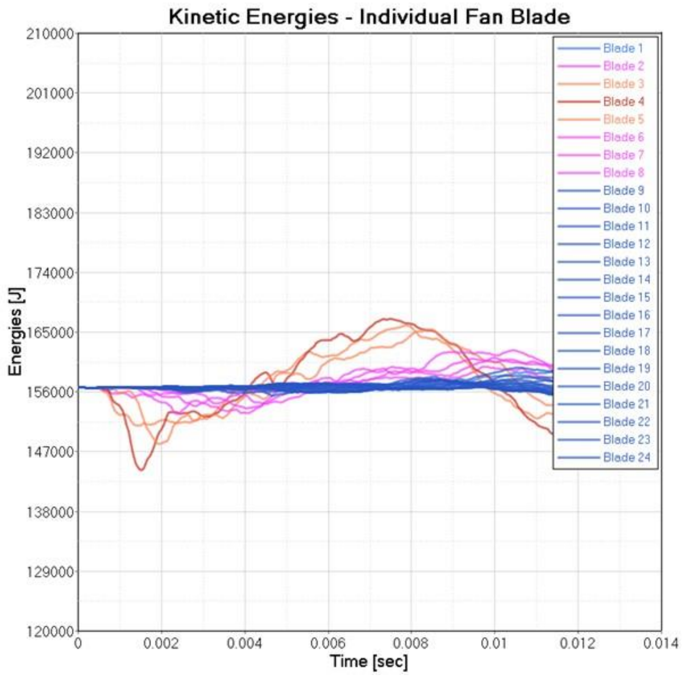

(a) kinetic energy

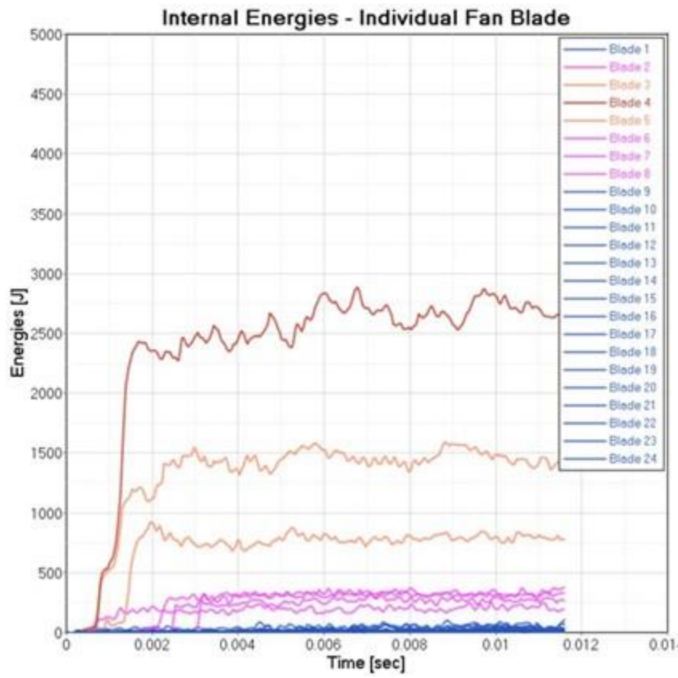

(b) internal energy

Figure 94. Energies in individual fan blades during UAS ingestion simulation HFS_LRV_LRS_90P.

4.4.8 Simulation HFS_LRV_HRS_Nom

This case corresponded to a UAS ingestion with a high fan speed, low relative translational velocity, high radial span location, and the nominal orientation (see Figure 39). The kinematics of the ingestion are shown in Figure 95. In all of the high fan speed simulations the fan was simulated for a full fan rotation, about 11.6 ms. The UAS parts were also deleted in these cases once they had cleared the fan region, in this case at approximately 7 ms, to improve the computational efficiency of the simulation.

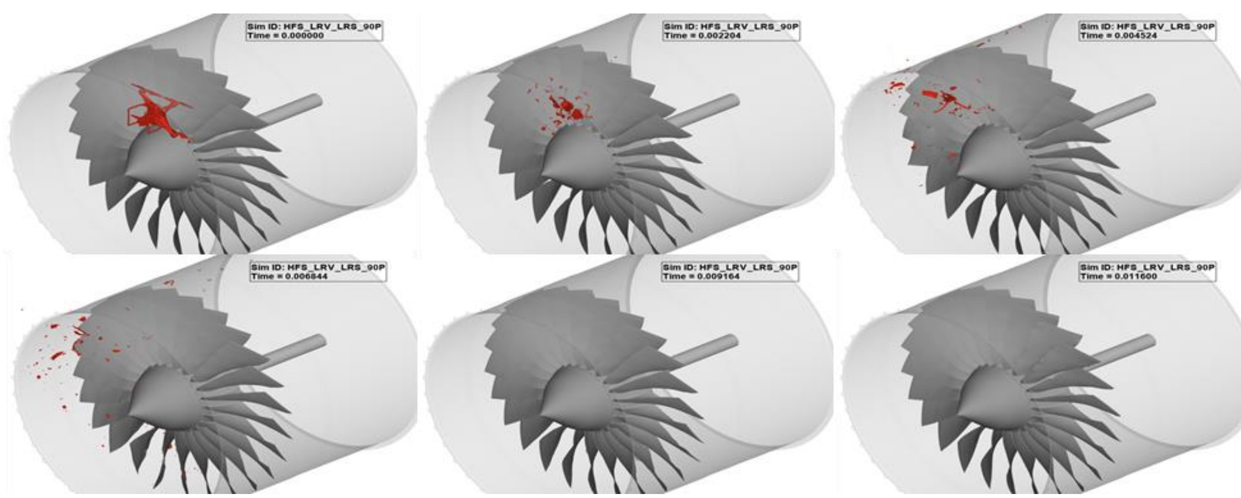

(a) isometric view

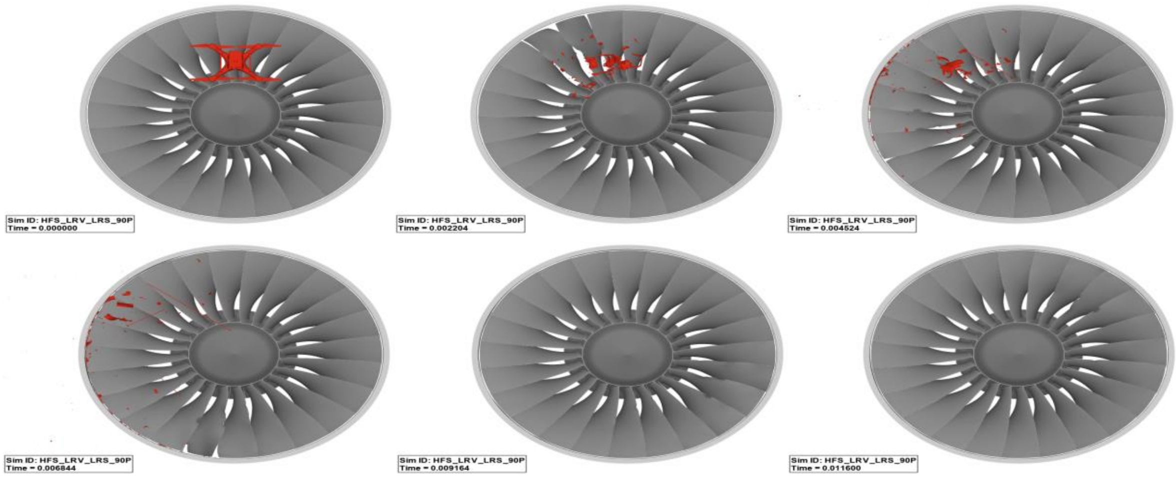

(b) front view

Figure 95. Kinematics of UAS ingestion simulation HFS_LRV_HRS_Nom.

The effective plastic strain in the fan at the end of one fan rotation is shown in Figure 96 (front and rear views).

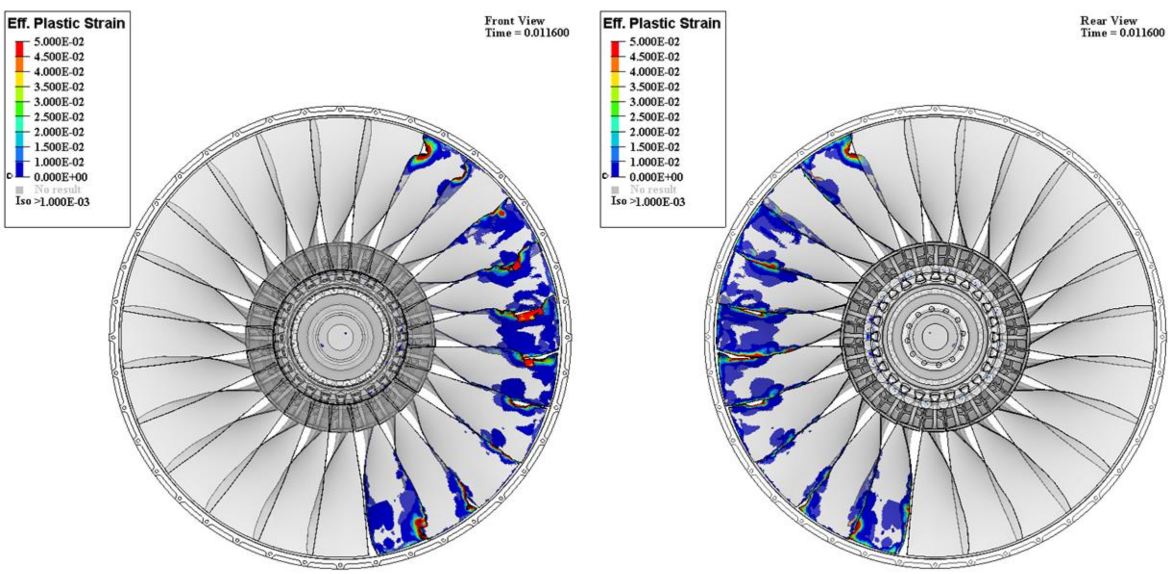

Figure 96. Effective plastic strain after UAS ingestion simulation HFS_LRV_HRS_Nom.

Each blade's radial center of mass pre- and post-ingestion are shown in Figure 97. The damage level D (defined in Section 4.2) in the damaged area of the fan model after the UAS ingestion is also shown. The damage clearly shows significant material loss on the leading edge of multiple blades, this corresponds to damage severity level 3.

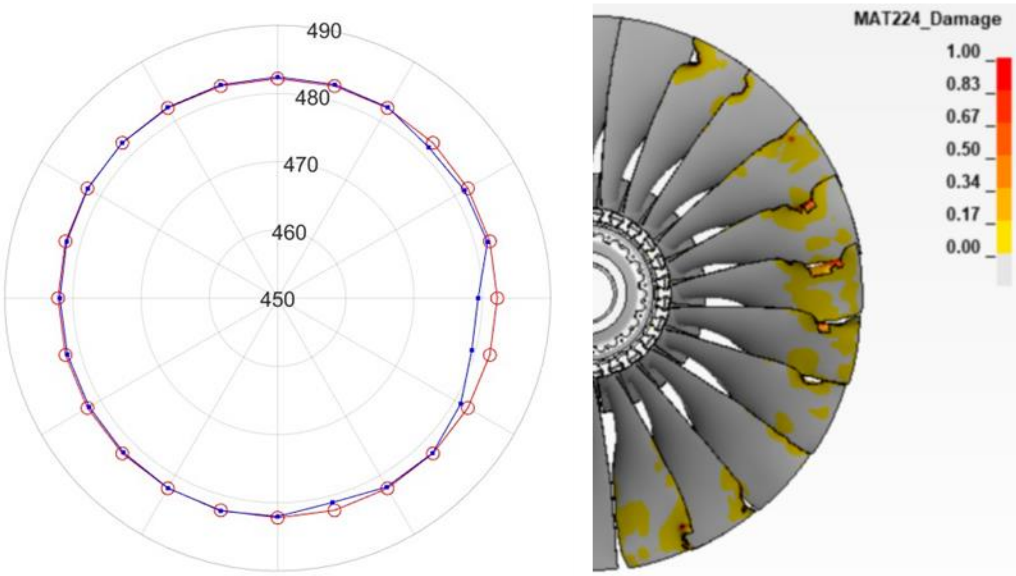

Figure 97. Center of mass of blades and fan model damage after UAS ingestion simulation HFS_LRV_HRS_Nom.

The resultant moments and forces in a sectional plane (see Figure 40) during the ingestion are shown in Figure 98. Note that the damaged airfoil has a significantly larger oscillation in the forcing and moment than the undamaged blade.

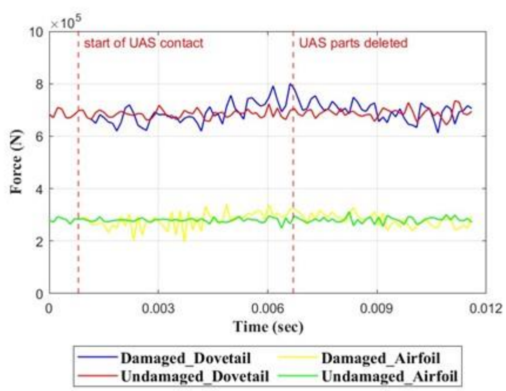

(a) forces

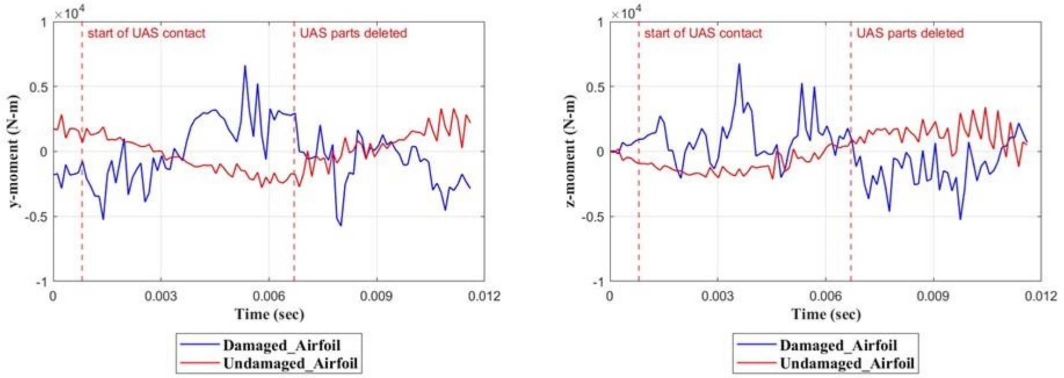

(b) moments about the y- and z-axes

Figure 98. Resultant (a) forces and (b) moments in a sectional plane of the airfoil and dovetail during UAS ingestion simulation HFS_LRV_HRS_Nom.

Figure 99(a) shows the overall energy ratio in the system not including the eroded energy. Note that there is a slight drop in the energy ratio term because of the erosion of elements in the UAS and fan during the ingestion and then a sudden drop when the UAS is deleted after it clears the fan stage to speed up the calculation. Figure 99(b) shows the overall energy in the system. The bulk of the energy in the system is the kinetic energy in the fan and the UAS. The reason why the total energy in the system increases is because of the external work of the driven shaft. There is some internal energy in the system that will be shown in the breakout of the UAS and fan energies.

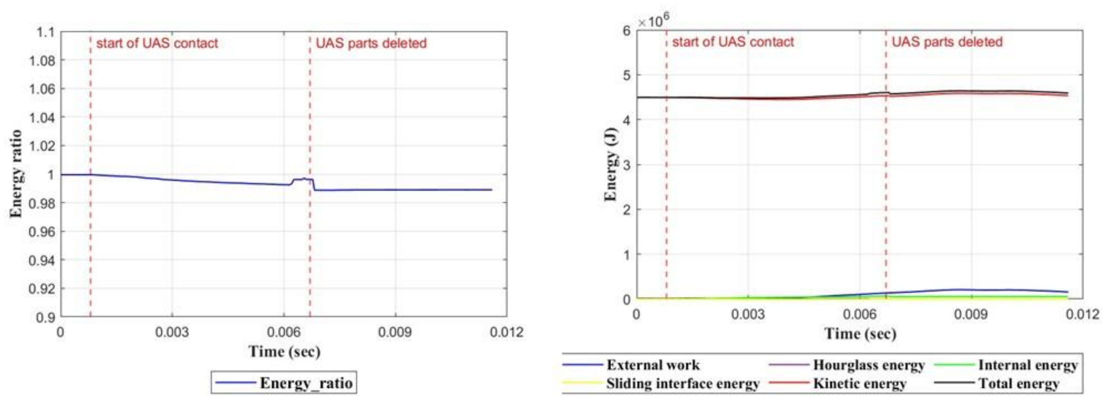

(a) energy ratio (b) energy in system

Figure 99. Overall energy in the system for HFS_LRV_HRS_Nom.

Figure 100 shows the internal and kinetic energy in the UAS during the ingestion up until it is deleted from the simulation. Note that, as contact is made, both the internal and kinetic energy of the UAS increases. The increase in the internal energy is due to the plastic deformation and failure of UAS components. The increase in the kinetic energy is due to the fact that the fan is rotating at a high speed and accelerates many UAS parts as they are swept outward radially by the fan. The kinetic energy then starts to level off as some of these components start impacting the stationary casing. The velocities of the motors, camera, and battery during the impact are all shown in Figure

101 and agree with this assessment. The different color lines for the velocities of each motor correspond to the motor colors in Figure 39.

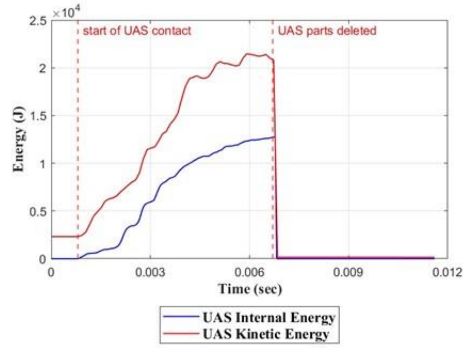

Figure 100. Internal and kinetic energies of the UAS for HFS_LRV_HRS_Nom.

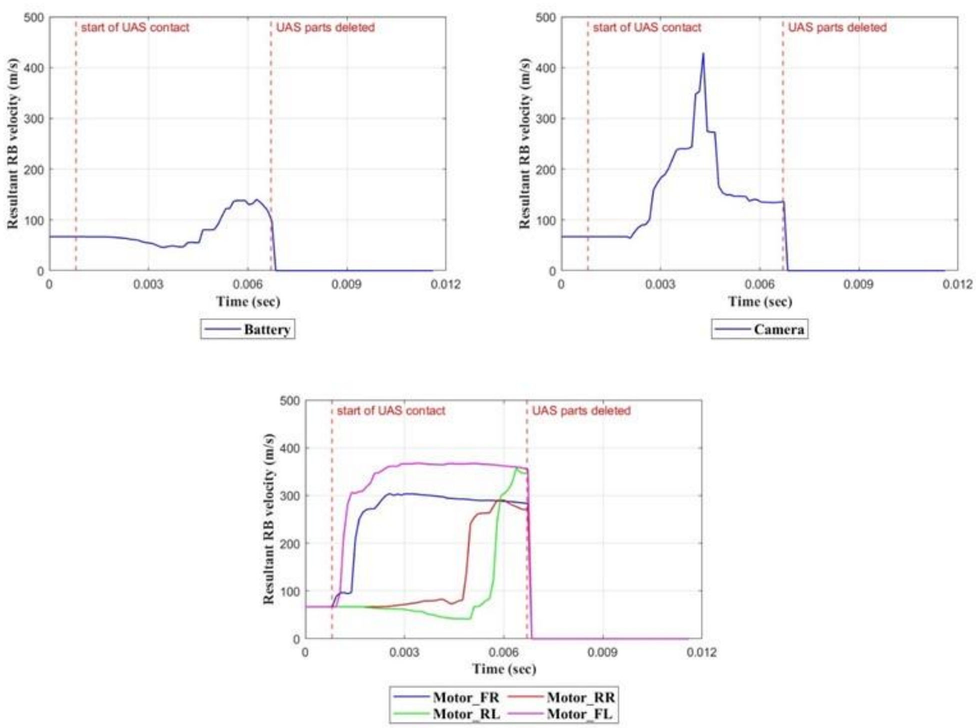

Figure 101. Resultant velocities of UAS components for HFS_LRV_HRS_Nom.

The kinetic and internal energy of the fan are shown in Figure 102. Note that the kinetic energy of the fan looks very similar to the overall energy in the system from Figure 99, since the bulk of the energy is in the fan. There is also significant damage in the fan through the internal energy that increases while the fan is impacting the UAS.

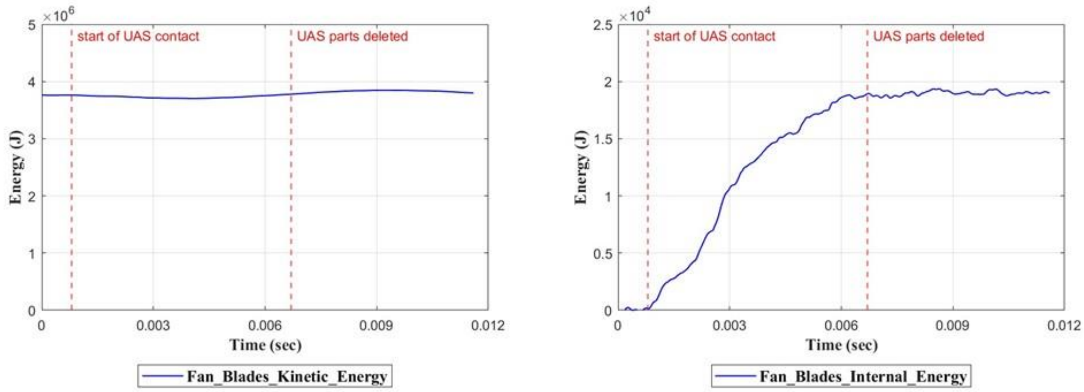

Figure 102. Energy in the fan blades during HFS_LRV_HRS_Nom.

Finally, the breakdown of the energy in each blade starting with the top vertical blade as number 1 and counting upwards clockwise from there can be seen in Figure 103. Depending on the relative translational speed of the UAS and rotational speed of the fan, one of the first few blades will be the first one to make contact with the UAS. In this case, mainly blades 3 through 12 made contact with the UAS during the ingestion. The blades with the largest variation in kinetic energy due to their deflection during impact tend to have the largest internal energy as well. In this case blade 7 has the largest increase in internal energy, followed by blades 3,6,8, and 12, and then blades 4-5 and 9-11.

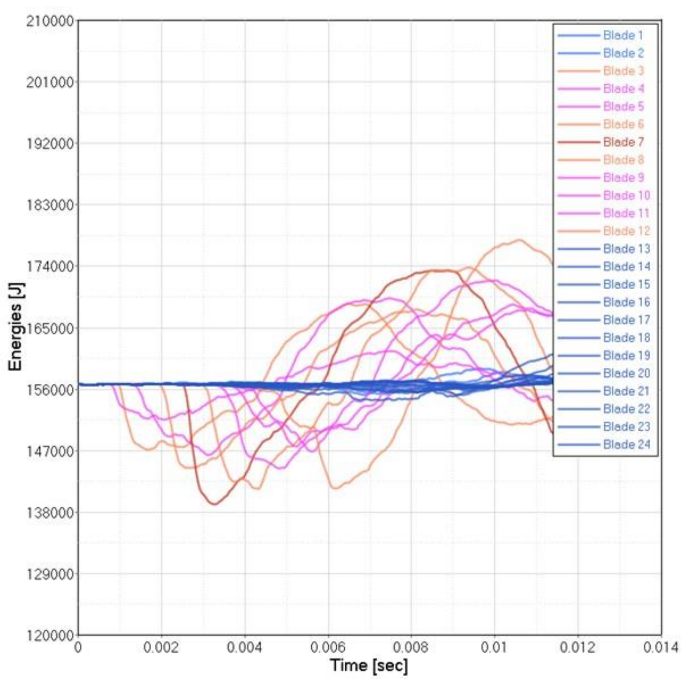

(a) kinetic energy

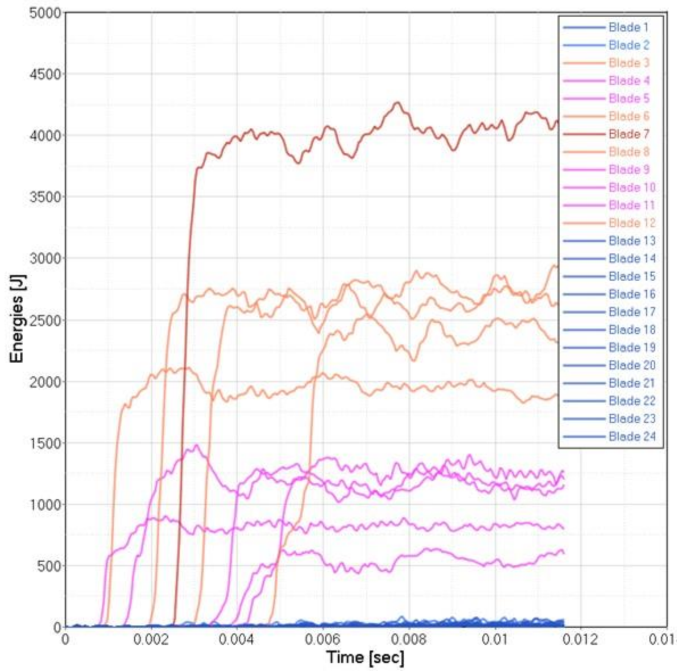

(b) internal energy

Figure 103. Energies in individual fan blades during UAS ingestion simulation HFS_LRV_HRS_Nom.

4.4.9 Simulation HFS_HRV_LRS_90P

This case corresponded to a UAS ingestion with a high fan speed, high relative translational velocity, low radial span location, and the 90 degree pitch orientation (see Figure 39). The kinematics of the ingestion are shown in Figure 104. In all of the high fan speed simulations, the fan was simulated for a full fan rotation, about 11.6 ms. The UAS parts were also deleted in these cases once they had cleared the fan region, in this case at approximately 5 ms, to improve the computational efficiency of the simulation.

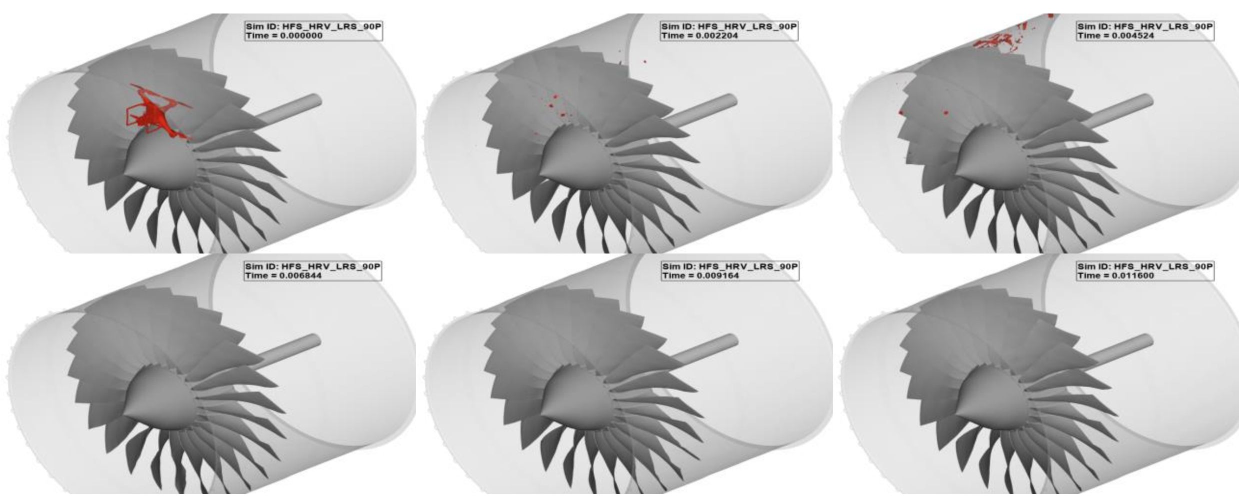

(a) isometric view

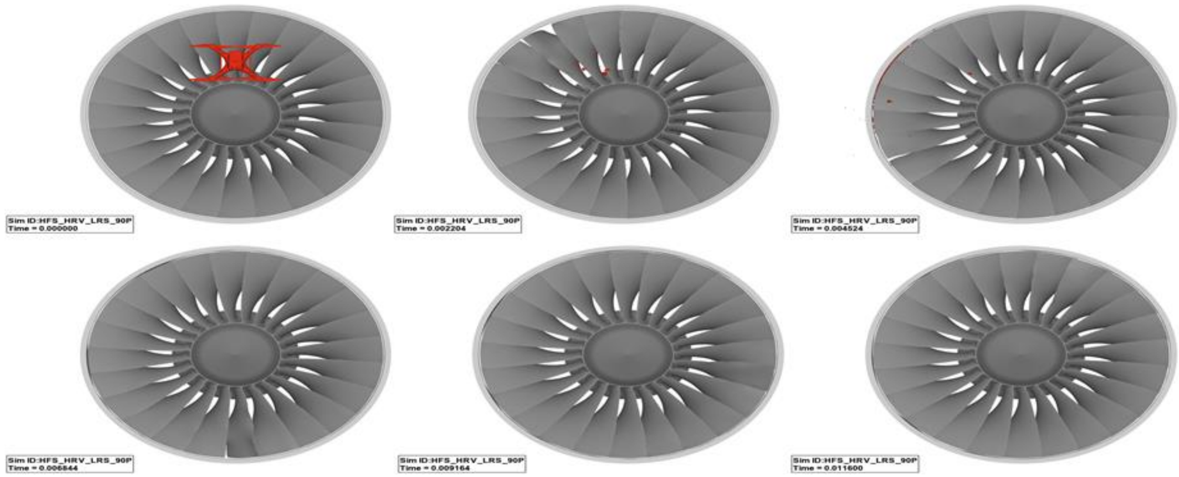

(b) front view

Figure 104. Kinematics of UAS ingestion simulation HFS_HRV_LRS_90P.

The effective plastic strain in the fan at the end of one fan rotation is shown in Figure 105 (front and rear views).

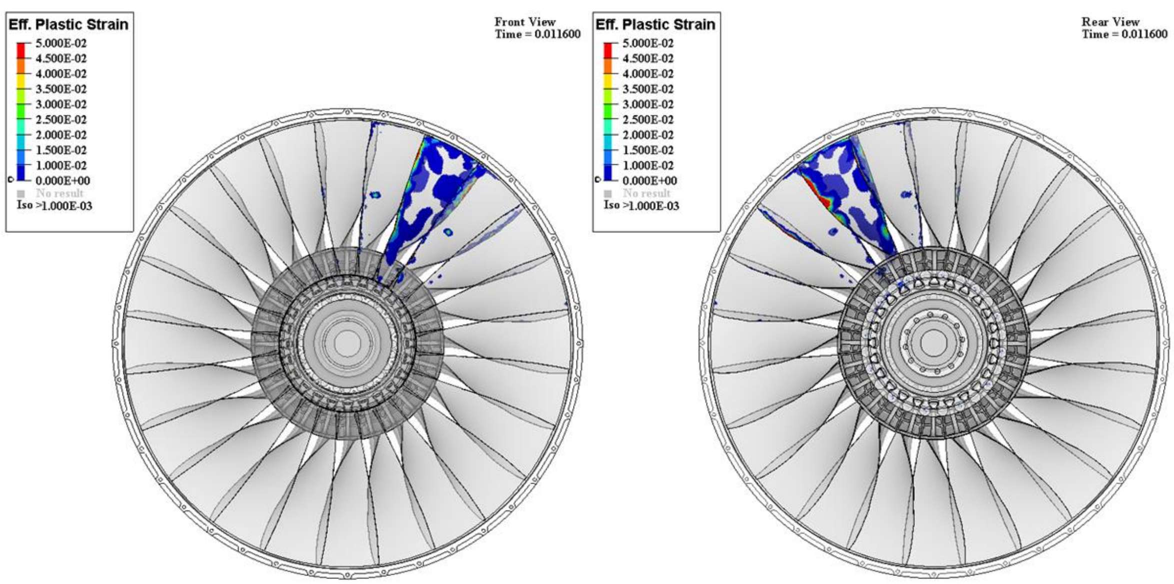

Figure 105. Effective plastic strain after UAS ingestion simulation HFS_HRV_LRS_90P.

Each blade's radial center of mass pre- and post-ingestion are shown in Figure 106. The damage level *D* (defined in Section 4.2) in the damaged area of the fan model after the UAS ingestion is also shown. The damage shows minor deformation in a few blades and corresponds to damage severity level 1.

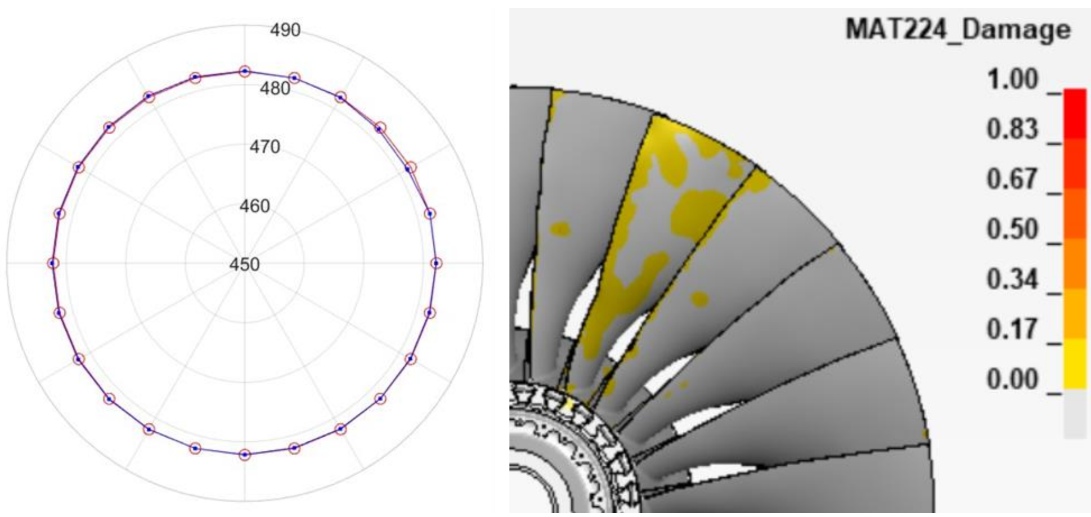

Figure 106. Center of mass of blades and fan model damage after UAS ingestion simulation .HFS_HRV_LRS_90P

The resultant moments and forces in a sectional plane (see Figure 40) during the ingestion are shown in Figure 107. Note that the damaged airfoil has a significantly larger oscillation in the forcing and moment than the undamaged blade.

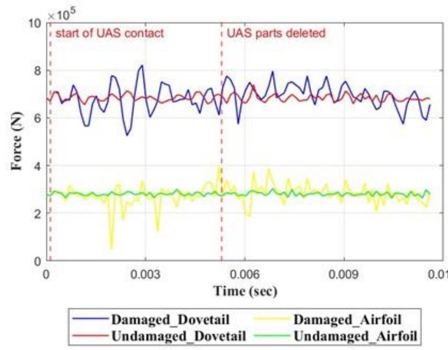

(a) forces

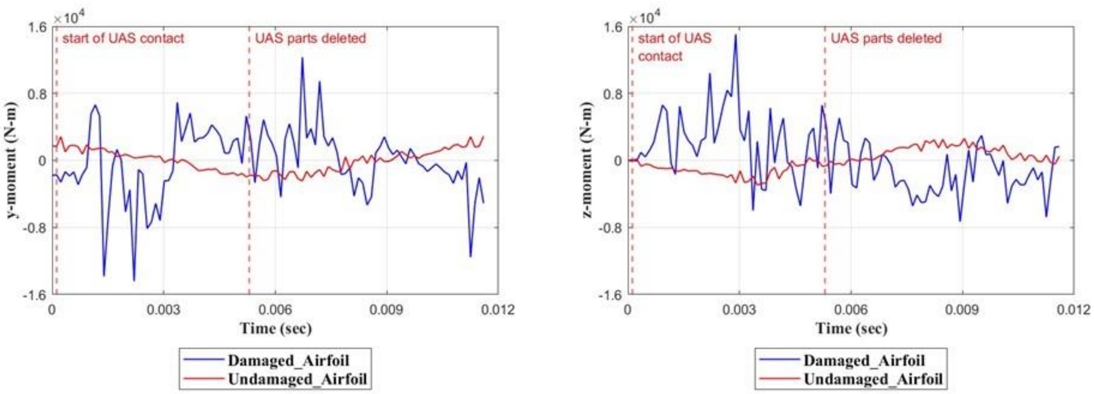

(b) moments about the y- and z-axes

Figure 107. Resultant (a) forces and (b) moments in a sectional plane of the airfoil and dovetail during UAS ingestion simulation HFS_HRV_LRS_90P.

Figure 108(a) shows the overall energy ratio in the system not including the eroded energy. Note that there is a slight drop in the energy ratio term because of the erosion of elements in the UAS during the ingestion and then a sudden drop when the UAS is deleted after it clears the fan stage to speed up the calculation. Figure 108(b) shows the overall energy in the system. The bulk of the energy in the system is the kinetic energy in the fan and the UAS. The reason why the total energy in the system increases is because of the external work of the driven shaft. There is some internal energy in the system that will be shown in the breakout of the UAS and fan energies.

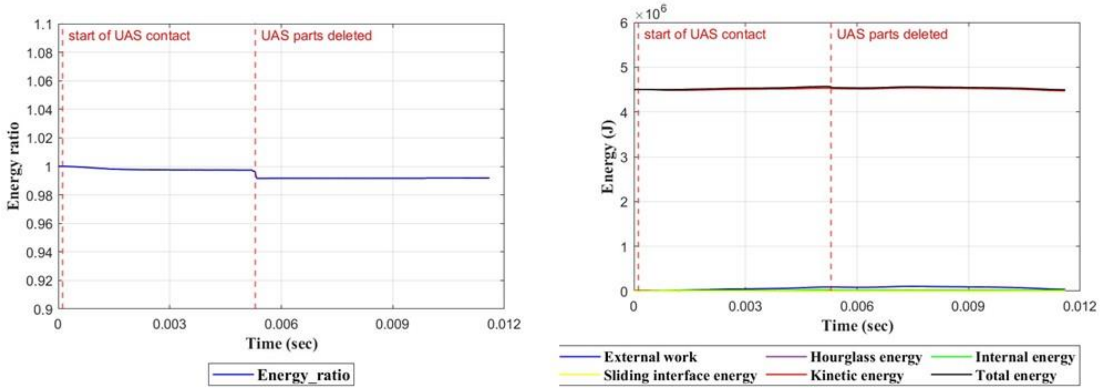

(a) energy ratio (b) energy in system

Figure 108. Overall energy in the system for HFS_HRV_LRS_90P.

Figure 109 shows the internal and kinetic energy in the UAS during the ingestion up until it is deleted from the simulation. Note that, as contact is made, both the internal and kinetic energy of the UAS increases. The increase in the internal energy is due to the plastic deformation and failure of UAS components. The increase in the kinetic energy is due to the fact that the fan is rotating at a high speed and accelerates many UAS parts as they are swept outward radially by the fan. The kinetic energy then starts to level off and decrease as some of these components start impacting the stationary casing. The velocities of the motors, camera, and battery during the impact are all shown in Figure 110 and agree with this assessment. The different color lines for the velocities of each motor correspond to the motor colors in Figure 39.

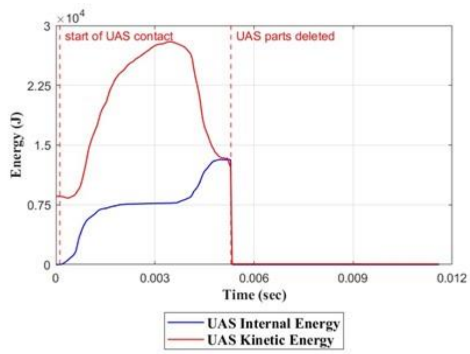

Figure 109. Internal and kinetic energies of the UAS for HFS_HRV_LRS_90P.

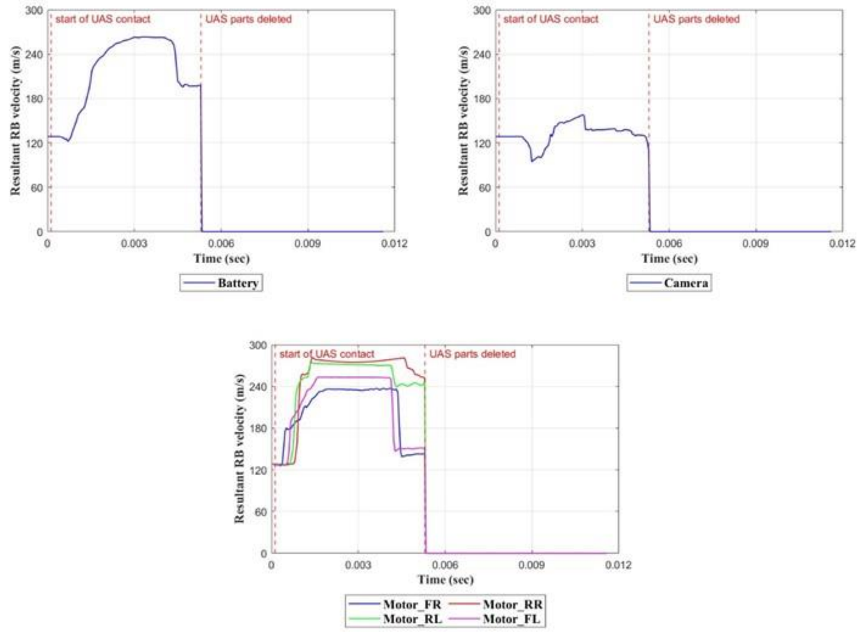

Figure 110. Resultant velocities of UAS components for HFS_HRV_LRS_90P.

The kinetic and internal energy of the fan are shown in Figure 111. Note that the kinetic energy of the fan looks very similar to the overall energy in the system from Figure 108, since the bulk of the energy is in the fan. There is also significant damage in the fan through the internal energy that increases while the fan is impacting the UAS.

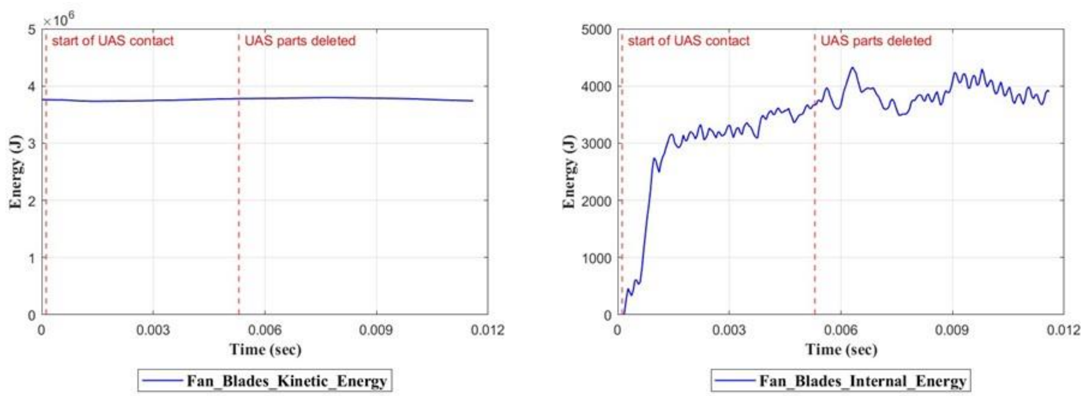

Figure 111. Energy in the fan blades during HFS_HRV_LRS_90P.

Finally, the breakdown of the energy in each blade starting with the top vertical blade as number 1 and counting upwards clockwise from there can be seen in Figure 112. Depending on the relative translational speed of the UAS and rotational speed of the fan one of the first few blades will be the first one to make contact with the UAS. In this case, mainly blades 2 through 4 made contact with the UAS during the ingestion. The blades with the largest variation in kinetic energy due to their deflection during impact tend to have the largest internal energy as well. In this case blade 3 has the largest variation in kinetic energy and increase in internal energy, followed by blades 2 and 4.

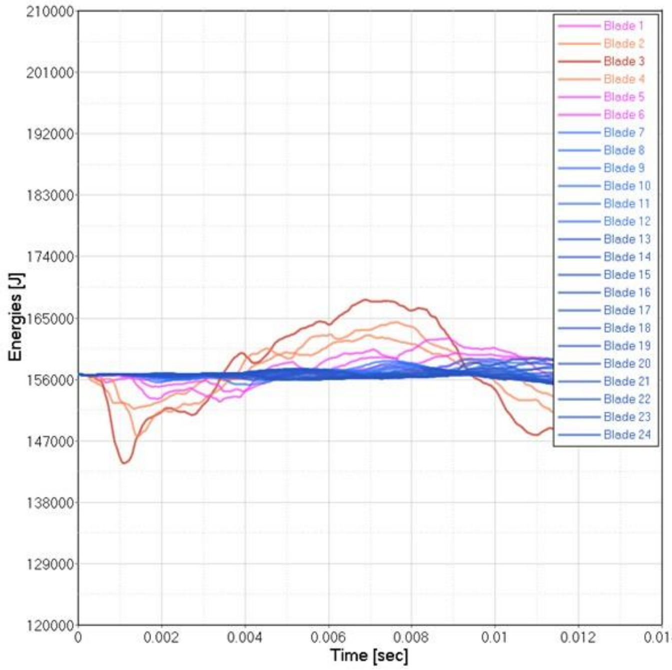

(a) kinetic energy

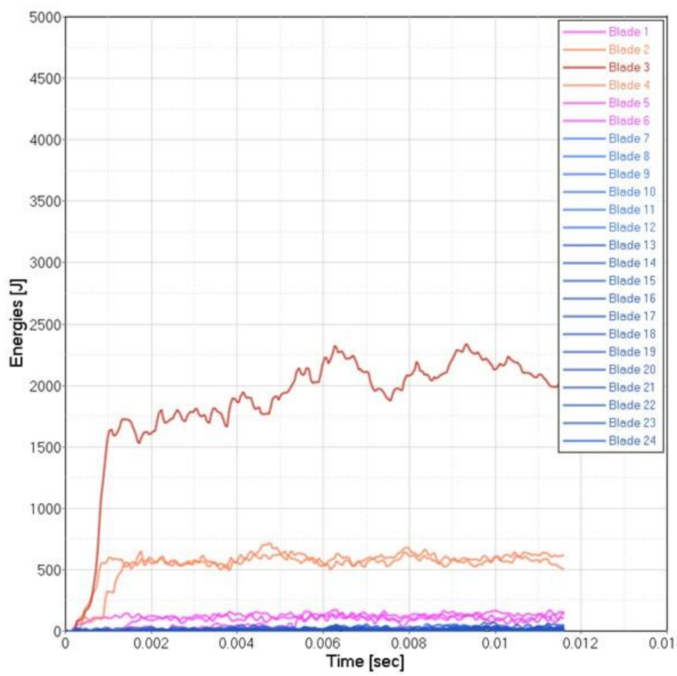

(b) internal energy

Figure 112 Energies in individual fan blades during UAS ingestion simulation HFS_HRV_LRS_90P.

4.4.10 Simulation HFS_HRV_HRS_Nom

This case corresponded to a UAS ingestion with a high fan speed, high relative translational velocity, high radial span location, and the nominal orientation (see Figure 39). The kinematics of the ingestion are shown in Figure 113. In all of the high fan speed simulations the fan was simulated for a full fan rotation, about 11.6 ms. The UAS parts were also deleted in these cases once they had cleared the fan region, in this case at approximately 6.6 ms, to improve the computational efficiency of the simulation.

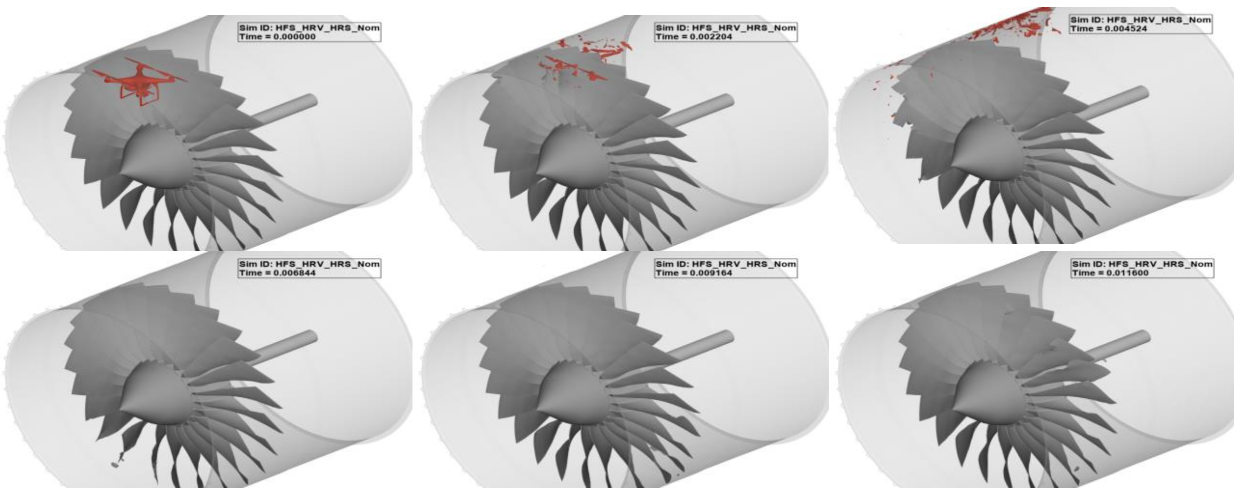

(a) isometric view

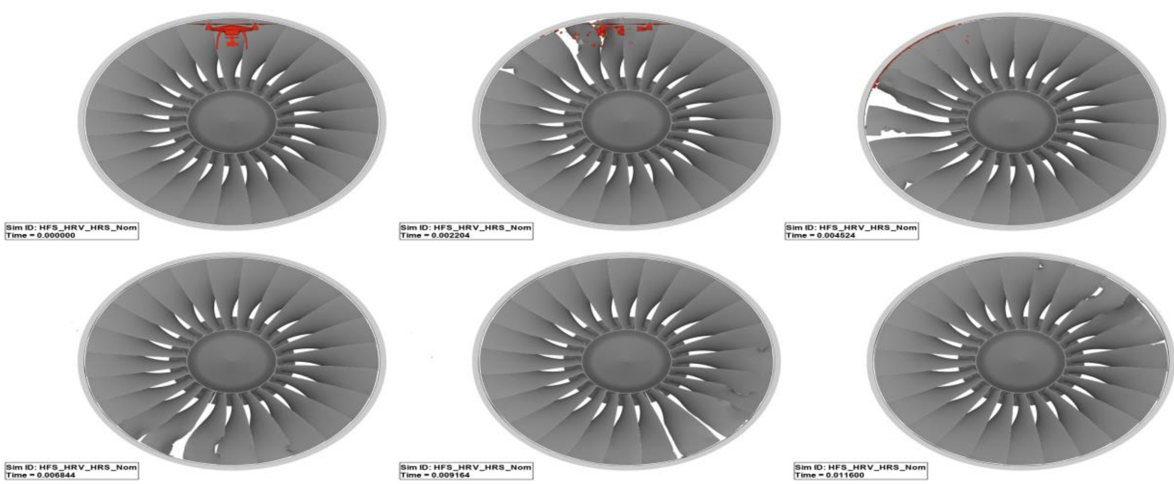

(b) front view

Figure 113. Kinematics of UAS ingestion simulation HFS_HRV_HRS_Nom.

The effective plastic strain in the fan at the end of one fan rotation is shown in Figure 114 (front and rear views).

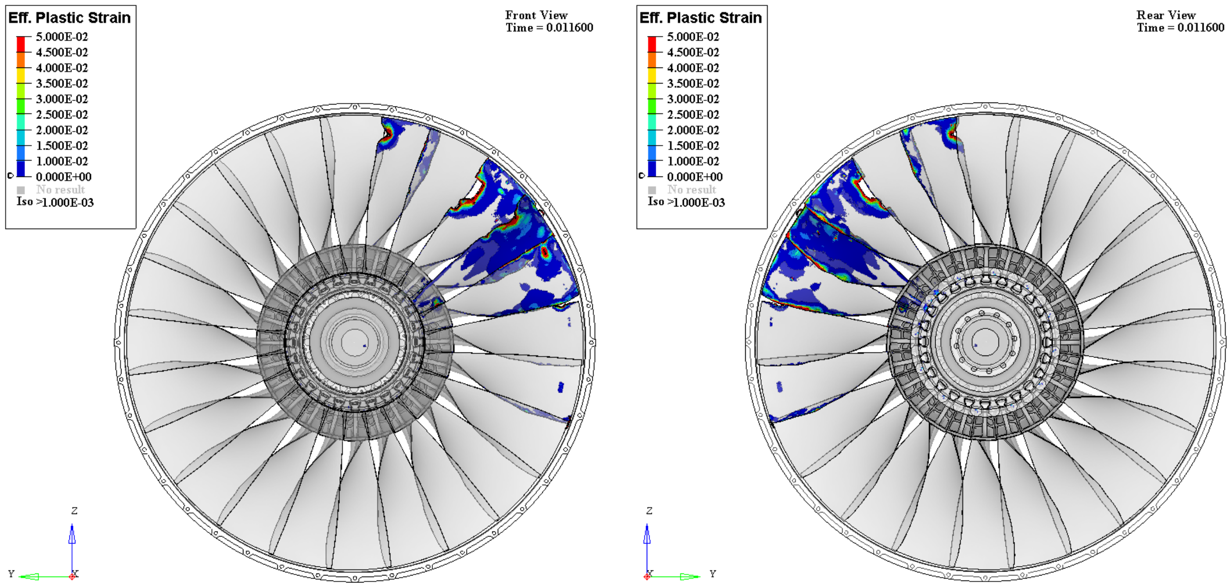

Figure 114. Effective plastic strain after UAS ingestion simulation HFS_HRV_HRS_Nom.

Each blade's radial center of mass pre- and post-ingestion are shown in Figure 115. The damage level *D* (defined in Section 4.2) in the damaged area of the fan model after the UAS ingestion is also shown. The damage clearly shows significant material loss on leading edge of multiple blades, but the imbalance would be less than that of a loss of a full blade, which corresponds to damage severity level 3.

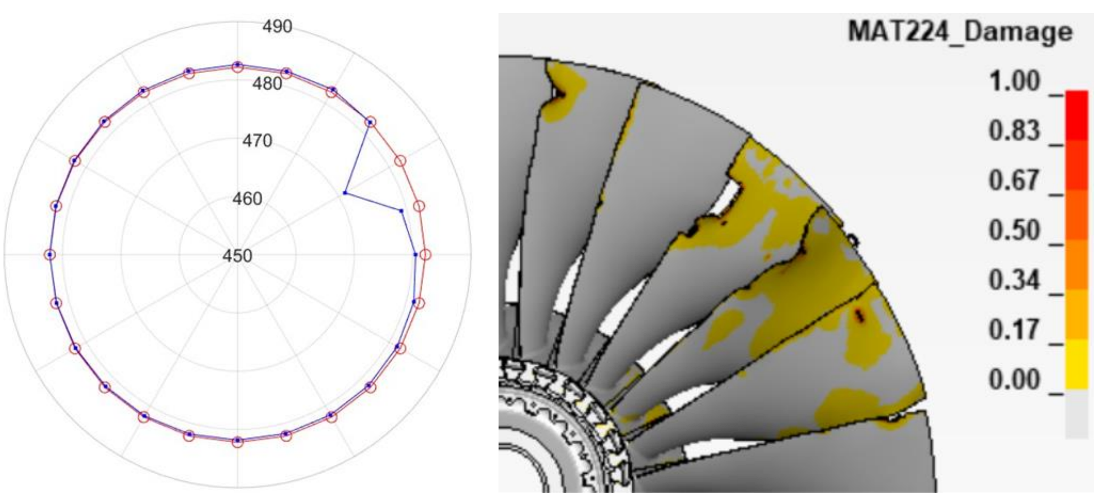

Figure 115. Center of mass of blades and fan model damage after UAS ingestion simulation HFS_HRV_HRS_Nom.

The resultant moments and forces in a sectional plane (see Figure 40) during the ingestion are shown in Figure 116. Note that the damaged airfoil has a significantly larger oscillations in the forcing and moment than the undamaged blade.

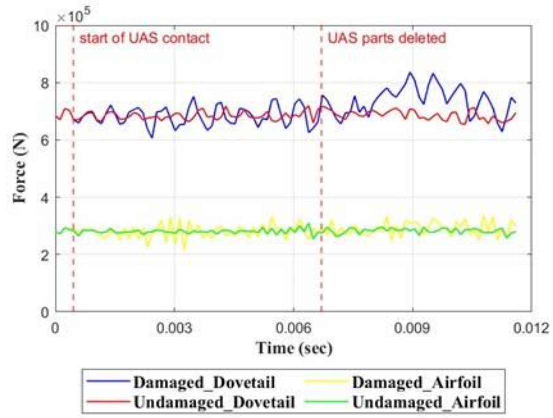

(a) forces

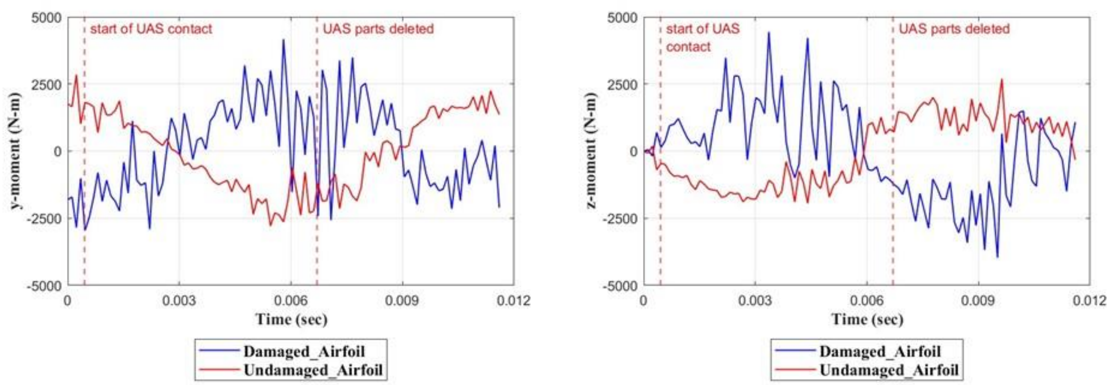

(b) moments about the y- and z-axes

Figure 116. Resultant (a) forces and (b) moments in a sectional plane of the airfoil and dovetail during UAS ingestion simulation HFS_HRV_HRS_Nom.

Figure 117(a) shows the overall energy ratio in the system, not including the eroded energy. Note that there is a drop in the energy ratio term because of the erosion of elements in the UAS and fan during the ingestion, and then a sudden drop when the UAS is deleted after it clears the fan stage to speed up the calculation. Figure 117(b) shows the overall energy in the system. The bulk of the energy in the system is the kinetic energy in the fan and the UAS. The reason why the total energy in the system increases is because of the external work of the driven shaft. There is some internal energy in the system that will be shown in the breakout of the UAS and fan energies.

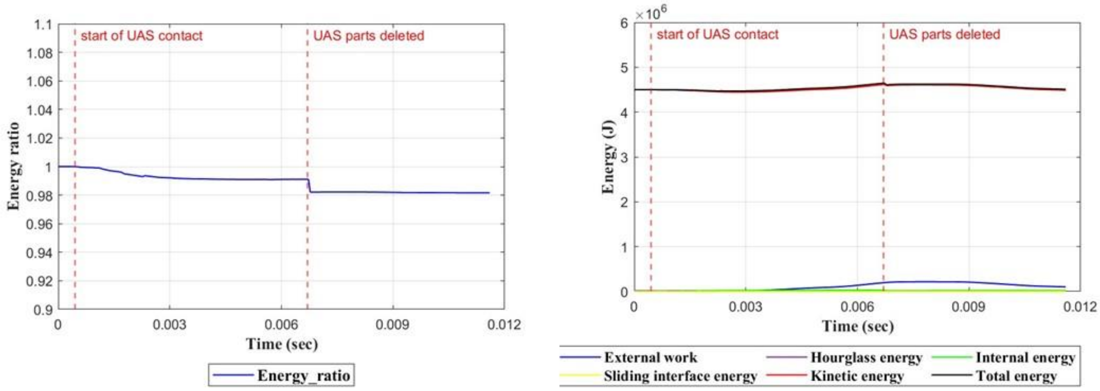

(a) energy ratio

(b) energy in system

Figure 117. Overall energy in the system for HFS_HRV_HRS_Nom.

Figure 118 shows the internal and kinetic energy in the UAS during the ingestion up until it is deleted from the simulation. Note that, as contact is made, both the internal and kinetic energy of the UAS increases. The increase in the internal energy is due to the plastic deformation and failure of UAS components. The increase in the kinetic energy is due to the fact that the fan is rotating at a high speed and accelerates many UAS parts as they are swept outward radially by the fan. The kinetic energy eventually levels off and decreases as UAS parts impact the stationary casing. The velocities of the motors, camera and battery during the impact are all shown in Figure 119 and agree with this assessment. The different color lines for the velocities of each motor correspond to the motor colors in Figure 39.

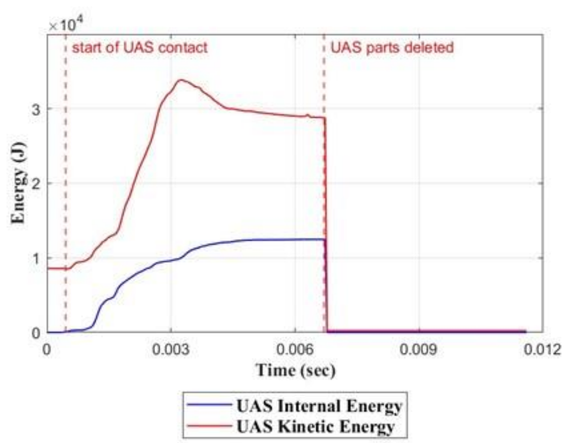

Figure 118. Internal and kinetic energies of the UAS for HFS_HRV_HRS_Nom.

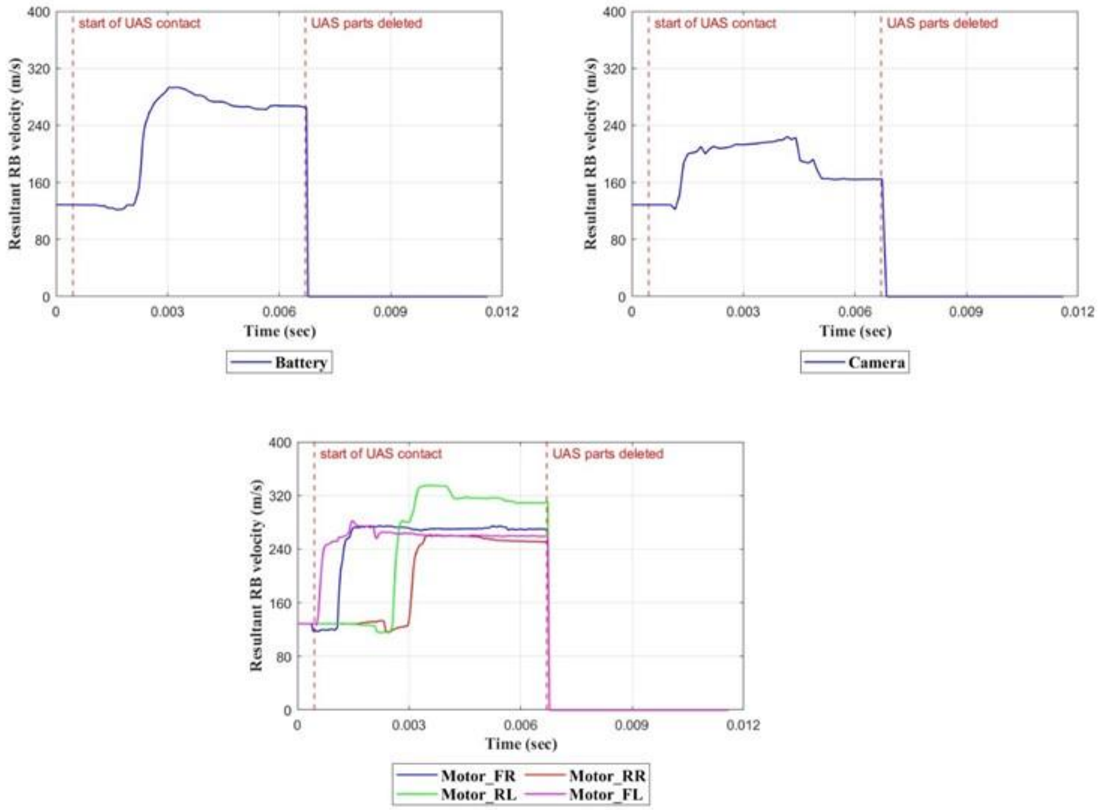

Figure 119. Resultant velocities of UAS components for HFS_HRV_HRS_Nom.

The kinetic and internal energy of the fan are shown in Figure 120. Note that the kinetic energy of the fan looks very similar to the overall energy in the system from Figure 117, since the bulk of the energy is in the fan. There is also significant damage in the fan through the internal energy that increases while the fan is impacting the UAS.

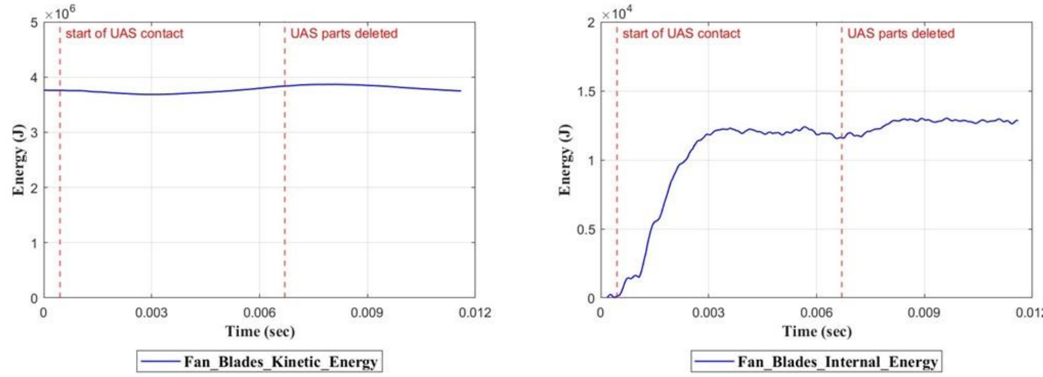

Figure 120. Energy in the fan blades during HFS_HRV_HRS_Nom.

Finally, the breakdown of the energy in each blade starting with the top vertical blade as number 1 and counting upwards clockwise from there can be seen in Figure 121. Depending on the relative translational speed of the UAS and rotational speed of the fan, one of the first few blades will be the first one to make contact with the UAS. In this case, mainly blades 2 through 7 made contact with the UAS during the ingestion. The blades with the largest variation in kinetic energy due to their deflection during impact tend to have the largest internal energy as well. In this case, blades 4 and 5 have the largest oscillation in kinetic energy and increase in internal energy, followed by blades 2 and 6, and then blades 7 and 3.

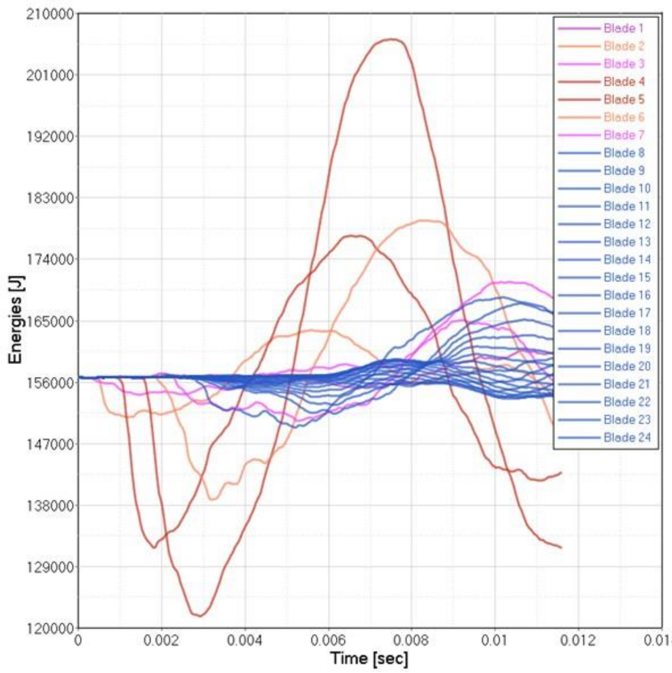

(a) kinetic energy

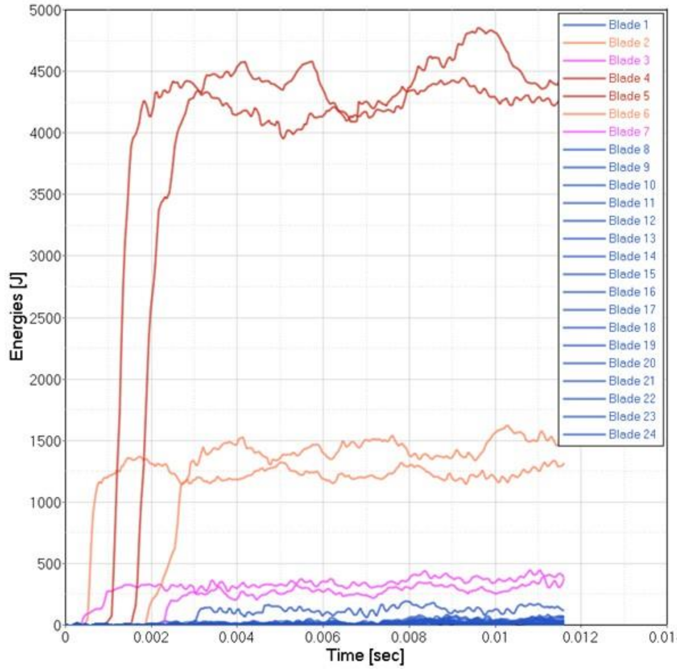

(b) internal energy

Figure 121. Energies in individual fan blades during UAS ingestion simulation HFS_HRV_HRS_Nom.

4.4.11 Simulation HFS_HRV_HRS_45R

This case corresponded to a UAS ingestion with a high fan speed, high relative translational velocity, high radial span location, and the 45 degree roll orientation (see Figure 39). The kinematics of the ingestion are shown in Figure 122. In this case, the UAS parts are out of the fan region and most of the components had their initial impact with the fan casing at about 7 ms, and were deleted to improve the computational efficiency of the simulation.

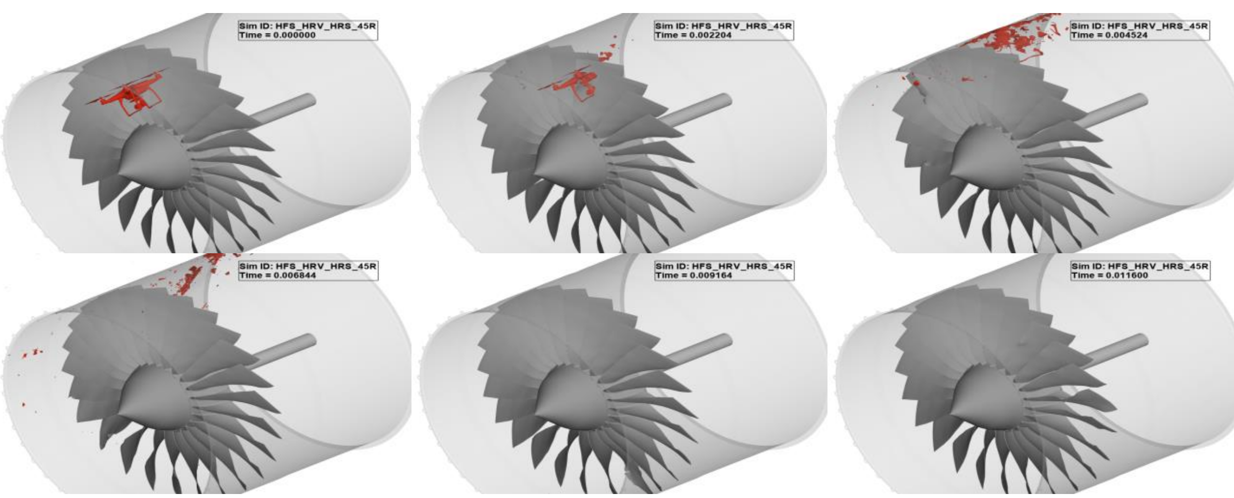

(a) isometric view

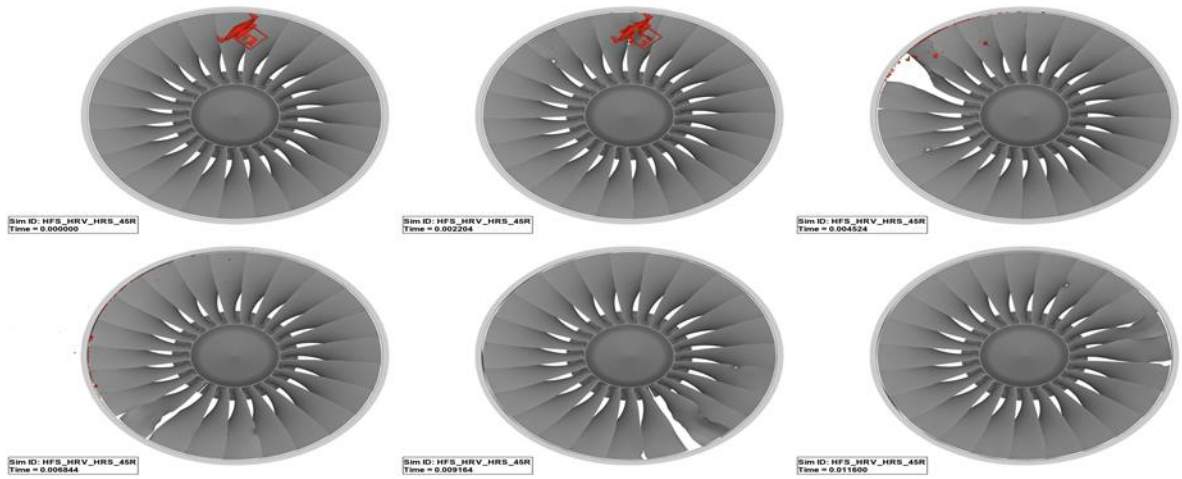

(b) front view

Figure 122. Kinematics of UAS ingestion simulation HFS_HRV_HRS_45R.

The effective plastic strain in the fan at the end of one fan rotation is shown in Figure 123 (front and rear views).

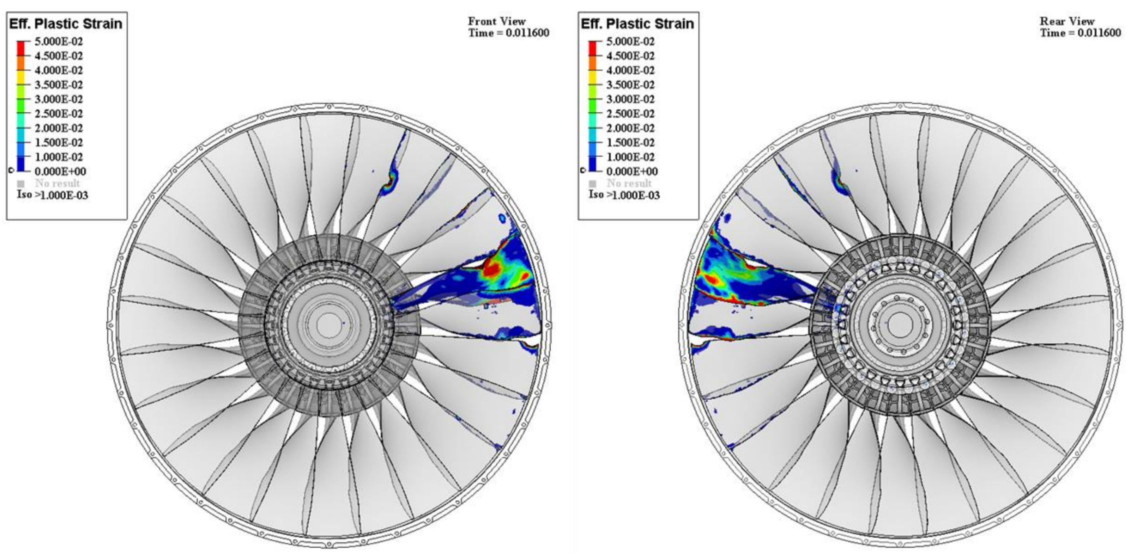

Figure 123. Effective plastic strain after UAS ingestion simulation HFS_HRV_HRS_45R.

Each blade's radial center of mass pre- and post-ingestion are shown in Figure 124. The damage level *D* (defined in Section 4.2) in the damaged area of the fan model after the UAS ingestion is also shown. The damage clearly shows significant material loss on leading edge of multiple blades, but the imbalance would be less than that of a loss of a full blade, which corresponds to damage severity level 3.

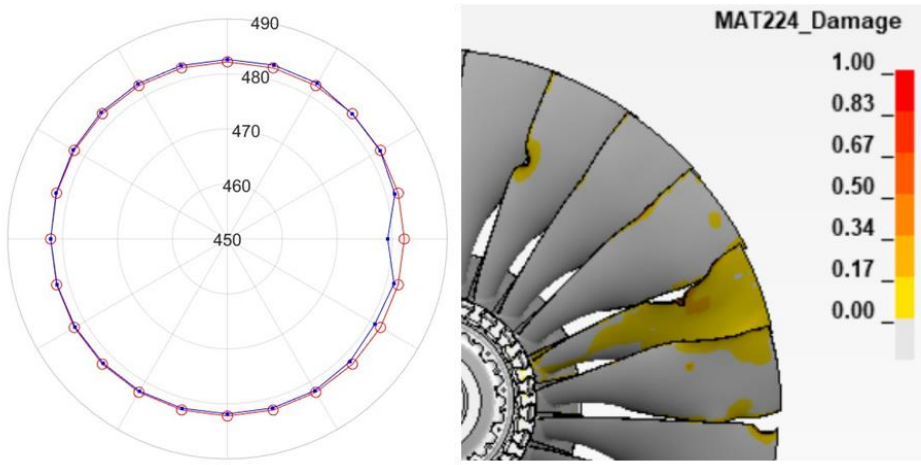

Figure 124. Center of mass of blades and fan model damage after UAS ingestion simulation HFS_HRV_HRS_45R.

The resultant moments and forces in a sectional plane (see Figure 40) during the ingestion are shown in Figure 125. Note that the damaged airfoil has a significantly larger oscillation in the moments than the undamaged blade.

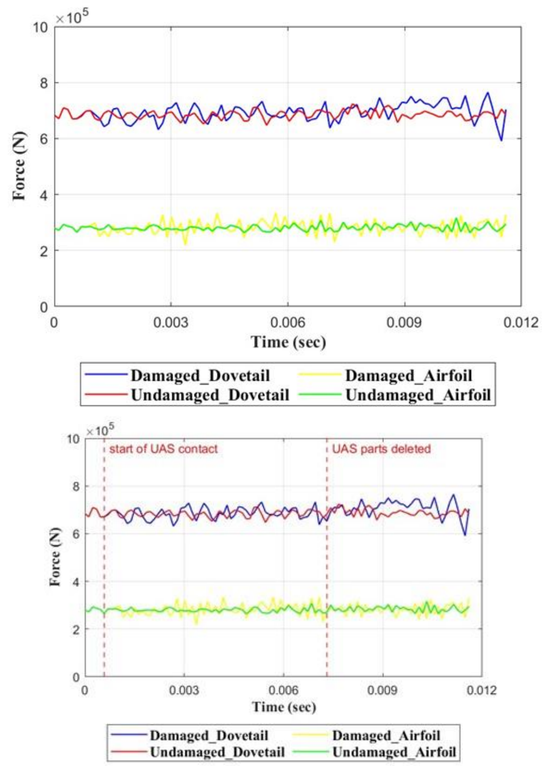

(a) forces

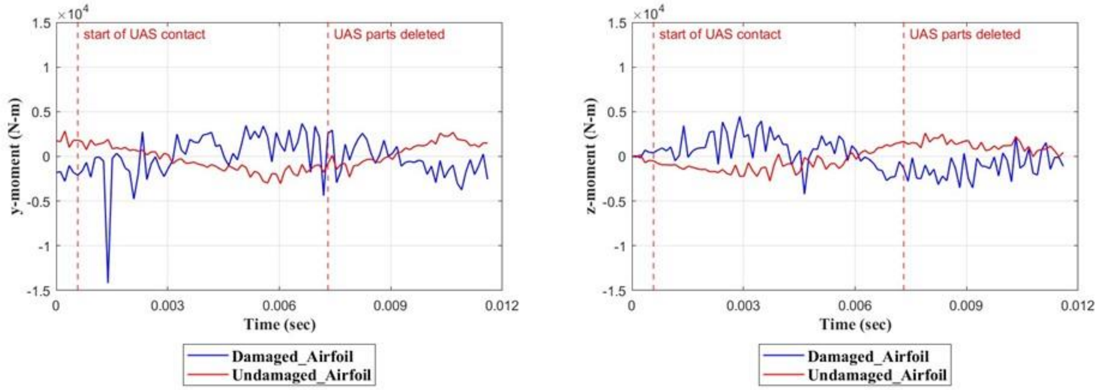

(b) moments about the y- and z-axes

Figure 125. Resultant (a) forces and (b) moments in a sectional plane of the airfoil and dovetail during UAS ingestion simulation HFS_HRV_HRS_45R.

Figure 126(a) shows the overall energy ratio in the system, not including the eroded energy. Note that there is a drop in the energy ratio term because of the erosion of elements in the UAS and fan during the ingestion, and then a sudden drop when the UAS is deleted after it clears the fan stage to speed up the calculation. Figure 126(b) shows the overall energy in the system. The bulk of the energy in the system is the kinetic energy in the fan and the UAS. The reason why the total energy in the system increases is because of the external work of the driven shaft. There is some internal energy in the system that will be shown in the breakout of the UAS and fan energies.

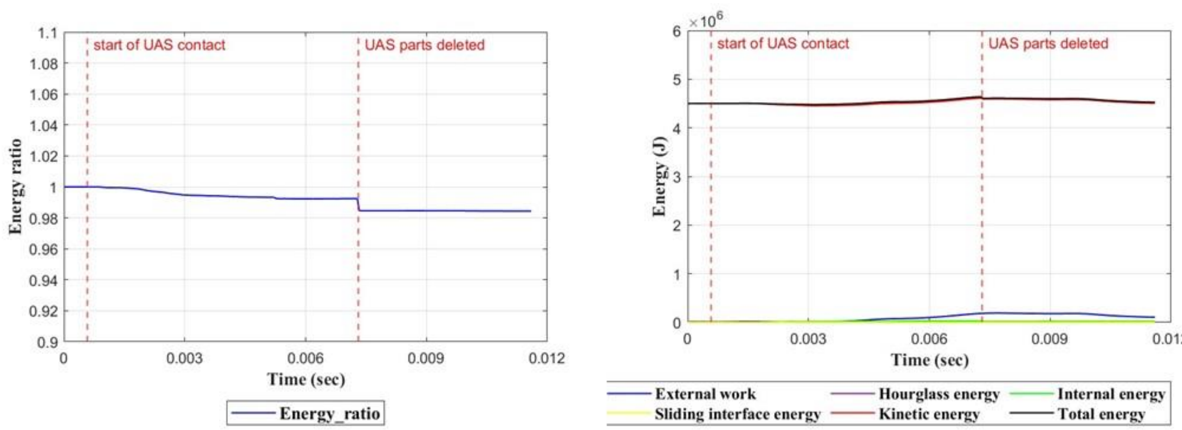

(a) energy ratio (b) energy in system

Figure 126. Overall energy in the system for HFS_HRV_HRS_45R.

Figure 127 shows the internal and kinetic energy in the UAS during the ingestion up until it is deleted from the simulation. Note that, as contact is made, both the internal and kinetic energy of the UAS increases. The increase in the internal energy is due to the plastic deformation and failure of UAS components. The increase in the kinetic energy is due to the fact that the fan is rotating at a high speed and accelerates many UAS parts as they are swept outward radially by the fan. The kinetic energy eventually levels off and decreases as UAS parts impact the stationary casing. The velocities of the motors, camera, and battery during the impact are all shown in Figure 128 and agree with this assessment. The different color lines for the velocities of each motor correspond to the motor colors in Figure 39.

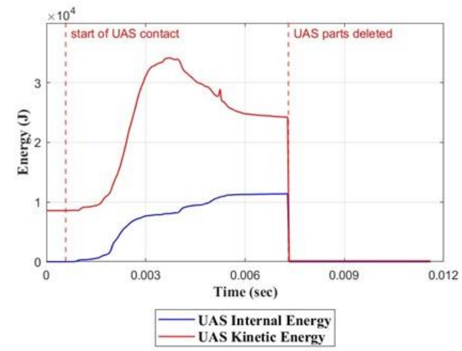

Figure 127. Internal and kinetic energies of the UAS for HFS_HRV_HRS_45R.

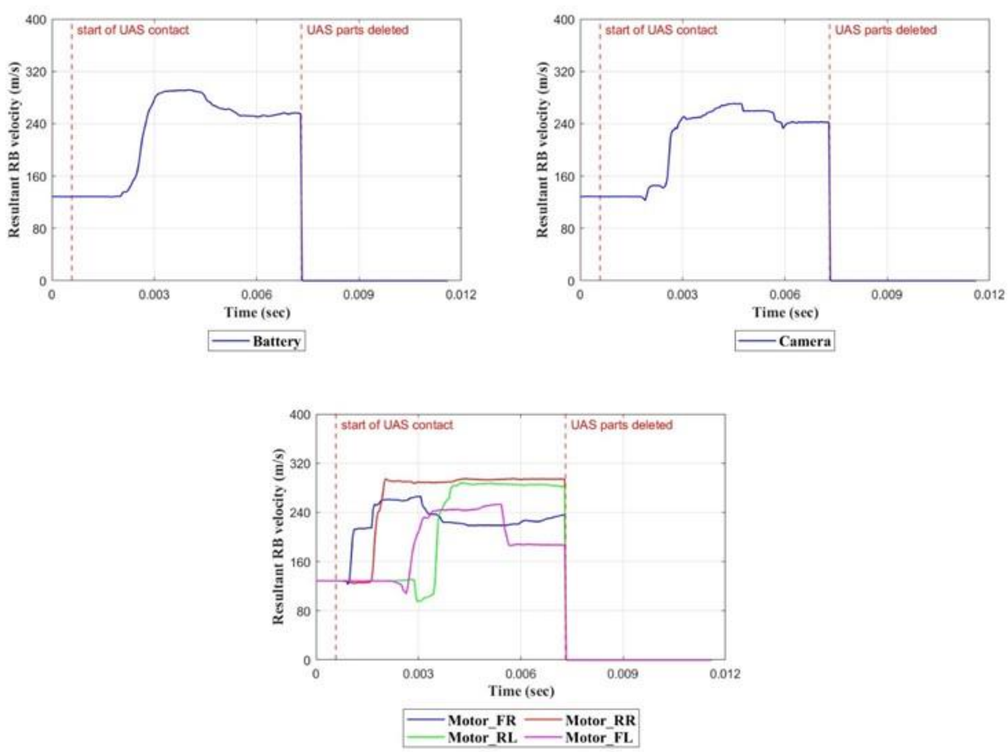

Figure 128. Resultant velocities of UAS components for HFS_HRV_HRS_45R.

The kinetic and internal energy of the fan are shown in Figure 129. Note that the kinetic energy of the fan looks very similar to the overall energy in the system from Figure 126, since the bulk of the energy is in the fan. There is also significant damage in the fan through the internal energy that increases while the fan is impacting the UAS.

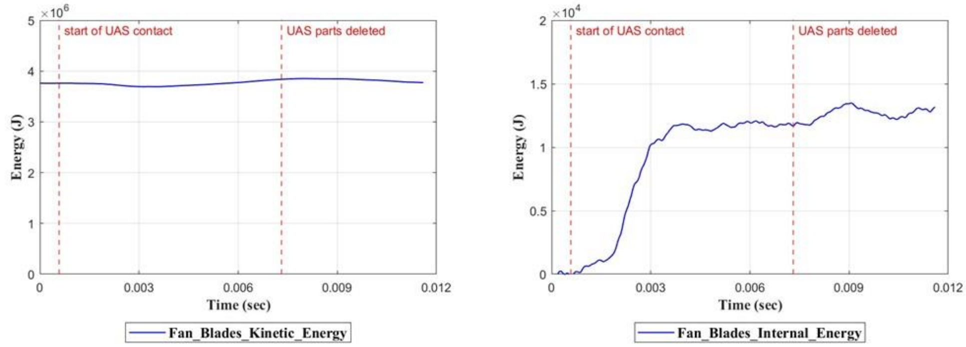

Figure 129. Energy in the fan blades during HFS_HRV_HRS_45R.

Finally, the breakdown of the energy in each blade starting with the top vertical blade as number 1 and counting upwards clockwise from there can be seen in Figure 130. Depending on the relative translational speed of the UAS and rotational speed of the fan, one of the first few blades will be the first one to contact the UAS. In this case, mainly blades 3 through 11 made contact with the UAS during the ingestion. The blades with the largest variation in kinetic energy due to their deflection during impact tend to have the largest internal energy as well. In this case, blade 3 has the largest oscillation in kinetic energy and increase in internal energy, followed by blades 3-5 and 7-11.

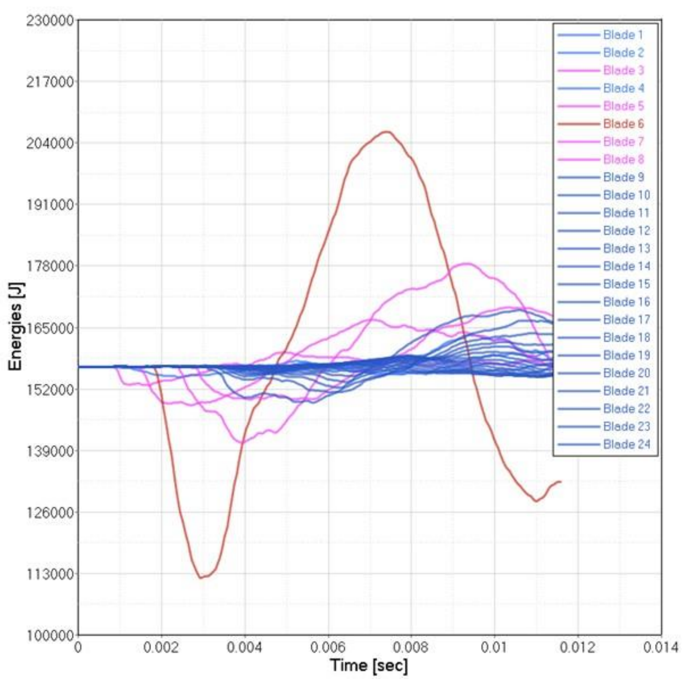

(a) kinetic energy

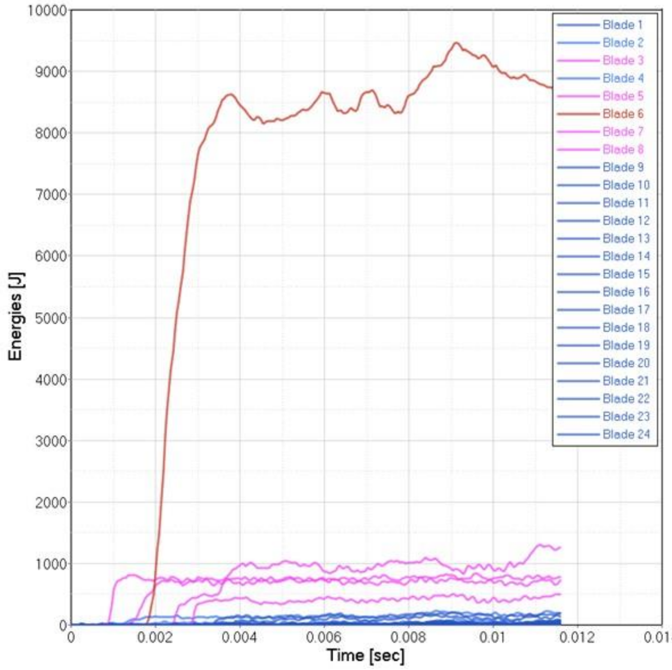

(b) internal energy

Figure 130. Energies in individual fan blades during UAS ingestion simulation HFS_HRV_HRS_45R.

4.4.12 Simulation HFS_HRV_HRS_90R

This case corresponded to a UAS ingestion with a high fan speed, high relative translational velocity, high radial span location, and the 90 degree roll orientation (see Figure 39). The kinematics of the ingestion are shown in Figure 131. In all of the high fan speed simulations the fan was simulated for a full fan rotation, about 11.6 ms. The UAS parts were also deleted in these cases once they had cleared the fan region, in this case at approximately 7 ms, to improve the computational efficiency of the simulation. It should also be noted that in this case there was element distortion in a few elements of the UAS post impact with the fan. These elements caused a significant increase in the computational time by reducing the time increment in the simulation. Therefore, the UAS part corresponding to the distorted element was deleted prior to the other parts of the UAS in this simulation.

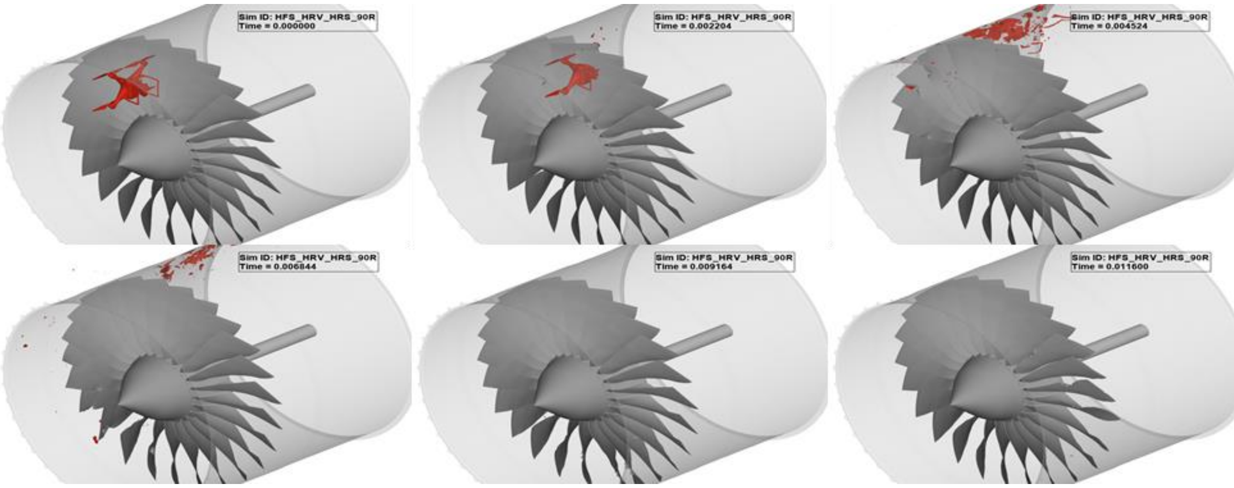

(a) isometric view

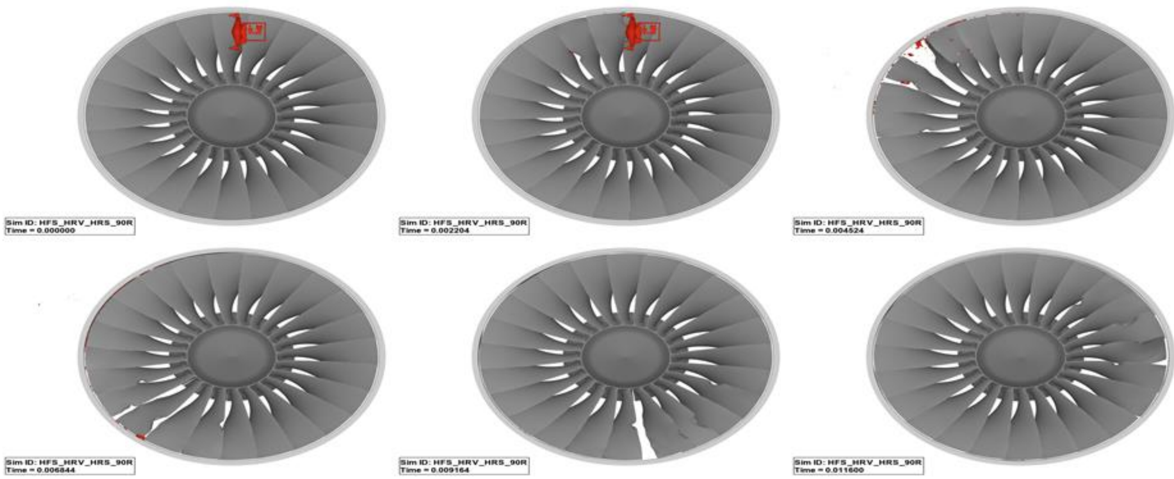

(b) front view

Figure 131. Kinematics of UAS ingestion simulation HFS_HRV_HRS_90R.

The effective plastic strain in the fan at the end of one fan rotation is shown in Figure 132 (front and rear views).

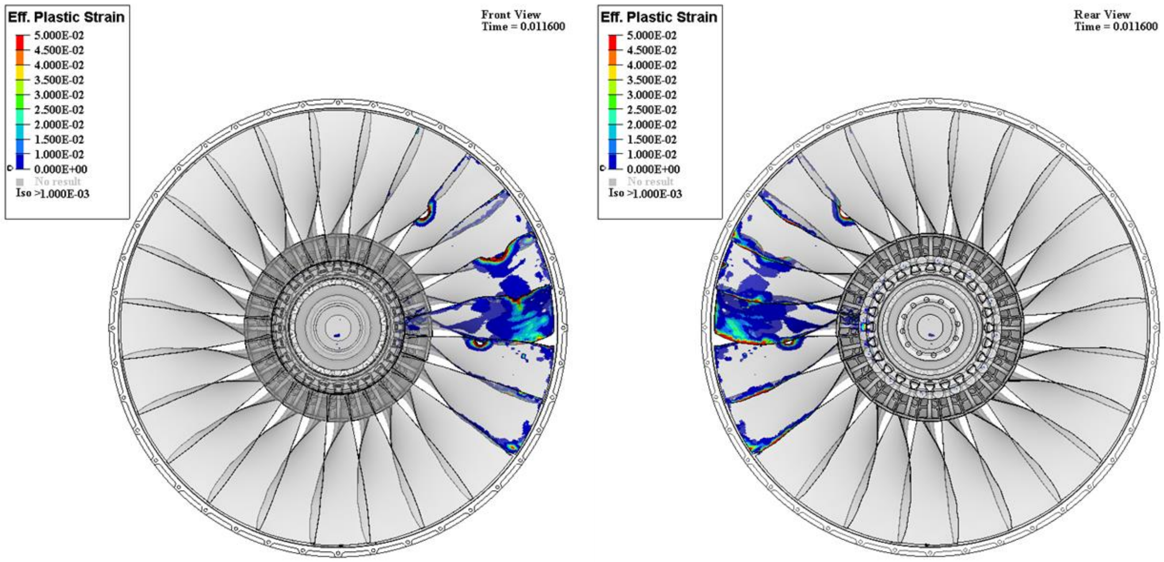

Figure 132. Effective plastic strain after UAS ingestion simulation HFS_HRV_HRS_90R.

Each blade's radial center of mass pre- and post-ingestion are shown in Figure 133. The damage level D (defined in Section 4.2) in the damaged area of the fan model after the UAS ingestion is also shown. The damage clearly shows significant material loss on leading edge of multiple blades, but the imbalance would be less than that of a loss of a full blade, which corresponds to damage severity level 3.

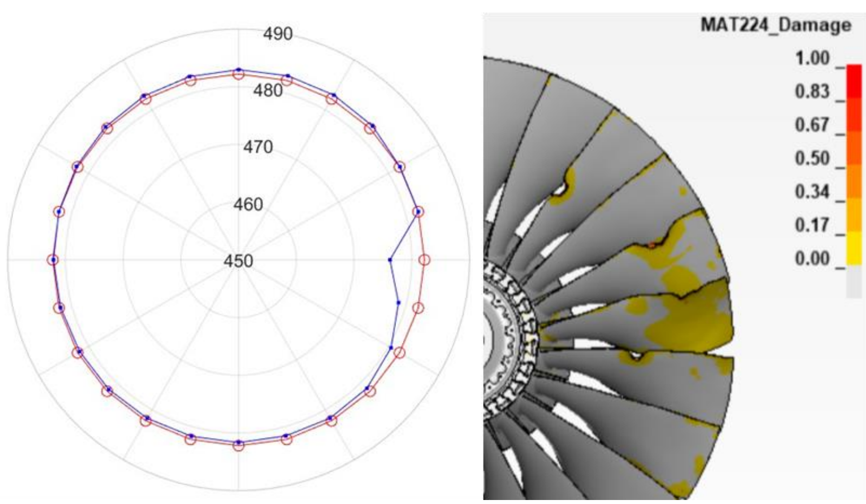

Figure 133. Center of mass of blades and fan model damage after UAS ingestion simulation HFS_HRV_HRS_90R.

The resultant moments and forces in a sectional plane (see Figure 40) during the ingestion are shown in Figure 134. Note that the damaged airfoil does not have a significantly larger oscillation in the forcing and moment than the undamaged blade for this case.

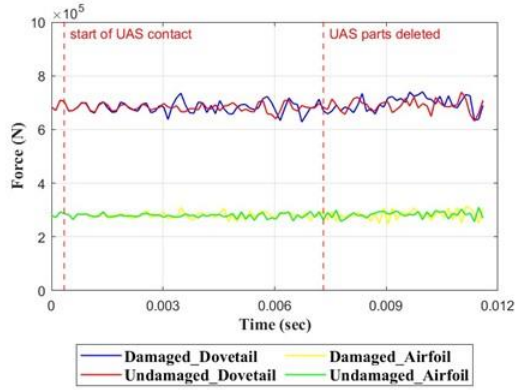

(a) forces

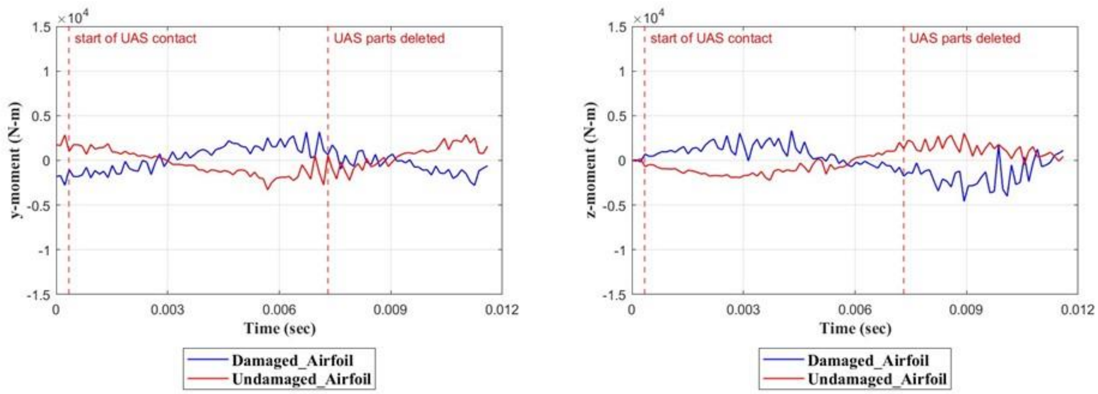

(b) moments about the y- and z-axes

Figure 134. Resultant (a) forces and (b) moments in a sectional plane of the airfoil and dovetail during UAS ingestion simulation HFS_HRV_HRS_90R.

Figure 135(a) shows the overall energy ratio in the system, not including the eroded energy. Note that there is a drop in the energy ratio term because of the erosion of elements in the UAS and fan during the ingestion and then a sudden drop when the UAS is deleted after it clears the fan stage to speed up the calculation. Figure 135(b) shows the overall energy in the system. The bulk of the energy in the system is the kinetic energy in the fan and the UAS. The reason why the total energy in the system increases is because of the external work of the driven shaft. There is some internal energy in the system that will be shown in the breakout of the UAS and fan energies.

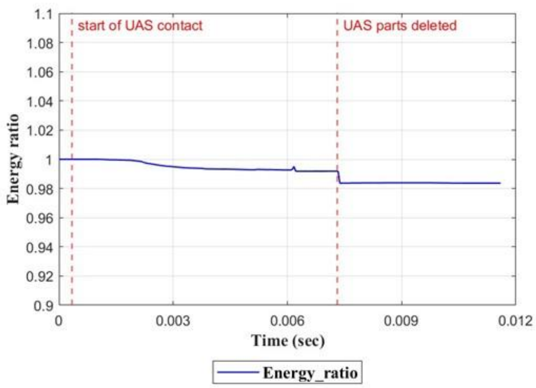

(a) energy ratio

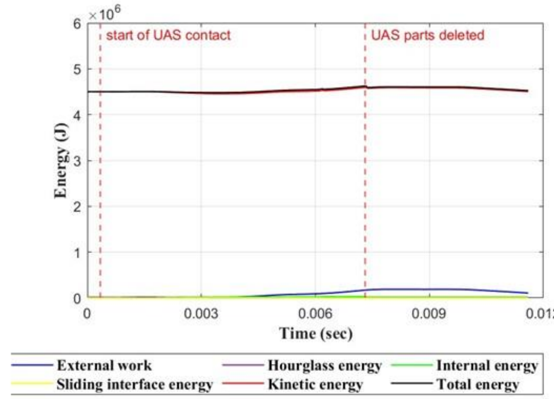

(b) energy in system

Figure 135. Overall energy in the system for HFS_HRV_HRS_90R.

Figure 136 shows the internal and kinetic energy in the UAS during the ingestion up until it is deleted from the simulation. Note that, as contact is made, both the internal and kinetic energy of the UAS increases. The increase in the internal energy is due to the plastic deformation and failure of UAS components. The increase in the kinetic energy is due to the fact that the fan is rotating at a high speed and accelerates many UAS parts as they are swept outward radially by the fan. The kinetic energy eventually levels off and decreases as UAS parts impact the stationary casing. The velocities of the motors, camera, and battery during the impact are all shown in Figure 137 and agree with this assessment. The different color lines for the velocities of each motor correspond to the motor colors in Figure 39.

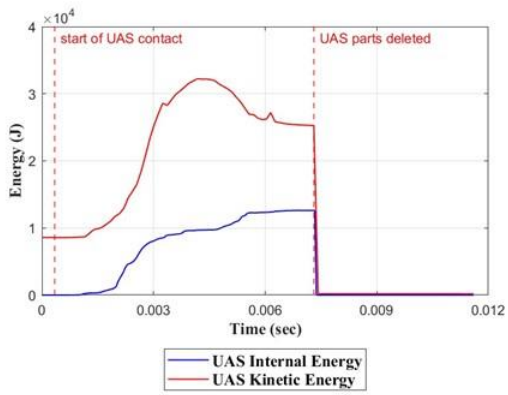

Figure 136. Internal and kinetic energies of the UAS for HFS_HRV_HRS_90R.

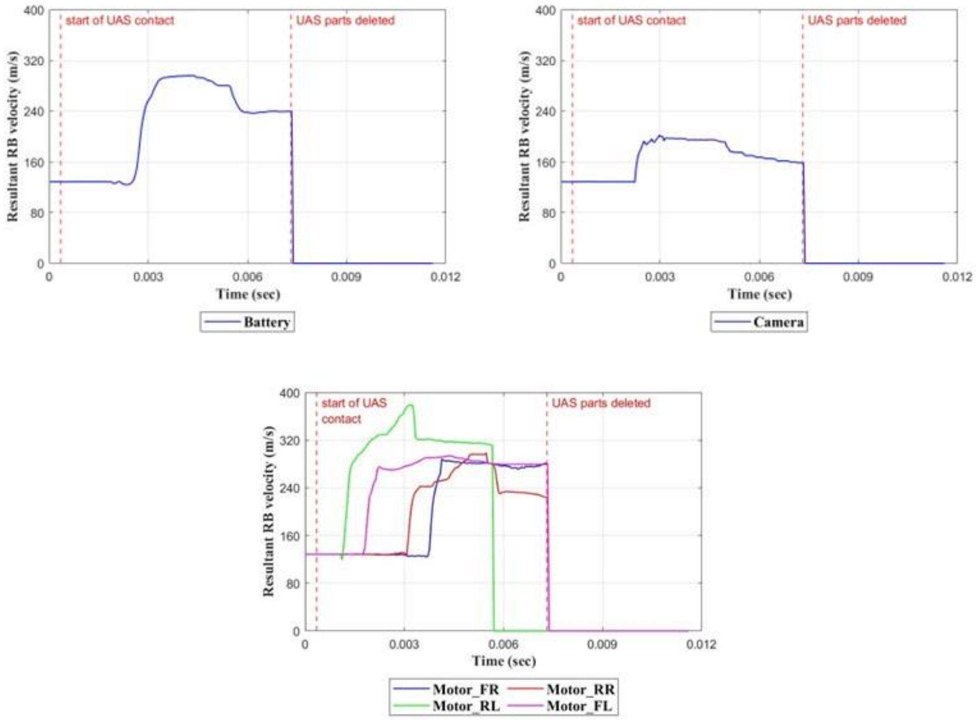

Figure 137. Resultant velocities of UAS components for HFS_HRV_HRS_90R.

The kinetic and internal energy of the fan are shown in Figure 138. Note that the kinetic energy of the fan looks very similar to the overall energy in the system from Figure 135, since the bulk of the energy is in the fan. There is also significant damage in the fan through the internal energy that increases while the fan is impacting the UAS.

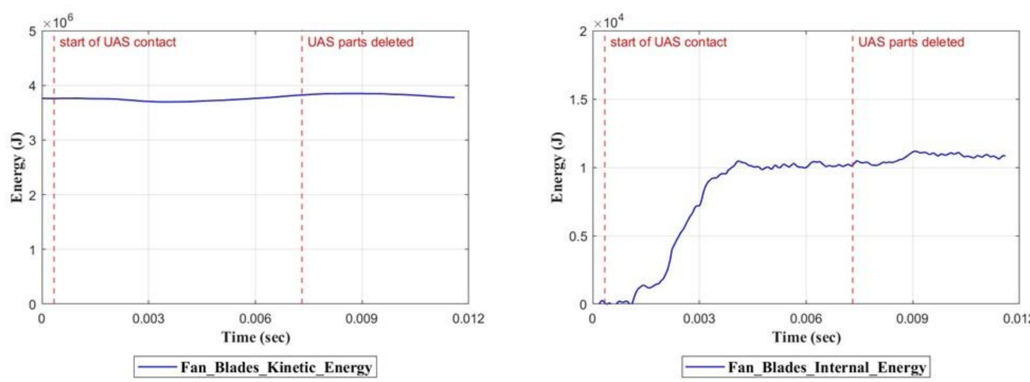

Figure 138. Energy in the fan blades during HFS_HRV_HRS_90R.

Finally, the breakdown of the energy in each blade starting with the top vertical blade as number 1 and counting upwards clockwise from there can be seen in Figure 139. Depending on the relative translational speed of the UAS and rotational speed of the fan, one of the first few blades will be the first one to contact the UAS. In this case, mainly blades 4 through 9 made contact with the UAS during the ingestion. The blades with the largest variation in kinetic energy due to their deflection during impact tend to have the largest internal energy as well. In this case, blades 6 and 7 have the largest oscillation in kinetic energy and increase in internal energy, followed by blades 4 and 8, and then blades 5 and 9.

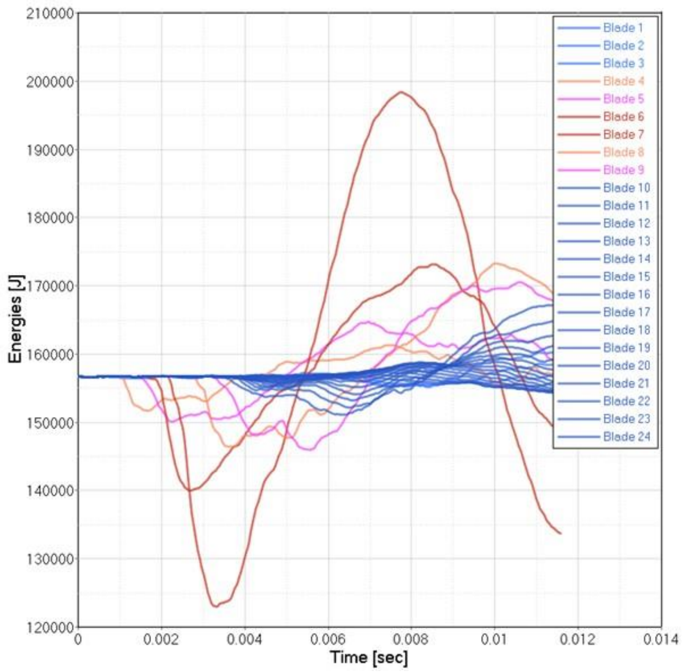

(a) kinetic energy

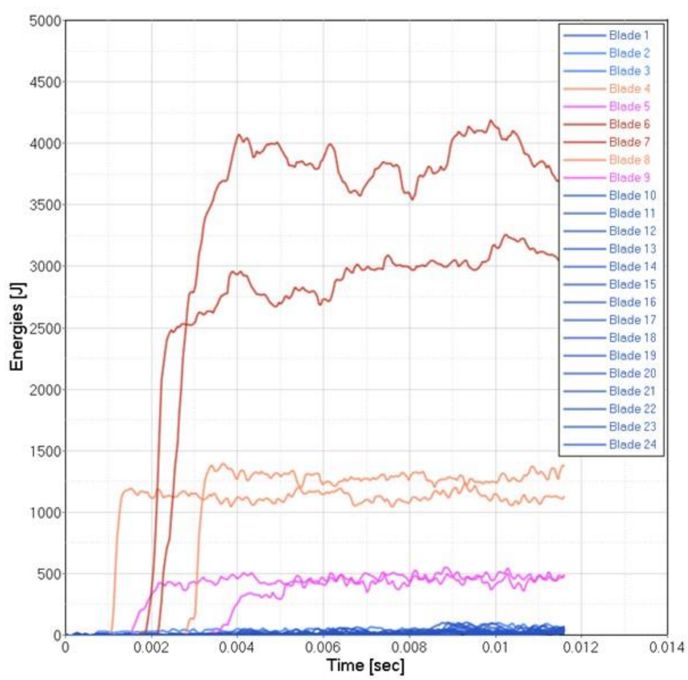

(b) internal energy

Figure 139. Energies in individual fan blades during UAS ingestion simulation HFS_HRV_HRS_90R.

4.4.13 Simulation HFS_HRV_HRS_45Y

This case corresponded to a UAS ingestion with a high fan speed, high relative translational velocity, high radial span location, and the 45 degree yaw orientation (see Figure 39). The kinematics of the ingestion are shown in Figure 140. In all of the high fan speed simulations, the fan was simulated for a full fan rotation, about 11.6 ms. The UAS parts were also deleted in these cases once they had cleared the fan region, in this case at approximately 5 ms, to improve the computational efficiency of the simulation.

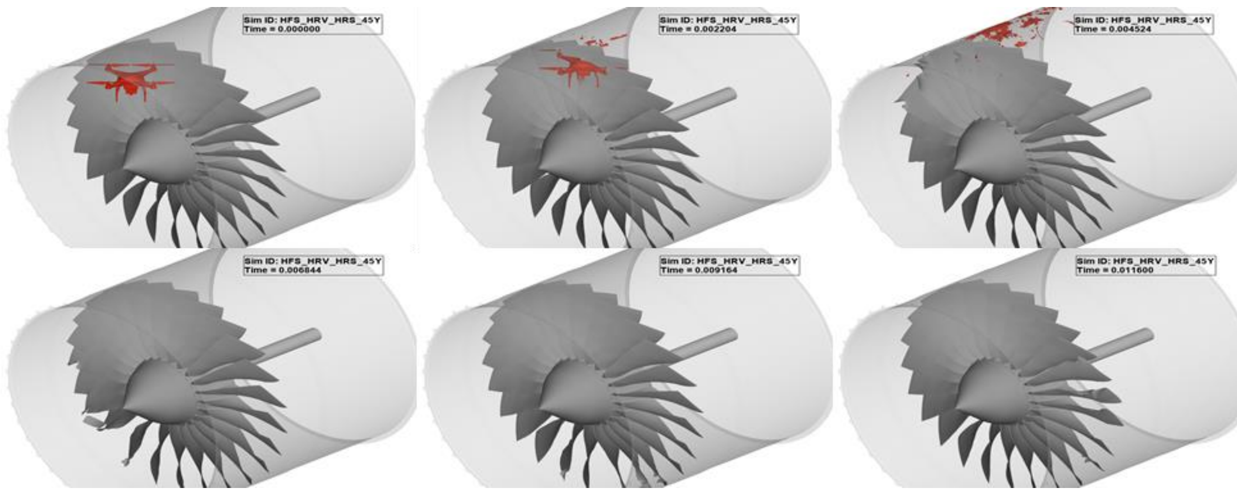

(a) isometric view

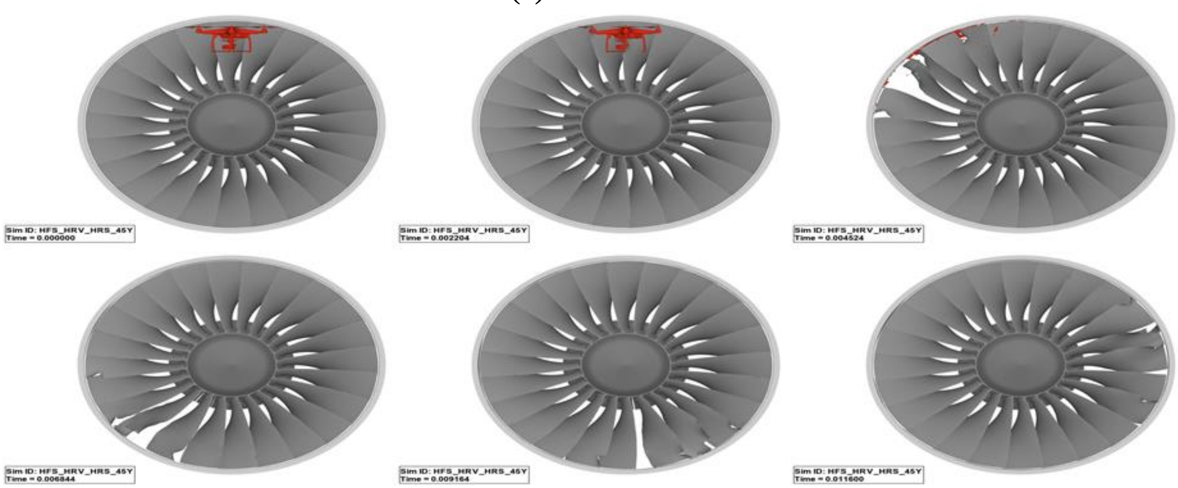

(b) front view

Figure 140. Kinematics of UAS ingestion simulation HFS_HRV_HRS_45Y.

The effective plastic strain in the fan at the end of one fan rotation is shown in Figure 141 (front and rear views).

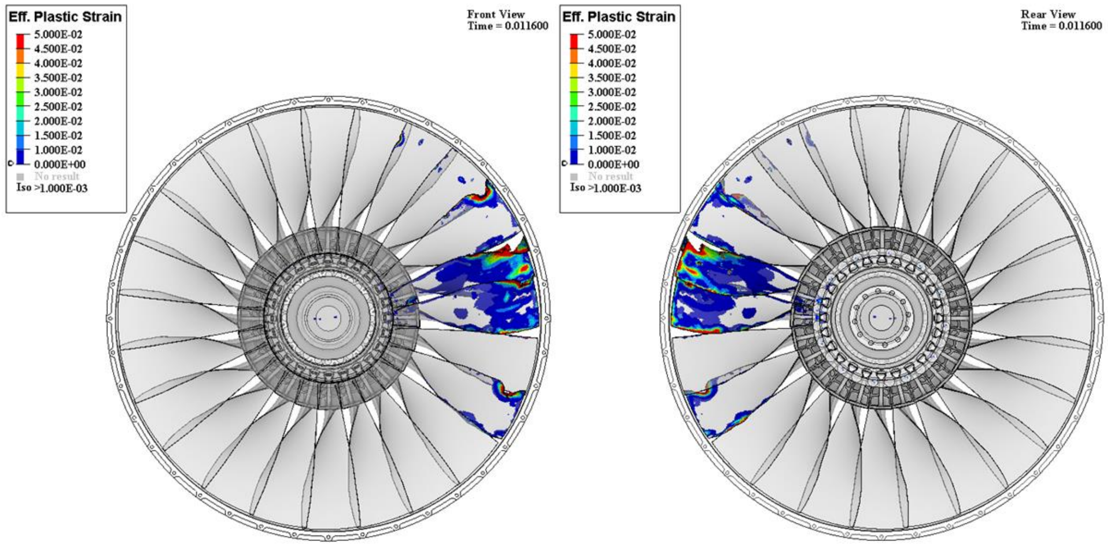

Figure 141. Effective plastic strain after UAS ingestion simulation HFS_HRV_HRS_45Y.

Each blade's radial center of mass pre- and post-ingestion are shown in Figure 142. The damage level *D* (defined in Section 4.2) in the damaged area of the fan model after the UAS ingestion is also shown. The damage clearly shows significant material loss on leading edge of multiple blades, but the imbalance would be less than that of a loss of a full blade, which corresponds to damage severity level 3.

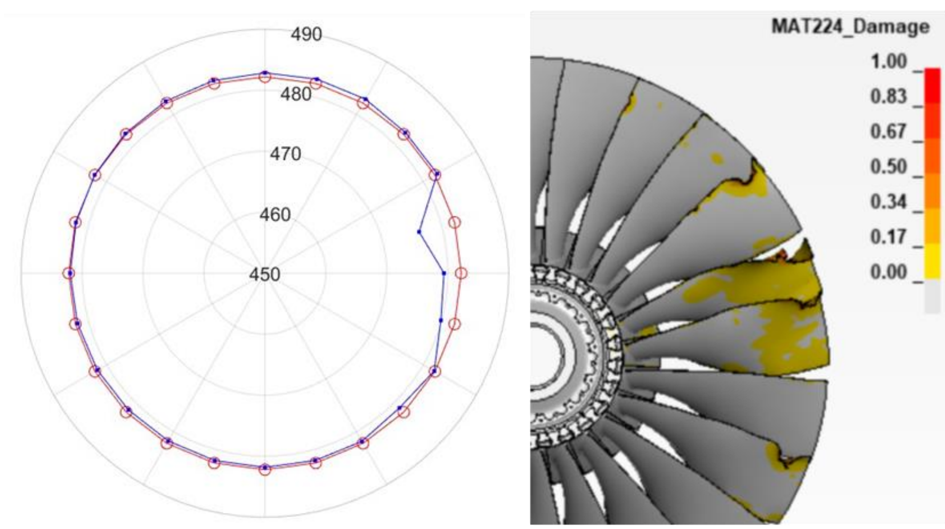

Figure 142. Center of mass of blades and fan model damage after UAS ingestion simulation HFS_HRV_HRS_45Y.

The resultant moments and forces in a sectional plane (see Figure 40) during the ingestion are shown in Figure 143. Note that the damaged airfoil does not have a significantly larger oscillation in the forcing and moment than the undamaged blade for this case.

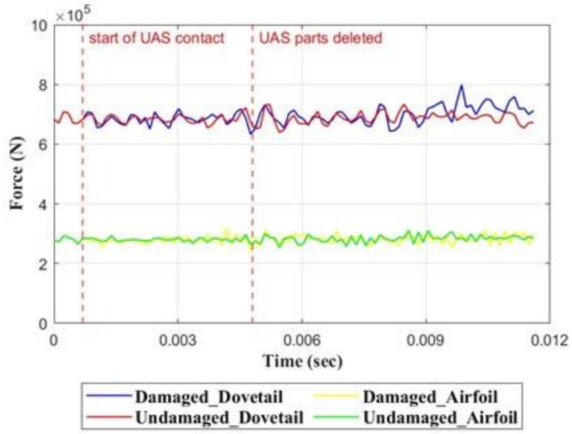

(a) forces

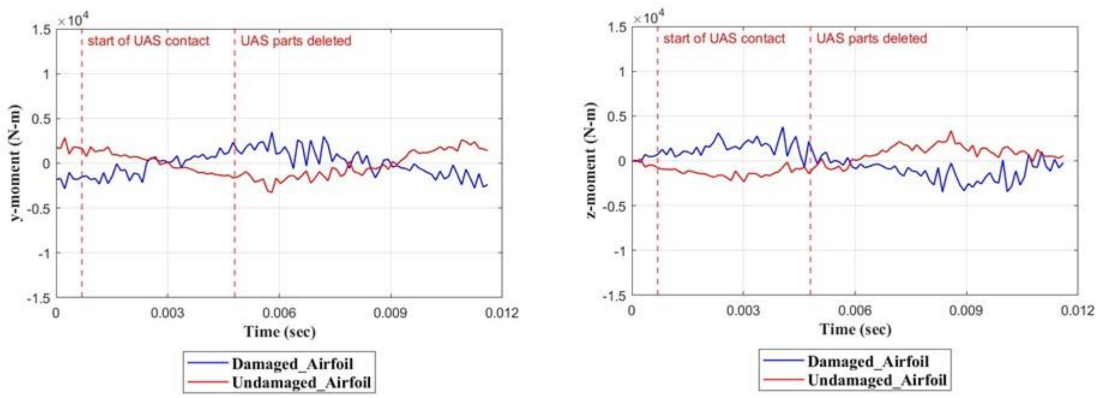

(b) moments about the y- and z-axes

Figure 143. Resultant (a) forces and (b) moments in a sectional plane of the airfoil and dovetail during UAS ingestion simulation HFS_HRV_HRS_45Y.

Figure 144(a) shows the overall energy ratio in the system, not including the eroded energy. Note that there is a drop in the energy ratio term because of the erosion of elements in the UAS and fan during the ingestion and then a sudden drop when the UAS is deleted after it clears the fan stage to speed up the calculation. Figure 144(b) shows the overall energy in the system. The bulk of the energy in the system is the kinetic energy in the fan and the UAS. The reason why the total energy in the system increases is because of the external work of the driven shaft. There is some internal energy in the system that will be shown in the breakout of the UAS and fan energies.

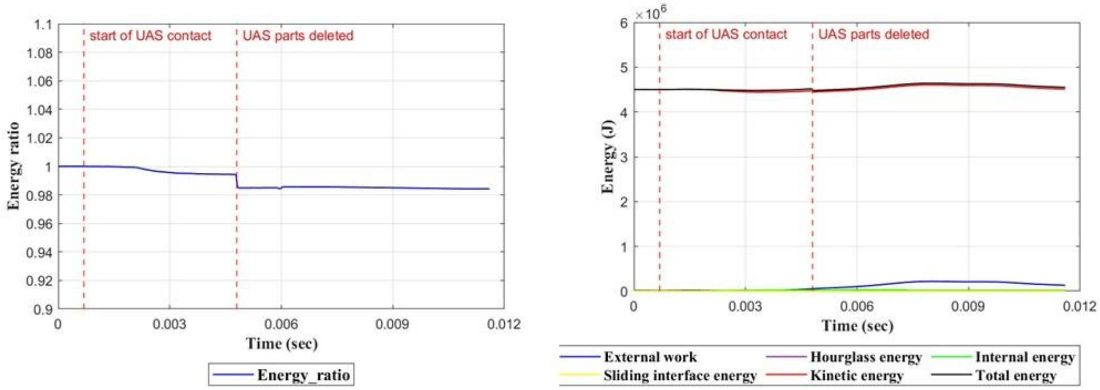

(a) energy ratio (b) energy in system

Figure 144. Overall energy in the system for HFS_HRV_HRS_45Y.

Figure 145 shows the internal and kinetic energy in the UAS during the ingestion up until it is deleted from the simulation. Note that, as contact is made, both the internal and kinetic energy of the UAS increases. The increase in the internal energy is due to the plastic deformation and failure of UAS components. The increase in the kinetic energy is due to the fact that the fan is rotating at a high speed and accelerates many UAS parts as they are swept outward radially by the fan. The kinetic energy eventually levels off and decreases as UAS parts impact the stationary casing. The velocities of the motors, camera, and battery during the impact are all shown in Figure 146 and agree with this assessment. The different color lines for the velocities of each motor correspond to the motor colors in Figure 39.

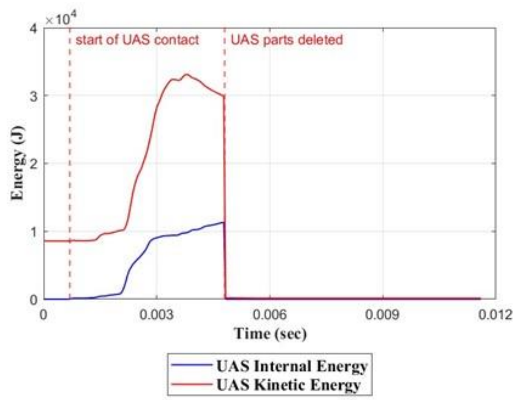

Figure 145. Internal and kinetic energies of the UAS for HFS_HRV_HRS_45Y.

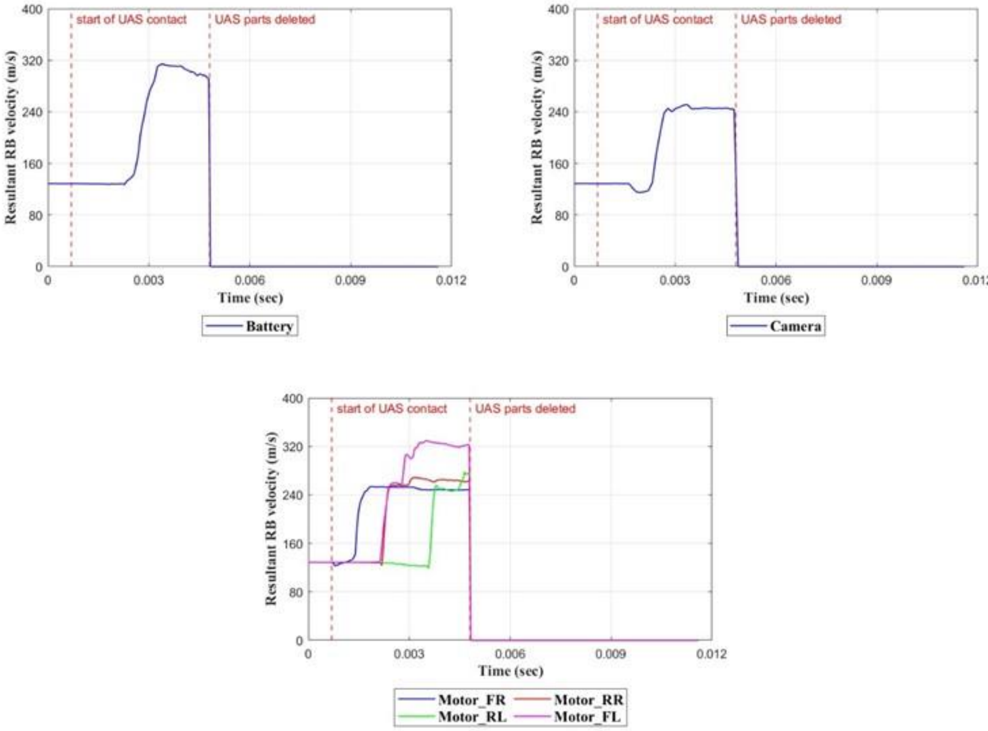

Figure 146. Resultant velocities of UAS components for HFS_HRV_HRS_45Y.

The kinetic and internal energy of the fan are shown in Figure 147. Note that the kinetic energy of the fan looks very similar to the overall energy in the system from Figure 144, since the bulk of the energy is in the fan. There is also significant damage in the fan through the internal energy that increases while the fan is impacting the UAS.

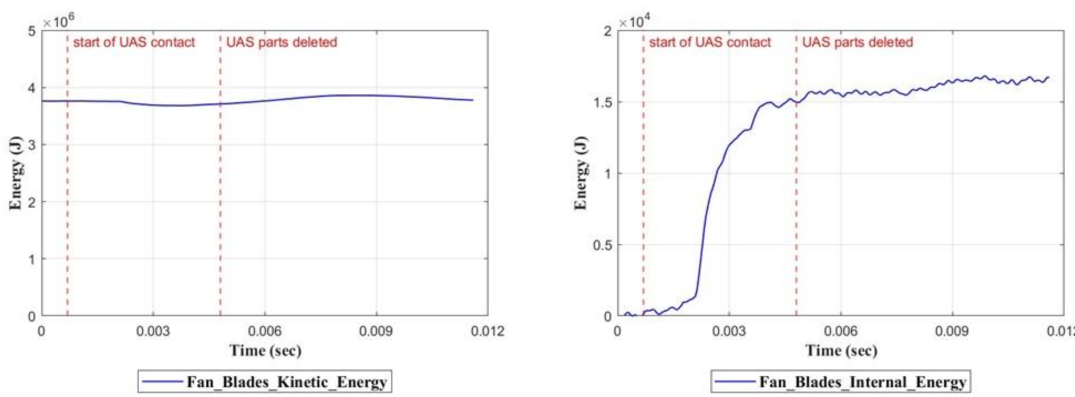

Figure 147. Energy in the fan blades during HFS_HRV_HRS_45Y.

Finally, the breakdown of the energy in each blade starting with the top vertical blade as number 1 and counting upwards clockwise from there can be seen in Figure 121. Depending on the relative

translational speed of the UAS and rotational speed of the fan, one of the first few blades will be the first one to contact the UAS. In this case, mainly blades 5 through 9 made contact with the UAS during the ingestion. The blades with the largest variation in kinetic energy due to their deflection during impact tend to have the largest internal energy as well. In this case, blade 6 has the largest oscillation in kinetic energy and increase in internal energy, followed by blades 5, 7 and 9.

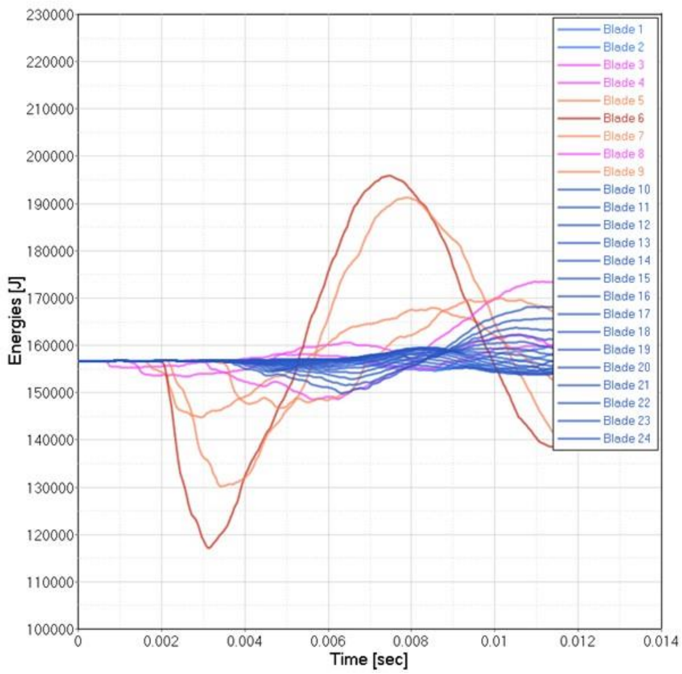

(a) kinetic energy

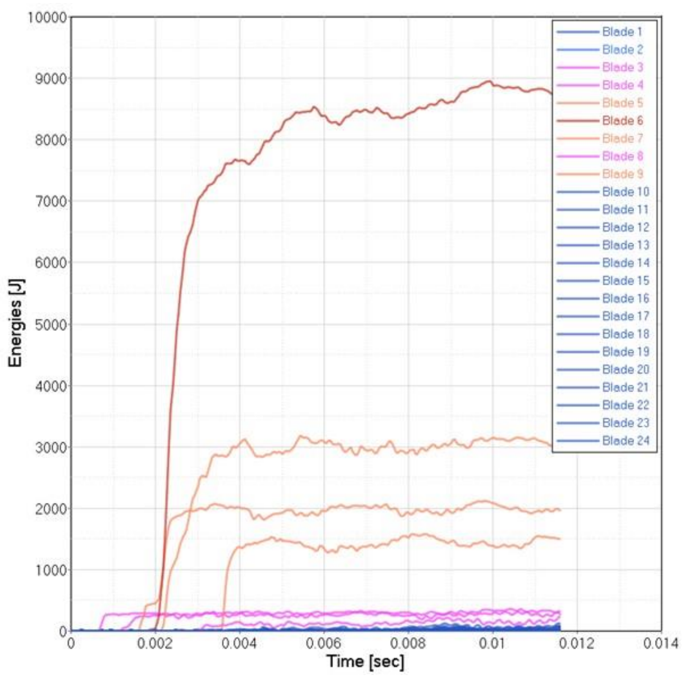

(b) internal energy

Figure 148. Energies in individual fan blades during UAS ingestion simulation HFS_HRV_HRS_45Y.

4.4.14 Simulation HFS_HRV_HRS_90Y

This case corresponded to a UAS ingestion with a high fan speed, high relative translational velocity, high radial span location, and the 90 degree yaw orientation (see Figure 39). The kinematics of the ingestion are shown in Figure 149. In all of the high fan speed simulations, the fan was simulated for a full fan rotation, about 11.6 ms. The UAS parts were also deleted in these cases once they had cleared the fan region, in this case at approximately 5 ms, to improve the computational efficiency of the simulation.

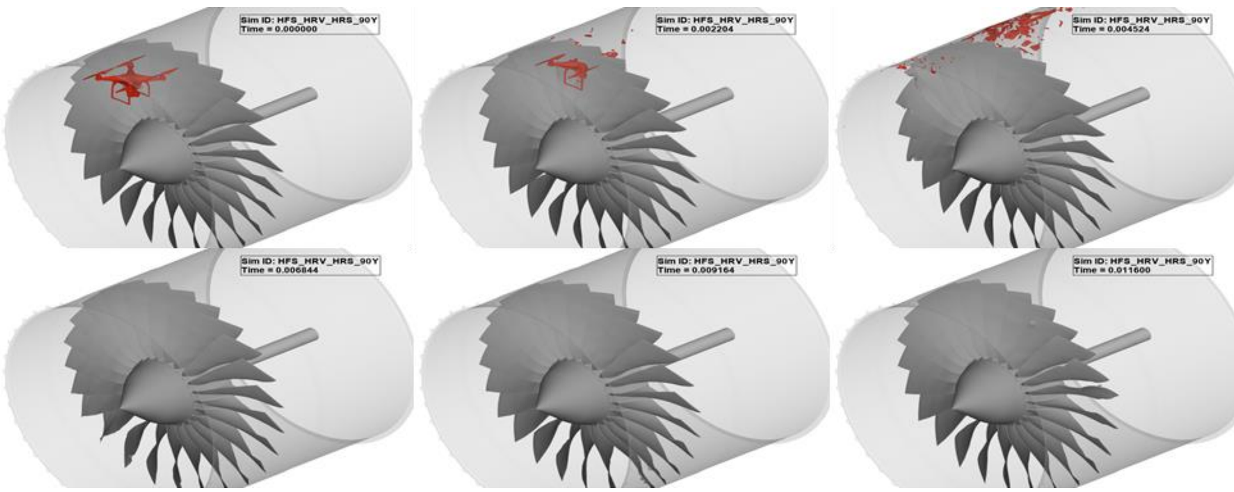

(a) isometric view

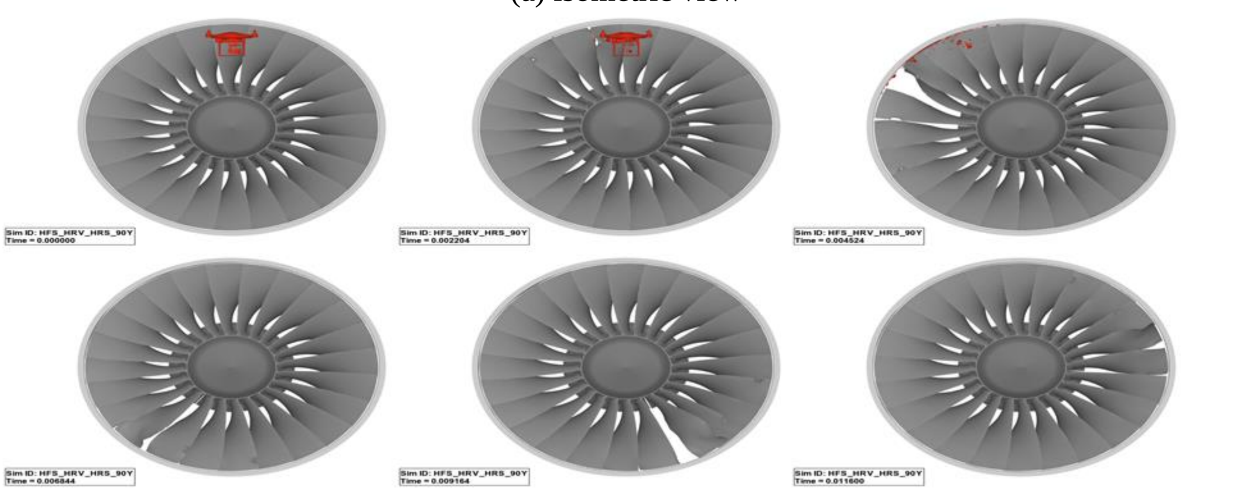

(b) front view

Figure 149. Kinematics of UAS ingestion simulation HFS_HRV_HRS_90Y.

The effective plastic strain in the fan at the end of one fan rotation is shown in Figure 150 (front and rear views).

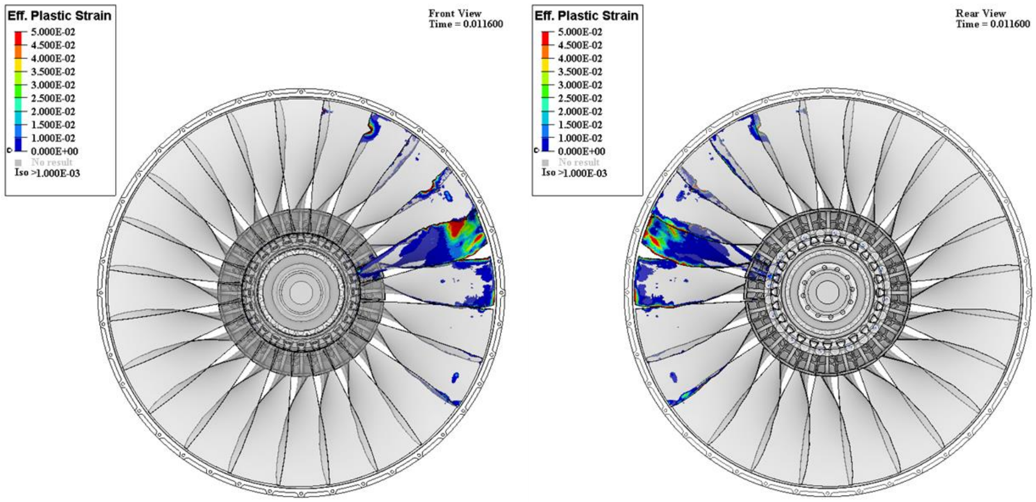

Figure 150. Effective plastic strain after UAS ingestion simulation HFS_HRV_HRS_90Y.

Each blade's radial center of mass pre- and post-ingestion are shown in Figure 151. The damage level D (defined in Section 4.2) in the damaged area of the fan model after the UAS ingestion is also shown. The damage clearly shows significant material loss on leading edge of multiple blades, but the imbalance would be less than that of a loss of a full blade, which corresponds to damage severity level 3.

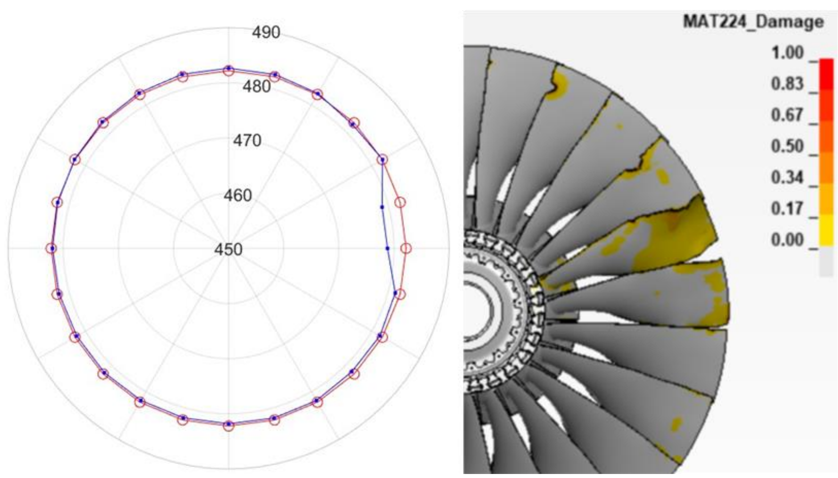

Figure 151. Center of mass of blades and fan model damage after UAS ingestion simulation HFS_HRV_HRS_90Y.

The resultant moments and forces in a sectional plane (see Figure 40) during the ingestion are shown in Figure 152. Note that the damaged airfoil has a significantly larger oscillation in the forcing and moment than the undamaged blade.

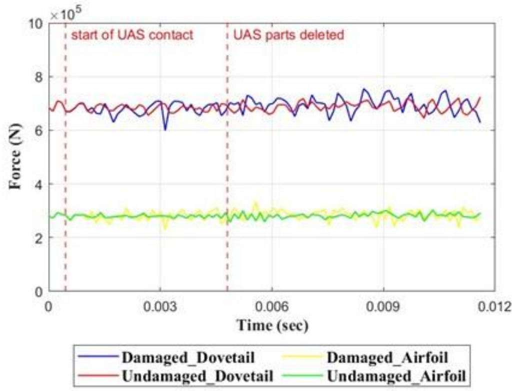

(a) forces

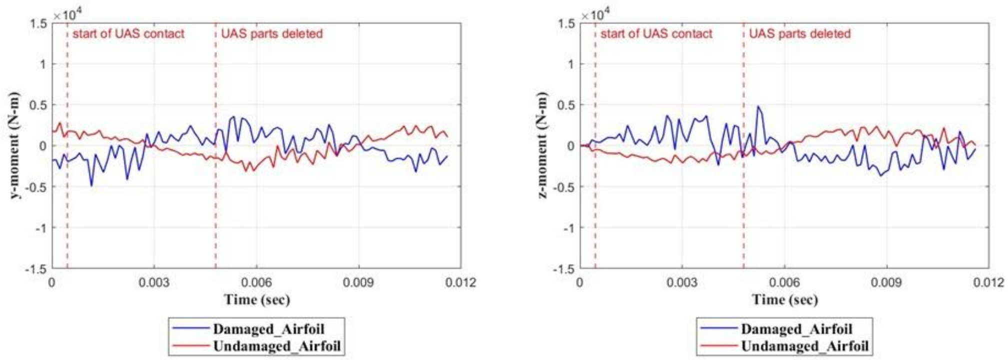

(b) moments about the y- and z-axes

Figure 152. Resultant (a) forces and (b) moments in a sectional plane of the airfoil and dovetail during UAS ingestion simulation HFS_HRV_HRS_90Y.

Figure 153(a) shows the overall energy ratio in the system, not including the eroded energy. Note that there is a drop in the energy ratio term because of the erosion of elements in the UAS and fan during the ingestion and then a sudden drop when the UAS is deleted after it clears the fan stage to speed up the calculation. Figure 153(b) shows the overall energy in the system. The bulk of the energy in the system is the kinetic energy in the fan and the UAS. The reason why the total energy in the system increases is because of the external work of the driven shaft. There is some internal energy in the system that will be shown in the breakout of the UAS and fan energies.

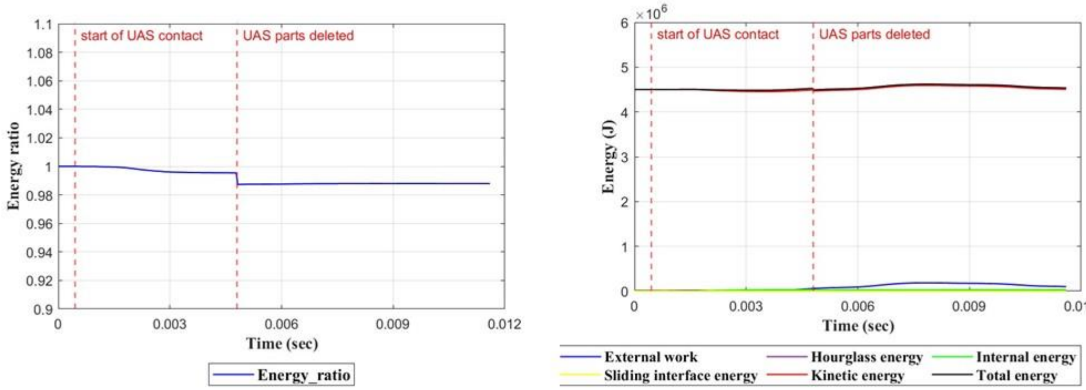

(a) energy ratio (b) energy in system

Figure 153. Overall energy in the system for HFS_HRV_HRS_90Y.

Figure 154 shows the internal and kinetic energy in the UAS during the ingestion up until it is deleted from the simulation. Note that, as contact is made, both the internal and kinetic energy of the UAS increases. The increase in the internal energy is due to the plastic deformation and failure of UAS components. The increase in the kinetic energy is due to the fact that the fan is rotating at a high speed and accelerates many UAS parts as they are swept outward radially by the fan. The kinetic energy eventually levels off and decreases as UAS parts impact the stationary casing. The velocities of the motors, camera, and battery during the impact are all shown in Figure 155 and agree with this assessment. The different color lines for the velocities of each motor correspond to the motor colors in Figure 39.

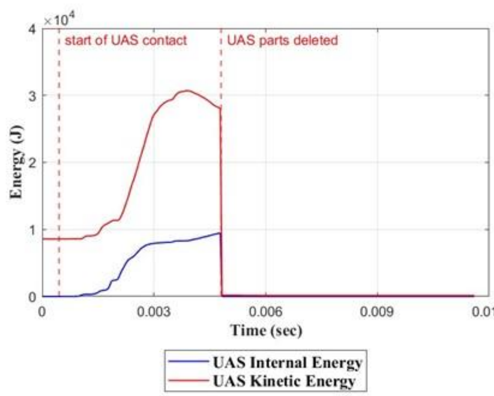

Figure 154. Internal and kinetic energies of the UAS for HFS_HRV_HRS_90Y.

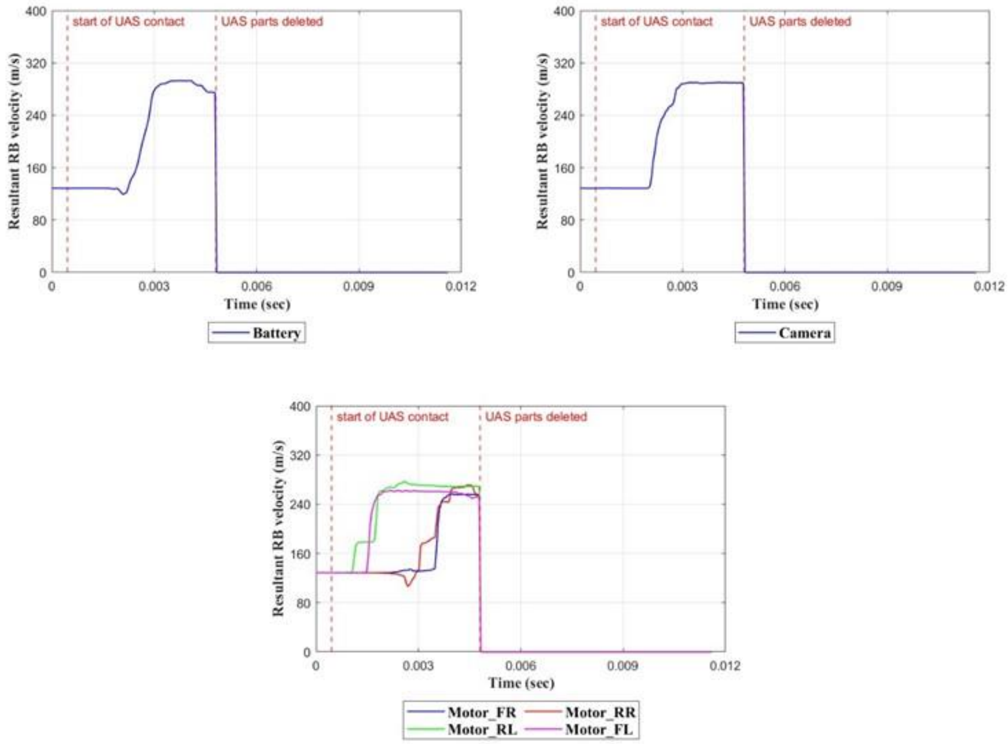

Figure 155. Resultant velocities of UAS components for HFS_HRV_HRS_90Y.

The kinetic and internal energy of the fan are shown in Figure 156. Note that the kinetic energy of the fan looks very similar to the overall energy in the system from Figure 153, since the bulk of the energy is in the fan. There is also significant damage in the fan through the internal energy that increases while the fan is impacting the UAS.

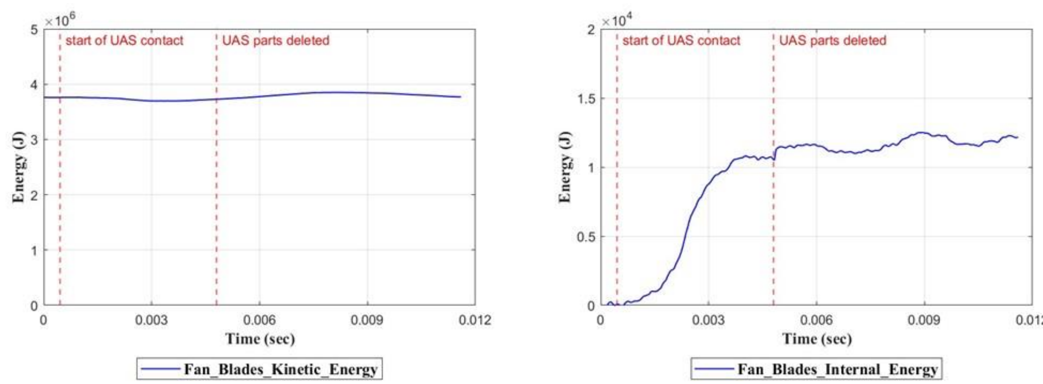

Figure 156. Energy in the fan blades during HFS_HRV_HRS_90Y.

Finally, the breakdown of the energy in each blade starting with the top vertical blade as number 1 and counting upwards clockwise from there can be seen in Figure 157. Depending on the relative

translational speed of the UAS and rotational speed of the fan, one of the first few blades will be the first one to contact the UAS. In this case, mainly blades 3 through 7 made contact with the UAS during the ingestion. The blades with the largest variation in kinetic energy due to their deflection during impact tend to have the largest internal energy as well. In this case, blade 6 has the largest oscillation in kinetic energy and increase in internal energy, followed by blades 3, 5 and 7.

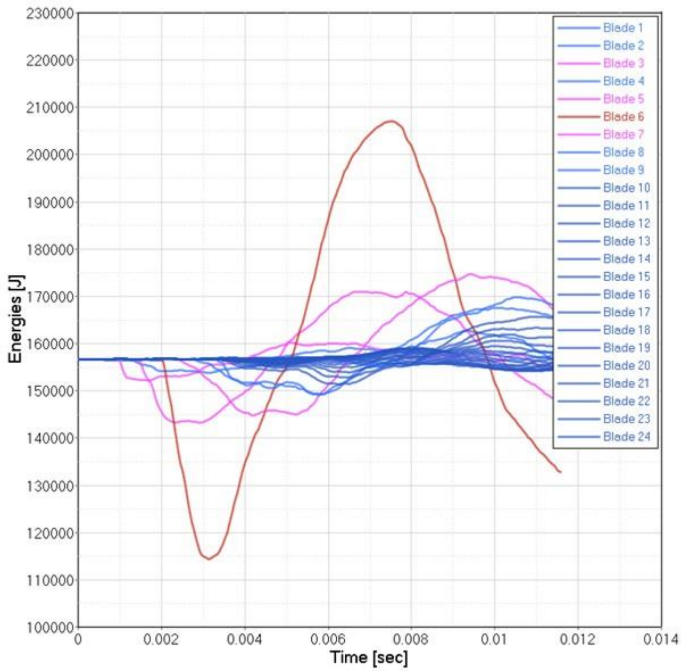

(a) kinetic energy

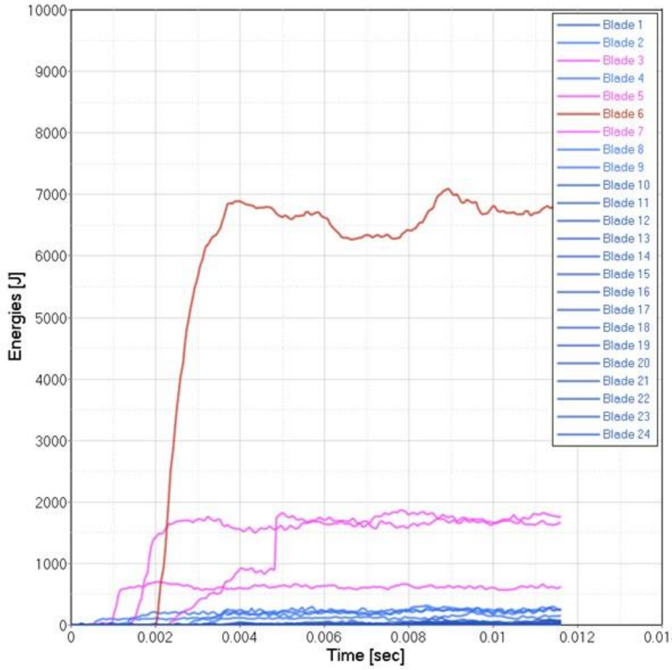

(b) internal energy

Figure 157. Energies in individual fan blades during UAS ingestion simulation HFS_HRV_HRS_90Y.

4.4.15 Simulation HFS_HRV_HRS_180R

This case corresponded to a UAS ingestion with a high fan speed, high relative translational velocity, high radial span location, and the 180 degree roll orientation (see Figure 39). The kinematics of the ingestion are shown in Figure 158. In all of the high fan speed simulations, the fan was simulated for a full fan rotation, about 11.6 ms. The UAS parts were also deleted in these cases once they had cleared the fan region, in this case at approximately 7 ms, to improve the computational efficiency of the simulation. It should also be noted that in this case there was element distortion in a few elements of the UAS post impact with the fan. These elements caused a significant increase in the computational time by reducing the time increment in the simulation. Therefore, the UAS part corresponding to the distorted element was deleted prior to the other parts of the UAS in this simulation.

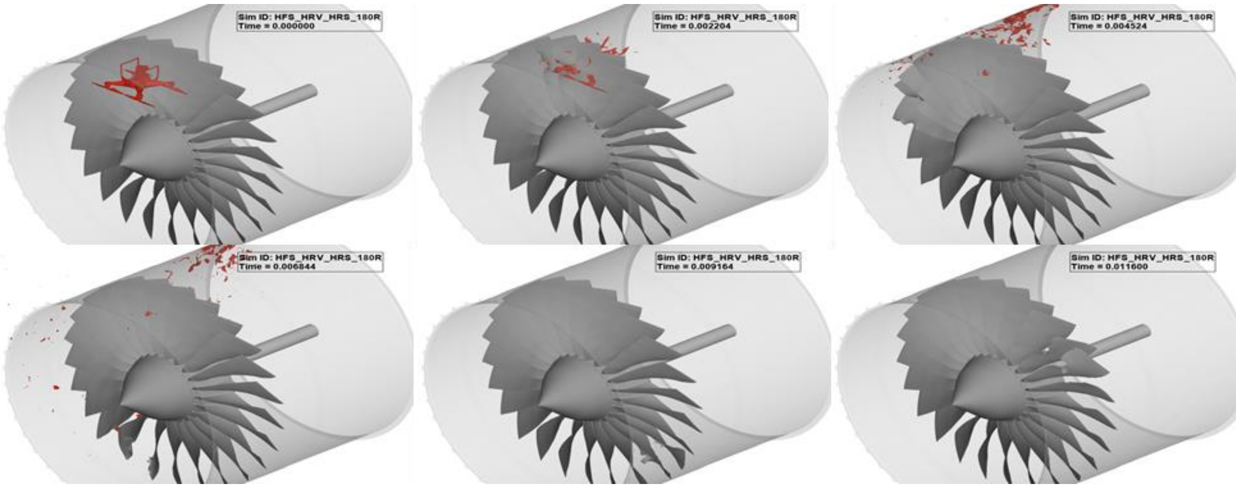

(a) isometric view

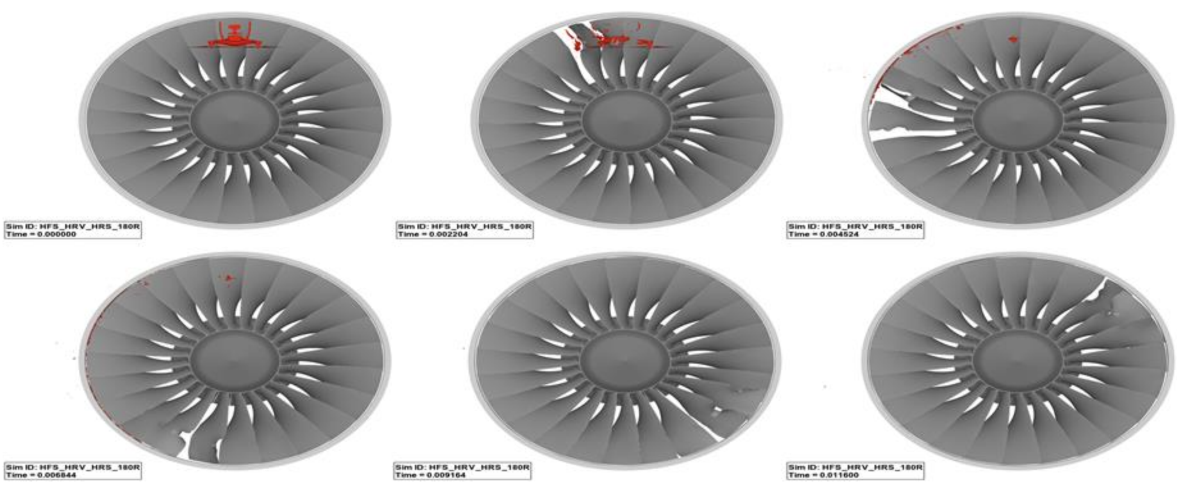

(b) front view

Figure 158. Kinematics of UAS ingestion simulation HFS_HRV_HRS_180R.

The effective plastic strain in the fan at the end of one fan rotation is shown in Figure 159 (front and rear views).

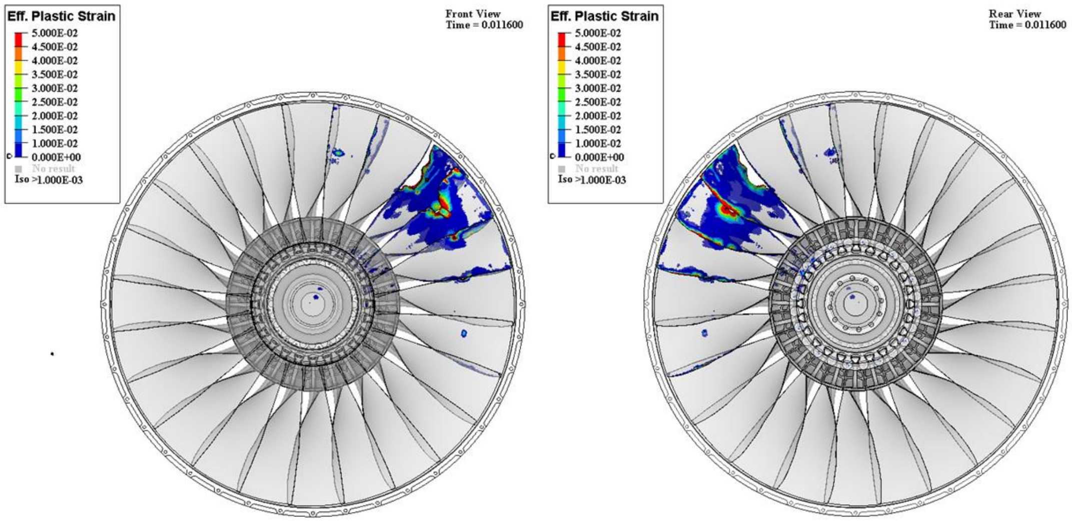

Figure 159. Effective plastic strain after UAS ingestion simulation HFS_HRV_HRS_180R.

Each blade's radial center of mass pre- and post-ingestion are shown in Figure 160. The damage level *D* (defined in Section 4.2) in the damaged area of the fan model after the UAS ingestion is also shown. The damage clearly shows significant material loss on leading edge of two blades, but the imbalance would be less than that of a loss of a full blade, which corresponds to damage severity level 3.

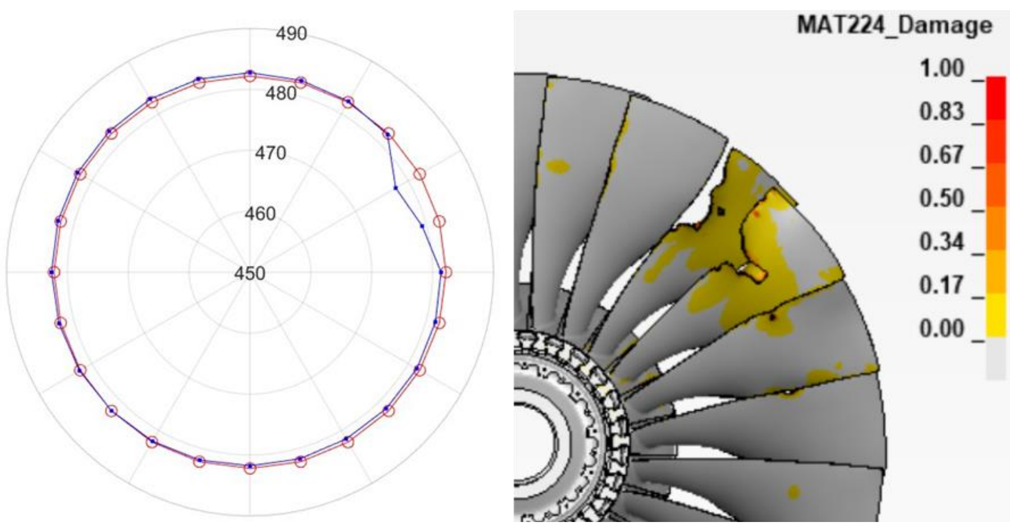

Figure 160. Center of mass of blades and fan model damage after UAS ingestion simulation HFS_HRV_HRS_180R.

The resultant moments and forces in a sectional plane (see Figure 40) during the ingestion are shown in Figure 161. Note that the damaged airfoil has a significantly larger oscillation in the forcing and moment than the undamaged blade.

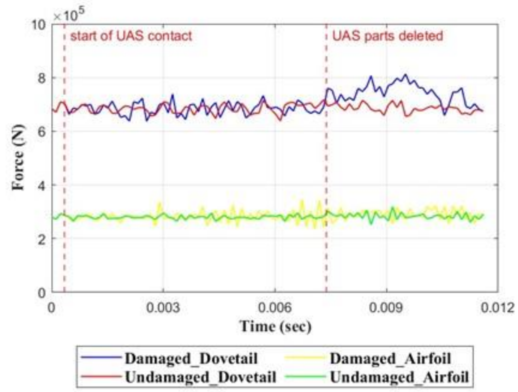

(a) forces

(b) moments about the y- and z-axes

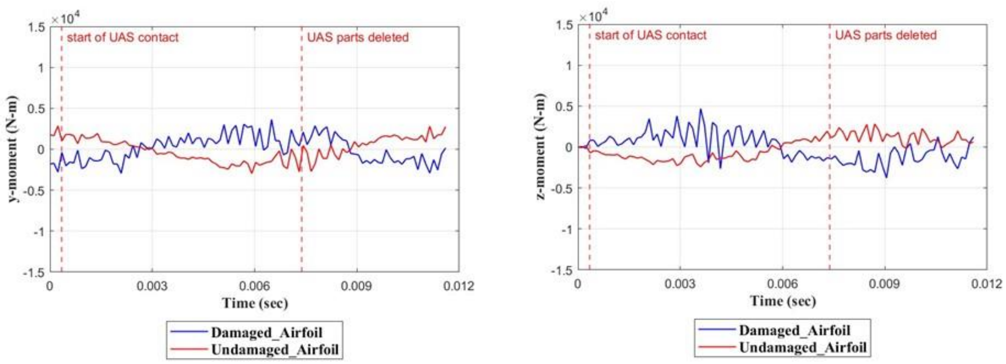

Figure 161. Resultant (a) forces and (b) moments in a sectional plane of the airfoil and dovetail during UAS ingestion simulation HFS_HRV_HRS_180R.

Figure 162(a) shows the overall energy ratio in the system, not including the eroded energy. Note that there is a drop in the energy ratio term because of the erosion of elements in the UAS and fan during the ingestion and then a sudden drop when the UAS is deleted after it clears the fan stage to speed up the calculation. Figure 162(b) shows the overall energy in the system. The bulk of the energy in the system is the kinetic energy in the fan and the UAS. The reason why the total energy in the system increases is because of the external work of the driven shaft. There is some internal energy in the system that will be shown in the breakout of the UAS and fan energies.

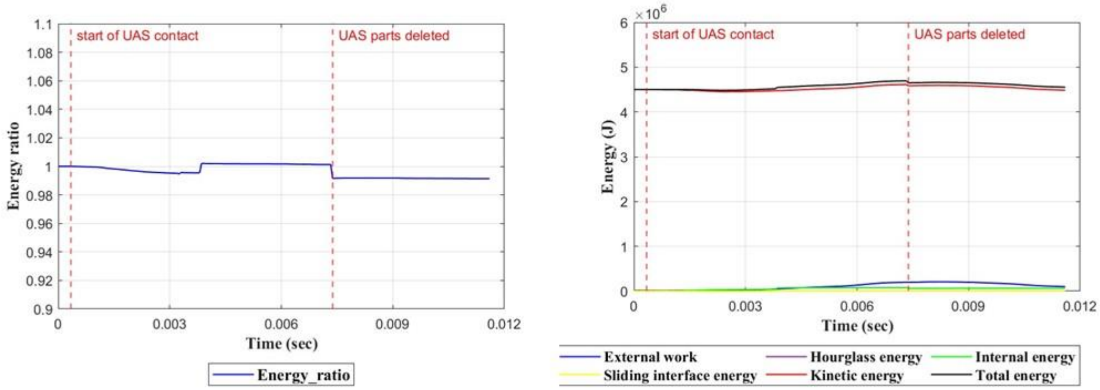

(a) energy ratio (b) energy in system

Figure 162. Overall energy in the system for HFS_HRV_HRS_180R.

Figure 163 shows the internal and kinetic energy in the UAS during the ingestion up until it is deleted from the simulation. Note that, as contact is made, both the internal and kinetic energy of the UAS increases. The increase in the internal energy is due to the plastic deformation and failure of UAS components. The increase in the kinetic energy is due to the fact that the fan is rotating at a high speed and accelerates many UAS parts as they are swept outward radially by the fan. The kinetic energy eventually levels off and decreases as UAS parts impact the stationary casing. The velocities of the motors, camera, and battery during the impact are all shown in Figure 164 and agree with this assessment. The different color lines for the velocities of each motor correspond to the motor colors in Figure 39.

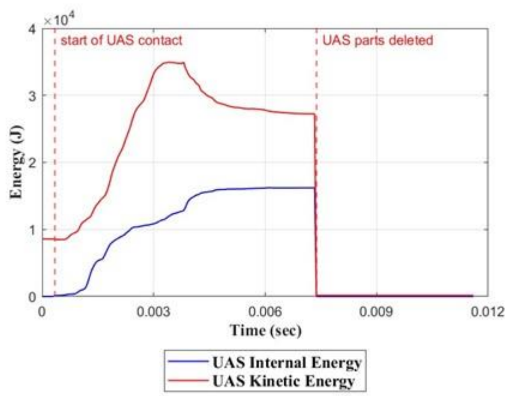

Figure 163. Internal and kinetic energies of the UAS for HFS_HRV_HRS_180R.

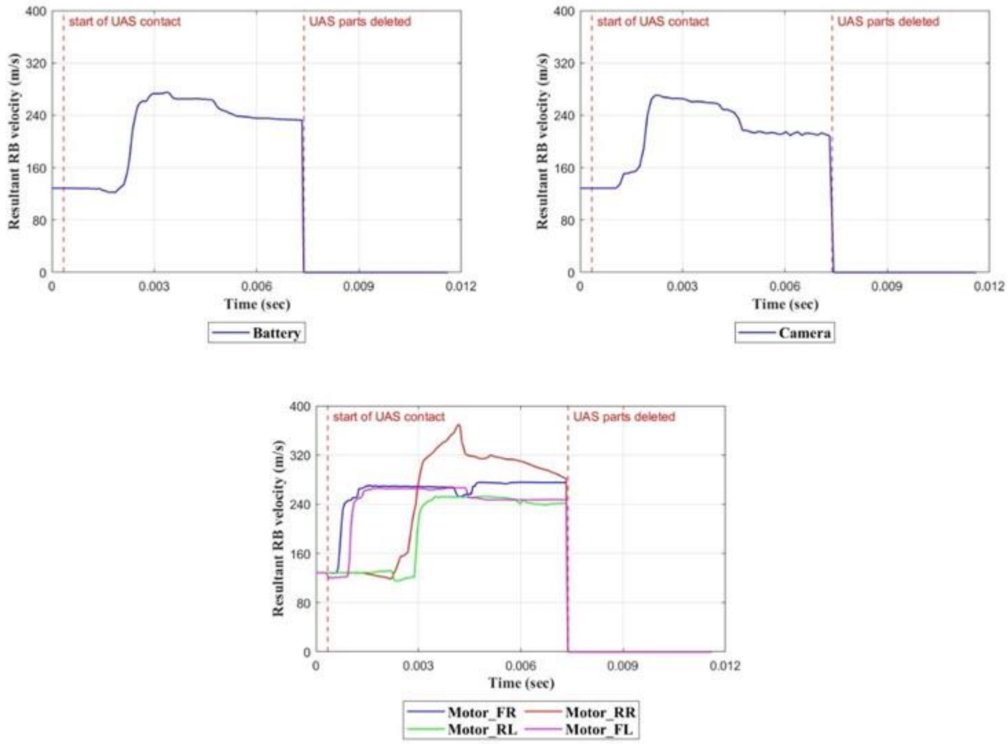

Figure 164. Resultant velocities of UAS components for HFS_HRV_HRS_180R.

The kinetic and internal energy of the fan are shown in Figure 165. Note that the kinetic energy of the fan looks very similar to the overall energy in the system from Figure 162, since the bulk of the energy is in the fan. There is also significant damage in the fan through the internal energy that increases while the fan is impacting the UAS.

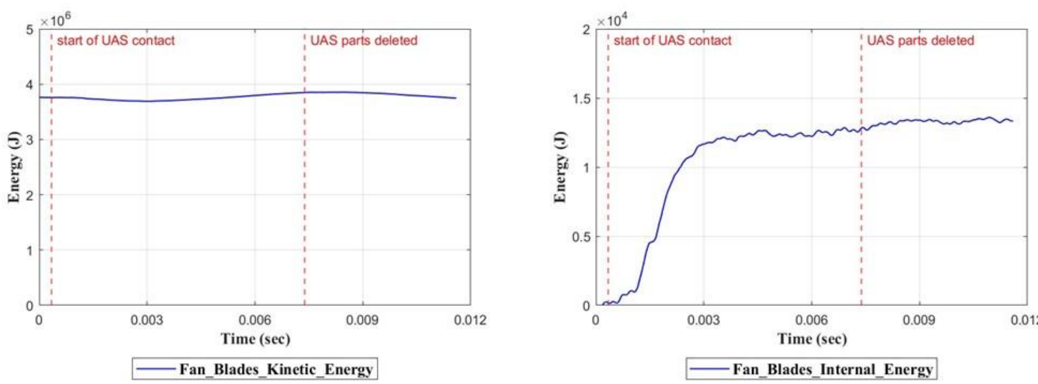

Figure 165. Energy in the fan blades during HFS_HRV_HRS_180R.

Finally, the breakdown of the energy in each blade starting with the top vertical blade as number 1 and counting upwards clockwise from there can be seen in Figure 166. Depending on the relative

translational speed of the UAS and rotational speed of the fan, one of the first few blades will be the first one to contact the UAS. In this case, mainly blades 2 through 7 made contact with the UAS during the ingestion. The blades with the largest variation in kinetic energy due to their deflection during impact tend to have the largest internal energy as well. In this case, blades 4 and 5 have the largest oscillation in kinetic energy and increase in internal energy, followed by blades 2-3 and 6-7.

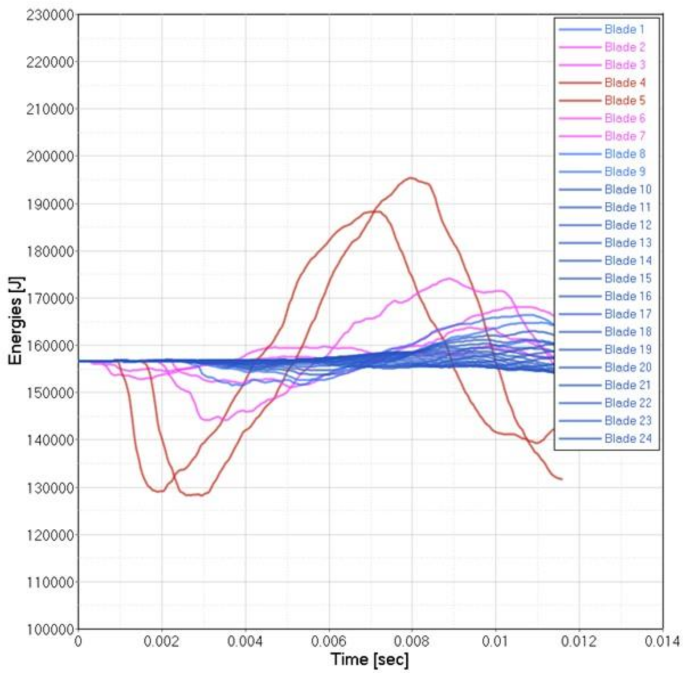

(a) kinetic energy

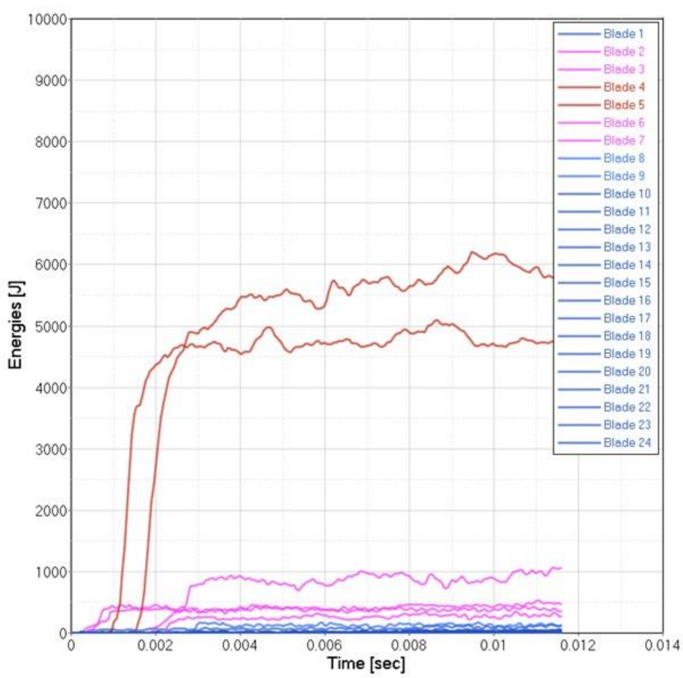

(b) internal energy

Figure 166. Energies in individual fan blades during UAS ingestion simulation HFS_HRV_HRS_180R.

4.4.16 Simulation HFS_HRV_LRS_Nom

This case corresponded to a UAS ingestion with a high fan speed, high relative translational velocity, low radial span location, and the nominal orientation (see Figure 39). The kinematics of the ingestion are shown in Figure 167. In all of the high fan speed simulations, the fan was simulated for a full fan rotation, about 11.6 ms. The UAS parts were also deleted in these cases once they had cleared the fan region, in this case at approximately 8 ms, to improve the computational efficiency of the simulation.

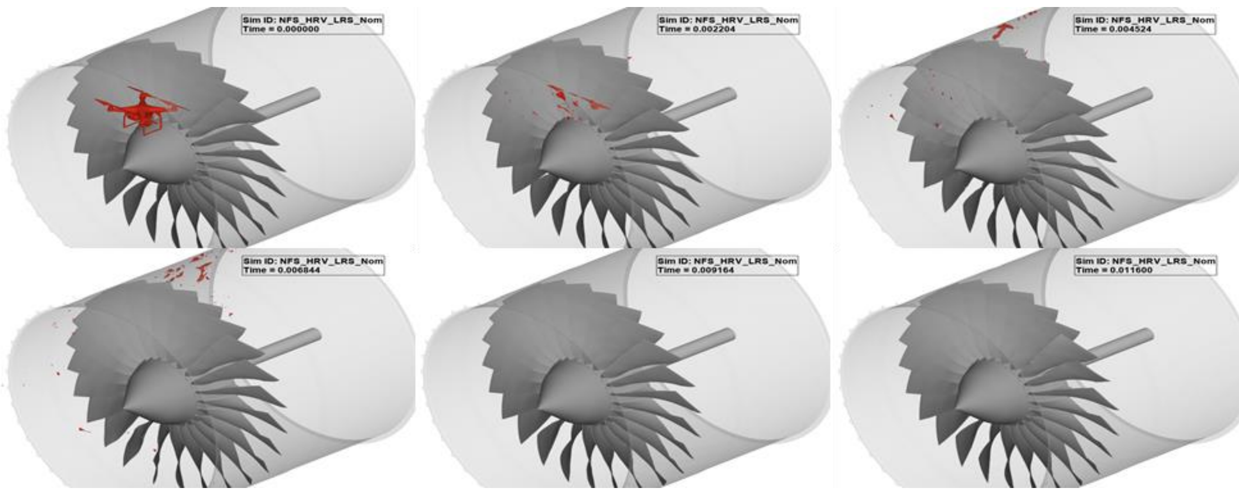

(a) isometric view

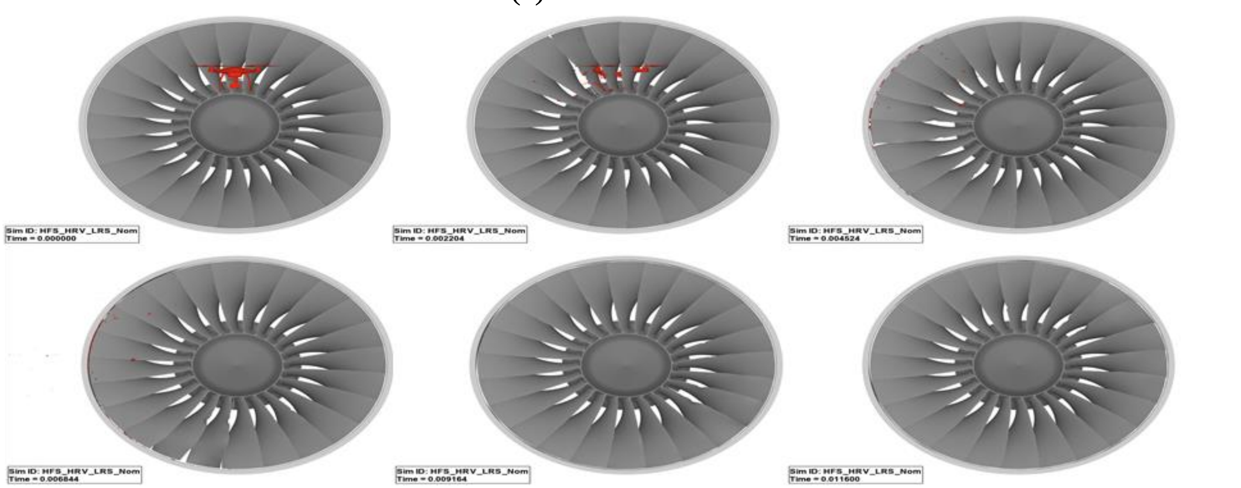

(b) front view

Figure 167. Kinematics of UAS ingestion simulation HFS_HRV_LRS_Nom.

The effective plastic strain in the fan at the end of one fan rotation is shown in Figure 168 (front and rear views).

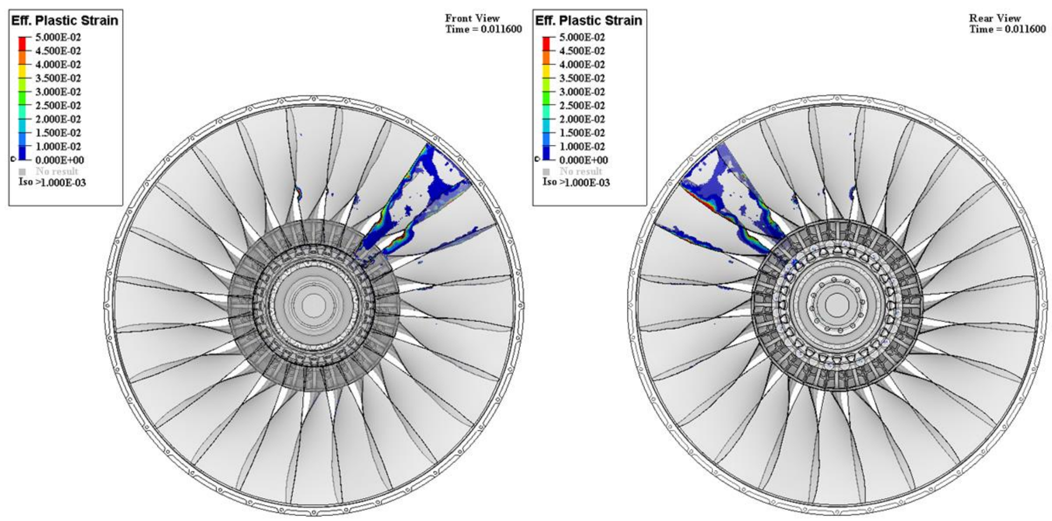

Figure 168. Effective plastic strain after UAS ingestion simulation HFS_HRV_LRS_Nom.

Each blade's radial center of mass pre- and post-ingestion are shown in Figure 169. The damage level *D* (defined in Section 4.2) in the damaged area of the fan model after the UAS ingestion is also shown. The damage clearly shows some material loss on leading edge of multiple blades and plastic deformation, which corresponds to damage severity level 2.

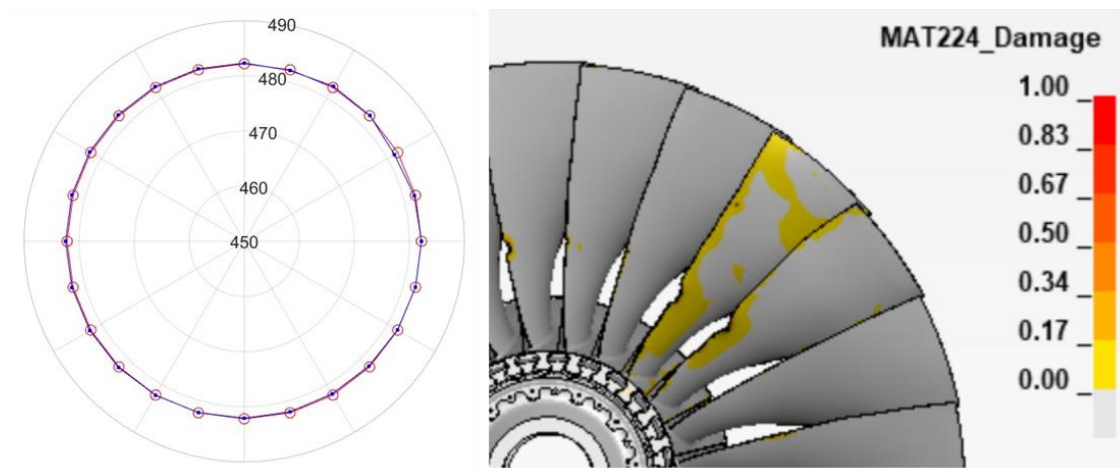

Figure 169. Center of mass of blades and fan model damage after UAS ingestion simulation HFS_HRV_LRS_Nom.

The resultant moments and forces in a sectional plane (see Figure 40) during the ingestion are shown in Figure 170. Note that the damaged airfoil has a significantly larger oscillation in the forcing and moment than the undamaged blade.

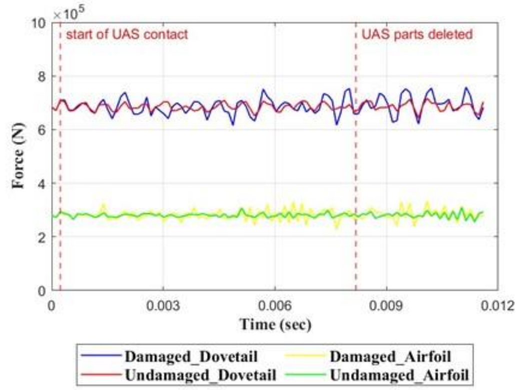

(a) forces

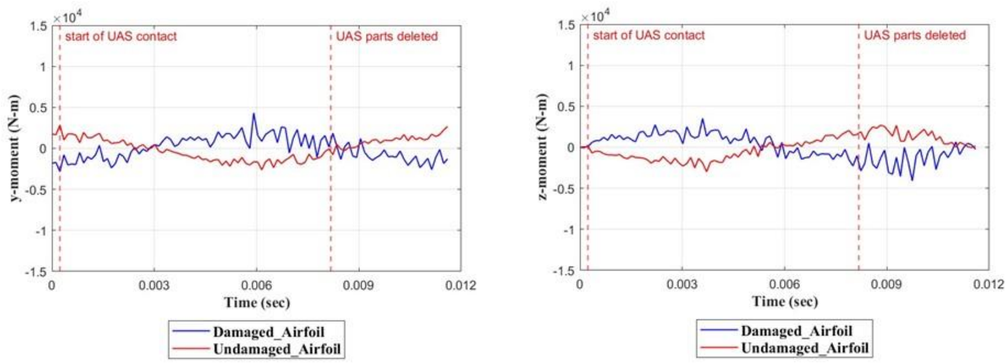

(b) moments about the y- and z-axes

Figure 170. Resultant (a) forces and (b) moments in a sectional plane of the airfoil and dovetail during UAS ingestion simulation HFS_HRV_LRS_Nom .

Figure 171(a) shows the overall energy ratio in the system, not including the eroded energy. Note that there is a drop in the energy ratio term because of the erosion of elements in the UAS and fan during the ingestion and then a sudden drop when the UAS is deleted after it clears the fan stage to speed up the calculation. Figure 171(b) shows the overall energy in the system. The bulk of the energy in the system is the kinetic energy in the fan and the UAS. The reason why the total energy in the system increases is because of the external work of the driven shaft. There is some internal energy in the system that will be shown in the breakout of the UAS and fan energies.

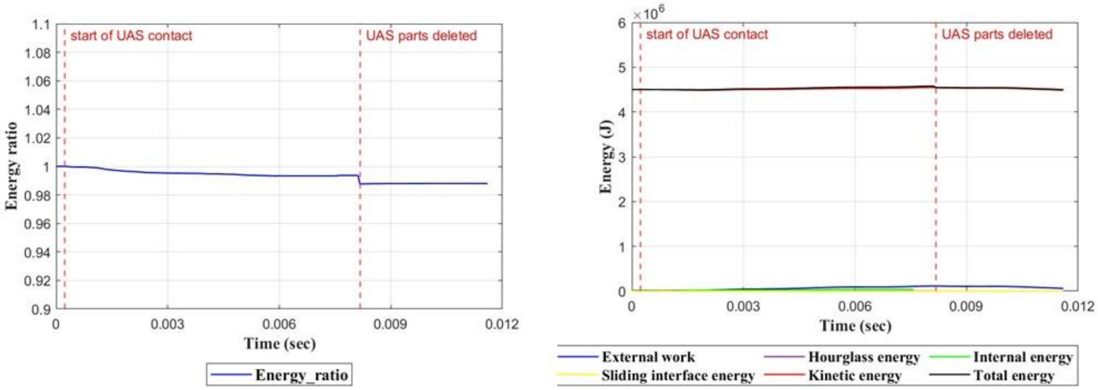

(a) energy ratio (b) energy in system

Figure 171. Overall energy in the system for HFS_HRV_LRS_Nom.

Figure 172 shows the internal and kinetic energy in the UAS during the ingestion up until it is deleted from the simulation. Note that, as contact is made, both the internal and kinetic energy of the UAS increases. The increase in the internal energy is due to the plastic deformation and failure of UAS components. The increase in the kinetic energy is due to the fact that the fan is rotating at a high speed and accelerates many UAS parts as they are swept outward radially by the fan. The kinetic energy eventually levels off and decreases as UAS parts impact the stationary casing. The velocities of the motors, camera, and battery during the impact are all shown in Figure 173 and agree with this assessment. The different color lines for the velocities of each motor correspond to the motor colors in Figure 39.

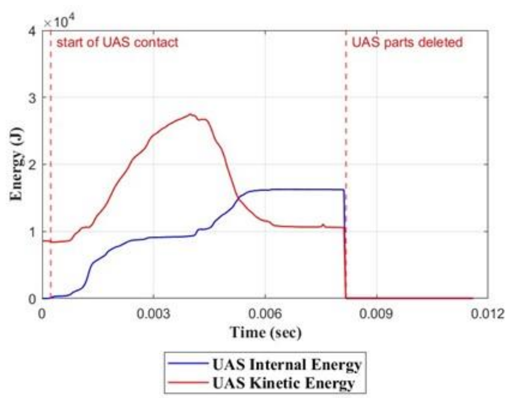

Figure 172. Internal and kinetic energies of the UAS for HFS_HRV_LRS_Nom.

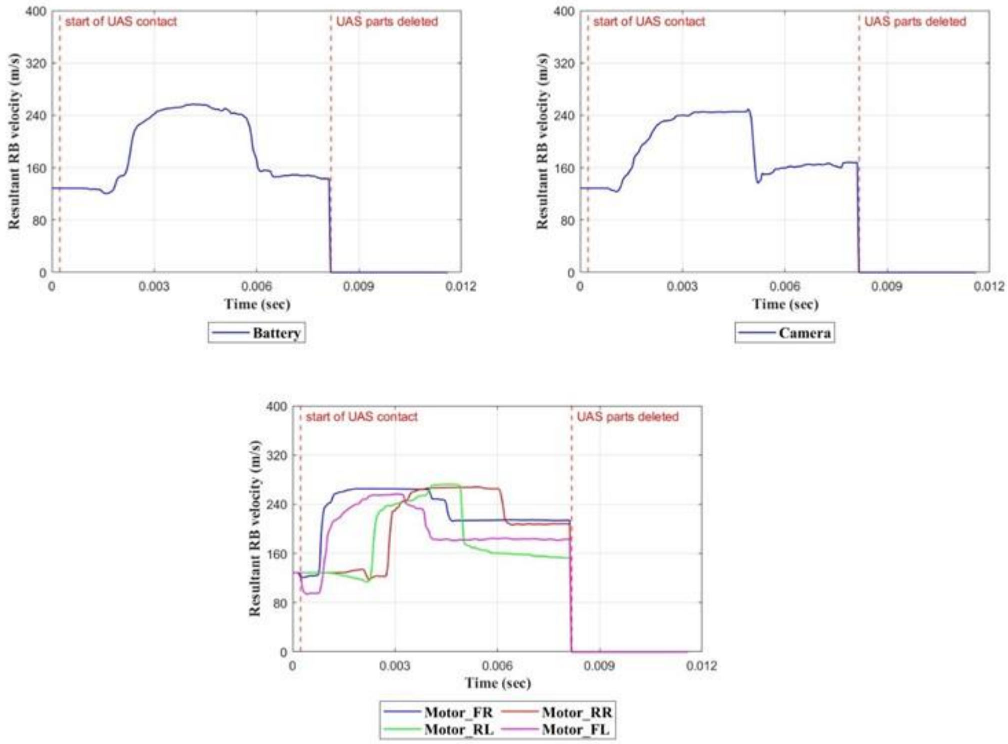

Figure 173. Resultant velocities of UAS components for HFS_HRV_LRS_Nom.

The kinetic and internal energy of the fan are shown in Figure 174. Note that the kinetic energy of the fan looks very similar to the overall energy in the system from Figure 171, since the bulk of the energy is in the fan. There is also significant damage in the fan through the internal energy that increases while the fan is impacting the UAS.

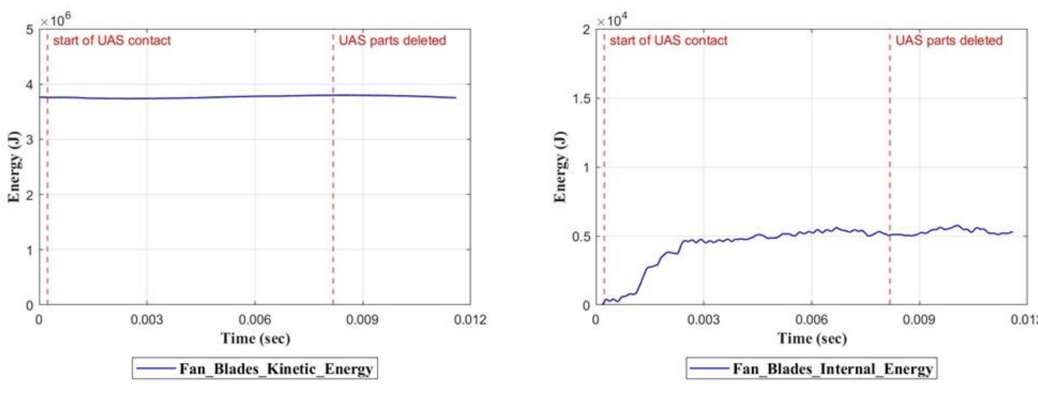

Figure 174. Energy in the fan blades during HFS_HRV_LRS_Nom.

Finally, the breakdown of the energy in each blade starting with the top vertical blade as number 1 and counting upwards clockwise from there can be seen in Figure 175. Depending on the relative

translational speed of the UAS and rotational speed of the fan, one of the first few blades will be the first one to contact the UAS. In this case, mainly blades 1 through 7 made contact with the UAS during the ingestion. The blades with the largest variation in kinetic energy due to their deflection during impact tend to have the largest internal energy as well. In this case blade 4 has the largest oscillation in kinetic energy and increase in internal energy, followed by blade 5, and then blades 1-3 and 6-7.

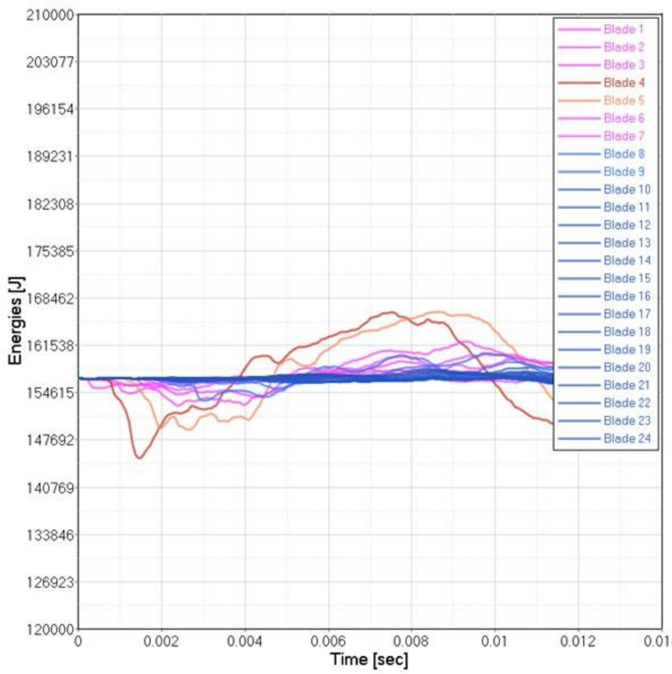

(a) kinetic energy

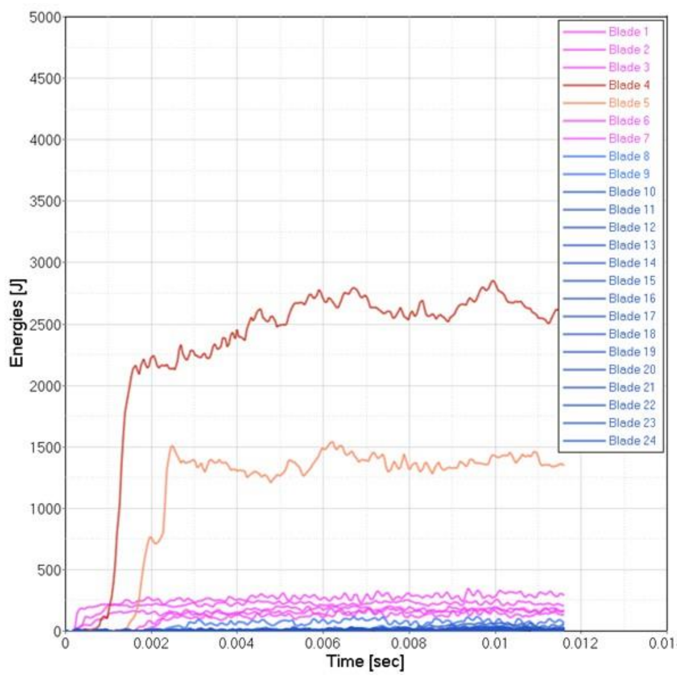

(b) internal energy
Figure 175. Energies in individual fan blades during UAS ingestion simulation HFS_HRV_LRS_Nom.

4.5 SUMMARY OF SENSITIVITY STUDY RESULTS

In this section, each of the cases from the sensitivity study are compared based on their overall damage in the fan, imbalance loads, forces on retention systems, and energy imparted to the casing and then the severity evaluation is given for each case.

The overall damage in the fan, D_{fan}, defined in Eq. (10), for each of the cases is summarized in

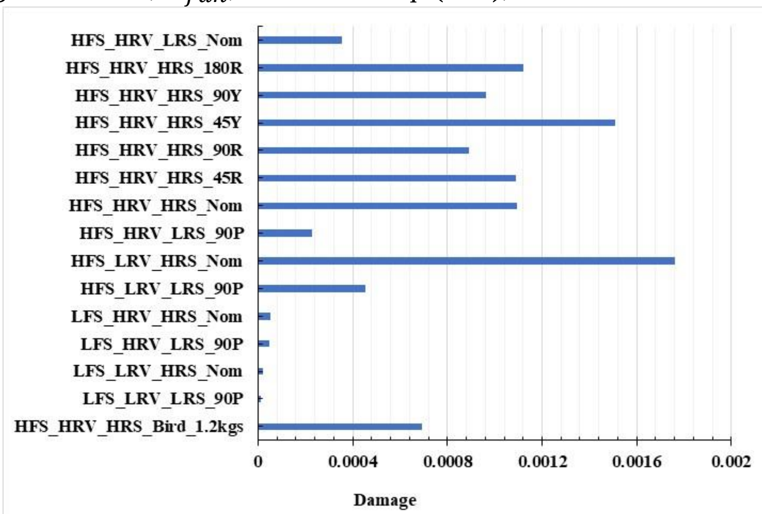

(b) D_{fan} for all cases except FBO

Figure 176. Note that the blade-out simulation has an overall damage of approximately 0.045. This is to be expected, since it includes the loss of a full blade and platform (1/24 = 0.0417) and the plastic deformation of the adjacent blades that come into contact with it.

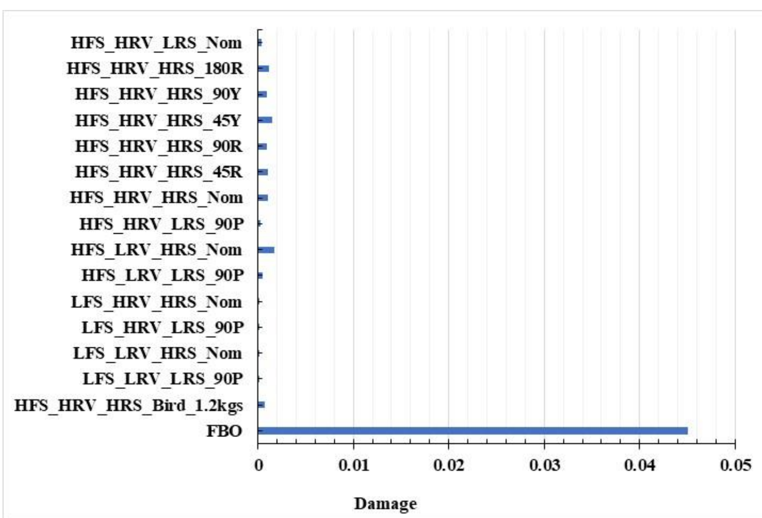

(a) D_{fan} for all cases

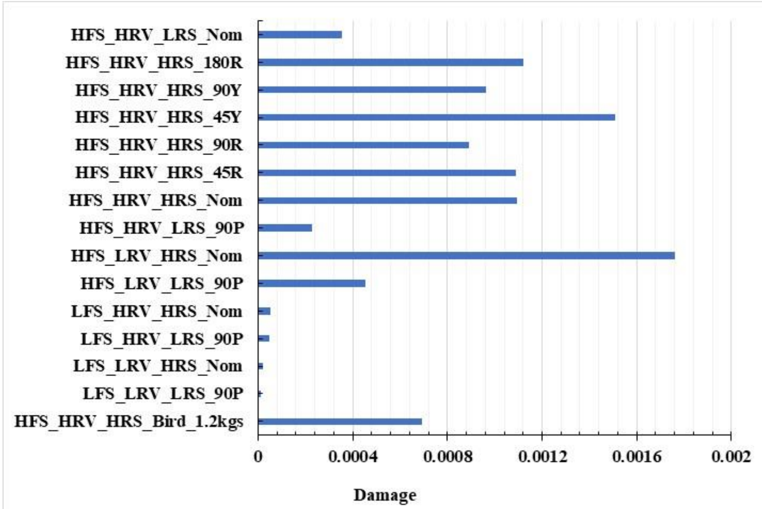

(b) D_{fan} for all cases except FBO

Figure 176. Comparison of damage levels for each of the cases.

First, it should be noted that the high fan speed case consistently has significantly more damage than the low fan speed. High fan speed cases having more damage than low fan speed cases is expected since the impacts happen at a much higher speed imparting more energy into the UAS and fan blades. Second, the higher radial span impact causes significantly more damage than the lower radial span impact since at the higher radial span, the relative velocity between the UAS and fan blades is much higher. Third, the case that causes the most damage to the fan is the lower translational relative velocity case, HFS_LRV_HRS_Nom. This is because the additional energy from the translational velocity of the UAS is less significant compared to the high fan speed and high span location conditions. With a lower translational velocity, the UAS not pass through the fan quickly, leading to more blades impacting the UAS and being damaged. At low fan speeds, the relative translational velocity is more significant. Considering the lower fan speed and high radial impact location conditions, the high translational relative velocity case (i.e., LFS_HRV_HRS_Nom) does more damage to the fan than the lower translational relative velocity case (i.e., LFS_LRV_HRS_Nom). Finally, when comparing the orientations of the UAS, the 45 degree yaw orientation caused the most damage by a significant margin for the HFS_HRV_HRS condition.

The loads acting on the shaft due to the impact and imbalance over time is shown in Figure 177. A node set is defined at the rear of the disk to apply the axial boundary and disk rotation conditions. The resultant total force in different simulations is obtained using this node set through BNDOUT file output. The fan-blade out case clearly leads to a much larger imbalance compared to the other cases investigated in the sensitivity study.

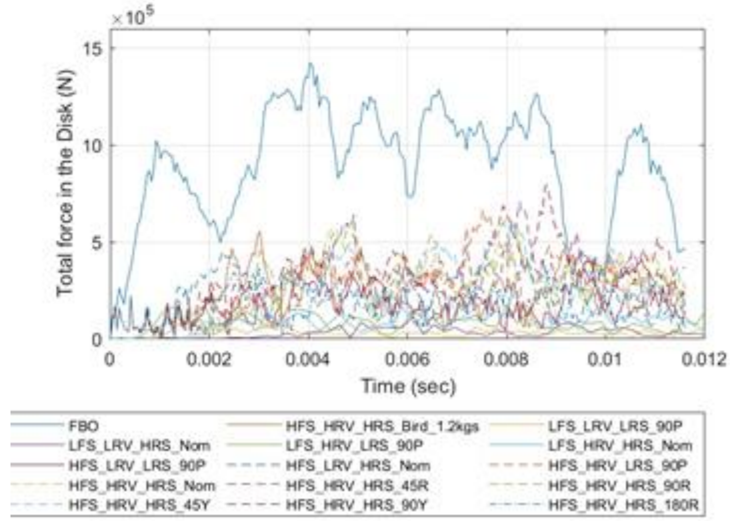

Figure 177. Forces acting from the disk on to the shaft due to the impact and imbalance loads.

The corresponding average and peak loads acting on the shaft are given in Figure 178. This similarly highlights that the fan blade-out leads to higher imbalance loads compared to any of the other presented UAS ingestion simulations. It should be noted that most of the high fan speed and high radial impact cases (UAS and bird) yield a similar average loading on the shaft, with slightly more variation in peak loading. It should also be noted that the imbalance does not directly correlate with the damage level in the fan (e.g., the bird ingestion has a fairly low damage level, but a relatively large imbalance due to the plastic deformation in some blades).

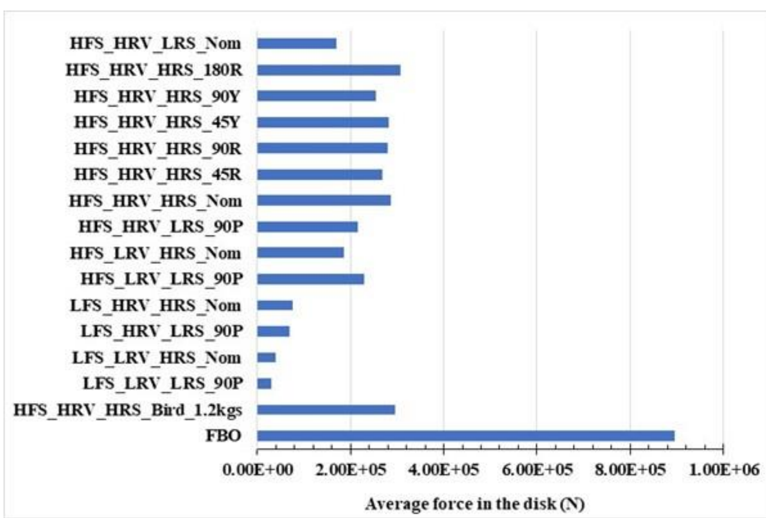

(a) average force

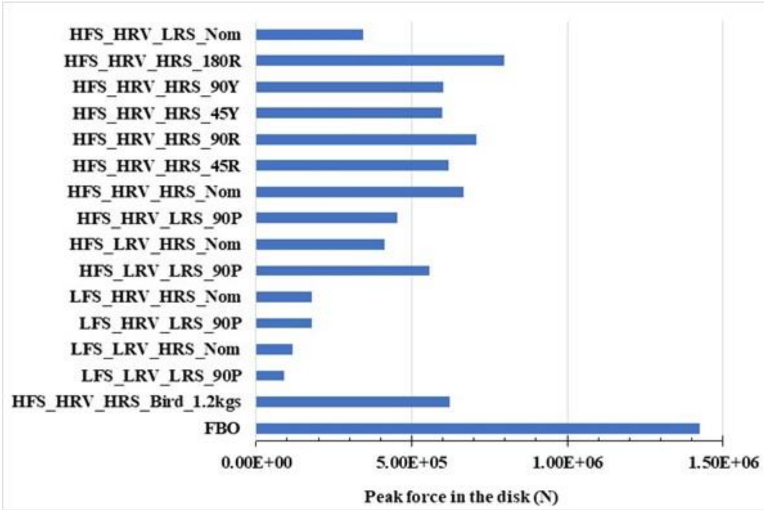

(b) peak force

Figure 178. Force acting from the disk onto the shaft.

The resultant forces on the retainer and retention ring over time are shown in Figure 179. Moreover, the average and peak loads on the retainer and retention ring are shown in Figure 180 and Figure 181, respectively. The fan blade-out case leads to a larger load on the retainer and the retention ring compared to the other ingestion simulations. The bird ingestion simulation has a similar load as the UAS for the high fan speed, high translational relative velocity, and outer radial impact cases.

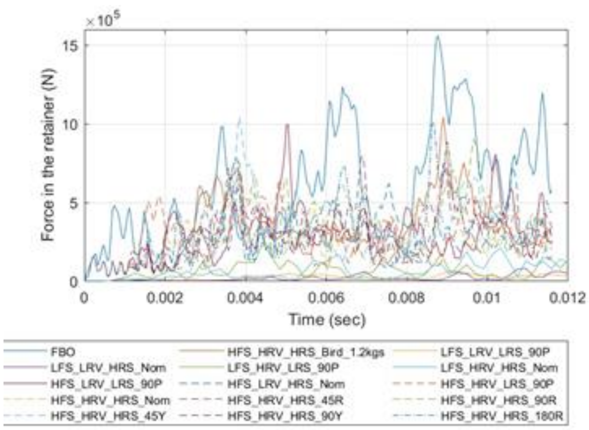

(a) retainer

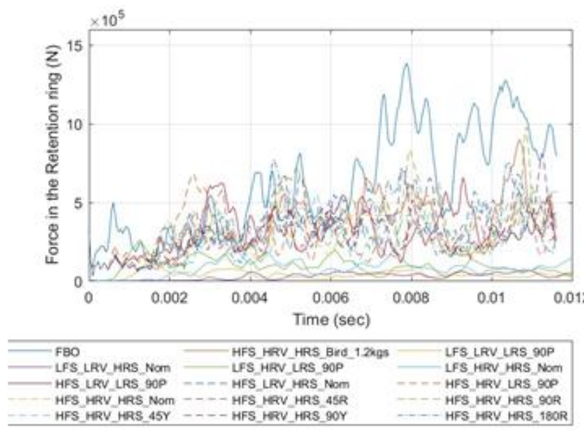

(b) retention ring

Figure 179. Resultant forces on the retainer and retention ring over time.

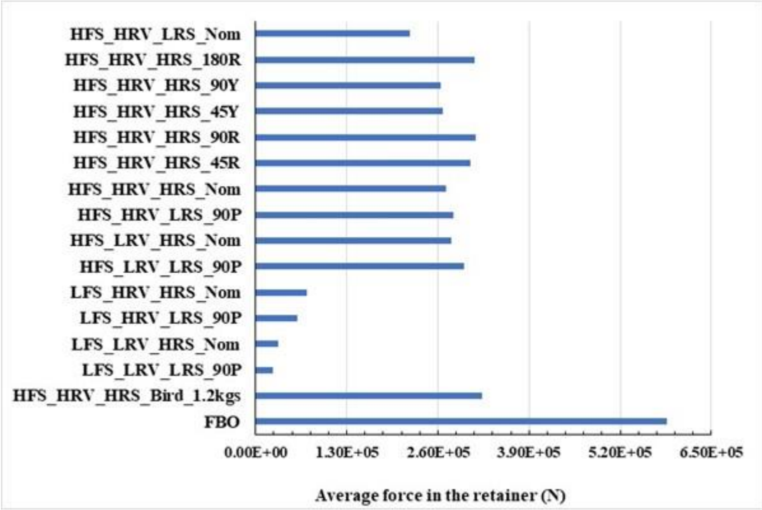

(a) average force

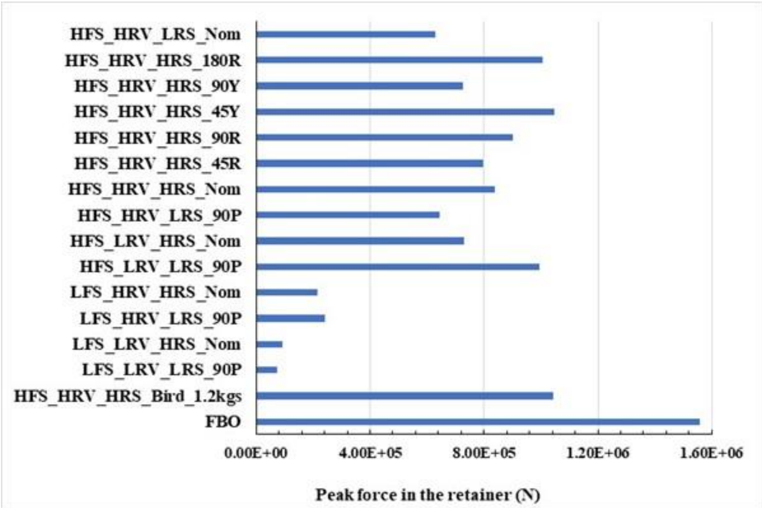

(b) peak force

Figure 180. Force acting on retainer.

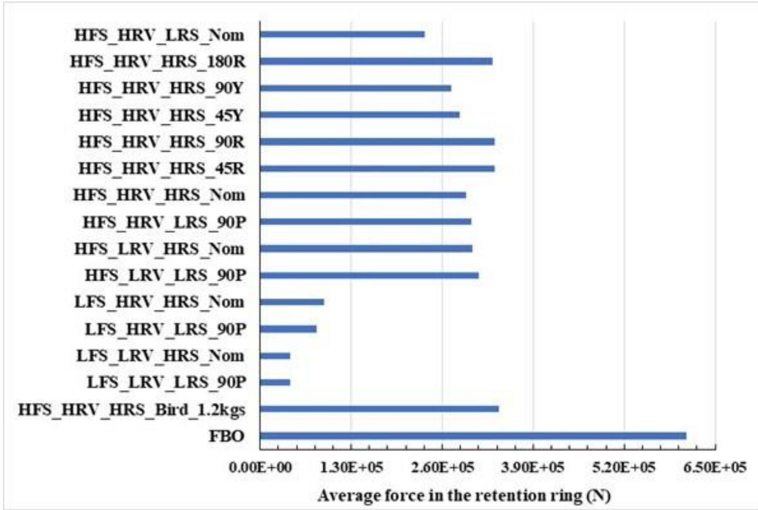

(a) average force

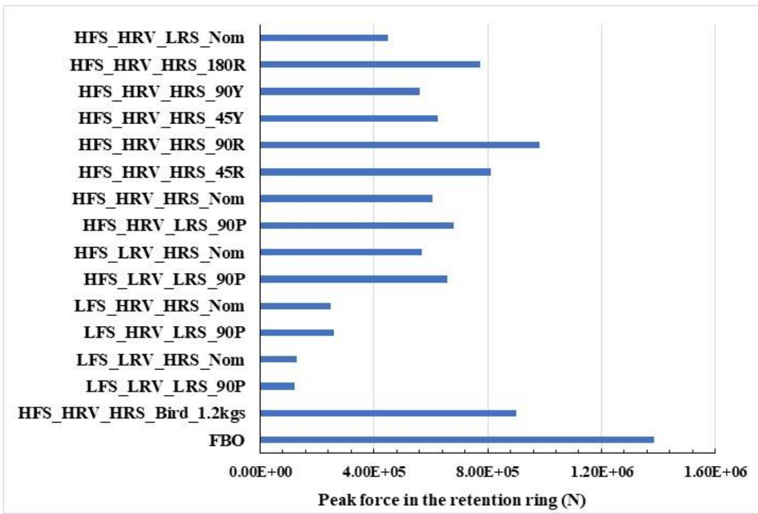

(b) peak force

Figure 181. Force acting on retention ring.

The average energy imparted to the casing is shown in Figure 182. From these results, the energy imparted onto the casing is much lower for the ingestion cases than the fan blade-out case. It should be noted that no analysis was conducted to extrapolate the damage and material loss predicted by the end of the simulation. The kinetic and internal energies in the casing have very similar values for most of the cases, which has been previously reported[22].

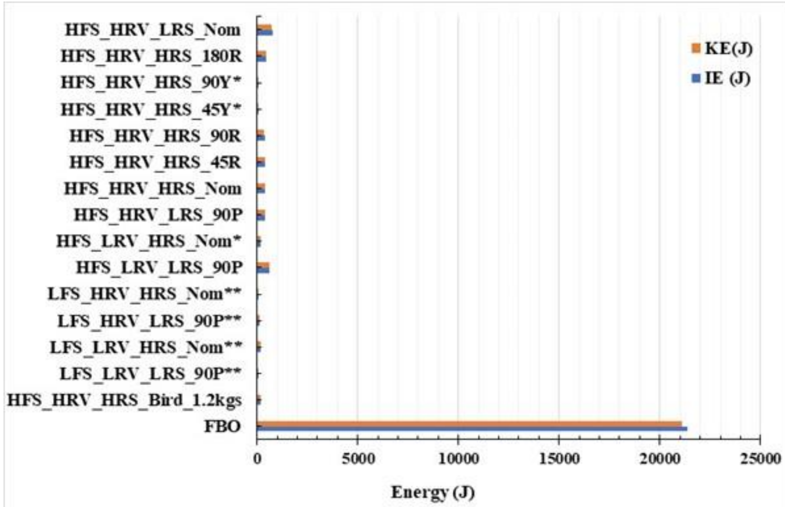

(a) all simulations

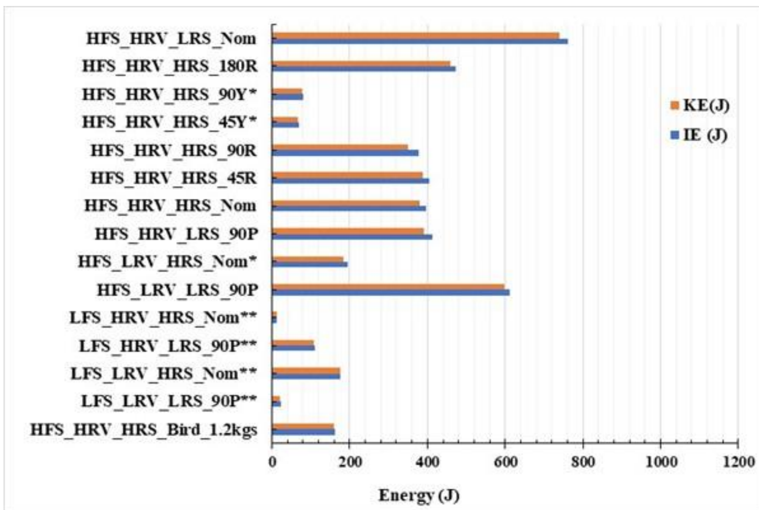

(b) all simulations except FBO

Figure 182. Average energy imparted to casing (* indicates that the UAS parts are deleted as they moved away from the fan model and prior to many parts hitting the casing, ** indicates simulations at different time scales, since low fan speed simulations are conducted for half fan rotation only).

A summary of each of the simulations and severity level evaluation from Table 5 is given in

Table 8. The largest forces in the disk and retention systems, and highest damage in the fan is from the FBO case. The comparison of the UAS ingestion cases with the FBO is presented since a full blade-out case is part of the current regulatory framework. Engine designs are certified to demonstrate safe containment and shutdown from an FBO event. The largest values for the ingestion cases are emphasized with bold, red font, and the second largest values are denoted by red font.

Table 8. Summary of sensitivity results and severity level evaluation.

Simulation ID	Average force in Disk (N)	Average force in retention ring (N)	Average force in retainer (N)	Damage in blade model	Severity level	Associated damage
FBO	**8.98E+05**	**6.10E+05**	**5.86E+05**	**0.04508**	Level 3	Significant material loss leading to an imbalance that is equal to a single blade loss and additional plastic deformation
HRS_HRV_HRS_ Bird_1.2kgs	2.95E+05	**3.41E+05**	**3.24E+05**	0.000692	Level 2	Cupping of leading edge of multiple blades
LFS_LRV_LRS_90P	3.09E+04	4.27E+04	2.53E+04	1.04E-05	Level 1	Small deformation of blades and no crack initiation
LFS_LRV_HRS_Nom	3.84E+04	4.32E+04	3.18E+04	2.27E-05	Level 1	Small deformation of blades and no crack initiation
LFS_HRV_LRS_90P	6.96E+04	8.03E+04	5.99E+04	4.75E-05	Level 1	Small deformation of blades and no crack initiation
LFS_HRV_HRS_Nom	7.65E+04	9.09E+04	7.28E+04	5.24E-05	Level 1	Small deformation of blades and no crack initiation
HFS_LRV_LRS_90P	2.31E+05	3.12E+05	2.97E+05	0.000452	Level 2	Material loss and deformation along leading of multiple blades
HFS_LRV_HRS_Nom	1.85E+05	3.04E+05	2.79E+05	**0.001763**	Level 3	Significant material loss on leading edge of multiple blades
HFS_HRV_LRS_90P	2.16E+05	3.02E+05	2.82E+05	0.000227	Level 1	Small deformation of blades and no crack initiation
HFS_HRV_HRS_Nom	2.87E+05	2.94E+05	2.72E+05	0.001096	Level 3	Significant material loss on leading edge of multiple blades
HFS_HRV_HRS_45R	2.69E+05	3.35E+05	3.06E+05	0.001091	Level 3	Significant material loss on leading edge of multiple blades
HFS_HRV_HRS_90R	2.80E+05	3.34E+05	3.14E+05	0.000892	Level 3	Significant material loss on leading edge of multiple blades
HFS_HRV_HRS_45Y	2.81E+05	2.85E+05	2.67E+05	0.001509	Level 3	Significant material loss on leading edge of multiple blades
HFS_HRV_HRS_90Y	2.54E+05	2.73E+05	2.64E+05	0.000961	Level 3	Significant material loss on leading edge of multiple blades

HFS_HRV_HRS_180R	**3.08E+05**	3.32E+05	3.13E+05	0.00112	Level 3	Significant material loss on leading edge of multiple blades
HFS_HRV_LRS_Nom	1.71E+05	2.34E+05	2.20E+05	0.000353	Level 2	Material loss and deformation along leading of multiple blades

It should be noted that LS-DYNA is not a crack propagation tool (it is capable of accurately predicting damage, but it is not capable of predicting any subsequent fracture mechanics growth), and significant damage in the leading edge of the blades in some cases could lead, in practice, to breaking-off of portions of such blades. The results being presented are focused on what is being providing by LS-DYNA and are not assessing the possibility of portions of the blades breaking off after the initial damage is initiated. So, in this way the results could be non-conservative since damage may progress due to crack propagation or aeromechanical effects, which could change the severity level evaluation of some cases.

Overall, the damage severity tracks closely with the D_{fan} parameter. The high fan speed case consistently has significantly more damage than the low fan speed cases, which is expected since the impacts happen at a much higher speed, therefore imparting more energy into the UAS and fan blades. The higher radial span impact cases cause significantly more damage than the lower radial span impact cases since, at the higher radial span, the relative velocity between the UAS and fan blades is much higher than at the lower radial span (which are at severity level 1 or 2). The high fan speed, high radial impact cases for the UAS ingestion are at severity level 3, as opposed to the bird of the same mass, which is at severity level 2. The case that causes the most damage to the fan is the lower translational relative velocity case (with high fan speed and high radial span location), which has been previously noted. Finally, in comparing the varying orientation cases, the 45 degree yaw orientation caused the most damage for the studied cases, which is focused on the HFS_HRV_HRS condition.

4.6 PHASE OF FLIGHT INGESTION STUDIES

Generally, there are three phases of flight where a manned aircraft is most likely to encounter a UAS: i) take-off; ii) flight below 3,048 m (10,000 ft); and iii) approach.

The take-off condition is a critical flight condition because the fan is rotating at full speed, which is the most important parameter regarding damage to the fan, as discussed in the sensitivity study. The outer radial span was another critical factor in understanding fan damage, leading to that location being of high interest for the following impact cases. Also, it was determined that for high fan speeds, the low relative translational velocity causes more damage to the fan than the high translational velocity because more of the hard components like the motors and camera tend to impact more blades. Finally, the orientation that caused the most damage in the sensitivity study was the 45 degree yaw orientation case. The critical takeoff case can be designated as HFS_LRV_HRS_45Y.

The flight below 3,048 m (10,000 ft) has the fan rotating at 70% speed (see Table 1), which is a Mid-level Fan Speed (MFS). The other options for this critical case will be chosen to match the take-off case. So the critical flight below 3,048 m case can be designated as MFS_LRV_HRS_45Y.

The approach case has the lowest fan speed. From the sensitivity study it was shown that the low fan speed resulted in minimal damage. Due to the long computational time of these low fan speed simulations and understanding that minimal damage would occur, no additional approach case was simulated.

4.6.1 Takeoff: HFS_LRV_HRS_45Y

This case corresponded to a UAS ingestion with a high fan speed, low relative translational velocity, high radial span location, and the 45 degree yaw orientation (see Figure 39). The kinematics of the ingestion are shown in Figure 183. The simulation is focused on understanding the damage in the fan and was therefore focused on the impact of the UAS and fan, and was terminated around 6 ms.

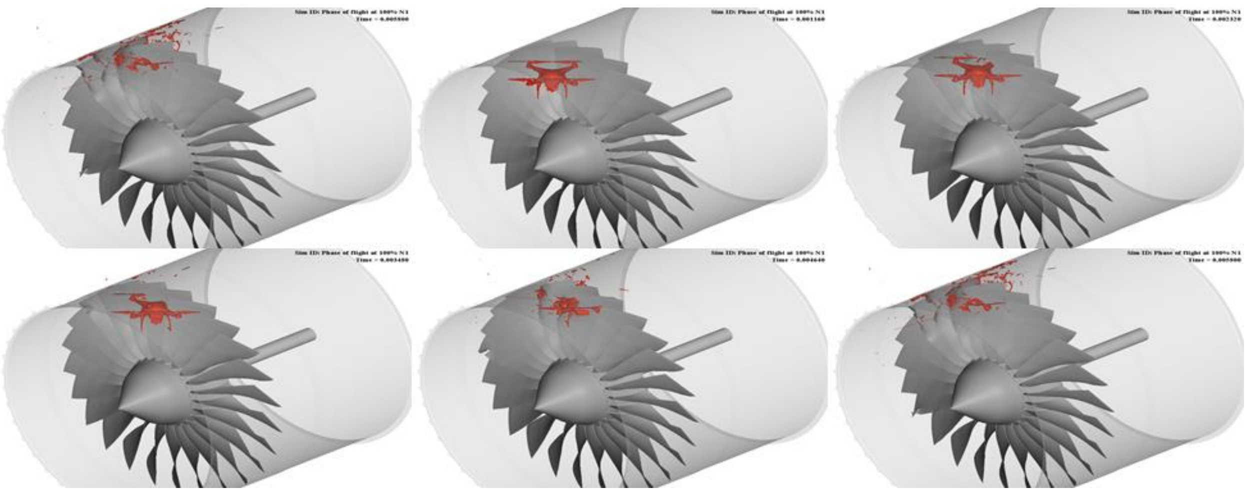

(a) isometric view

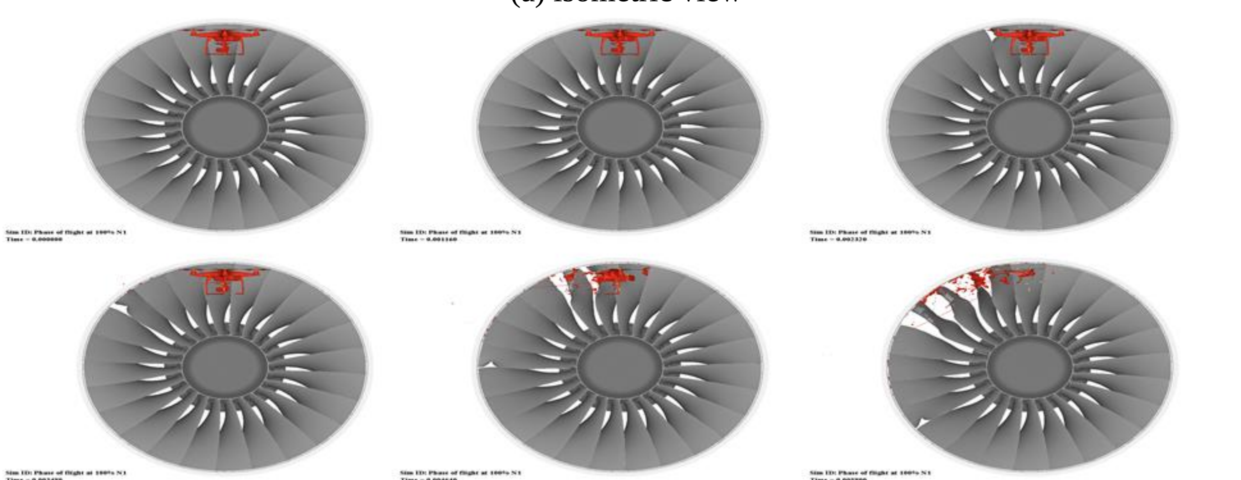

(b) front view

Figure 183. Kinematics of UAS ingestion simulation HFS_LRV_HRS_45Y.

The effective plastic strain in the fan at the end of the simulation is shown in Figure 184 (front and rear views).

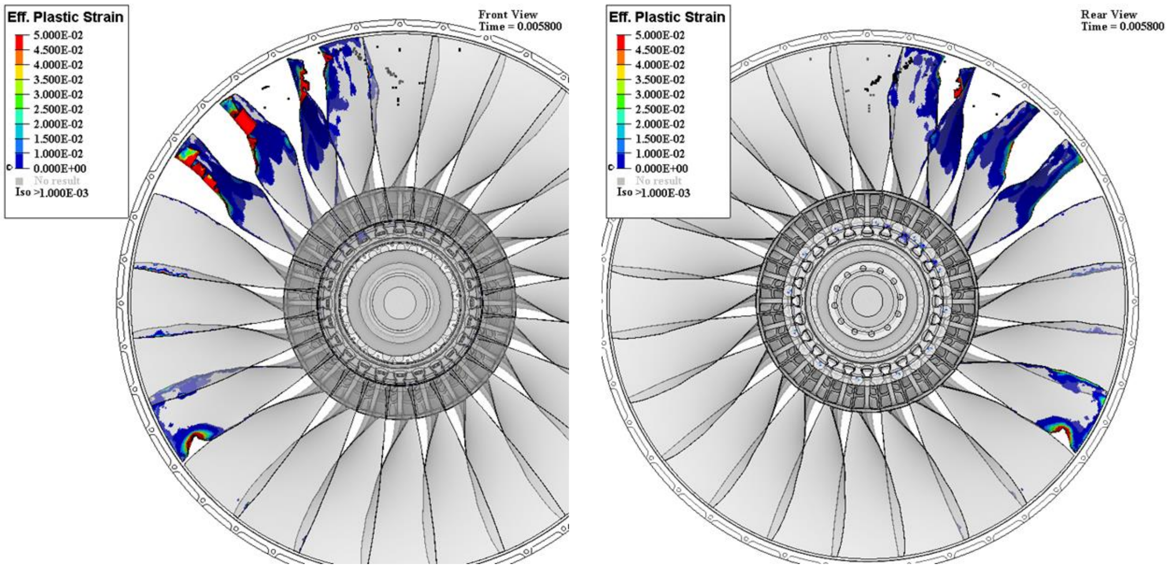

Figure 184. Effective plastic strain after UAS ingestion simulation HFS_LRV_HRS_45Y.

Each blade's radial center of mass pre- and post-ingestion are shown in Figure 185. The damage level *D* (defined in Section 4.2) in the damaged area of the fan model after the UAS ingestion is also shown. The damage clearly shows significant material loss on leading edge of two blades, which corresponds to damage severity level 3, since the imbalance would be less than that of a loss of a full blade.

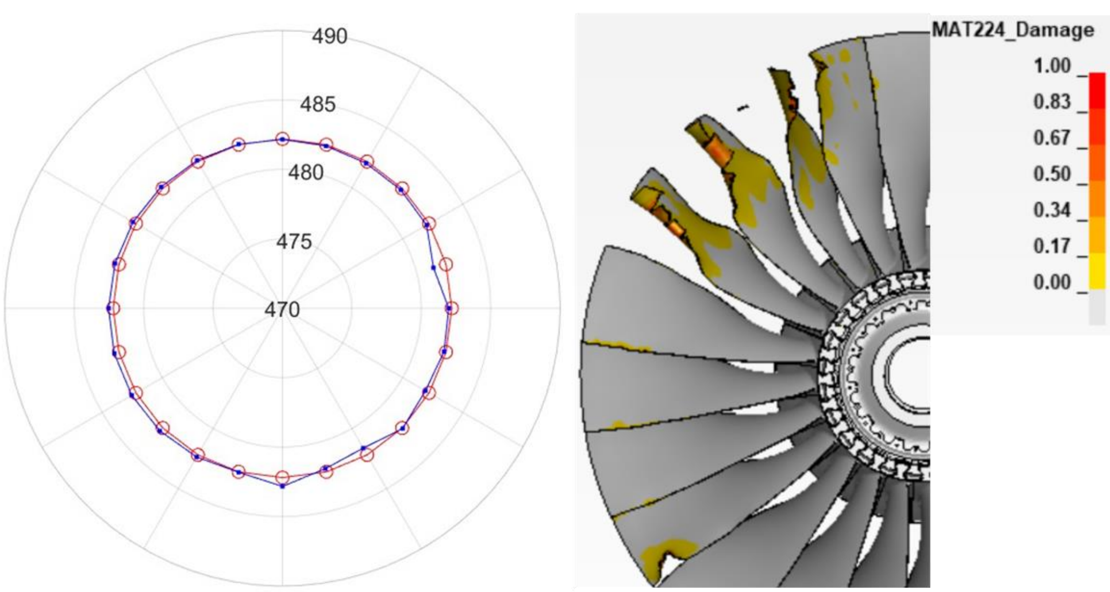

Figure 185. Center of mass of blades and fan model damage after UAS ingestion simulation HFS_LRV_HRS_45Y.

The resultant moments and forces in a sectional plane (see Figure 40) during the ingestion are shown in Figure 186. Note that the damaged airfoil does not have a significantly larger oscillation in the forcing and moment than the undamaged blade.

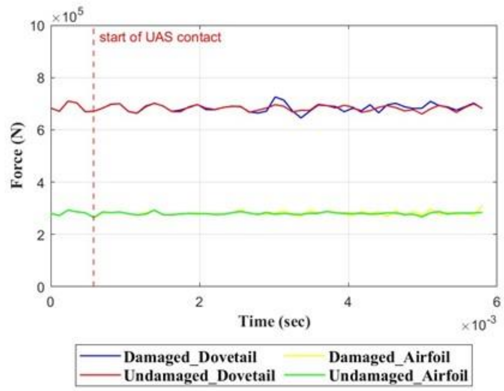

(a) forces

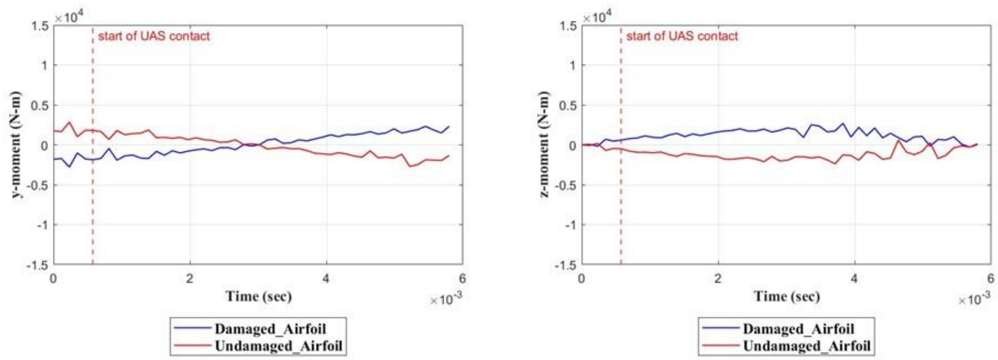

(b) moments about the y- and z-axes

Figure 186. Resultant (a) forces and (b) moments in a sectional plane of the airfoil and dovetail during UAS ingestion simulation HFS_LRV_HRS_45Y.

Figure 187(a) shows the overall energy ratio in the system, not including the eroded energy. Note that there is a slight decrease in the energy ratio term over time because of the erosion of elements in the UAS and fan during the ingestion. Figure 187(b) shows the overall energy in the system. The bulk of the energy in the system is the kinetic energy in the fan and the UAS.. There is some internal energy in the system that will be shown in the breakout of the UAS and fan energies.

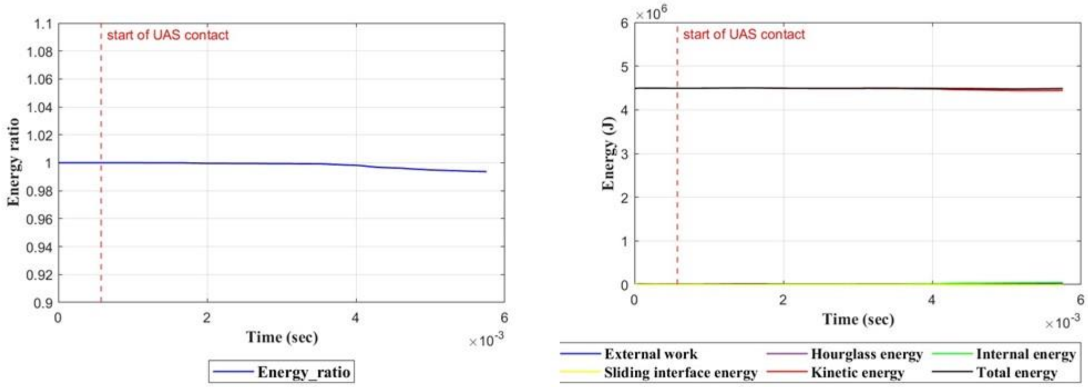

(a) energy ratio (b) energy in system

Figure 187. Overall energy in the system for HFS_LRV_HRS_45Y.

Figure 188 shows the internal and kinetic energy in the UAS during the ingestion up until it is deleted from the simulation. Note that, as contact is made, both the internal and kinetic energy of the UAS increases. The increase in the internal energy is due to the plastic deformation and failure of UAS components. The increase in the kinetic energy is due to the fact that the fan is rotating at a high speed and accelerates many UAS parts as they are swept outward radially by the fan. The velocities of the motors, camera, and battery during the impact are all shown in Figure 189 and agree with this assessment. The different color lines for the velocities of each motor correspond to the motor colors in Figure 39.

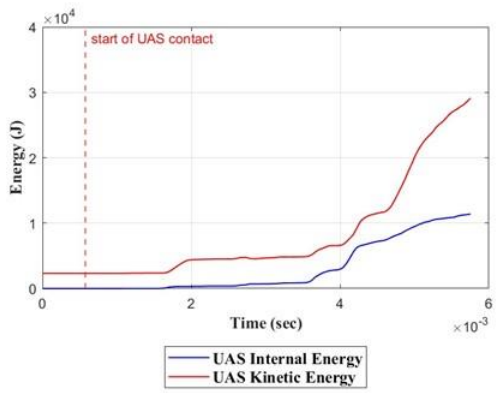

Figure 188. Internal and kinetic energies of the UAS for HFS_LRV_HRS_45Y.

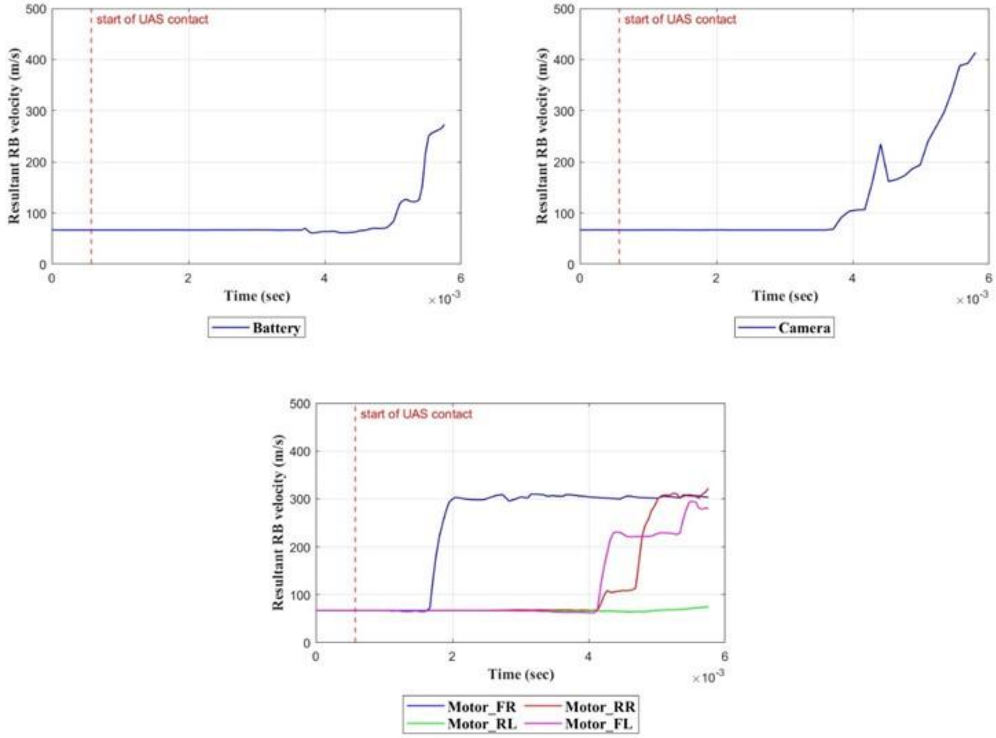

Figure 189. Resultant velocities of UAS components for HFS_LRV_HRS_45Y.

The kinetic and internal energy of the fan are shown in Figure 190. Note that the kinetic energy of the fan looks very similar to the overall energy in the system from Figure 187, since the bulk of the energy is in the fan. There is also significant damage in the fan through the internal energy that increases while the fan is impacting the UAS.

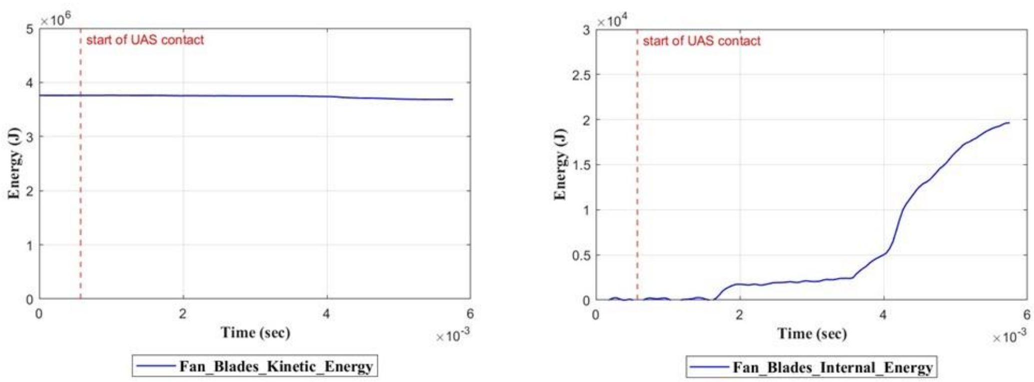

Figure 190. Energy in the fan blades during HFS_LRV_HRS_45Y.

4.6.2 Flight Below 3048 m: MFS_LRV_HRS_45Y

This case corresponded to a UAS ingestion with 70% fan speed, low -relative translational velocity, high radial span location, and the 45 degree yaw orientation (see Figure 39). The kinematics of the ingestion are shown in Figure 191. The simulation is focused on understanding the damage in the fan and was therefore focused on the impact of the UAS and fan, and was terminated around 8.25 ms.

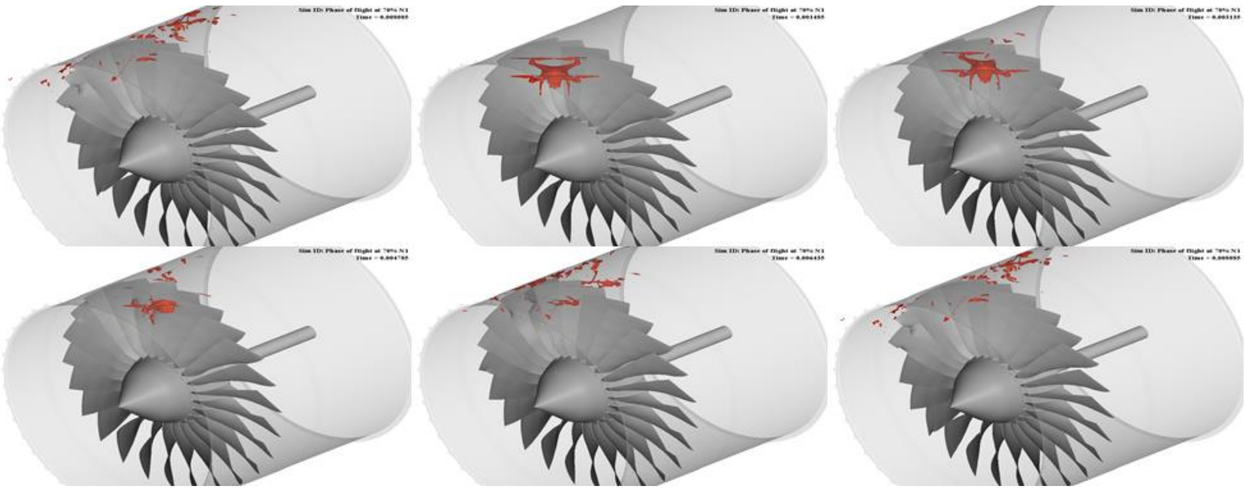

(a) isometric view

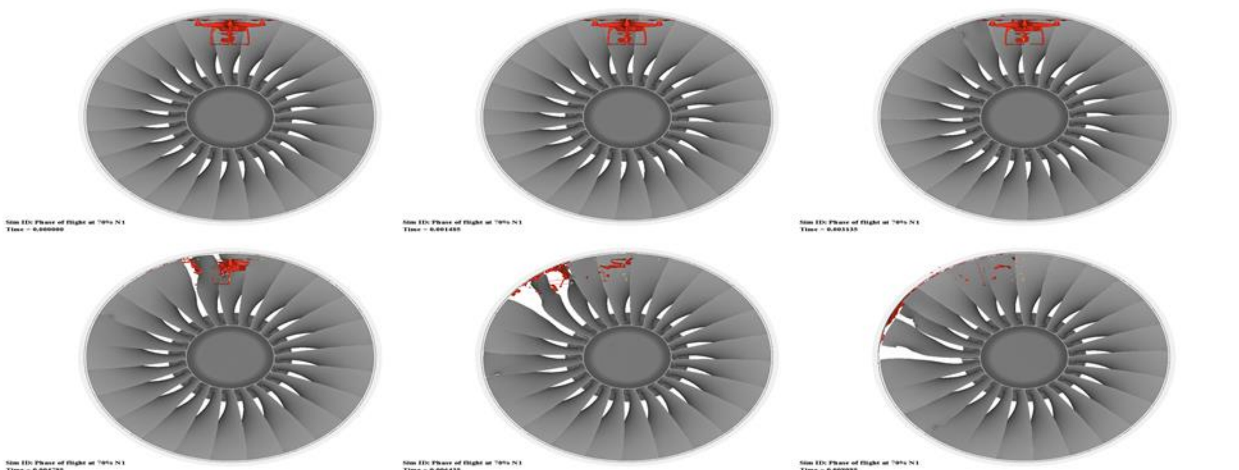

(b) front view

Figure 191. Kinematics of UAS ingestion simulation MFS_LRV_HRS_45Y.

The effective plastic strain in the fan at the end of one fan rotation is shown in Figure 192 (front and rear views).

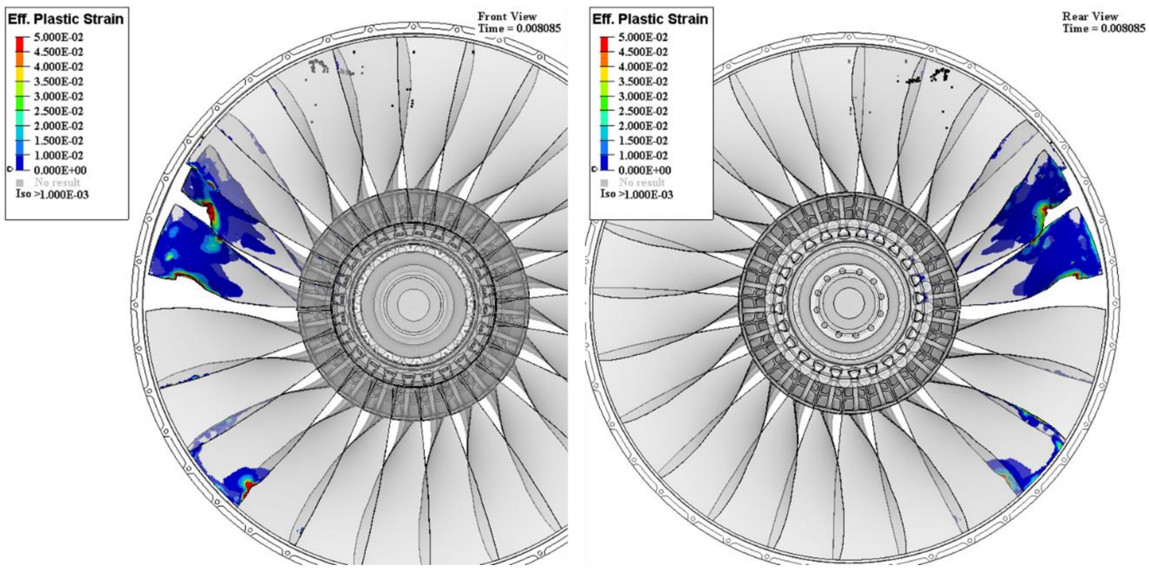

Figure 192. Effective plastic strain after UAS ingestion simulation MFS_LRV_HRS_45Y.

Each blade's radial center of mass pre- and post-ingestion are shown in Figure 193. The damage level *D* (defined in Section 4.2) in the damaged area of the fan model after the UAS ingestion is also shown. The damage clearly shows significant material loss on leading edge of two blades, which corresponds to damage severity level 3, since the imbalance would be less than that of a loss of a full blade.

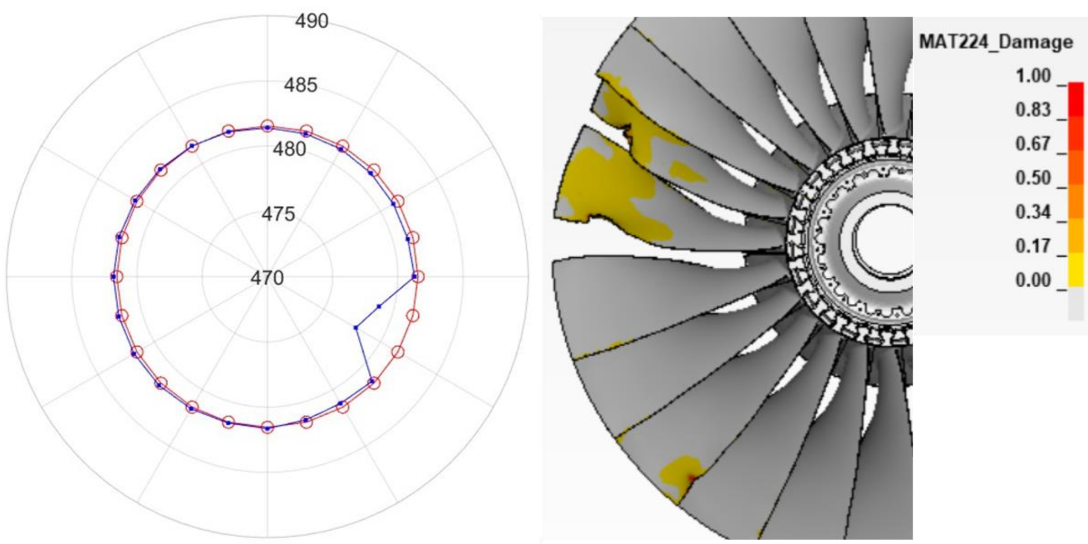

Figure 193. Center of mass of blades and fan model damage after UAS ingestion simulation MFS_LRV_HRS_45Y.

The resultant moments and forces in a sectional plane (see Figure 40) during the ingestion are shown in Figure 194. Note that the damaged airfoil does not have a significantly larger oscillation in the forcing and moment than the undamaged blade.

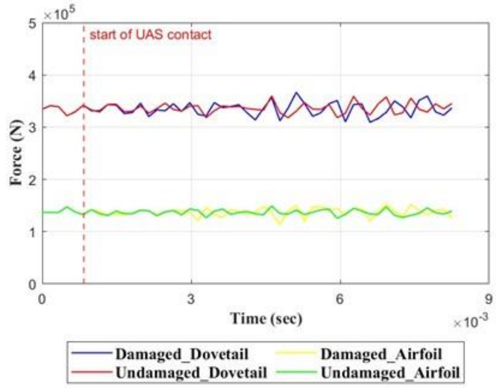

(a) forces

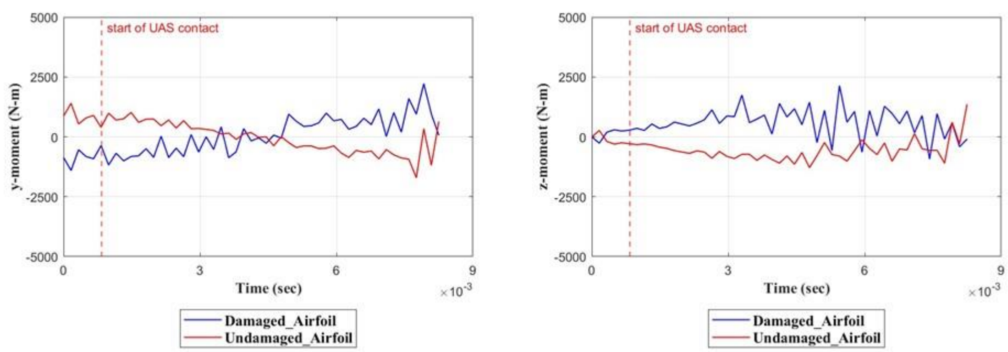

(b) moments about the y- and z-axes

Figure 194. Resultant (a) forces and (b) moments in a sectional plane of the airfoil and dovetail during UAS ingestion simulation MFS_LRV_HRS_45Y.

Figure 195(a) shows the overall energy ratio in the system, not including the eroded energy. Note that there is a drop in the energy ratio term because of the erosion of elements in the UAS and fan during the ingestion and then a sudden drop when the UAS is deleted after it clears the fan stage to speed up the calculation. Figure 195(b) shows the overall energy in the system. The bulk of the energy in the system is the kinetic energy in the fan and the UAS. The reason why the total energy (Figure 195(b)) in the system increases is because of the external work of the driven shaft. There is some internal energy in the system that will be shown in the breakout of the UAS and fan energies.

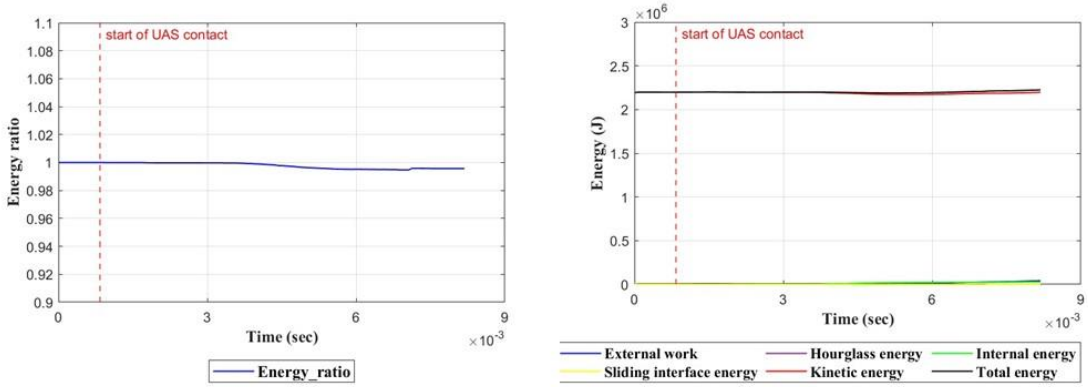

(a) energy ratio (b) energy in system

Figure 195. Overall energy in the system for MFS_LRV_HRS_45Y.

Figure 196 shows the internal and kinetic energy in the UAS during the ingestion up until it is deleted from the simulation. Note that, as contact is made, both the internal and kinetic energy of the UAS increases. The increase in the internal energy is due to the plastic deformation and failure of UAS components. The increase in the kinetic energy is due to the fact that the fan is rotating at a high speed and accelerates many UAS parts as they are swept outward radially by the fan. The kinetic energy eventually levels off and decreases as UAS parts impact the stationary casing. The velocities of the motors, camera, and battery during the impact are all shown in Figure 197 and agree with this assessment. The different color lines for the velocities of each motor correspond to the motor colors in Figure 39.

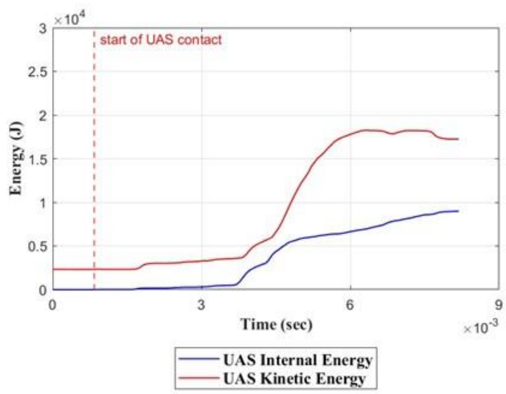

Figure 196. Internal and kinetic energies of the UAS for MFS_LRV_HRS_45Y.

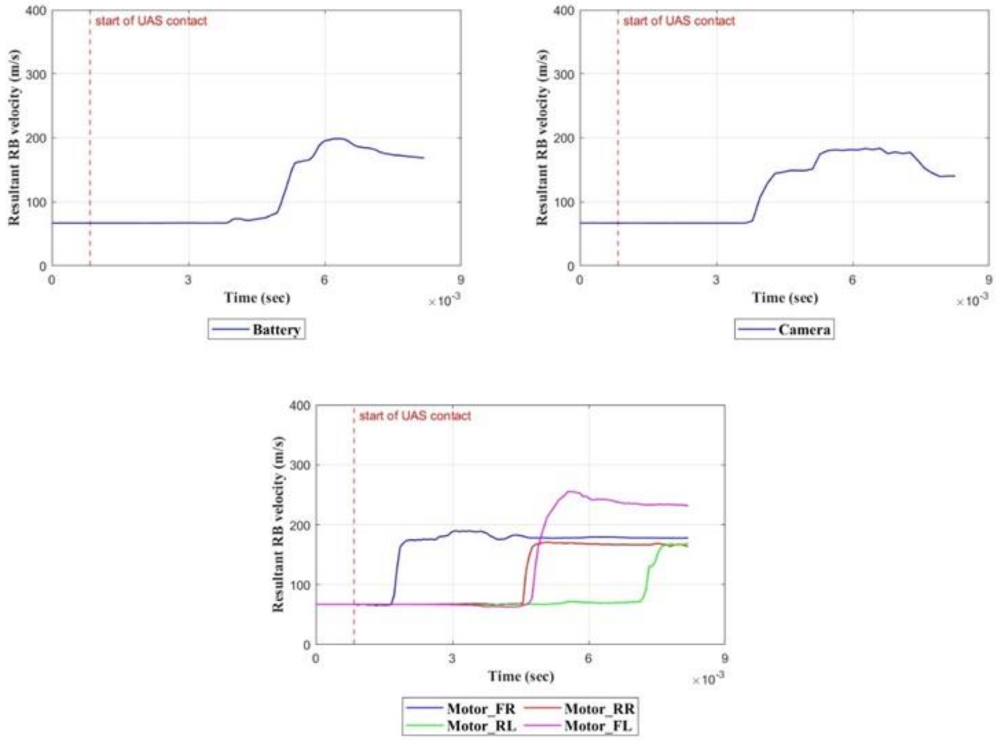

Figure 197. Resultant velocities of UAS components for MFS_LRV_HRS_45Y.

The kinetic and internal energy of the fan are shown in Figure 198. Note that the kinetic energy of the fan looks very similar to the overall energy in the system from Figure 195, since the bulk of the energy is in the fan. There is also significant damage in the fan through the internal energy that increases while the fan is impacting the UAS.

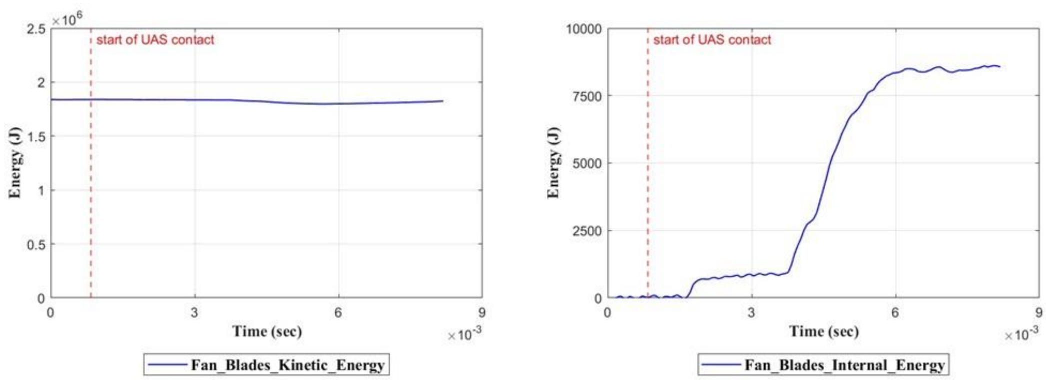

Figure 198. Energy in the fan blades during MFS_LRV_HRS_45Y.

4.6.3 Summary of Phase of Flight Cases

A summary of the average forces in the disk, retainer and retention ring, damage in blades, and severity level for the reference cases, cases with the highest values for the ingestion studies and the phase of flight simulations are summarized in Table 9.

Table 9. Summary of phase of flight results and severity level evaluation.

Simulation ID	Average force in Disk (N)	Average force in retention ring (N)	Average force in retainer (N)	Damage in blade model	Severity level	Associated damage
FBO	**8.98E+05**	**6.10E+05**	**5.86E+05**	**0.04508**	Level 3	Significant material loss leading to an imbalance that is equal to a single blade loss and additional plastic deformation
HFS_HRV_HRS_ Bird_1.2kgs	2.95E+05	**3.41E+05**	**3.24E+05**	0.000692	Level 2	Cupping of leading edge of multiple blades
HFS_LRV_HRS_Nom	1.85E+05	3.04E+05	2.79E+05	**0.001763**	Level 3	Significant material loss on leading edge of multiple blades
HFS_HRV_HRS_45R	2.69E+05	3.35E+05	3.06E+05	0.001091	Level 3	Significant material loss on leading edge of multiple blades
HFS_HRV_HRS_90R	2.80E+05	3.34E+05	3.14E+05	0.000892	Level 3	Significant material loss on leading edge of multiple blades
HFS_HRV_HRS_45Y	2.81E+05	2.85E+05	2.67E+05	0.001509	Level 3	Significant material loss on leading edge of multiple blades
HFS_HRV_HRS_180R	**3.08E+05**	3.32E+05	3.13E+05	0.00112	Level 3	Significant material loss on leading edge of multiple blades
Phase of flight: Takeoff HFS_LRV_HRS_45Y	1.16E+05	2.00E+05	1.49E+05	0.001712	Level 3	Significant material loss on leading edge of multiple blades
Phase of flight: Flight below 3048 m MFS_LRV_HRS_45Y	1.18E+05	1.47E+05	1.27E+05	0.000627	Level 3	Material loss and deformation along leading of multiple blades

The two phase of flight simulations agree with the sensitivity study results. The level of damage and the type of damage of the fan indicate a damage severity level 3 is possible, and quite likely for outer radial UAS impacts during takeoff and general flight below 3,048 m (10,000 ft).

5. CONCLUSIONS AND FURTHER WORK

The work presented in this report was focused on completing two major research tasks and supporting a third research task for the A17 research project focused on better understanding the effects of a UAS ingestion on a representative fan rig model.

Task A: The team worked closely with industry in developing an open fan model that is representative of the structural and vibratory features of high bypass ratio fans commonly used for commercial transport. The fan rig model consisted of the fan blades and disk, which were analyzed to ensure that it would meet stress loads when rotating at full speed (Section 2.4.2), bird ingestion requirements for a fan of its size (Section 2.4.3), and did not have an engine order one crossing on the Campbell diagram (Section 2.4.1). Each fan blade was held in place with a retention ring in the rear and a retainer in the front. The model was driven by a rigid shaft. For the boundary conditions for the fan model in this study, a bi-conic nose cone was connected to the disk through a flange, and a cylindrical casing encompassed the fan. Containment was not investigated in this work, and a linear elastic material model was chosen for the casing to capture first-order effects and provide information about the expected loads transferred to the casing during the events. The work leveraged past FAA research programs' development of a titanium alloy model for the fan material. Multiple meshes were generated for the fan model and could be used for different cases depending on the fidelity of the simulation and ingested object.

Task B: The team worked closely with the research partners and industry to help define relevant experiments that would represent a UAS ingestion (particularly with the representative fan rig model developed in this study). The research team helped define the experimental test conditions and the final test article design so the experimental validation of the UAS would be at the harshest conditions expected to be seen in an ingestion event. This work is detailed in the appendices of this Annex.

Task C: The team worked closely with NIAR to ensure the compatibility of their experimentally validated UAS model from Task B with the representative fan model during the ingestion. Moreover, the mesh sizing for the fan blades was determined based on the experimental validation with the UAS. The team also worked closely with industry and research partners to determine what information should be extracted and analyzed from the simulations. An initial sensitivity study was completed to identify the importance of a number of parameters during the ingestion such as the fan rotational speed, the relative translational velocity of UAS and fan, the radial location of the UAS impact on the fan, and the orientation of the UAS during the impact. Based on the sensitivity study, two phase of flight simulations were defined to study some of the worst-case ingestions an aircraft might encounter during feasible flight conditions.

This work led to the development of a damage severity index for the fan rig assembly model subject to foreign object ingestion that consists of four levels. Level 1 is minor damage to the fan blades and would likely lead to minimal impact on engine performance. Level 2 is significant deformation of the blades with minimal loss of elements in the blades. Level 3 is deformation in blades and loss of blade material that leads up to an imbalance due to a single blade loss. Levels 1-3 are all within the engine certification envelope. Level 4 damage is loss of material leading to an imbalance greater than a single blade loss or disk crack initiation. The sensitivity study and all the phase of flight cases in this work resulted in severity levels between 1-3.

Overall, the damage severity in each of the cases tracks closely with the accumulation of the overall plastic strain in the whole fan (D_{fan} parameter defined in the report). The high fan speed case consistently has significantly more damage than the low fan speed, which is expected since the impacts happen at a much higher speed imparting more energy into the UAS and fan blades. The higher radial span impact causes significantly more damage than the lower radial span impact, since, at the higher radial span, the relative velocity between the UAS and fan blades is much higher than at the lower radial span (which are severity level 1 or 2). All of the high fan speed, high radial impact cases for the UAS ingestion are severity level 3, as opposed to the bird of the same mass which is severity level 2. The case that causes the most damage to the fan is the lower translational relative velocity scenario (with high fan speed and high radial span location). Finally, in comparing the UAS orientations, the 45 degree yaw orientation caused the most damage in the sensitivity study for the HFS_HRV_HRS condition.

The two phase of flight cases studied in this work focused on what were expected to be worst ingestion cases. For the take-off case, the worst-case impact was maximum rotational speed (100% N1), high radial span impact and a low relative translational velocity. The nominal orientation case for this condition was done in the sensitivity study and provided the worst damage. An additional take-off case with a 45 degree yaw orientation case was also conducted since that orientation caused the most damage in the HFS_HRV_HRS condition. This resulted in a slightly lower damage than the nominal orientation. It should be noted that the translational relative velocity and orientation are secondary factors in the damage level and depend on the other parameters of the ingestion. For the flight below 3,048 m (10,000 ft), corresponding to the mid-level rotational speed (70% N1), high radial span impact with the 45-degree yaw orientation case, and a low relative translational velocity, a significant but lower level of damage was observed. Both of the additional phase of flight simulations studied resulted in a severity level 3 damage, and were in line with the damage seen during the sensitivity study.

The completion of this research program provides an open representative fan rig model that can be used for additional foreign object ingestion studies in industry and academia to improve models and compare results through this work. Moreover, the UAS has been experimentally validated at the conditions of an ingestion and can be used in industry on their proprietary models to better understand the threat posed to their engines.

6. REFERENCES

[1] D’Souza K, Lyons T, Lacy T, Kota K. Volume IV: UAS Airborne Collision Severity Evaluation: Engine Ingestion. FAA; 2017.

[2] Sengoz K, Kan S, Eskandarian A. Development of a Generic Gas Turbine Engine Fan Blade-out Full Fan Rig Model. FAA Report DOT/FAA/TC-14/43; 2015.

[3] Olivares G, Gomez L, Monteros JE, Baldridge R, Zinzuwadia C, Aldag T. Volume II – UAS Airborne Collision Severity Evaluation – Quadcopter. FAA; 2017.

[4] Lyons T, D'Souza K. Parametric Study of an UAV Ingestion into a Business Jet Size Fan Assembly Model. ASME Journal of Engineering for Gas Turbines and Power 2019;141(7).

[5] Olivares G, Gomez L, Ly H. Annex B to Task A17: NIAR/WSU sUAS Numerical Model Validation (Component and Full-Scale Level) for Engine Ingestion Analysis. 2023.

[6] http://awg.lstc.com/tiki/tiki-index.php?page=MGD. LS-DYNA Aerospace Working Group Modeling Guidelines Document. 2016.
[7] Cordasco D, Emmerling W. Turbofan Engine System Safety of a UAV Ingestion Hazard. 2015.
[8] Dewhurst TB. The Impact Load on Containment Rings During a Multiple Blade Shed in Aircraft Gas Turbine Engines. International Gas Turbine and Aeroengine Congress and Exposition. Orlando, FL; 1991.
[9] Stepanov GV. Speed of Propagation of Elasto-Plastic Shock Waves in Metals. Institute for Study of Strength of Materials (Translated from Problemy Prochnosti) 1971;2(109-112).
[10] Haight S, Wang, L., Du Bois, P., Carney K., Kan C. D. Development of a Titanium Alloy Ti-6Al-4V Material Model Used in LS-DYNA. FAA.
[11] CFM. Training Manual CFM56-5B, Basic Engine. 2000.
[12] Hammer JT. Plastic Deformation and Ductile Fracture of Ti-6Al-4V under Various Loading Conditions. FAA Report DOT/FAA/TC-TT14/2; 2014.
[13] LS-DYNA Keyword User’s Manual Vol. 1. Livermore, California; 2016.
[14] http://awg.lstc.com/tiki/tiki-index.php?page=Resources. LS-DYNA Aerospace Working Group *Mat_224 User Guide. 2016.
[15] Duling C, Zweiner M, Arteburn D. Annex C to Task A17: UAH High Speed Impacts of Full sUAS and Components with Angled Plates 2023.
[16] Seidt JD. Part 3: Plastic Deformation and Ductile Fracture of 2024 Aluminum under Various Loading Conditions. Development of a New Metal Material Model in LS-DYNA: FAA Report DOT/FAA/TC-13/25, P3; 2014.
[17] https://awg.lstc.com/tiki-index.php?page=Material+Parameter+Sets. LS-DYNA Aerospace Working Group *Mat_224 User Guide. 2016.
[18] FAA. Wildlife Strikes to Civil Aircraft in the United States, 1990 - 2021. FAA; 2022.
[19] FAA. Code of Federal Regulations, Part 33 - Airworthiness Standards: Aircraft Engines. US; 2011.
[20] https://awg.lstc.com/tiki-index.php?page=Test+Case+Suite. AWG ERIF Test Case Suite Overview. LS-DYNA Aerospace Working Group.
[21] Lyons T, Sirivolu D, D'Souza K. Stress State Characterization for a Generic Titanium Fan During Bird Ingestion. AIAA Journal 2022:1-12.
[22] Vintilescu IV. Explicit Finite Element Modeling of Multilayer Composite Fabric for Gas Turbine Engine Containment Systems, Phase II - Part 4: Model Simulation for Ballistic Tests, Engine Fan Blade-out, and Generic Engine. FAA Report DOT/FAA/AR-08/37,P4; 2009.

7. APPENDICES

APPENDIX A: Experimental Test Matrix

The quadcopter model had been developed and validated using a variety of static, quasi-static, and blunt impact tests against aluminum plates at speeds up to 129 m/s (250 knots)[3]. This ensured the accuracy of the model for impacts with the structure of the airframe at elevations below 3,048 m (10,000 ft) where the flight speed is limited to 129 m/s (250 knots). The purpose of conducting the additional experiments in this research program was to validate the quadcopter model against experimental conditions it would see in an ingestion into an engine. In particular, the impact would be a slicing impact with a titanium test article at higher speeds that would be seen during an ingestion of the UAS at the outer span of the fan.

The focus of the experiments was on updating the critical components of the quadcopter that would have the largest damage on the fan based on their weight and density. These three components are the motor, battery, and camera. Each of these components were planned to have two different impact cases to capture two of the more extreme impact cases that would be seen in an engine ingestion. Additionally, each of the tests were to be repeated 3 times to understand the variation in the tests to better validate these component models. Also, the entire UAS was planned to have two different impact cases with three repetitions of each case.

The initial analysis of ingestions at the mid-span and the 80% radial span gave the threat matrix shown in Table 10. Note that the Leading Edge (LE) and 127 mm (5”) aft of LE as well as the relative angle are defined in Figure 199.

Table 10. Impact conditions for UAS ingestion.

Static Test ID	Phase of Flight	Radial Span (%)	Relative Angle (degrees)	Approx. Speed Range	Impact Location
1	Take-off	50	30	290-366 m/s (950-1200 ft/s)	LE
2	Cruise	50	0	290-366 m/s (950-1200 ft/s)	LE
3	Descent	50	20	152 m/s (500 ft/s)	127 mm (5") aft of LE
4	Take-off	80	25	381 m/s (1250 ft/s)	LE
5	Cruise	80	0	427 m/s (1400 ft/s)	LE
6	Descent	80	20	152 m/s (500 ft/s)	127 mm (5") aft of LE

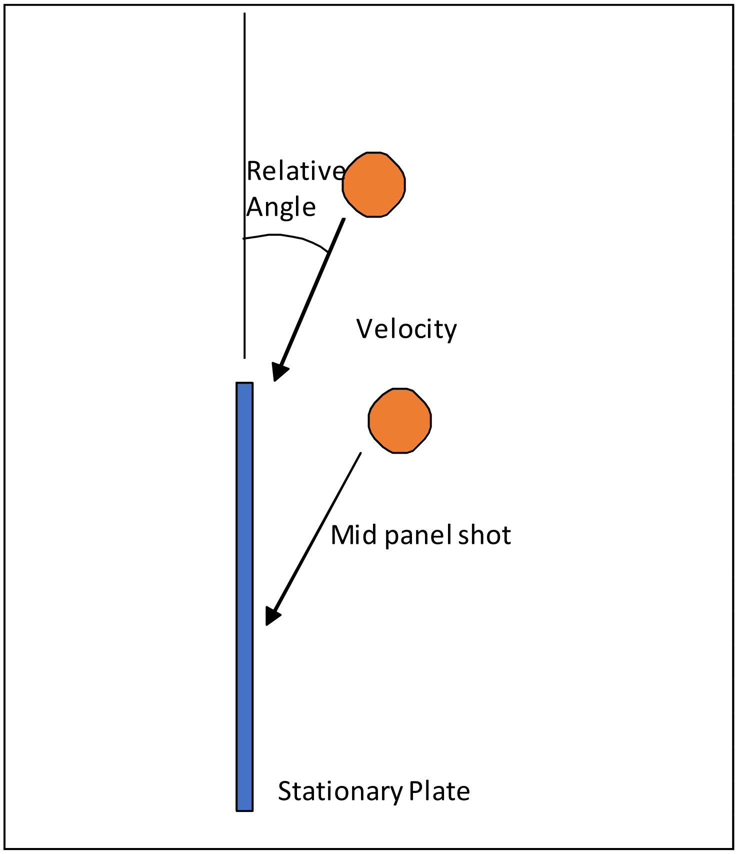

Figure 199. Definition of relative angle of impact as well as LE and 127 mm aft of LE impacts with stationary plate.

The team selected the Take-off phase of flight (Static Test ID 1 & 4) as the focus since the cruise conditions are much less likely to occur (since cruise happens above 3,048 m). The Descent case was not selected since the relative velocity of the impact is much lower than the Take-off case, and would result in substantially less damage in the test article. The initial test matrix for the UAS components is given in Table 11 and for the full UAS is given in Table 12.

Table 11. Initial test matrix for UAS component experiments.

Test Number	Static Test ID	Phase of Flight	Component	Span (%)	Relative angle	Impact location	Speed (m/s)
M80L7-001	4	Take-off	Motor	80	25°	LE	365
M80L7-002	4	Take-off	Motor	80	25°	LE	365
M80L7-003	4	Take-off	Motor	80	25°	LE	365
M50L5-004	1	Take-off	Motor	50	30°	LE	290
M50L5-005	1	Take-off	Motor	50	30°	LE	290
M50L5-006	1	Take-off	Motor	50	30°	LE	290
B80A5-007			Battery	80	25°	127 mm aft of LE	290

B80A5-008			Battery	80	25°	127 mm aft of LE	290
B80A5-009			Battery	80	25°	127 mm aft of LE	290
B50L7-010	1	Take-off	Battery	50	30°	LE	365
B50L7-011	1	Take-off	Battery	50	30°	LE	365
B50L7-012	1	Take-off	Battery	50	30°	LE	365
C80L7-013	4	Take-off	Camera	80	25°	LE	365
C80L7-014	4	Take-off	Camera	80	25°	LE	365
C80L7-015	4	Take-off	Camera	80	25°	LE	365
C50L5-016	1	Take-off	Camera	50	30°	LE	290
C50L5-017	1	Take-off	Camera	50	30°	LE	290
C50L5-018	1	Take-off	Camera	50	30°	LE	290

Table 12. Initial test matrix for full UAS impact experiments.

Test Number	Static Test ID	Phase of Flight	Span (%)	Relative Angle	Impact Location	Speed (m/s)
D80L7-001	4	Take-off	80	25°	LE	365
D80L7-002	4	Take-off	80	25°	LE	365
D80L7-003	4	Take-off	80	25°	LE	365
D50L5-004	1	Take-off	50	30°	LE	290
D50L5-005	1	Take-off	50	30°	LE	290
D50L5-006	1	Take-off	50	30°	LE	290

Note that, in addition to the take-off phase of flight conditions, a slightly harsher version of the descent case (Static Test ID 6) was used for one of the battery sets of experiments. The battery was chosen since it was the heaviest component and it was desired to determine what the effect of the aft of LE impact would be for this case. A slightly harsher case was chosen in terms of speed of impact and the orientation angle was adjusted slightly to simplify the test matrix (in terms of the number of speeds and angles of impact that the experimental setup had to cover).

The impact of the UAS and each of the key components (motor, camera, and battery) could feasibly occur at any orientation based on how the quadcopter is flying when it is ingested into the engine. The experimental test matrix and orientations were chosen to be likely worst cases where the bulk of the UAS component or full UAS is hitting the leading edge in a way that nearly splits the UAS or component in half, ensuring good contact and more damage to the test article. The orientation was also dependent on both the precision and accuracy the UAS components and full UAS could be delivered to the target. An exploded view of the UAS is shown in Figure 200 and the top views of the planned orientation of the components during the impacts are shown in Figure 201.

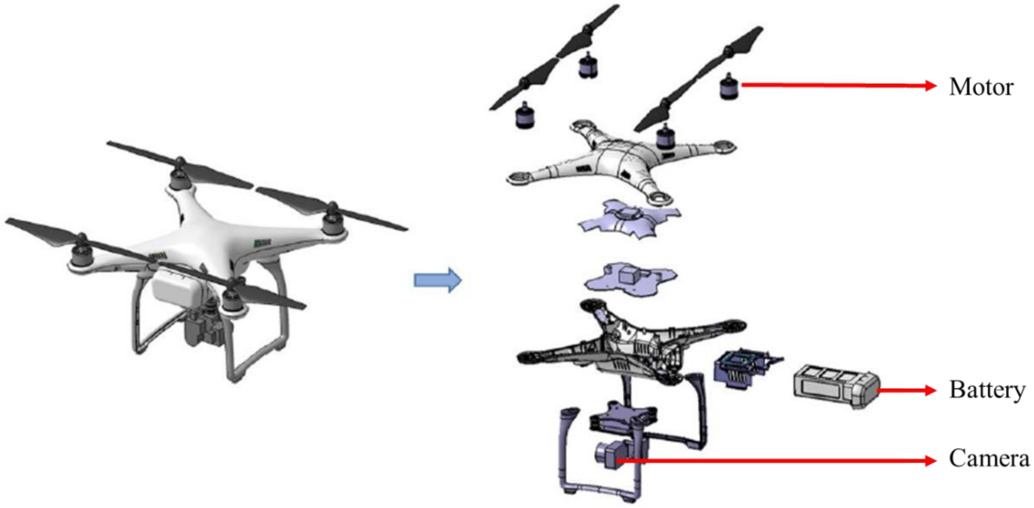

Figure 200. Blown up view of quadcopter with key components noted[3].

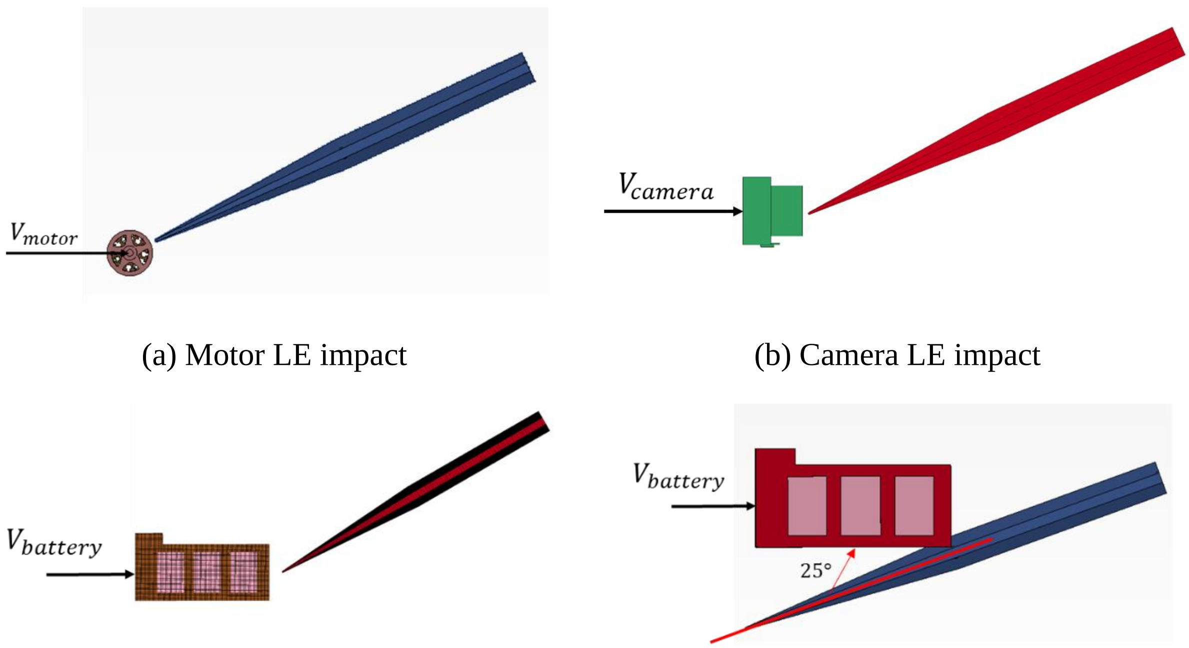

(a) Motor LE impact

(b) Camera LE impact

(c) Battery LE impact

(d) Battery 127 mm aft of LE

Figure 201. Planned orientation of quadcopter component impacts with test article.

Through discussions within the team and with industrial partners, it was decided to remove the camera and legs from the UAS for the UAS impacts with the test articles. There were significant technical challenges and delays related to trying to secure the camera to the UAS body as well as launching the UAS with its legs and camera due to the size of the full UAS. The focus of these tests was to validate the quadcopter body model (since the key components had their own dedicated tests), and the system as a whole. Some comparative studies were conducted by NIAR before testing, with and without the quadcopter legs and camera, to ensure the change would be acceptable. The top view of the planned orientation of the quadcopter impacts are shown in Figure 202.

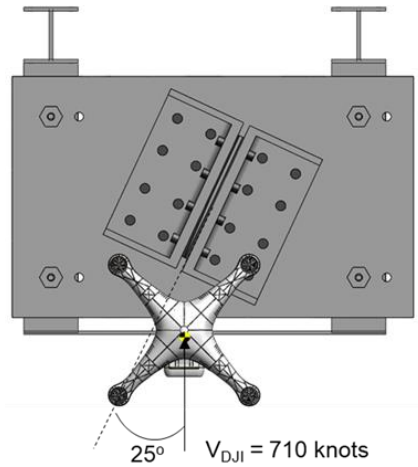

(a) UAS impact test numbers 19-21

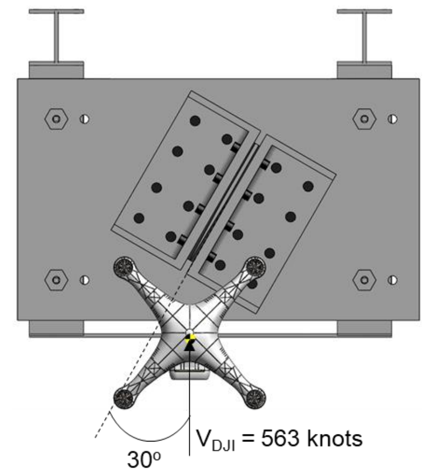

(b) UAS impact test numbers 22-24

Figure 202. Planned UAS impact orientations.

The final test matrix is provided in Annex C[15]. The test matrix had to be altered for two reasons. First, a test article was damaged during machining. This damaged test article was given to NIAR to conduct some static materials testing to better understand the material properties of this specific test batch. The loss of the test article led to the removal of one motor test case in the component experiments. It was decided that the motor model had the least uncertainty, so the removal of one of the lower speed motor impacts was removed from the test matrix. The second alteration to the test matrix was that certain speeds could not be reached without significantly damaging the UAS battery or UAS to launch it at the desired speed. The battery speed was reduced to 290 m/s (563 kts) which was still in the range of speeds for Static Test ID 1 for both sets of battery experiments. The full UAS had to be reduced to 219 m/s (425 kts) because of the technical challenges of getting the UAS launched at high speeds with a slow enough acceleration that the UAS would be intact when launched as described in Annex C[15]. It was determined that this was satisfactory since the components are softer and are not the components that are imparting significant damage to the test article, which are the battery, camera and motor which were each independently validated at higher speeds.

APPENDIX B: Test Article Definition and Meshing

The test article for the experiments was defined to capture key features of the airfoil defined for the representative fan model discussed in Section 2.2.1. Namely, the airfoil geometry was simplified for manufacturability out of titanium plates. Note that the material selection was the titanium alloy TI-6Al-4V, which extensive testing has been done on by the FAA to create an open public LS-DYNA material model[10]. Moreover, the same material supplier of the titanium alloy as the one that supplied the material for developing the model was chosen to limit variability in the material and the model.

An image of the airfoil and the originally designed test article are shown in Figure 203. Note that the key regions of the airfoil that are trying to be captured for the testing are noted in the figure (the 50% and 80% span). In particular, the thickness of the airfoil matches that of the test article at those locations.

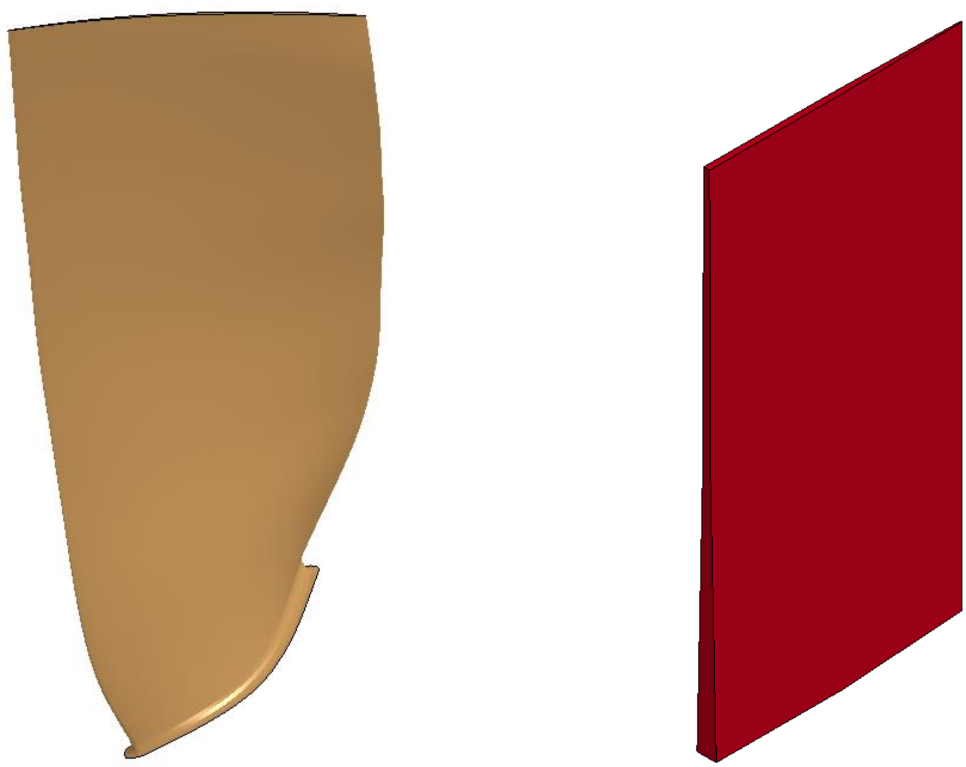

(a) Airfoil from representative fan model (b) Initially designed test article

Figure 203. Airfoil and originally designed test article.

A mesh refinement study was conducted on this initial test article design to understand the convergence of the mesh for subsequent studies and for informing mesh sizing for the UAS ingestion simulations with the fan assembly model. Table 13 shows some of the key properties of the mesh for different levels of refinement.

Table 13. Mesh properties of test article.

Elements through thickness	4	5	6	8
Total number of elements	131,500	227,400	544,500	2,123,800
Maximum warpage	0.14	0.026	0.0195	0.11
Maximum aspect ratio	7.66 (5% elements > 5)	7.12 (6% elements > 5)	5.67 (1% elements > 5)	6.21 (1% elements > 5)
Minimum length	0.265 mm (0.0104 in)	0.238 mm (0.0093 in)	0.199 mm (0.0078 in)	0.099 mm (0.0039 in)
Maximum length	4.76 mm (0.187 in)	3.81 mm (0.15 in)	3.175 mm (0.125 in)	2.38 mm (0.093 in)
Minimum Jacobian	0.61	0.60	0.60	0.66

Simulations using a motor were performed at 80% radial span and 50% radial span for mesh refinement studies. Shell elements were placed at 8 different locations on the test article to measure strains during the impact. Figure 204 to Figure 207 highlight the difference in strain values at an element close to the impact point for the different mesh refinement levels for both the 80% and 50% radial span impact cases. The figures also show the final damage in the test article for the two cases. From the results, it was determined that 6 elements through the thickness was sufficiently converged and would be used for the subsequent analysis when modifying the test article design to improve the manufacturability.

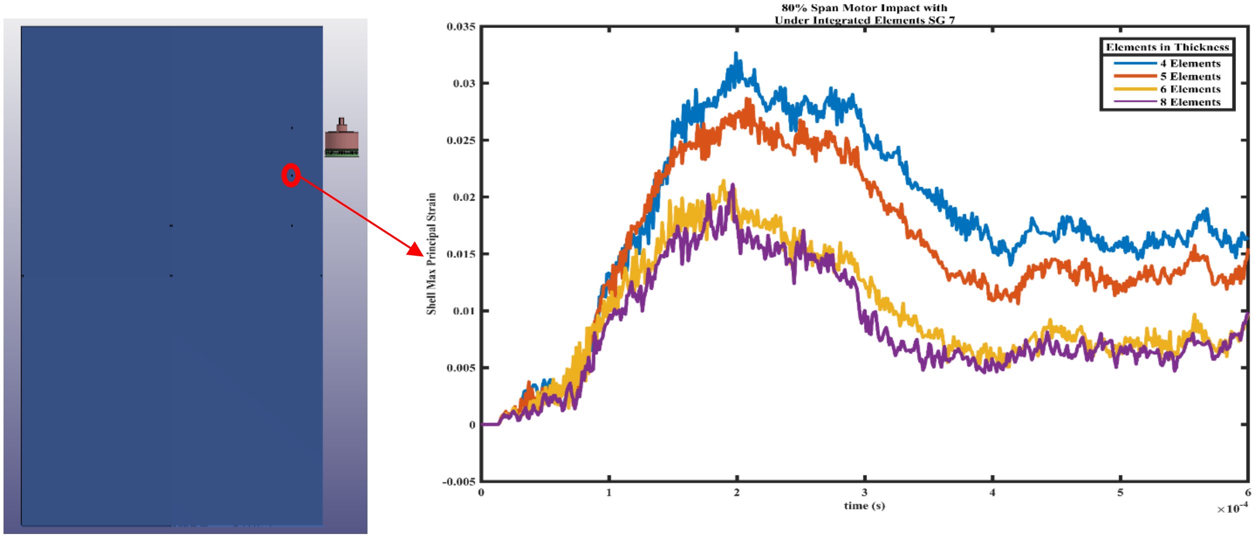

(a) (b)

Figure 204. Strain comparison for different mesh refinements in the test article due to the motor impact at 80% radial span.

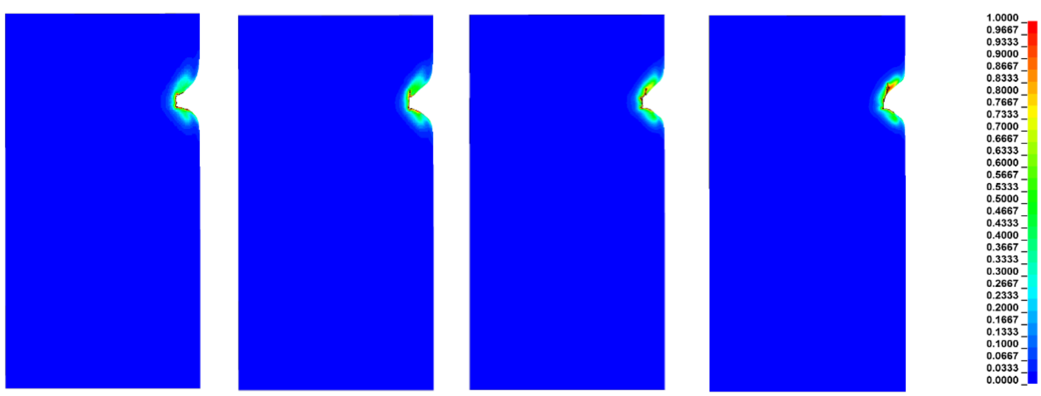

4 Elements 5 Elements 6 Elements 8 Elements

Figure 205. Damage comparison in the test article due to the motor impact at 80% radial span.

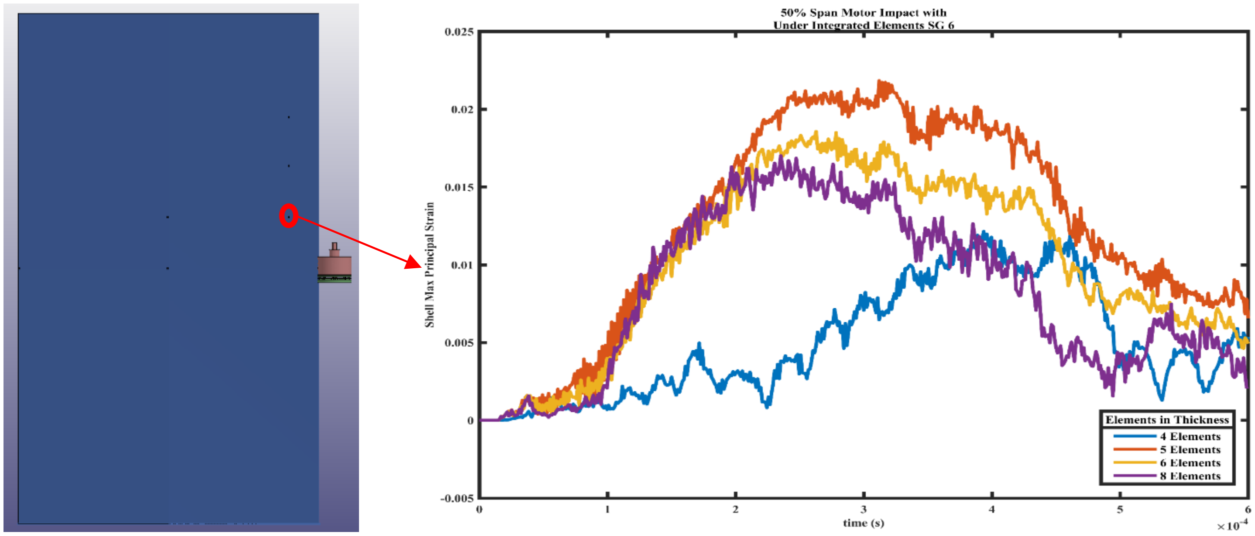

Figure 206. Strain comparison for different mesh refinements in the test article due to the motor impact at 50% radial span.

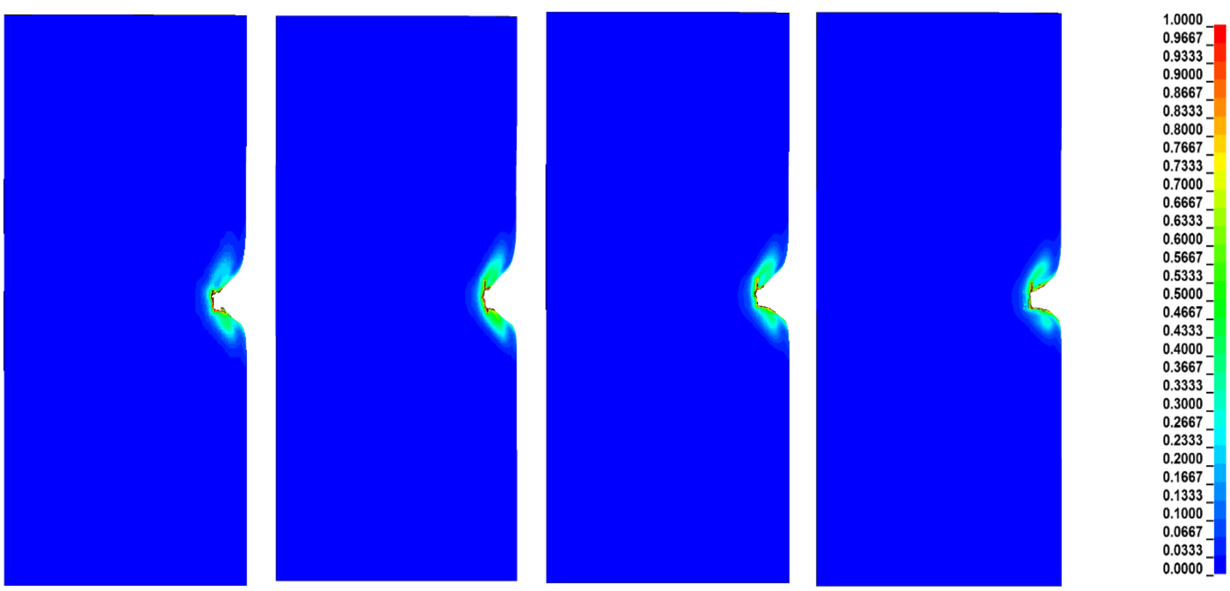

4 Elements 5 Elements 6 Elements 8 Elements

Figure 207. Damage comparison in the test article due to the motor impact at 50% radial span.

Due to the challenges with respect to cost and time in machining the titanium alloy, it was desired to reduce the amount of material removed and the size of the test article. Images of the top view of the original and final geometry for the 50% and 80% radial impact test article are shown in Figure 208.

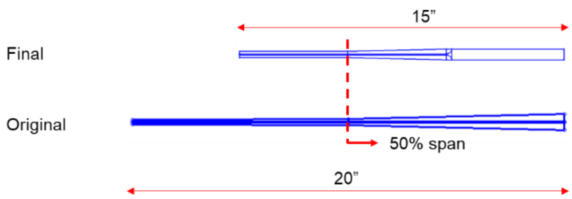

(a) 50% radial impact test article top view

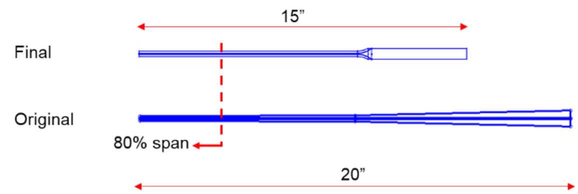

(b) 80% radial impact test article top view

Figure 208. Comparison of initial and final test article geometries.

Computational simulations with the initial UAS motor and battery model were conducted to compare the results for the two different test articles and were found to be in very good agreement. The impact location, damage level D, and von Mises stress for both test articles for the 50% motor impact (M50L5: 50% radial span, 30° angle of impact against the LE at 290 m/s) are shown in Figure 209.

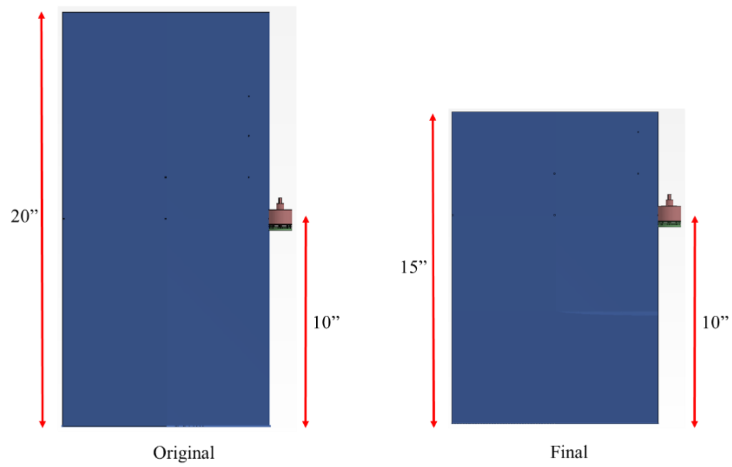

(a) Location of motor impacts on test articles

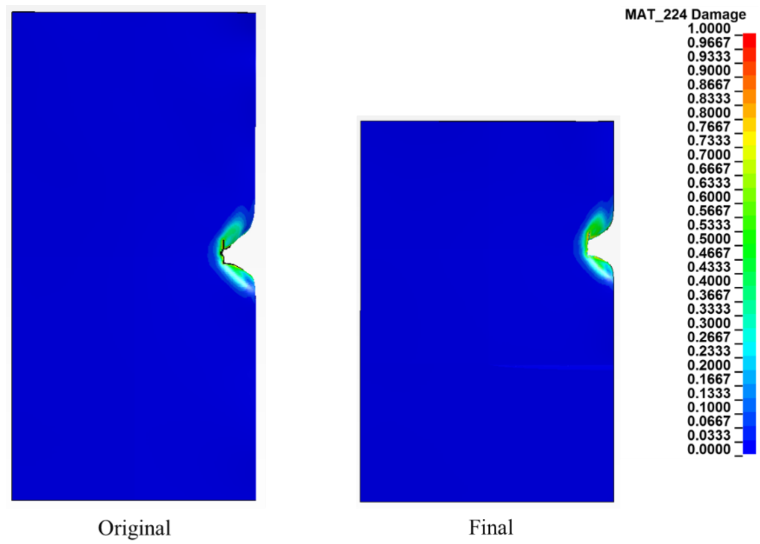

(b) Comparison of damage level (front view)

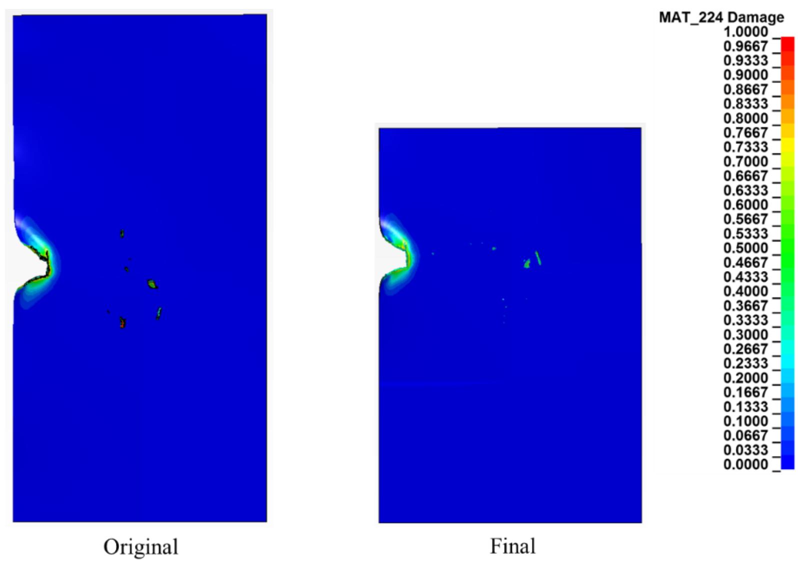

(c) Comparison of damage level (back view)

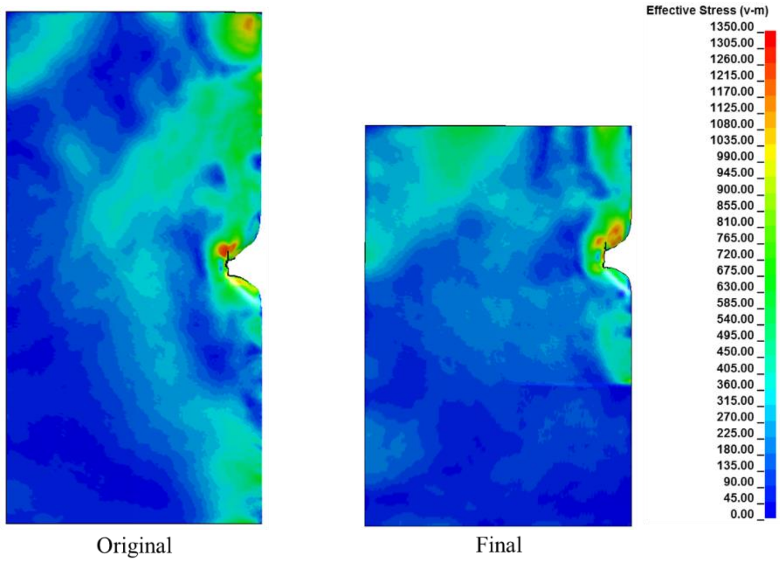

(d) Comparison of von-Mises stress (front view)

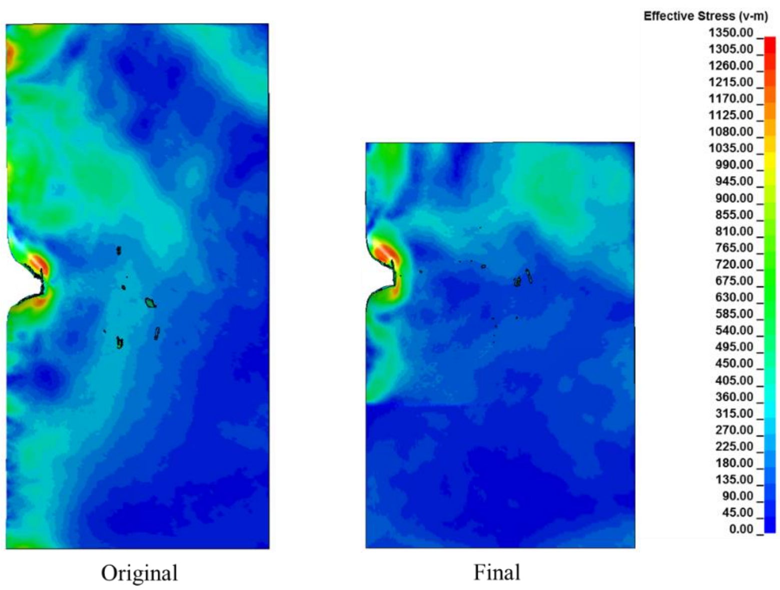

(e) Comparison of von-Mises stress (back view)

Figure 209. Comparison of original and final test article for test number M50L5.

Similarly the impact location, damage level D, and von Mises stress for both test articles for the 80% motor impact (M80L7) are shown in Figure 210.

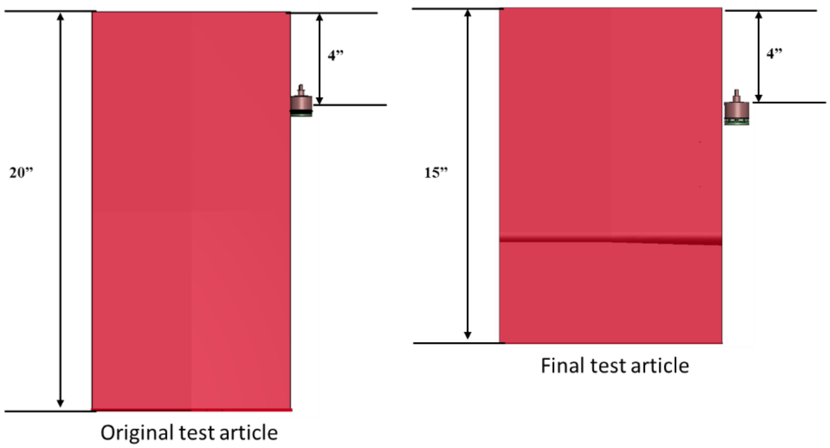

(a) Location of motor impacts on test articles

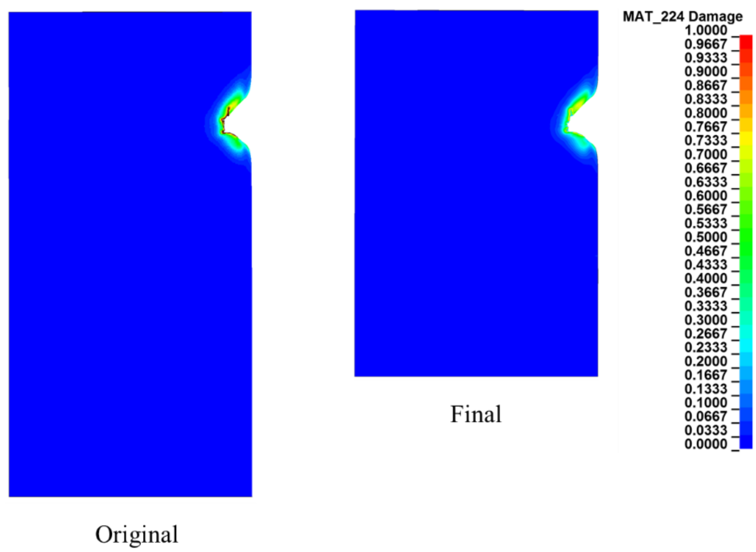

(b) Comparison of damage level (front view)

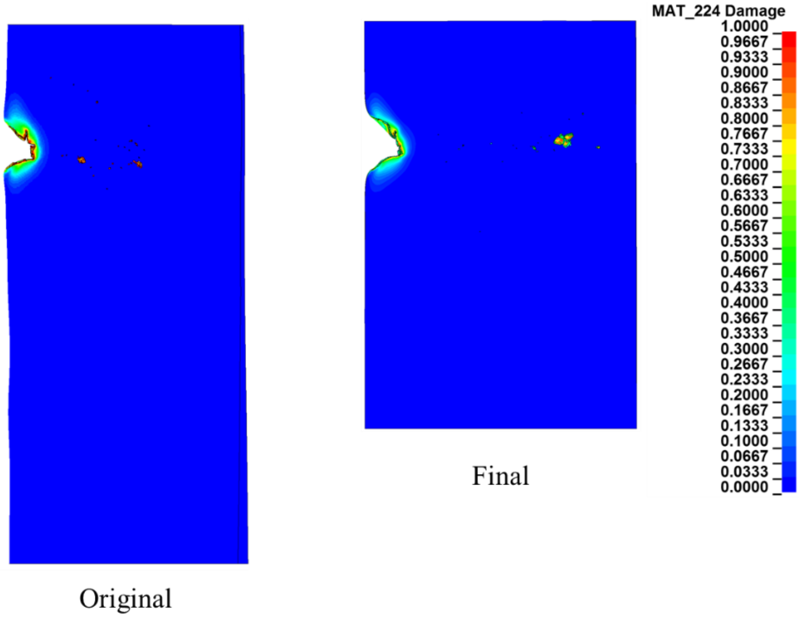

(c) Comparison of damage level (back view)

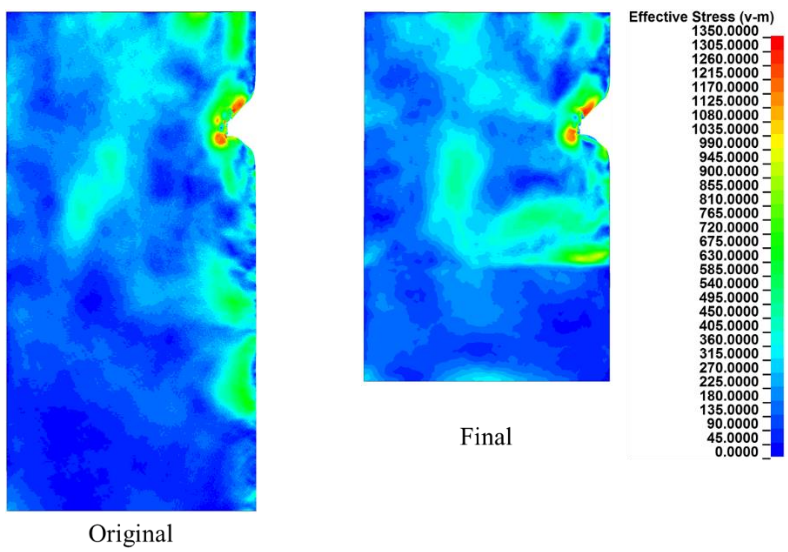

(d) Comparison of von-Mises stress (front view)

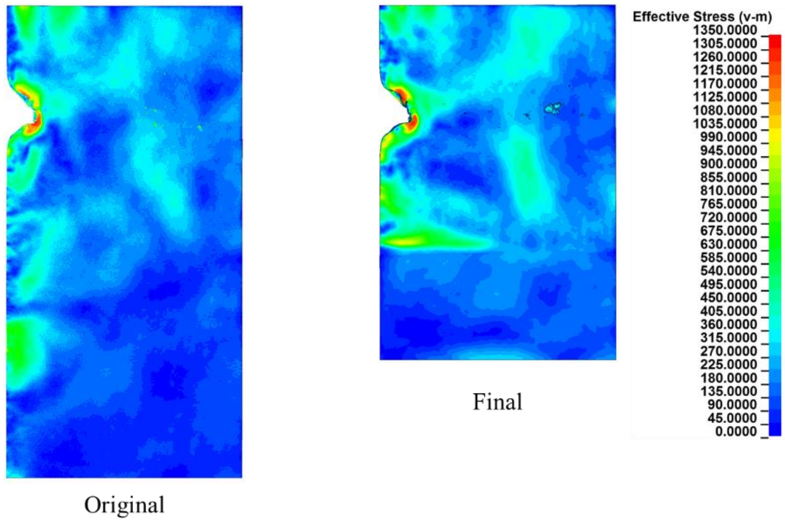

(e) Comparison of von-Mises stress (back view)

Figure 210. Comparison of original and final test article for test number M80L7.

Similarly, the impact location, damage level D, and von Mises stress for both test articles for the 50% battery impact (B50L7) are shown in Figure 211.

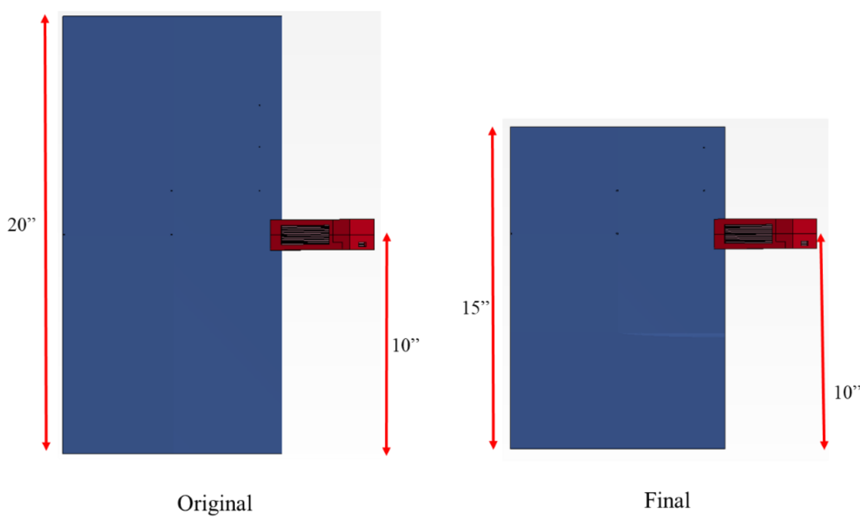

(a) Location of battery impacts on test articles

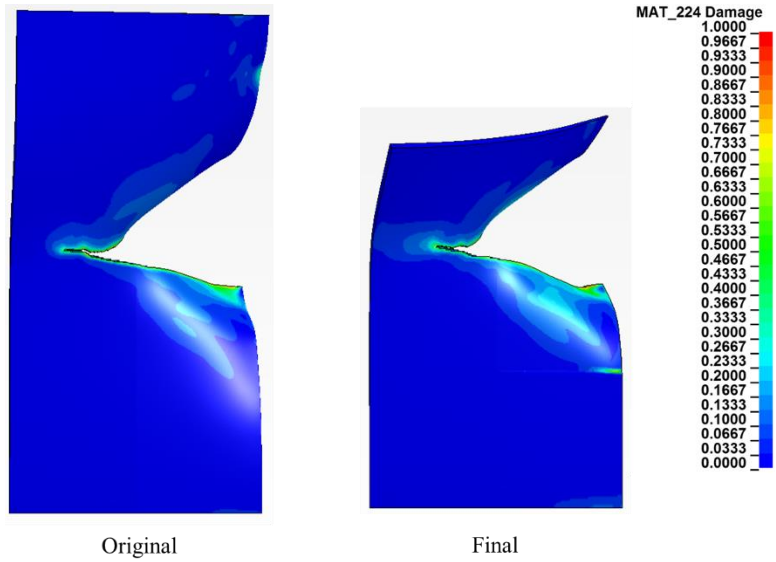

(b) Comparison of damage level (front view)

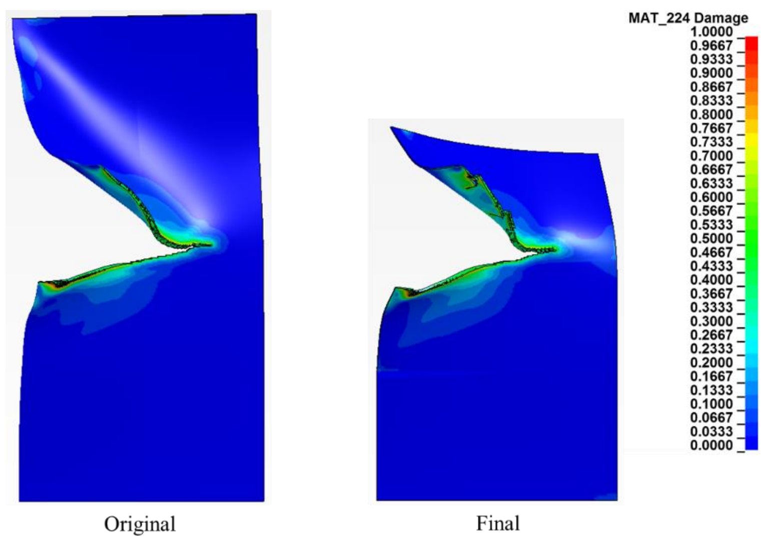

(c) Comparison of damage level (back view)

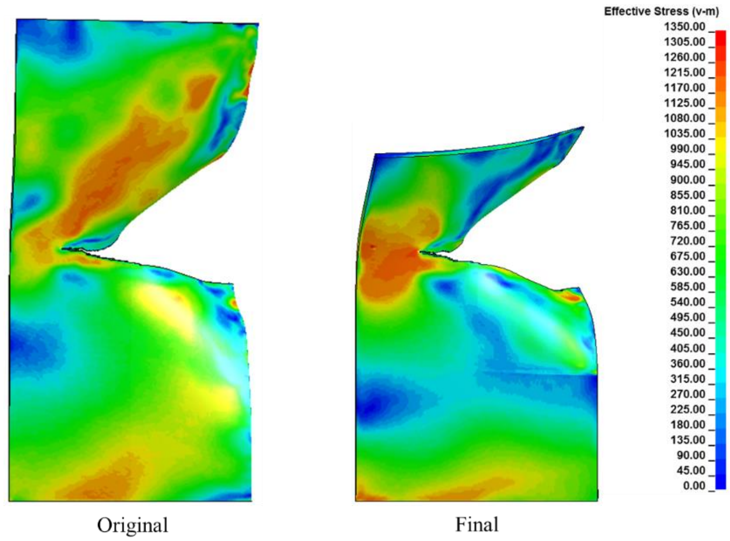

(d) Comparison of von-Mises stress (front view)

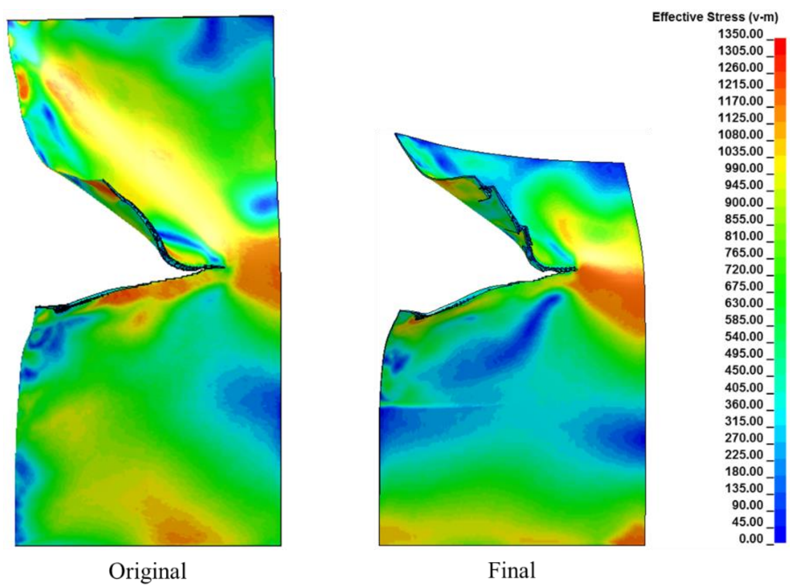

(e) Comparison of von-Mises stress (back view)

Figure 211. Comparison of original and final test article for test number B50L7.

Finally, the impact location, damage level D, and von Mises stress for both test articles for the 50% battery impact (B80A5) are shown in Figure 212.

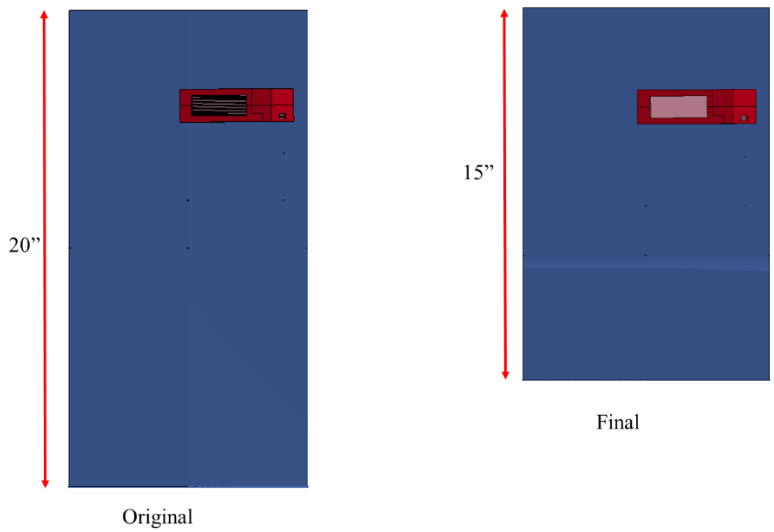

(a) Location of battery impacts on test articles

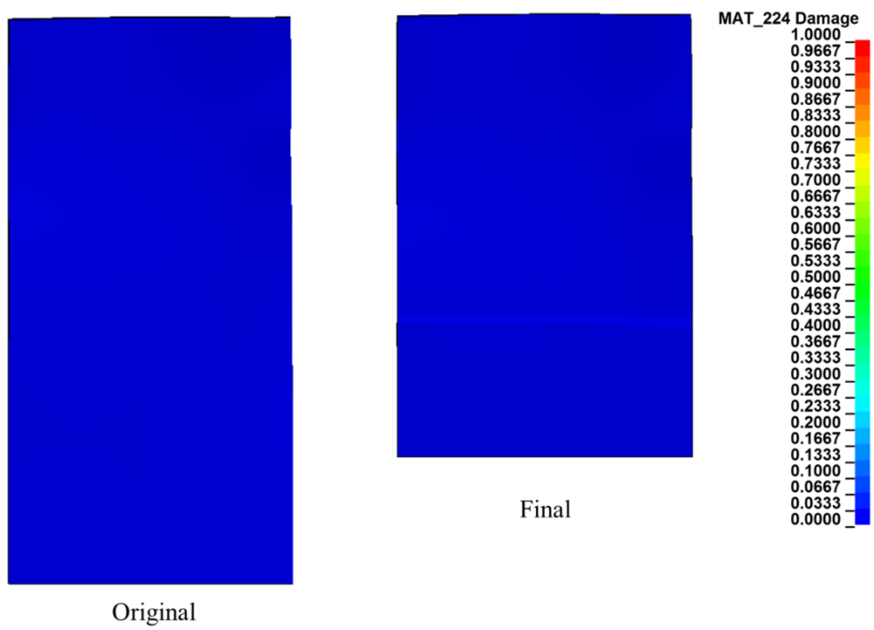

(b) Comparison of damage level (front view)

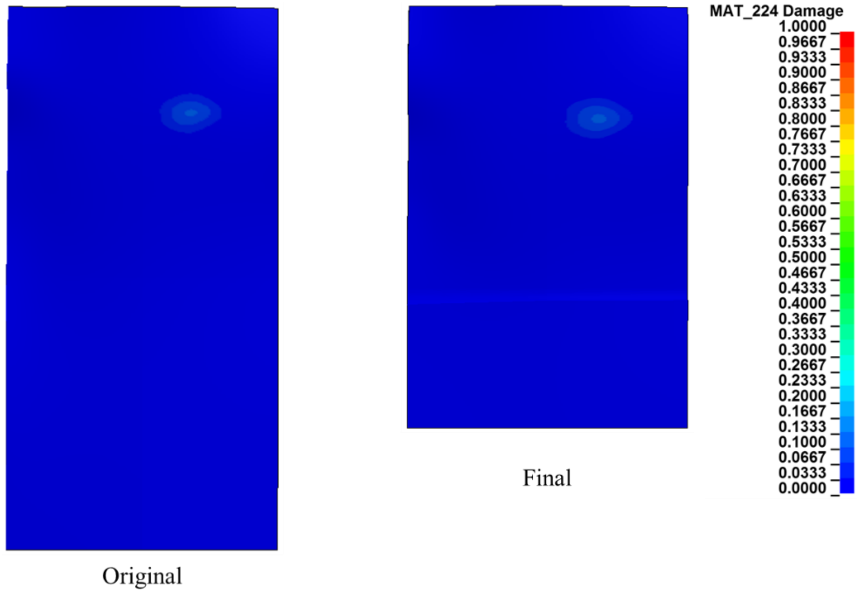

(c) Comparison of damage level (back view)

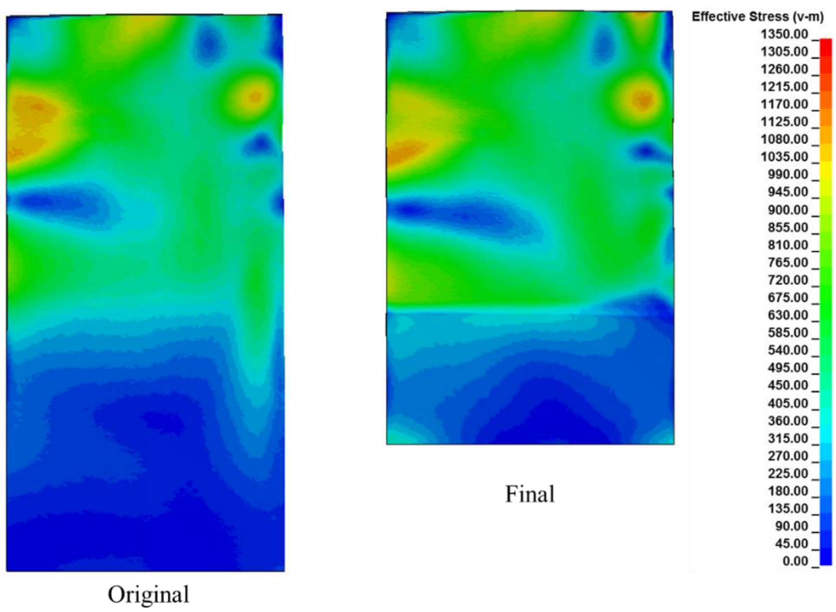

(d) Comparison of von-Mises stress (front view)

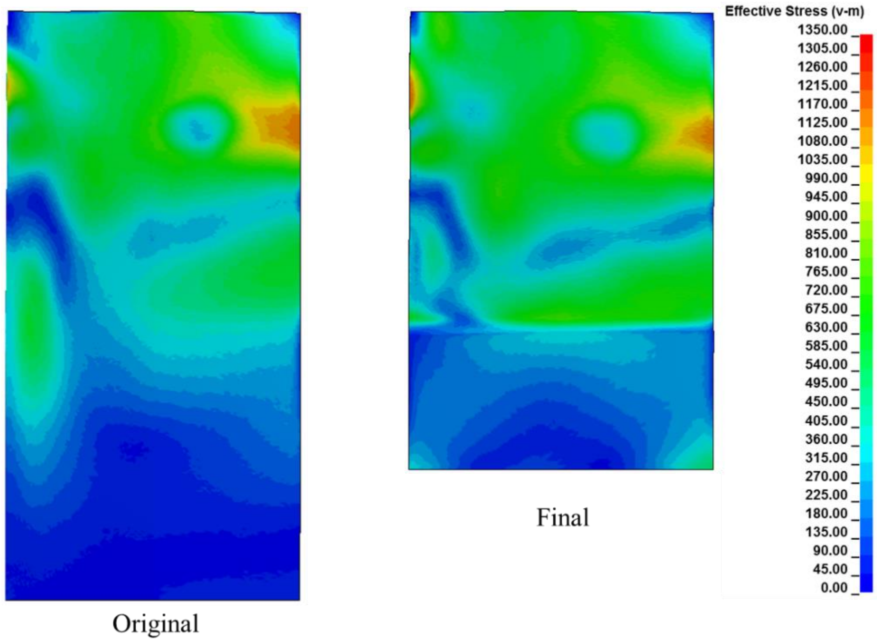

(e) Comparison of von-Mises stress (back view)

Figure 212. Comparison of original and final test article for test number B80A5.

It is clear from Figure 209 to Figure 212 that the level and types of damage and stress are very similar in all four cases studied, with the largest differences being in the fillet region in the final test article design. The fillet region is far enough away from the impact region to not have a significant overall impact on the results.

Due to the difference in size of the full UAS and the quadcopter components different test articles needed to be created so that the test article would not impact the fillet region of the test article. Images of the front and side view of the original and final geometry for the 50% radial impact test article are shown in Figure 213 and the 80% radial impact are shown in Figure 214.

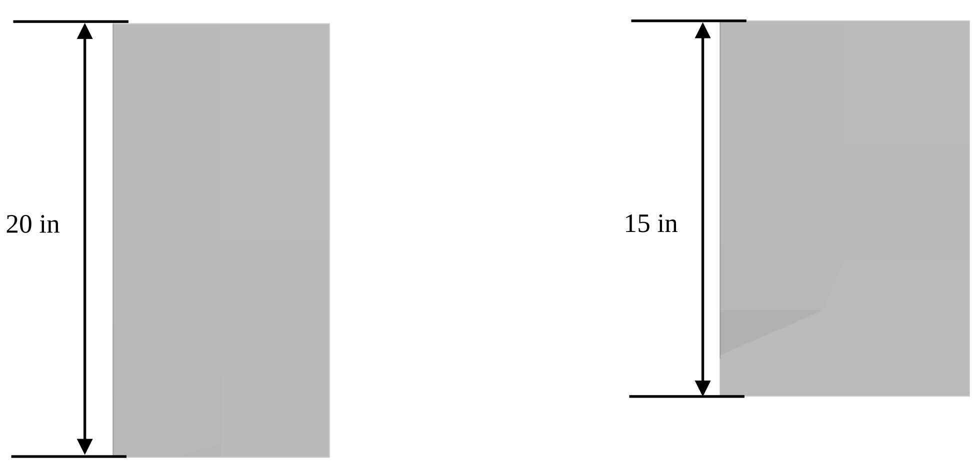

(a) Side view original (b) Side view final

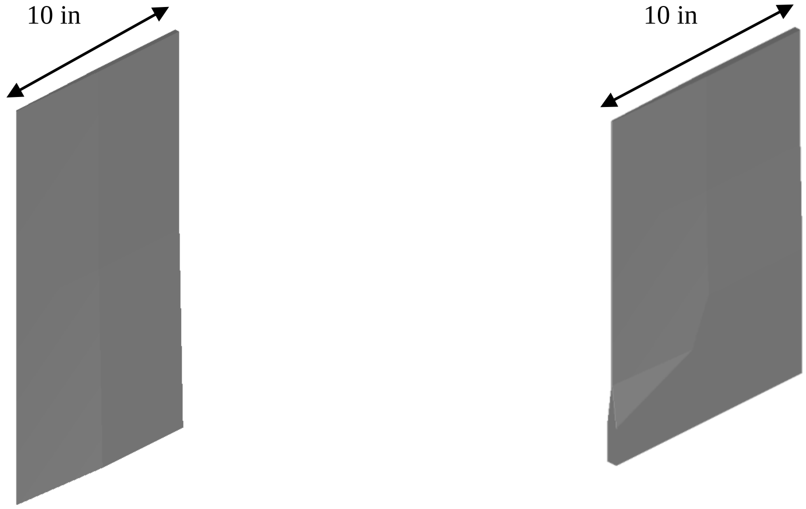

(c) Isometric view original (d) Isometric view final

Figure 213. Original and final test article for the 50% radial impact with full UAS (D50L5).

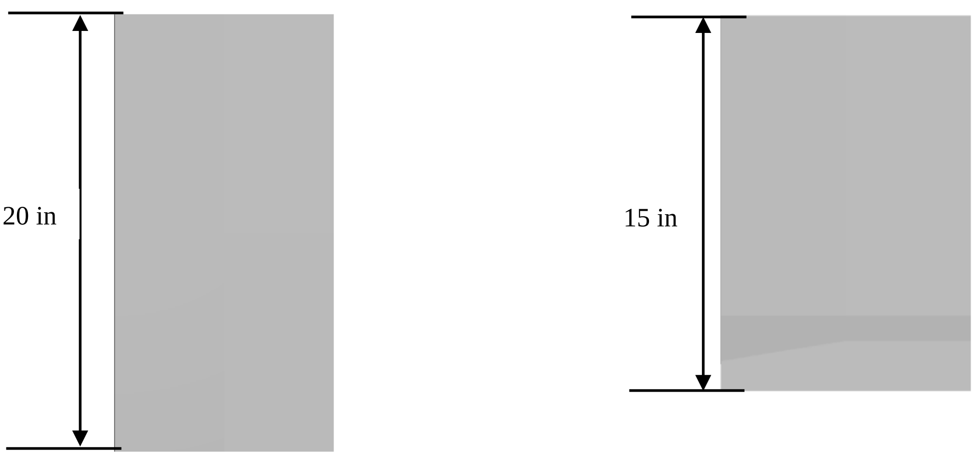

(a) Side view original (b) Side view final

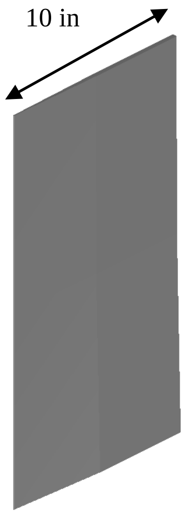

(c) Isometric view original

(d) Isometric view final

Figure 214. Original and final test article for the 80% radial impact with full UAS (D80L7).

Computational simulations with the initial full UAS model were conducted to compare the results for the two different test articles and were found to be in very good agreement. The impact location, damage level D, and von Mises stress for both test articles for the 50% UAS impact (D50L5: 50% radial span at 30° angle of impact from nominal orientation against the LE at 290 m/s) are shown in Figure 215.

Original test article

Final test article

Location of full UAS impacts on test articles

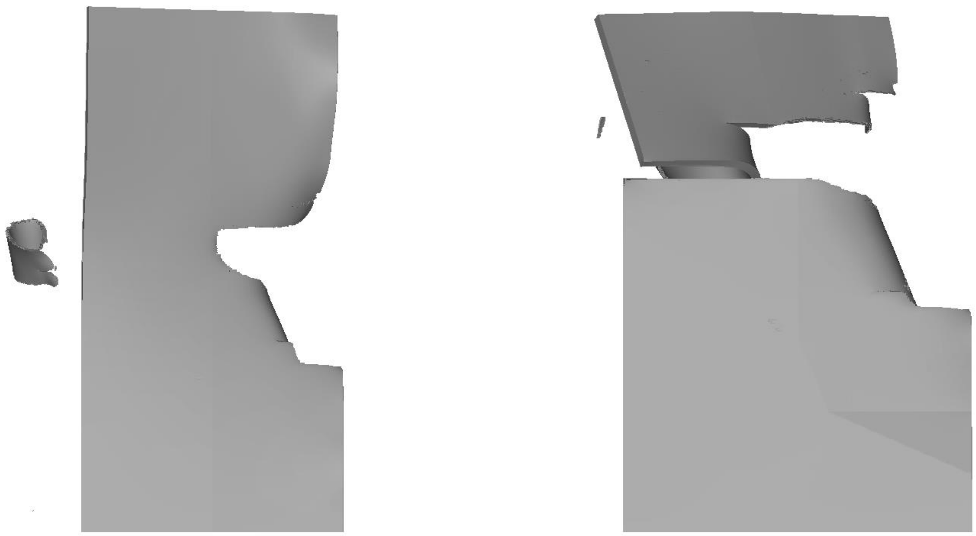

(b) Comparison of damage level (front view)

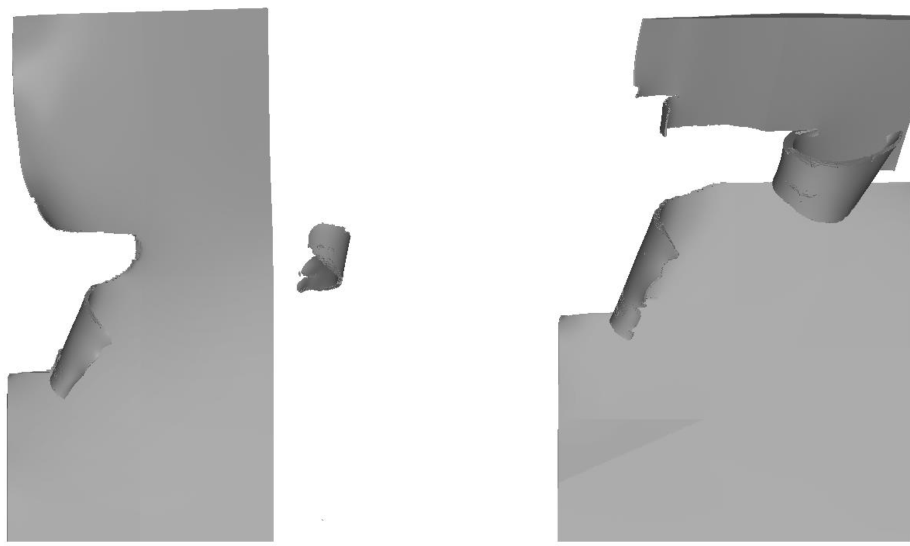

(c) Comparison of damage level (back view)

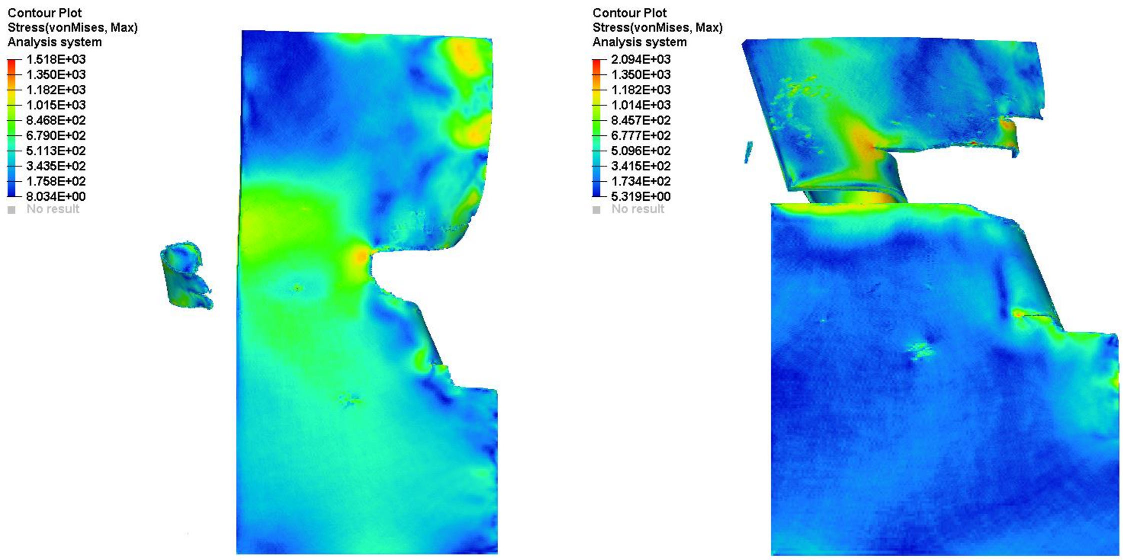

Original test article Final test article

(d) Comparison of von-Mises stress (front view)

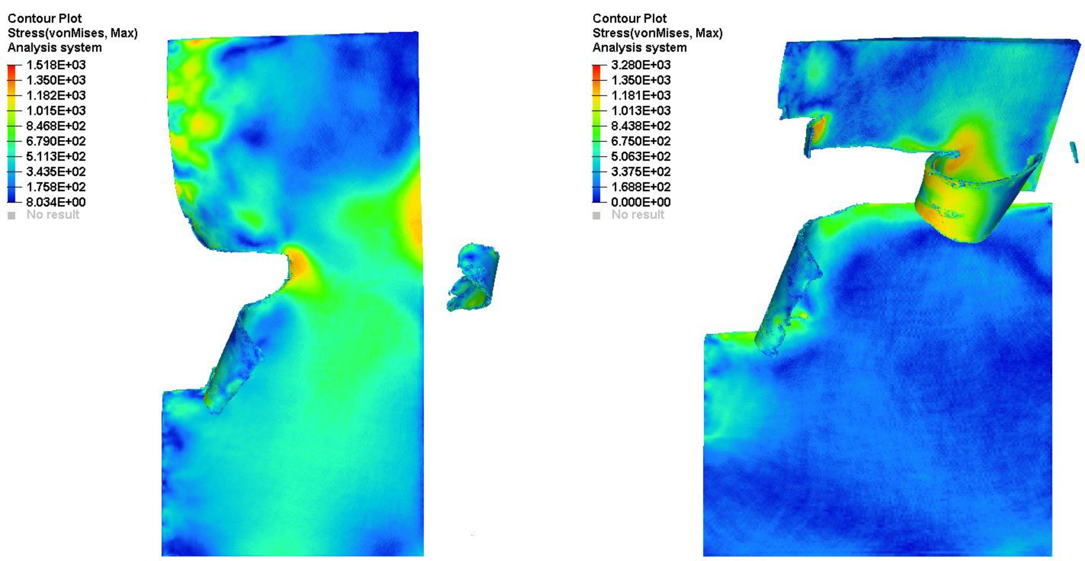

Original test article Final test article

(e) Comparison of von-Mises stress (back view)

Figure 215. Comparison of original and final test article for test number D50L5.

Finally, the impact location, damage level D, and von Mises stress for both test articles for the 80% UAS impact (D80L7) are shown in Figure 216.

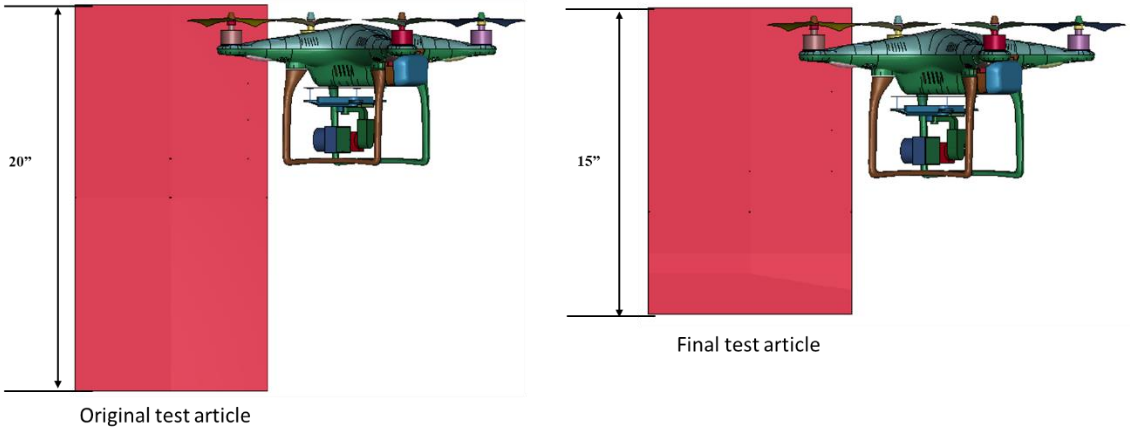

(a) Location of full UAS impacts on test articles

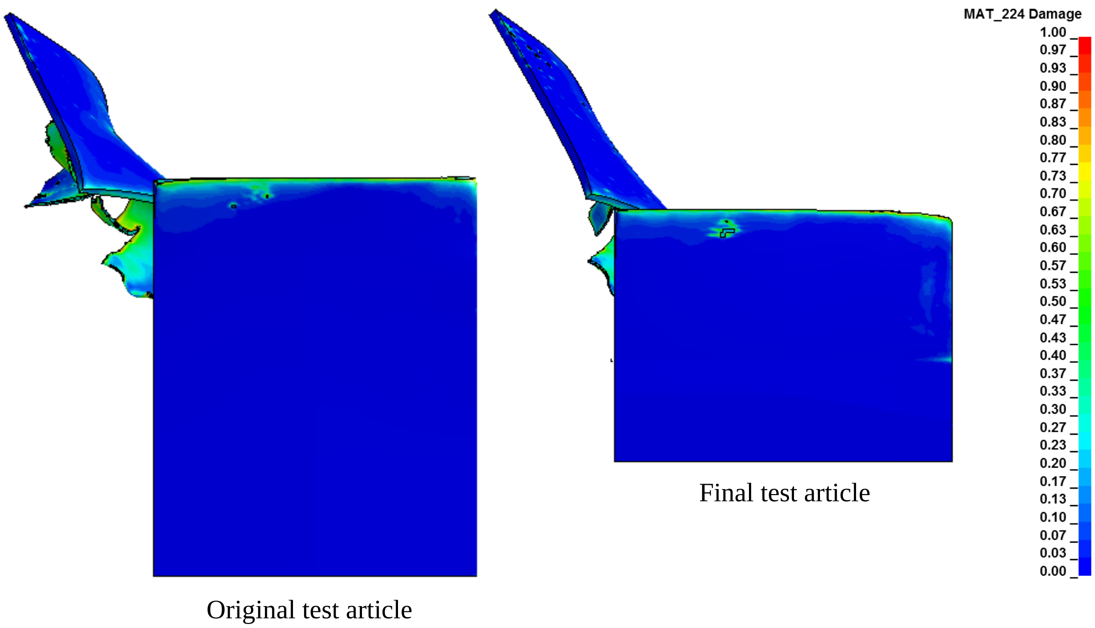

(b) Comparison of damage at 6.3 ms (front view)

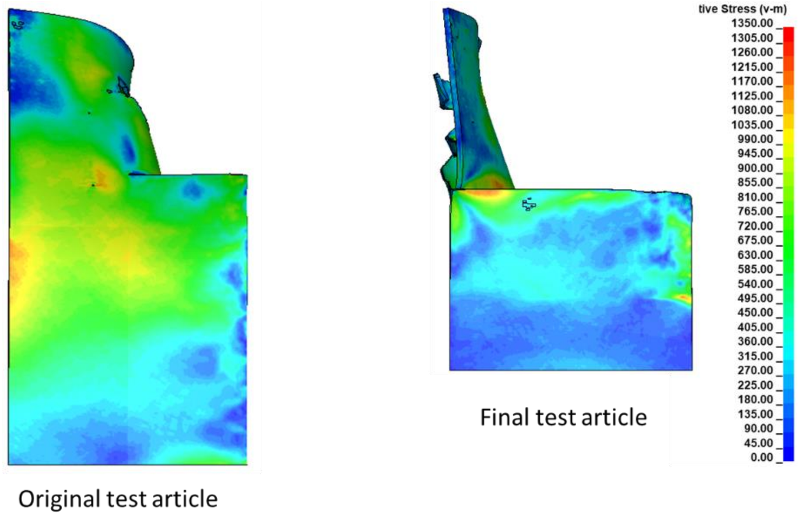

(c) Comparison of von-Mises stress at 3.5 ms (front view)

Figure 216. Comparison of original and final test article for test number D80L7.

It is clear from Figure 215-Figure 216 that the level and types of damage and stress are very similar in both cases studied with the largest differences being in the fillet region in the final test article design.